Université du Québec
Institut National de la Recherche Scientifique (INRS)
Centre Énergie, Matériaux et Télécommunications (EMT)

SPECTRAL GENERATION AND CONTROL OF LINEAR AND NONLINEAR SELF-ACCELERATING BEAMS AND PULSES

Par

Domenico Bongiovanni

Thèse présentée pour l'obtention du grade de
Philosophiae doctor (Ph.D.)
en Énergie, Matériaux et Télécommunications (EMT)
Varennes, Québec, Canada

Jury d'évaluation

Président du jury et Examinateur interne	Prof. François Vidal INRS-EMT, Québec, Canada
Examinateur externe	Prof. Mohammad Mojahedi University of Toronto, Ontario, Canada
Examinateur externe	Prof. Michel Piché Université Laval, Québec, Canada
Directeur de recherche	Prof. Roberto Morandotti INRS-EMT, Québec, Canada
Codirecteur de recherche	Prof. Yi Hu Nankay University, China
Codirecteur de recherche	Dr. Benjamin Wetzel INRS-EMT, Québec, Canada

Questa tesi e’dedicata a
Santa Rosalia, a mio papa’,
a mia mamma e tutta la mia famiglia.

Abstract

Unlike a conventional laser propagating along a straight line, a self-accelerating beam has the characteristic to follow a curved trajectory in a linear homogeneous medium, thus introducing transverse acceleration. Research on this field started in 2007 with the introduction of the Airy beam in an optical context. Such a beam propagates without diffraction along a parabolic trajectory, while exhibiting an Airy-shaped amplitude profile. Another property associated to the Airy beam is its capability of “self-healing”. Should one attempt to block a part of the beam at a certain distance, the Airy beam would “regenerate” during propagation. These intriguing features have made the Airy beam ideal for several applications in diverse fields of science. To name a few, we can mention optical bullets, curved plasma channels, electron accelerating beams and optical trapping. In the time domain, the counterpart to an Airy beam is an Airy pulse, showing the same properties in time when propagating in a linear regime. Nevertheless, in nonlinear media, an Airy beam/pulse behaves differently, due to the breakup of its acceleration by the nonlinearity. This constitutes a clear disadvantage, eventually limiting the possible range of applications of these wave packets. Meanwhile, over the last few years, the concept of acceleration has been extended beyond the parabolic case. In particular, further research advances on this topic have reported self-accelerating beams propagating along any arbitrary trajectory. Interestingly, the possibility to generate self-accelerating beams has also been investigated in the framework of the so-called “non-paraxial” regime, where beams accelerating along large bending angles have been demonstrated.

In this dissertation, we numerically and experimentally investigate the linear and nonlinear dynamics of optical self-accelerating wave packets. In the linear regime, one of the technique used to generate such wave packets is based on the spectral amplitude and phase modulation of a standard laser beam. We introduce an analytical approach able to predict theirs curved paths, in the one- (or (1+1)D), two- (or (2+1)D) and three-dimensional (i.e. spatio-temporal or (3+1)D) cases, starting from the knowledge of the applied spectral modulation. Conversely, our method allow us to achieve any desired convex path by accordantly designing the spectral modulation.

Based on this study, we also propose and demonstrate a practical and easy technique to confine the energy of self-accelerating wave packets. In particular, we show that a significant enhancement of the peak intensity of these beams can be achieved, while preserving their intrinsic properties.

Finally, we study the nonlinear propagation of Airy beams and pulses. Specifically, we show that these self-accelerating wave packets are capable to preserve their accelerating properties in Kerr and photorefractive nonlinear media when their initial spectral modulation is properly engineered.

Supervisor: Roberto Morandotti, Ph.D.
Title: Professor and Program Director

Contents

Chapter 1

Chapter 2

Chapter 3

Chapter 4

Chapter 5

Appendix A

Appendix B

Introduction

One of most apparent property of light which we observe in our daily life is its rectilinear propagation. Fundamental physics reports that light can behave either as a particle or as a wave, for which most optical phenomena can be described by the classical electromagnetic theory [1]. Actually, such a description can also be provided by means of simplified models, either based on geometric optics or wave optics. An essential result of geometric optics is that light, described as a collection of rays, travels through a straight line in free space or in a medium. At the interface between different media where the refractive index changes (and hence the light velocity), the light rays are refracted and reflected at the interface, thus changing their directions according to the Snell's law.

Depending on the exact interface shape, light rays that are refracted or reflected can be used to reshape light propagation (as required for example for reading glasses), or even lead to the formation of so-called "caustic" patterns. The word "caustic" comes from Latin and means "burning". In the optical context, a caustic is a curve or surface where an intense concentration of light is observed. In particular, a caustic corresponds to the envelope of a family of light rays that defines a boundary between two regions where the light intensity is respectively zero and nonzero. On one side of the caustic, the intensity decreases rapidly to zero, whereas on the other side, a complex pattern of interference fringes can be observed. Such an interference pattern arises from the interaction between at least two coherent waves, resulting in a change of the light intensity distribution. Depending on the phase of each wave, the optical intensity will increase (decrease) if a constructive (destructive) interference occurs. A typical example is shown below, where two cases of caustics commonly observed are those formed by the sunlight shining on a glass of water or at the bottom of a swimming pool.

Diffraction is another phenomenon that is known to deviate light from its rectilinear propagation. In contrast with refraction or reflection, diffraction is connected with light transmitted by an aperture or opaque obstruction. This phenomenon is explained by the Huygens's principle [2]. Such principle states that each point of a wave front acts as source of a secondary waves, which interfere so to create a new wave front. Diffraction is also responsible for the divergence of a standard laser beam along free space propagation, whose most famous example is the case of a Gaussian beam evolution and spatial spreading. However, diffraction can be overcome in order to preserve the beam profile shape, by employing optical waveguide or exploiting the nonlinear properties of some materials to compensate diffractive effects (through the generation of so-called solitons).

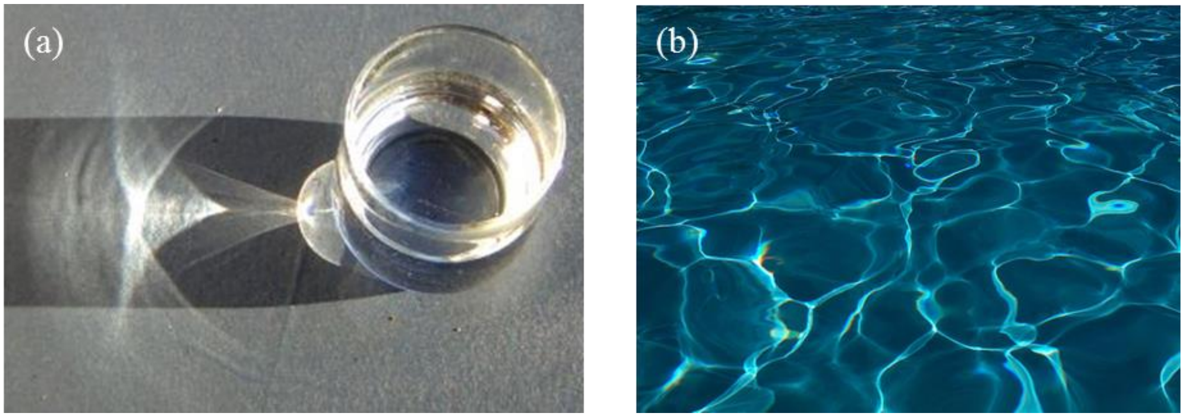

Figure I.1: Light caustics formed by sunlight incident on a glass of water and at the bottom of a swimming pool (Figure adapted from Wikipedia: www.wikipedia.org/wiki/Caustic_(optics)).

In 1987, J. Durnin introduced and demonstrated the zero-order Bessel beam [3-4], whose transversal intensity profile is described by a Bessel function. More importantly, a Bessel beam maintains invariant its intensity profile during the propagation, and is therefore referred as non-diffracting beam. Since its discovery, the term "non-diffracting beam" has been extended to the free-space case, while more general types of shape-preserving beams have also been reported [5-8]. The diffraction invariance of these beams is explained by looking at the particular composition of their spectra, which rely on the superposition of plane waves whose wavevectors are localized onto a conical surface, while carrying an infinite energy.

This is the reason why ideal non-diffracting beams cannot be physically realized. In practice, only a finite energy version of these beams can be experimentally obtained, by ‘bounding’ an ideal non-diffracting beam through a transmitting finite or Gaussian aperture. A way to obtain such finite-energy non-diffractive beams is to employ light modulation methods. In particular, the wave front of a collimated Gaussian beam is amplitude or/and phase modulated by means of optical devices that can be either passives (e.g. slit, wedge, grating, axicon lens, etc.) or actively controlled (such as Spatial Light Modulator (SLM). By properly engineering the amplitude and phase masks, the modulation results in the formation of an electric field profile corresponding to the desired non-diffracting beam. It is worth mentioning that light can be generally controlled by modulating its wave front both in amplitude and phase in either the real or Fourier space.

Nevertheless, the above-mentioned non-diffracting beams are only found in the two spatial dimensions (2+1)D regime. Non-diffracting spatio-temporal (or (3+1)D) configurations that are impervious to both dispersion and diffraction have also been proposed [9-10]. Similar to diffraction in space, dispersion broadens the temporal profile of a wave packet because its different frequency components travel with different phase velocities, due to the frequency-dependence of the refractive index of the material. In the (1+1)D regime, an Airy wave packet is the unique free-dispersive configuration. Such mathematical function was introduced in the field of quantum mechanics more than thirty years ago by Berry and Balazas [11], as a singular solution of the Schrödinger equation describing the motion of a particle in absence of an external potential. Its profile is analytically described by an Airy function [12] and tends to accelerate with a parabolic evolution. In 2007, the Airy beam was also introduced and demonstrated in the optical framework by G. Siviloglou *et al.* [13-14]. Like its counterpart in quantum mechanics, an Airy beam is able to propagate in free-space along a parabolic trajectory. In particular, it possesses the properties of non-diffraction and self-healing (i.e. it regenerates itself after being obstructed at a given distance [15]). The main outcome of the Airy beam (re)discovery lies in the possibility to “engineer” light that does not propagate along a straight line. From a physical viewpoint, the bending propagation of such a beam can be explained as an interference of optical waves resulting in the formation of a caustic appearing in the Airy intensity profile of the beam. Such a beam is physically generated by impressing a cubic phase modulation to an input laser in the Fourier domain. Over the last few years, important research efforts on this topic have been dedicated to extend and expand the concept of Airy beam to a more general class of self-accelerating wave packets. For example, self-accelerating beams propagating along any arbitrary convex trajectory can be designed by engineering the phase of a light-beam in the real space [16-17] or in its Fourier counterpart [16,18]. Such self-accelerating beams exhibit Airy-like intensity profiles, but are ultimately affected by diffraction and remain non-broadening only over a limited propagation range. The concept of self-accelerating beam has been also extended into the non-paraxial regime, where the curved trajectories of larger bending angles do not comply anymore with the paraxial approximation [1]. It should be mention that Airy beams tend to break up in such a non-paraxial regime, and their use is therefore limited in many applications. To date, we can generate beams propagating along a circular, a parabolic and an elliptical trajectory, respectively corresponding to the patterns described by a half-Bessel [19-20], a Weber or a Mathieu [21] function. Besides these methods, non-paraxial beams can also propagate along any arbitrary convex trajectory by means of engineering the initial beam phase structure in both real [17,22-24] and Fourier regime [18].

Under nonlinear propagation regime (i.e. when the refractive index is dependent of the local beam intensity), the accelerating property of a spatial or temporal Airy wave packet is affected by the nonlinearity, especially when considering an evolution under a so called “self-focusing” nonlinear regime [25-27]. Several efforts have been made to control and preserve the self-accelerating trajectory under different nonlinear effects, such as Kerr, photorefractive (PR) and quadratic media [26,28-31]. The formation of accelerating self-trapped optical beams was alternatively proposed by employing different self-focusing and defocusing nonlinearities [31-32].

In contrast to all the non-diffractive beams reported in the literature, an Airy beam can exist in the one-dimensional (1D) configuration. This offers an opportunity to generate Airy pulse as a result of time-space duality. In analogy with its counterpart in the spatial domain, an Airy pulse propagates without the pulse spreading typically arising from dispersion, and for which the pulse envelope tends to either accelerate or decelerate. In this context, several works have been reported regarding Airy pulse propagating under different dispersion regimes (i.e. with the inclusion of higher-order dispersion) or mediated by nonlinear effects, especially in fiber optics systems [27,33-36]. One of most interesting applications of Airy pulses is the synthetization of linear optical Airy bullets, which are both non-diffractive and non-dispersive spatio-temporal wave packets. Such types of bullets can be achieved by combining an Airy pulse and a two-dimensional (2D) non-diffractive beam, such as for example Bessel and 2D Airy beams [37-38]. In particular, an Airy bullet obtained by combining an Airy pulse and a 2D Airy beam retains all the intriguing properties of its two-dimensional counterpart, such as both a parabolic trajectory and self-healing. In this framework, self-accelerating beams have been proposed for several applications in optics and many other fields. For instance, their bending trajectory have been employed to generate curved plasma channels [39]. In the field of bio-photonics, they have been utilized for optical trapping, e.g., attracting and moving particles from one box to another along a curved trajectory [40]. It should be noted that the concept has also been extended to other fields of physics. Very recently, Airy electron beams and curved electric discharge were also observed [41-42].

In the following, we report our results and achievements on self-accelerating wave packets evolving in both a linear and a nonlinear regime. In particular, we study their propagation dynamics by focusing our attention on the spectral features displayed by these peculiar optical wave packets.

In Chapter 1, we provide an overview on the linear and nonlinear generation and control of self-accelerating wave packets and recent developments in this area. At first, the propagation dynamics and the intriguing properties of optical Airy beams are reviewed. Then, we introduce in some details the state-of-the-art regarding paraxial and non-paraxial self-accelerating beams and their propagation dynamics in free-space. An overview of the most important works studying the nonlinear dynamics of these beams is also provided in this chapter. In the temporal domain, we provide examples illustrating the propagation dynamics of Airy pulses in optical fibers under different dispersive and nonlinear regimes. In the spatio-temporal regime, we also explain the concept of linear optical Airy bullet and present the efforts carried out so far to their achievement. Finally, we succinctly provide a summary of the most important applications proposed and demonstrated to date for self-accelerating beams in optics and other related physical systems.

Although self-accelerating beams can be engineered along any arbitrary convex trajectory in the linear regime, until now most efforts were focused into the study of smooth and single-path light localizations. From a physical point of view, this beam evolution relies on the application of specific monotonic phase modulations, in the either the real or Fourier domain. To date, the presence of non-monotonic phase modulations has not been investigated. Therefore, it is natural to wonder whether the application of a non-monotonic phase can lead to multi-path accelerating beams or analogous dynamics. Furthermore, several studies have also introduced self-accelerating beams propagating along curved and periodic trajectories rather than smooth paths [20,43-44]. Such periodic accelerating beams can be realized by applying both a phase and an amplitude modulation in the Fourier regime. Nevertheless, they lack of a general and detailed explanation which may pave the way to the design of beams with any desired profiles. Besides, most of the works reported to date are limited to the consideration of 1D beam configurations only, and mainly focused on engineering the beam trajectory. The 2D dynamics and spatio-temporal configurations that can provide useful tools for practical applications has not been examined in a general way. Another aspect that is worth investigating is the possibility to optimally confine the energy carried by these 2D and three-dimensional (3D) wave packets, usually associated with patterns occupying a large area filled by an intense main lobe and several sub-lobes. This feature constitutes a disadvantage, especially for applications where low energies and a high confinement are simultaneously required. Oddly, the relevant problem of the optimal energy confinement has been ignored up to now, especially for arbitrary trajectories. Although some works reported 2D self-accelerating beams with a short tail of sub lobes, those were only limited to a parabolic trajectory case, and do not quantify the energy confinement achieved by these beam profiles [45-47]. In the nonlinear regime, the main issue comes from maintaining the accelerating property of these wave packets in the presence of various nonlinear effects. As mentioned above, several works reported that an Airy beam (as well as an Airy pulse) is not able to preserve the self-accelerating features when propagating in photorefractive or Kerr media [25-

26]. Thus, it is reasonable to question whether it is possible to find a method to maintain, even in the presence of a strong self-focusing or de-focusing nonlinearity, the accelerating properties of high-intensity Airy beams or pulses.

In this dissertation, we specifically address these issues by investigating the linear and nonlinear dynamics of self-accelerating wave packets from the viewpoint of the Fourier spectrum and, in particular, by emphasizing the connections with the real space features of these wave packets. The novel results reported in this thesis are organized according to the following structure:

In Chapter 2, we introduce the concept of spectral phase gradient. We show that this concept defines a spectrum-to-space mapping, in which different key spatial frequencies are related to different propagation distances. The trajectory of a self-accelerating beam can be thus determinated *a priori* through this mapping. Furthermore, our theory allows to estimate the spectral phase required for generating a beam with any desired convex trajectory. We show, both theoretically and experimentally, that this approach can be used to generate one-dimensional single- and multi-path self-accelerating beams, in the paraxial approximation. We also demonstrate that the method can be applied to non-paraxial self-accelerating beams as well as vectorial wave fronts. In particular, the breakup of the Airy beam in the non-paraxial regime is discussed from another viewpoint. In the same chapter, the combined influence of a spectral phase and amplitude modulation on the dynamics of curved beams is also investigated. We demonstrate, both analytically and experimentally, the possibility of generating self-accelerating beams evolving along any “periodic” convex path.

In Chapter 3, we generalize the concept of spectral phase gradient to the (2+1) and (3+1)D regime. Similarly to the case of 1D self-accelerating beams, we can either predict the convex trajectories or estimate the spectral phase associated to these self-accelerating wave packets through a spectrum-to-distance mapping. Taking advantage of the spectral features of these wave packets, i.e. by appropriately reshaping their Fourier spectra, we also propose and demonstrate a practical method to confine the energy of the beam predominantly into its main hump. We report experimental observations of optimized 2D self-accelerating beams for three typical trajectories generated by designing an appropriate spectral phase and amplitude modification based on our theoretical findings. In the spatio-temporal regime, i.e. (3+1)D, we investigate the extension of this approach for generating optical Airy bullets with a reduced spatio-temporal expansion, thus associated with an enhanced energy confinement. Finally, we verify that these optimized self-accelerating wave packets in both (2+1) and (3+1)D regimes retain both the expected acceleration profiles and the intrinsic self-healing properties.

In Chapter 4, we investigate the evolution of optical Airy beams and pulses under various scenarios of nonlinear propagation regimes. Spatial Airy beams are studied in photorefractive media in the presence of either a self-focusing or a self-defocusing nonlinearity, while temporal Airy pulses dynamics are considered in optical fiber propagation under the combined influence of a normal (and an anomalous) group velocity dispersion with a nonlinear Kerr effect. We demonstrate, both numerically and experimentally, a scheme to preserve and control the bending propagation and the spectral features of these optical wave packets even under nonlinear conditions. In particular, we experimentally observe that the linear spectrum of an Airy wave packet is dramatically reshaped under nonlinear propagation, and that most of the spectral content becomes concentrated into self-shifting positive or negative defect, formed by one or two peaks. In correspondence of the defect area, we show that the central frequency of both positive and negative defects linearly changes at each propagation distance, thus indicating a mapping between propagation distance and frequency domain.

Chapter 1

Review of the literature

Self-accelerating beams are optical light localizations that are capable of propagating along curved paths. The Airy beam was the first self-accelerating beam to be introduced and demonstrated in optics. This optical beam can propagate along a parabolic trajectory without experiencing diffraction. Over the last few years, the research on this field has been growing rapidly: New types of self-accelerating beams have been introduced and several applications have been proposed in optics and related fields of physics. In this chapter, we provide a brief overview of the state of the art regarding this subject. Since it expands well beyond the scope of the work reported in this thesis, this literature review does not mean to be exhaustive, but rather introduces the concepts required for understanding what is reported in the next chapters as well as to provide a broader context to the problematics treated in this thesis.

1.1 Diffractive and non-diffractive beams

When a typical laser beam propagates in free-space, its transversal Gaussian intensity profile undergoes a continuous broadening because of diffraction. In the temporal domain, dispersion affects the propagation of an optical Gaussian pulse in a dielectric medium, usually leading to the spreading of the pulse profile and to an increase of its duration. Over the years, non-diffractive and non-dispersive wave packet configurations have been reported in optics as well as in other physical systems. Such optical localized wave packets are shape-preserving during propagation, and can be introduced in the two-dimensional (2D) or three-dimensional (3D) regime. The most widely known non-diffracting wave packet is the Bessel beam which was first introduced by J. Durnin *et al.* [3-4]. This pioneering work has paved the way to the discovery of other non-diffractive solutions [5-8] including Mathieu [8] and parabolic beams

[6], as well as high-order Mathieu [7] and Bessel beams [5]. In optical systems, such as photonics crystals, exhibiting normal and anomalous diffractions along the two different directions, non-diffractive X-waves [9] and Bessel-like beams [10] have been also introduced. However, such non-diffractive beams exhibit non-diffractive propagation because they convey infinite power. Although not realistic from an experimental viewpoint, in practice, quasi "diffraction-free" beams can be obtained with a finite-energy version – essentially truncated by an aperture. In this case, the diffraction rate can be significantly slowed-down depending on the truncation factor used. Recently, self-accelerating wave packets capable of propagating along a curved trajectory have attracted a great deal of interest. Among them, the Airy beam (or pulse), first introduced in optics, propagates along a parabolic trajectory without any diffraction (or dispersion) [11,13]. Unlike other non-diffractive configurations, Airy wave packets can also exist in the 1D regime. Since its first demonstration, an ever increasing interest has been devoted not only to the study of Airy beams, but also of self-accelerating wave packets in general. In the following chapter, we provide an overview of the recent developments in this research area, essential to placing the results provided throughout this thesis in an appropriate multidisciplinary context, while offering the key scientific concept needed for its understanding. In particular, starting from the concept of Airy beams, we discuss a selection of publications reporting on numerical and experimental studies in the field of self-accelerating wave packets in different frameworks, such as spatial and temporal, linear and nonlinear regime, as well as the most relevant proposed and demonstrated applications.

1.2 Paraxial approximation of the light

In optics, the light propagation is generally described by the Maxwell's equations [1]. Let us consider a scenario where a one-dimensional (1D) optical beam (with *x*-axis variation) is propagating in free-space along the *z*-axis, and is also linearly polarized along the *x*-axis. In this case, the optical beam is only experiencing diffraction along the *x*-axis. Under this condition, the propagation dynamics of a linearly-polarized electric field $\mathbf{E}(x,z,t) = E_x(x,z,t)\boldsymbol{x}$ can be described by the scalar wave equation [2]:

$$\frac{\partial^2 E_x}{\partial z^2}+\frac{\partial^2 E_x}{\partial x^2}-\frac{n_0^2}{c^2}\frac{\partial^2 E_x}{\partial t^2}=0. \qquad (1.1)$$

In the Eq. (1.1), $E_x(x,z,t)$ the *x*-component of the electric field, *t* is the time coordinate. Solutions to Eq. (1.1) can be found by defining $E_x(x,z,t)$ as:

$$E_x(x,z,t)=E(x,z)e^{i(kz-\omega_0 t)}, \qquad (1.2)$$

where $E(x,z)$ and $k=n_0\omega_0/c$ refer to the complex envelope and the wavenumber, respectively, while ω_0 is the angular frequency, n_0 is the refractive index, and *c* the light velocity. By substituting the latter expression into Eq. (1.1), the complex envelope $E(x,z)$ of the *x*-component of the electric field obeys to the Helmholtz equation, explicitly expressed as:

$$2ik\frac{\partial E}{\partial z}+\frac{\partial^2 E}{\partial z^2}+\frac{\partial^2 E}{\partial x^2}=0, \qquad (1.3)$$

Under the paraxial condition, the approximation $|\partial^2 E/\partial z^2| << 2k|\partial E/\partial z|$ is valid, hence propagation dynamics can be described by the paraxial wave equation of diffraction so that:

$$i\frac{\partial E}{\partial z}+\frac{1}{2k}\frac{\partial^2 E}{\partial x^2}=0. \qquad (1.4)$$

1.3 Optical Airy beam

In the context of quantum mechanics, M. Berry and N. Balazas theoretically demonstrated in 1979 that the Schrödinger equation describing the propagation of a free particle admits an Airy wave packet as a unique non-spreading solution in the (1+1)D regime [11]. In this paper, not only they demonstrated that an Airy wave packet remains invariant in time, but also that the Airy solution is able to accelerate along a parabolic trajectory in the absence of any external potential. Nevertheless, this work has been set aside for about thirty years due to the fact that such an Airy wave packet could not be experimentally realized in quantum mechanics. Meanwhile, optics has offered, over the years, a fertile and straightforward ground to investigate and demonstrate the proprieties of non-spreading or non-dispersive wave configurations, even though initially introduced in other physical settings such as atom physics. This analogy origins from the mathematical correspondence between the paraxial Helmholtz equation in optics and the Schrödinger equation in quantum mechanics [48]. In 2007, G. Siviloglou *et al.* [13-14] proposed and demonstrated experimentally the first generation of an optical Airy wave packet in optics (commonly referred as Airy beam). In what follows, and in in order to introduce the reader to the context, we will provide a detailed digression about their work.

1.3.a Infinite-energy Airy beam

The analysis starts from the normalized (1+1) D paraxial Helmholtz equation that governs the propagation dynamics of the electric field envelope $\varphi(s,\xi) = E(s,\xi)$ of an optical beam:

$$i\frac{\partial\varphi}{\partial\xi}+\frac{1}{2}\frac{\partial^2\varphi}{\partial s^2}=0, \tag{1.5}$$

where $s = x/x_0$ and $\xi = z/k_0 n_0 x_0^2$ denote normalized transverse and longitudinal coordinates, k_0 is the vacuum wave number, and x_0 is an arbitrary length scale. This equation assumes that the angle between the propagation axis and wave vectors is small enough so that the wave does not significantly deviate from it. The solution to Eq. (1.5) is a non-spreading Airy beam [11,13]:

$$\varphi(s,\xi)=Ai\left[s-\frac{\xi^2}{4}\right]\exp\left(is\frac{\xi}{2}\right)\exp\left(-i\frac{\xi^3}{12}\right), \tag{1.6}$$

where Ai is the Airy function [12] and $\varphi(s,0) = Ai(s)$ is electric field envelope at the input ($\xi = 0$). Eq. (1.6) shows that this Airy solution is diffraction-free, and experiences a transverse shift along a parabolic curve ($s = \xi^2/4$) during propagation [Fig. 1.1]. An ideal Airy beam is characterized by an asymmetric amplitude profile, formed by a more intense main lobe and an oscillating tail of sub-lobes decaying very slowly for negative values of s, (i.e. $Ai(-s)\approx\pi^{-1/2}s^{-1/4}\sin(2/3s^{3/2}+\pi/4)$) as $s\to+\infty$) [12].

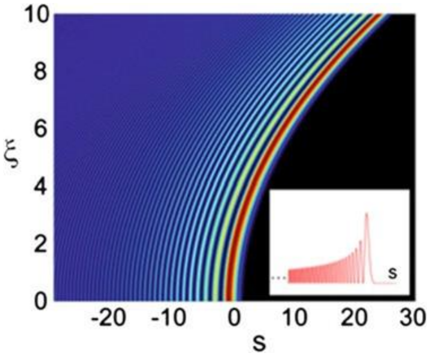

Figure 1.1: Propagation dynamics of an inifnite-energy Airy beam. False color plot of the spatial evolution of the Airy beam intensity. The red inset shows the corresponding input intensity profile. (Figure reproduced from Ref. [14]).

For positive values of *s*, the Airy solution decays exponentially. An interpretation of the acceleration process was provided by D. Greenberger through the principle of equivalence [49]. Other physical interpretations explain the origin of the bending propagation as an interference of straight line rays converging into a caustic [17-18,50-52]. The free-diffraction property is essentially associated with the inherent infinite-energy nature of the beam profile. In fact, an Airy beam is not square integrable $\left(\int_{-\infty}^{+\infty} |Ai(s)|^2 \, ds \to +\infty\right)$, and as consequence the center of mass cannot be defined. This means that the self-accelerating behavior does not violate the Ehrenfest's theorem [48], describing the motion of a center of mass. In practice, "ideal" Airy beams are impossible to realize experimentally, as they would require an infinite amount of energy. An Airy beam can still be synthesized by using a truncation aperture function, thus obtaining a finite-energy Airy beam (also commonly called Airy beam by extension) [13-14,53].

1.3.b Finite-energy Airy beam

The most common way to obtain a finite-energy Airy beam is by applying an exponential aperture function at the system's input such as [13-14]:

$$\varphi(s,0) = Ai(s)\exp(\alpha s), \tag{1.7}$$

Where $\alpha > 0$ is the truncation factor [Fig. 1.2(a)]. The solution to Eq. (1.5) with the initial condition of Eq. (1.7) is found to be:

$$\varphi(s,\xi) = Ai\left[s - \frac{\xi^2}{4} + i\alpha\xi\right]\exp\left(\alpha s - \alpha\frac{\xi^2}{2}\right)\exp\left(-i\frac{\xi^3}{12} + i\alpha^2\frac{\xi}{2} + is\frac{\xi}{2}\right), \qquad (1.8)$$

which reduces to the ideal case when $\alpha = 0$. Unlike the ideal case, the total power associated to this truncated Airy beam possesses a finite value that is dependent on the truncation parameter α as:

$$\int_{-\infty}^{+\infty} \left|Ai(s)\exp(\alpha s)\right|^2 ds = \sqrt{\frac{1}{8\pi\alpha}}\exp\left(\frac{2\alpha^3}{3}\right) \qquad (1.9)$$

Despite the initial truncation, this finite-energy Airy beam still exhibits the property of an ideal Airy beam. It tends to self-accelerate along the same parabolic trajectory with a quasi-diffraction free propagation. In the work proposed by G. Siviloglou *et al.* [13-14], an Airy beam was propagated up to a distance of 1.25 m, using $\alpha = 0.1$, $x_0 = 100$ µm and $\lambda = \lambda_0 / n_0 = 0.5$ µm. For these values, the intensity full-wave half maximum (FWHM) width of the (more intense) main lobe is 173 µm.

As shown in Figs. 1.2(b, c), such an Airy beam not only shifts transversally during propagation, but its main hump also remains almost invariant for 75 cm of propagation before being affected by diffraction. Interestingly, the authors also reported that a conventional Gaussian beam with the same initial width would, for the same propagation distance, have undergone a spatial expansion 6 times larger. Moreover, it is possible to define the center of mass of a finite-energy Airy beam. In particular, such a center of mass is constant with distance and is described by the following equation: $\langle s(\xi)\rangle = 1/N\int_{-\infty}^{+\infty} s\left|\varphi(s,\xi)\right|^2 ds = (4\alpha^3 - 1)/4\alpha$, where $N = \sqrt{1/(8\pi\alpha)}\,\exp(2\alpha^3/3)$ [54-55].

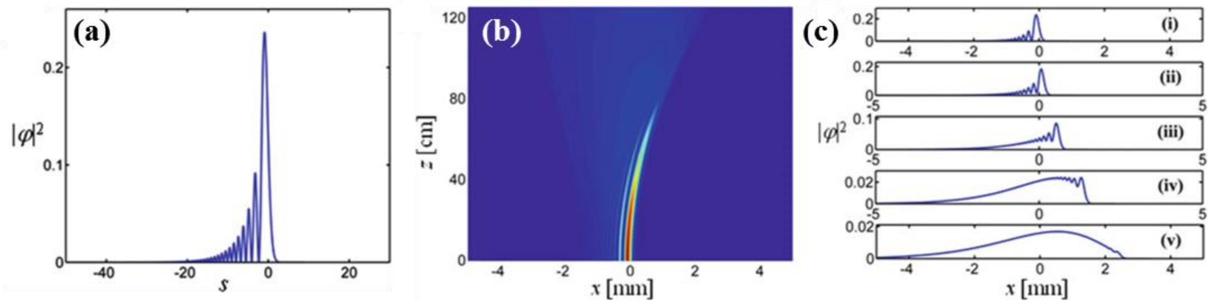

Figure 1.2: Propagation dynamics of a finite-energy Airy beam. (a) Input intensity profile as a function of the normalized trasversal coordinates *s*. (b) Intensity distribution showing the propagation dynamincs of a finite-energy Airy beam. (c) Intensity profiles as a function of the real trasversal coordinate *x* at selected distances *z* ((i) z = 0 cm, (ii) 31.4 cm, (iii) 62.8 cm, (iv) 94.3 cm, and (v) 125.7 cm). (Figure adapted from Ref. [13]).

The results obtained for the one-dimensional (1D) Airy beams were readily generalized to the (2+1)D scenario. In this case, the solution is found by solving the normalized (2+1)D paraxial equation:

$$i\frac{\partial\hat{\varphi}}{\partial\xi}+\frac{1}{2}\frac{\partial^2\hat{\varphi}}{\partial {s_x}^2}+\frac{1}{2}\frac{\partial^2\hat{\varphi}}{\partial {s_y}^2}=0 \tag{1.10}$$

where $\hat{\varphi}\left(s_x,s_y,\xi\right)$ is the electric field envelope, $s_x = x/w_0$ and $s_y = y/w_0$ are, respectively, the normalized transverse coordinates (with w_0 scale factor) along the *x* and *y* directions, and $\xi = z/k_0 n_0\ w_0^2$ denotes the normalized longitudinal coordinate. α_x and α_y are the truncation parameters along *x* and *y*. One easy way to find a two-dimensional (2D) Airy beam is obtained by multiplying two 1D Airy solutions, respectively along the *x* and *y* directions as:

$$\hat{\varphi}\left(s_x,s_y,0\right)=Ai\left(s_x\right)Ai\left(s_y\right)\exp\left(\alpha_x s_x\right)\exp\left(\alpha_y s_y\right), \tag{1.11}$$

The evolution of a 2D Airy beam is found as:

$$\hat{\varphi}\left(s_x,s_y,\xi\right)=\varphi\left(s_x,\xi\right)\varphi\left(s_y,\xi\right), \tag{1.12}$$

where $\varphi(s_i, \xi)$ ($i = x$ or y) are the 1D electric field profiles in Eq. (1.8). This 2D Airy beam has an asymmetric intensity profile composed by a highly-confined main lobe spot in the (x- y) plane, and two long tails of sub-lobes [Fig. 1.3(a)]. In the same study, Siviloglou *et al.* [2-3] also investigated numerically the evolutions of this 2D field configuration by using $\alpha_x = \alpha_y = 0.11$ and $w_0 = 53$ µm. In contrast to its counterpart in the 1D regime, results showed quasi non-diffractive propagation. The size of the main lobe spot remained almost invariant up to a distance of 25 cm, while accelerating in the longitudinal direction on the 2D parabolic trajectory with $s_x = s_y = \xi^2/4$. In the transverse plane, such acceleration corresponds to a shift of the 2D Airy intensity pattern along the 45° radial directions, as shown in Fig. 1.3(a, b).

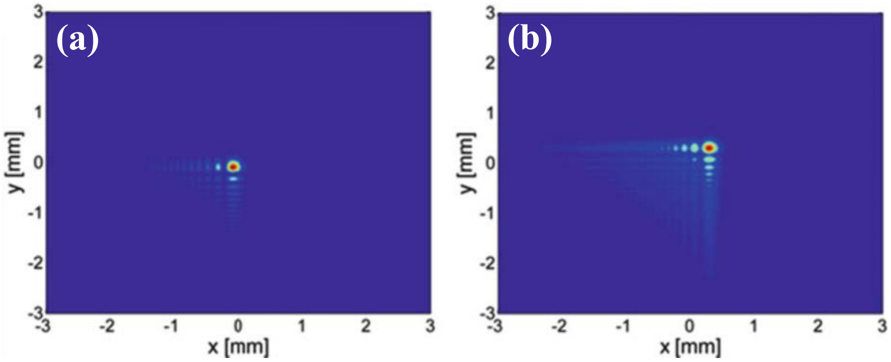

Figure 1.3: Propagation dynamics of a 2D finite-energy Airy beam. (a) Transverse intensity distributions of a 2D finite-energy Airy beam, (a) at the onset of the propagation (z = 0 cm) and (b) after propagation (z = 50 cm). (Figure adapted from Ref. [13]).

In addition to this analytical and numerical study, the same authors experimentally demonstrated the first generation of optical Airy beams by using a Fourier transform approach [56], as illustrated in Fig. 1.4(a). Their method was based on the properties of the Fourier spatial spectrum of an initial Airy beam in Eq. (1.7), given by:

$$\Phi(k,0) = \exp(\alpha k^2) \exp\left(\frac{i}{3}\left(k^3 - 3\alpha^2 k - i\alpha^3\right)\right). \quad (1.13)$$

Such spectrum possesses a Gaussian amplitude, and involves a cubic spectral phase. As a result, an Airy beam can be easily generated by phase-modulating an incident Gaussian beam with a cubic phase distribution in the Fourier domain [Fig. 1.4(b)], and then computing its inverse Fourier transform. The same principle can be readily generalized even for 2D Airy beams. Indeed, the spectrum associated to the envelope field of Eq. (1.11) is $\hat{\Phi}\left(k_x,k_y,0\right)=\Phi\left(k_x,0\right)\Phi\left(k_y,0\right)$.

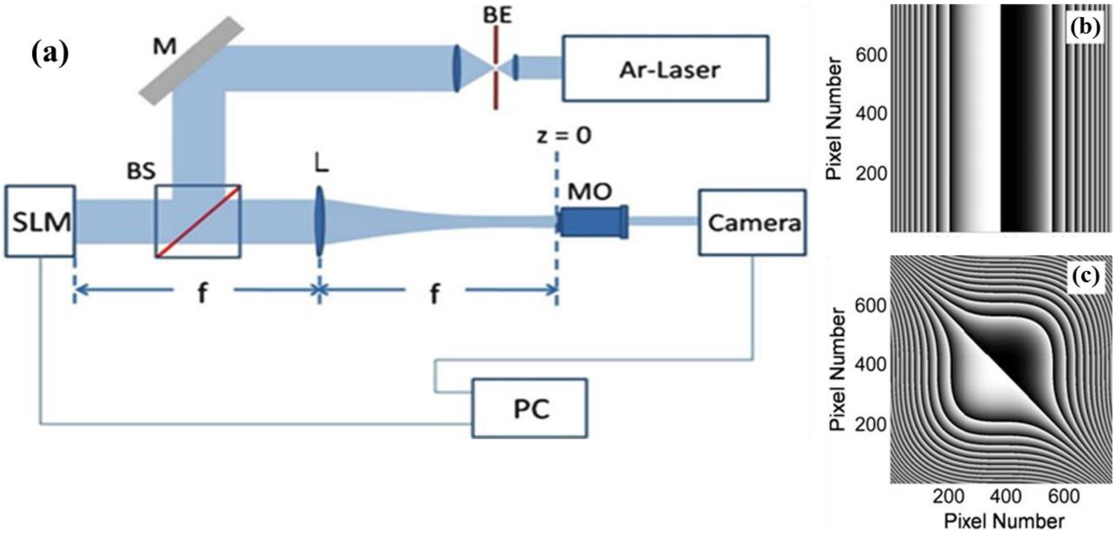

Figure 1.4: Experimental demonstration of 1D (and 2D) Airy beams. (a) Scheme of the experimental setup. (Figure adapted from the Ref. [54]). (b-c) Cubic phase masks imprinted onto the incident Gaussian beam to generate (b) a 1D and (c) a 2D Airy beam. (Figures adapted from Ref. [14]). The phase structures shown are "wrapped" between 0 and 2π (i.e. modulo 2π), as typically uploaded in the SLM. The boundary values 0 and 2π correspond, respectively, to the white and black color in the grey scale pattern.

Therefore, a 2D Airy beam can also be easily generated by phase-modulating a circular Gaussian beam with a 2D cubic phase distribution in the in the Fourier domain [Fig. 1.4(c)]. In the setup shown in Fig. 1.4(a), a linearly-polarized Argon-ion Gaussian laser (λ_0 = 0.4.88 μm) was firstly collimated to a FWHM of 6.7 mm and then sent to a spatial light modulator (SLM). Such a computer-controlled liquid crystal device was used to impress the 1D (or 2D) cubic phase modulation onto the incident beam. To generate 1D (or 2D) Airy beams, a converging cylinder (or spherical) lens (f = 1.2 m) was placed in front of the SLM in order to compute the Fourier transform of the spectrally phase-modulated Gaussian beam. The propagation of the Airy beam was monitored by imaging its intensity pattern using a CCD camera after the back focal plane of the Fourier-transforming lens.

1.4 "Self-healing" of an Airy beam

Along with the convex trajectory and a diffraction-free propagation, another remarkable characteristic of an Airy beam is its "self-healing" property. This feature refers to the ability of an Airy beam of self-reconstructing its shape during propagation, and is of particular importance when it propagates into inhomogeneous media or adverse environments. An infinite-energy Airy beam is able to self-heal at any propagation distance, while a finite-energy Airy beam manifests self-healing only in the range of distances where a quasi-diffraction free propagation is maintained (as mentioned above). J. Broky *et al.* studied the self-healing property of optical Airy beam [15]. They carried out a sequence of experimental observations where different parts of a 2D Airy beam were blocked. They observed that the 2D Airy beam could regenerate itself after being blocked by an opaque obstacle, as shown in Figs. 1.5(a, b). Depending on the severity of the perturbation, the distance of self-healing varied during the experiment. In another set of measurements, the authors also demonstrated that an Airy beam can maintain its shape in scattering environments as well as turbulent media, while a standard Gaussian beam was seriously deformed.

The self-healing property is not only a prerogative of Airy beams, but is a characteristic inherent to any non-diffractive beam. An explanation can be obtained using the Babinet's principle [57]. Indeed, if a non-diffractive beam $\hat{\varphi}(x, y, z = 0)$ is blocked at the onset of the propagation (z = 0) by a finite energy perturbation $\varepsilon(x, y, z = 0)$, the resulting field is expressed as: $U(x, y, 0) \cong \hat{\varphi}(x, y, 0) - \varepsilon(x, y, 0)$. Due its finite energy nature, the perturbation will diffract out during the propagation. As consequence, at very large distance only the non-diffractive beam will be present, i.e. $|U(x, y, z \to \infty)|^2 \cong |\hat{\varphi}(x, y, z \to \infty)|^2$.

For an Airy beam, such self-healing process can be understood by studying the internal transverse power flow $\vec{P}_\perp$ in the (s_x - s_y) plane. H. Sztul and R. Alfano investigated the

Pointing vector $\vec{P}$ and the angular moment of an unperturbed 2D Airy beam [58], reporting that $\vec{P}$ follows the tangential direction to the curved trajectory. At each propagation distance, the transverse component of the main lobe energy flow ($\vec{P}_{\perp}$) is thus directed along the 45^{o} radial direction. Correspondingly, the direction of $\vec{P}_{\perp}$ for the beam tails is initially oriented along the negative s_x and s_y axes, and then tends to rotate towards a direction orthogonal to these axes during propagation. However, the net energy flow remains constant and oriented along the 45^{o} radial direction.

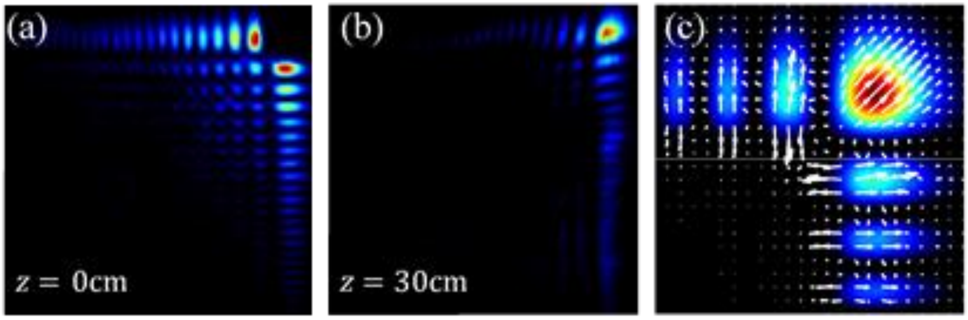

Figure 1.5: Self-healing demonstration of Airy beams. Experimental intensity distributions of a 2D Airy beam (a) at the input (z = 0) where its main lobe is blocked, and (b) after propagation at z = 30 cm. (c) Self-healing mechanism revealed by the transversal power flow $\vec{P}_{\perp}$ (white arrows), for a 2D Airy beam in which the internal sub-lobes are obstructed at the input distance z = 0. (Figures adapted from Ref. [15]).

Consequently to a perturbation, J. Broky [15] showed how the mechanism of self-healing occurs for an Airy beam. The power flows from the sub-lobes towards the region where the Airy beam has been perturbed by the obstacle. However, the Pointing vector of the main lobe is not involved in the self-healing process. The power flow associated to the main lobe is directed along the 45^{o} radial direction for sustaining the self-accelerating property, as shown Fig. 1.5(c).

1.5 Paraxial self-accelerating beams

Most of initial progress on the field of self-accelerating beams was limited to the case of parabolic trajectories. In this framework, M. Bandres [45,59] demonstrated that the only orthogonal and complete families of explicit accelerating and diffraction-free solutions of the 2D paraxial wave equation are the infinite-energy Airy and parabolic beams [45]. This means that if the light beam is constrained to remain diffraction-free, the unique valid bending propagation is in fact along a parabolic path. For finite-energy self-accelerating beams, this constraint does not apply. Indeed, E. Greenfield *et al.* [52] provided the first theoretical and experimental demonstration of quasi-free diffractive 1D self-accelerating beams along arbitrary convex trajectories. Using a caustic theory approach, they engineered the phase structures applied to an incident plane wave (in the real space) towards generating self-accelerating beams with arbitrary convex paths ($x = f(z)$). To illustrate their theory, several cases of convex trajectories have been considered such as light beams propagating along the curves $x = z^n$ (with n = 1.5, 2, 3, 4, 5) or along an exponential trajectory $x = b\left[e^{dz} - 1\right]$ (with b and d positive constants) [see e.g. Fig. 1.6(a1, a2), respectively]. The authors showed that the transverse intensity profiles of all these beams exhibit an Airy-like shape and remain non-spreading up to several Rayleigh lengths ($z_d = \pi x_0^2 / k$). To experimentally demonstrate their method, a setup very similar to the one described above for the Airy beams has been employed besides the suppression of the Fourier transform lens, due to the imprinting of the desired phase mask directly in the real space [Fig. 1.6(a3)]. Using this framework, we have demonstrated theoretically and experimentally the "Fourier-generation" of 1D (and 2D) self-accelerating beams along arbitrary convex trajectory, for which the caustic theory has been here applied to the Fourier domain (Y. Hu *et al.* [18]). Such a method permits the design of *spectral* phase modulations which can be applied to an incident plane wave in order to generate any desired convex beam path. Interesting, this approach is not only valid for self-accelerating beams with one single convex trajectory, but can also be generalized to multi-path self-accelerating beams exhibiting more than one light localization [Fig. 1.6(b1)]. Furthermore, by combining these estimated phase structures with appropriate amplitude modulations in the Fourier domain, it becomes possible to generate periodic self-accelerating beams, i.e. curved beams in which the main lobe evolves along periodical (or zigzag) paths [60], as illustrated in Fig. 1.6(b2). Note that part of these results (Ref. [18]) were actually obtained within the framework of this thesis, and will be further detailed in Chapter 2.

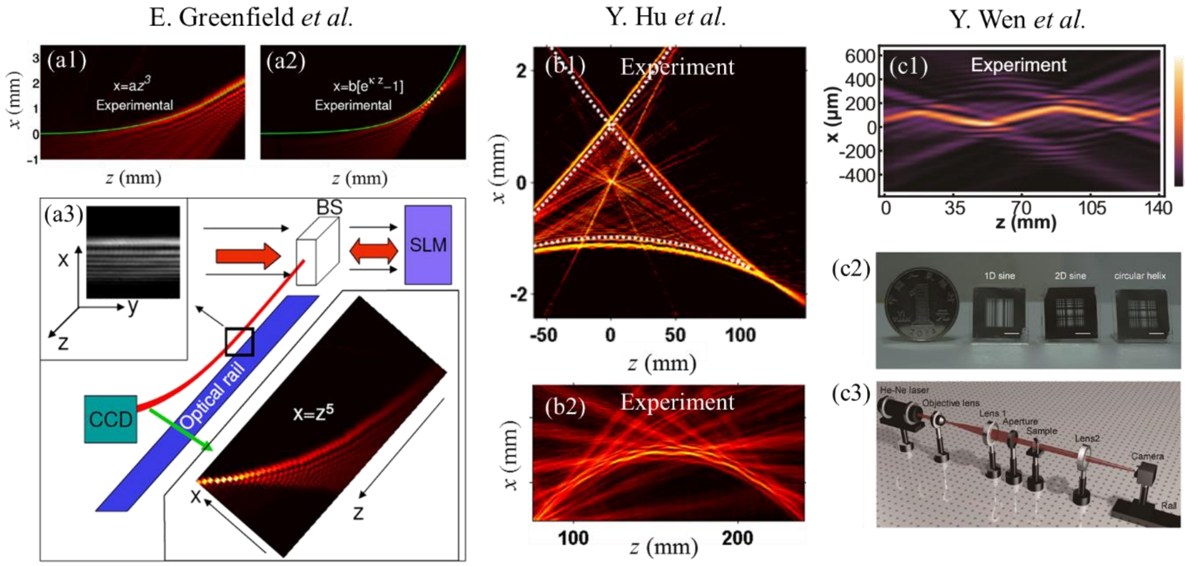

Figure 1.6: Examples of paraxial self-accelerating beams generation. (a1-a3) show the measured intensity distributions of 1D self-accelerating beams propagating along (a1) a cubic polynomial and (a2) an exponential trajectory, obtained by designing the phase modulation in the real space. (a3) shows the schematic experimental apparatus, while the solid green lines in (a1-a2) are analytical predictions. (Figures adapted from Ref. [52]). (b1-b2) show the experimental intensity patterns of (b1) a multi-path (composed by three trajectories) and (b2) a periodic self-accelerating beam, generated by engineering the phase modulation in the Fourier space. (Figures adapted from Refs. [18,60]). (c1-c3) show the experimental generation of non-convex self-accelerating beams. (c1) Experimental intensity distribution for a 1D sinusoidal beam propagating in free space. (c2) Fabricated samples for generating the 1D, 2D sinusoidal beams and circular helical beams. (c3) Experimental setup highlighting the use of the fabricated sample to imprint the desired phase modulation in the Fourier space. (Figures adapted from Ref. [61]).

Recently, Y. Wen *et al.* [61] developed a method based on a superposition of light caustics which enables the construction of self-accelerating beams whose main lobe follows a non-convex trajectory. In this work, the phase structure for 1D sinusoidal beams [Fig. 1.6(c1)] has been designed by dividing the entire trajectory in several segments. In each of these segments, the corresponding light localization is a convex path for which both associated spectral amplitude and phase structures are calculated. The entire sinusoidal trajectory was thus obtained by constructing the appropriate spectral amplitude and phase structures through a linear superposition of the initial spatial spectra corresponding to each convex sub-paths. In addition, the authors also demonstrated the generation of 2D sinusoidal and elliptic helical beams, by superimposing two 1D sinusoidal beams (one in the (x,z) plane and the other on the in the (y,z) plane) and controlling their respective phase shifts. An experimental implementation of these non-convex self-accelerating beams has also been performed. The experimental technique is similar as those implemented for typical Airy beams generation, but using, instead of an SLM, several micro-optical structures on quartz glass [Fig. 1.6(c2)] to perform the phase and amplitude modulation onto the incident light in the Fourier domain [Fig. 1.6 (c3)].

1.6 Control of self-accelerating beams

One of most useful feature of self-accelerating beams is the possibility to easily control their curved motion, as well as its transversal profile. As initially investigated by G. Siviloglou *et al*. [54], it has been showed experimentally and theoretically that an Airy beam can propagate along ballistic dynamics by introducing the input condition:

$$\varphi(s,0) = Ai(s)\exp(\alpha s)\exp(ivs), \tag{1.14}$$

where v is the initial launch angle. The solution to Eq. (1.5) with the initial condition of Eq. (1.14) is found to be [54]:

$$\begin{aligned}\varphi(s,\xi) = Ai\left[s-\frac{\xi^2}{4}+i\alpha\xi-v\xi\right]\exp\left(\alpha s-\alpha\frac{\xi^2}{2}-\alpha v\xi\right)\times \\ \exp\left[i\left(-\frac{\xi^3}{12}+\left(\alpha^2+s-v^2\right)\frac{\xi}{2}+vs-v\frac{\xi^2}{2}\right)\right].\end{aligned} \tag{1.15}$$

From Eq. (1.15), the Airy beam propagates along a ballistic trajectory given by $s=\xi^2/4+v\xi$.

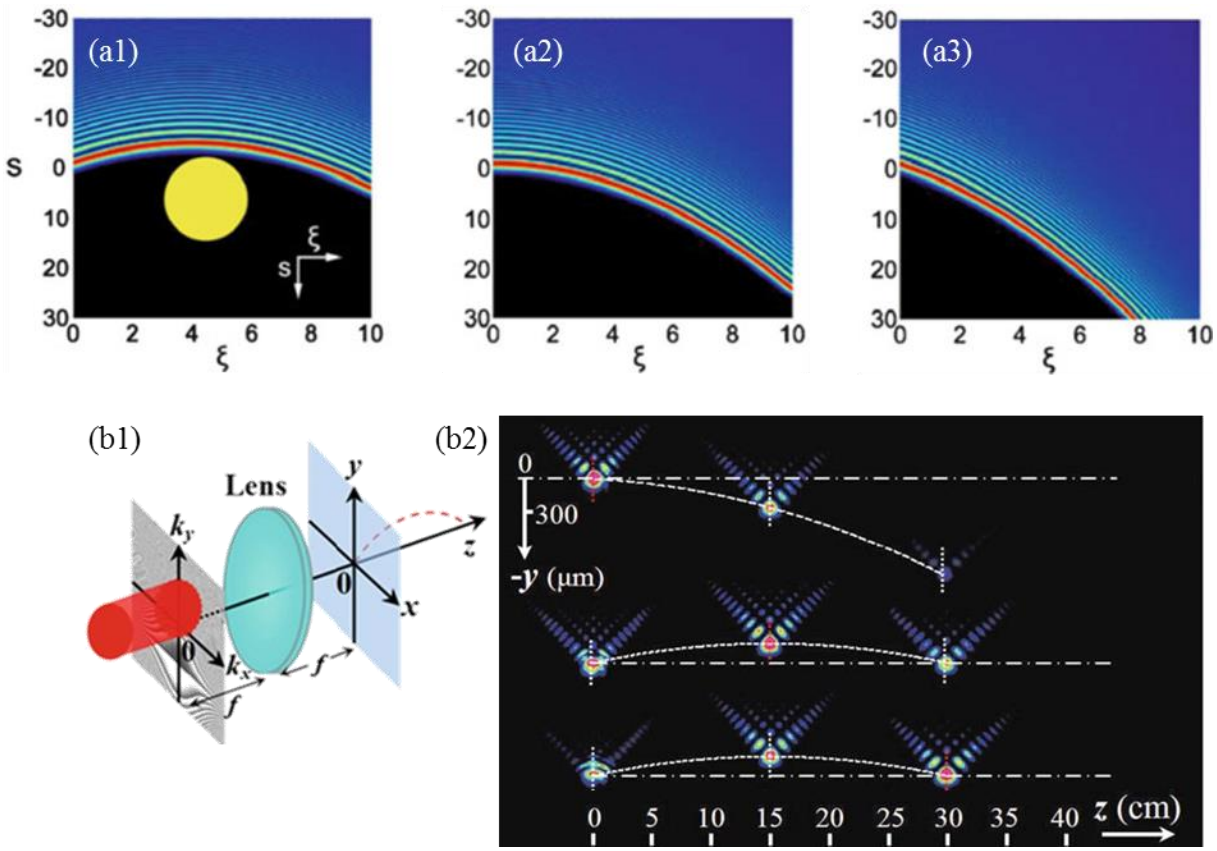

Figure 1.7: Ballistic control of Airy beams. (a1-a3) illustrate infinite-energy Airy beams ($\alpha = 0$) with initial launch angles (a) $v = -2$, (b) $v = 0$ and (c) $v = 2$. (Figures adapted from Ref. [54]). (b1-b2) illustrate the control of a 2D Airy beam enabled by shifting the relative position of the incident Gaussian beam and cubic phase mask in the Fourier space. (Figures adapted from Ref. [62]). (b1) shows the schematic experimental setup and (b2) shows several snapshots of the measured transverse intensity patterns at selected distances (z = 0, 15 and 30 cm), for two different propagation dynamics. Upper snapshots in (b2) correspond to a perfect axial alignment between the Gaussian beam and the cubic phase mask. Middle snapshots in (b2) highlight the ballistic dynamics of the 2D Airy beam when the cubic phase mask is shifted downward along the vertical direction k_y. Lower snapshots in (b2) highlights the dynamics of the 2D Airy beam when both the cubic phase mask and the Gaussian beam are oppositely shifted along the vertical direction k_y.

When v is positive (negative), the Airy beam is launched upwards (downwards) [Figs. 1.7(a2-a3)]. Airy beams with different angles can be launched by transversally shifting up or down the Fourier-transforming cylindrical lens [56], indicated with L in the setup shown in Fig. 1.4.

It is worth mentioning that, when the Airy beam moves along a ballistic path, the center of gravity evolves along the line given by: $\langle s(\xi)\rangle = v\xi + (4\alpha^3 - 1)/4\alpha$.

In a related work, Y. Hu *et al.* [62] demonstrated another way to control the motion of 2D Airy beams. The authors showed that, when both the cubic phase mask and incident Gaussian beam centers are overlapped on the *z*-axis, the 2D Airy beam propagates along a parabolic trajectory and the peak intensity is located at the onset distance [*z* = 0 cm in Figs. 1.7(b1, b2) (upper panel)]. By vertically shifting the cubic phase mask with respect to the *z*-axis, as shown in Fig. 1.7(b1), the 2D Airy beam evolves along a ballistic trajectory. In this case, the peak intensity is reached in correspondence of the maximum height [Fig. 1.7(b2) (middle panel)]. Additionally if the Gaussian beam is also shifted vertically at the opposite location of the cubic phase mask, the peak intensity of the 2D Airy beam appears at the end of the trajectory [*z* = 30 cm in Fig. 1.7(b2) (lower panel)]. In this way, the position of the peak intensity can be also controlled along the propagation distance. Moreover, the horizontal displacement of either the cubic phase mask or the Gaussian beam leads to a projectile motion which can be set into any arbitrary direction. In this case, the intensity profile of the 2D Airy beam shows asymmetric wings.

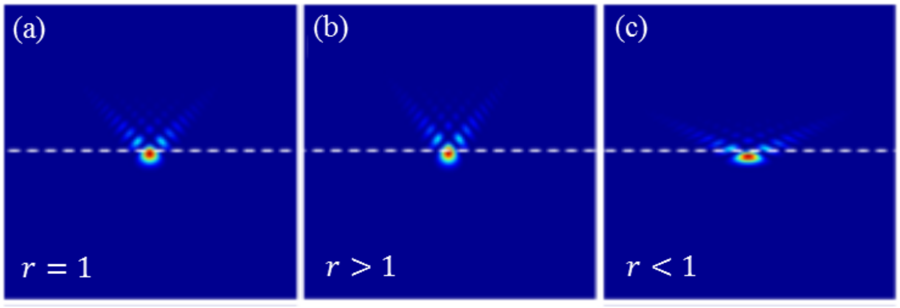

Figure 1.8: Deformed 2D Airy beams. Intensity distributions corresponding to a deformed Airy beam with (a) a right, (b) an acute and (c) an obtuse angle between the two wings. (Figure adapted from Ref. [63]).

Another way to control the parabolic trajectory of a 2D Airy beam is by deforming the two long sub-lobe tails [63]. In particular, the electric field envelope of a deformed Airy beam is expressed by:

$$\hat{\varphi}\left(S_x, S_y, 0\right) = Ai\left(S_x\right) exp(\alpha S_x) Ai\left(S_y\right) exp(\alpha S_y) \tag{1.16}$$

where $S_x = -(rs_x - s_y / r)/2$ and $S_y = (rs_x - s_y / r)/2$, and r is the parameter determining the degree of deformation of the Airy beam. A "classic" 2D Airy beam whose tails form a 90^o angle corresponds to $r = 1$ [Fig. 1.18(a)]. Otherwise, the angle between the Airy beam tails changes, as shown in Figs. 1.18(b-c). In particular, if $r > 1$ ($r < 1$) this angle is acute (obtuse), and the correspondingly deformed Airy beam experiences a decreased (increased) acceleration. Additionally, a slightly-deformed Airy beam tends to restore the standard angle (90^o degree) during propagation. However, large deviations lead to beam propagations where an initial obtuse angle evolves towards an acute one, and vice versa.

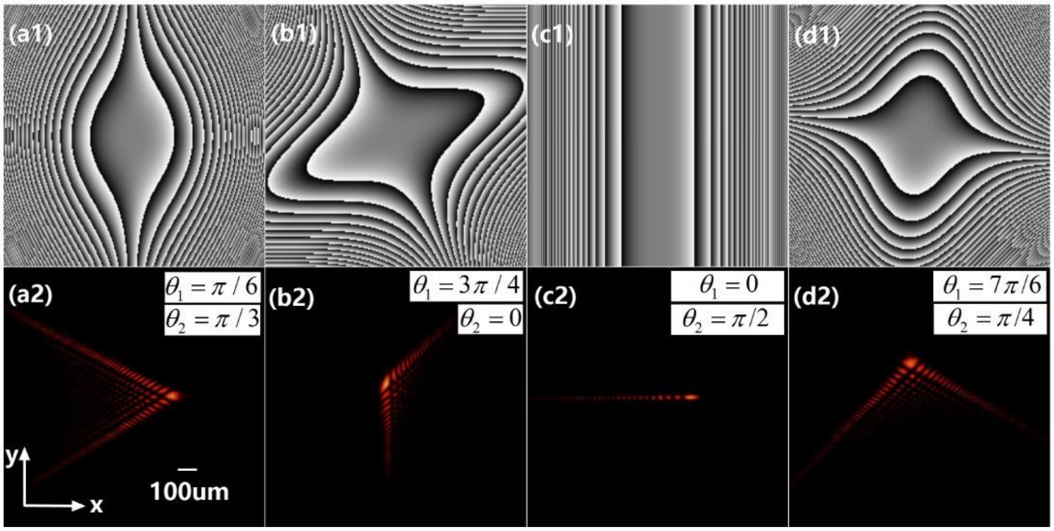

Figure 1.9: Experimentally obtained quasi-Airy beams corresponding to different disturbance factors θ_1 and θ_2. (a1-d1) illustrate the wrapped spectral phase masks obtained by setting the disturbance factors respectively to (a1) $\theta_1 = \pi/6$ and $\theta_2 = \pi/3$, (b1) $\theta_1 = 3\pi/4$ and $\theta_2 = 0$, (c1) $\theta_1 = 0$ and $\theta_2 = \pi/2$, (d1) $\theta_1 = 7\pi/6$ and $\theta_2 = \pi/4$. (a2-d2) are the corresponding transverse intensity distributions of the generated quasi-Airy beams. (Figure adapted from Ref. [64]).

In a similar work, Y. Qian and S. Zhang [64] deformed the spectral cubic phase mask by means of the two disturbance factors θ_1 and θ_2 (varying in the range between 0 and 2π), as:

$$\begin{aligned}\hat{\Phi}\left(k_x,k_y,0\right)=exp&\left[-\alpha\left(k_x cos\theta_1-k_y sin\theta_1\right)^2-\alpha\left(k_x sin\theta_2+k_y cos\theta_2\right)^2\right]\\ \times exp&\left[\,i\left(\,k_x cos\theta_1-k_y sin\theta_1\right)^3/3+i\left(k_x sin\theta_2+k_y cos\theta_2\right)^3/3\right].\end{aligned}\tag{1.17}$$

In this way, they introduced a new family of 2D Airy beams (called quasi-Airy beams), of which some examples are shown in Figs. 1.9(a1-d2). By adjusting the angle between the wings, such quasi-Airy beams can propagate along designed trajectories. The Airy beam can be regarded as special case of a quasi-Airy beam whose wings are reciprocally orthogonal. During propagation, a quasi-Airy beams generates two separate parabolic trajectories, one for the main lobe and the other one carrying the peak intensity. The two parabolic trajectories overlap when the angle between the wings is 90^o degree (2D Airy beam) - see Ref. [64] for more details.

However in all these previously mentioned cases, the control of Airy beams is achieved in free-space. It is worth mentioning briefly that other ways to manipulate the Airy beam dynamics exist by means of external potentials, such as linear [29,65-66] and harmonic [67-68] potentials. For example, an optically-induced refractive index gradient along the *x*-axis can modulate the bending propagation of 1D (or 2D) Airy beams, thus leading to beam dynamics where the parabolic acceleration is increased, reduced or even suppressed [29].

A linear potential can also be used to shape the propagation trajectory of an Airy beam. N. Efremidis [65] engineered the beam trajectory of 1D (and 2D) Airy beams by designing transversely linear potentials with longitudinal (*z*-axis) index gradients and finding the associated initial input conditions (i.e. spatial displacement and tilt). As an illustrative example, the author estimated the potential gradients and the initial parameters for an Airy beam to propagate along a polynomial law, sinusoidal, logarithmic and hyperbolic trajectory, as well as a 2D Airy beam to follow a spiral trajectory in space. Finally, under an external harmonic potential [67], the Airy beam follows an unusual oscillating propagation.

1.7 Non-paraxial self-accelerating beams

The self-accelerating beams described until now are solutions of the (1+1)D (or (2+1)D) paraxial Helmholtz equation of diffraction, whose normalized form is Eq. (1.5) (or correspondingly Eq. (1.10)). Nevertheless, this paraxial wave equation only represents an approximation to the Helmholtz equation, describing the actual propagation of linearly-polarized monochromatic optical beams. In the (2+1)D regime, this equation reads:

$$\frac{\partial^2 \hat{\varphi}}{\partial z^2}+\frac{\partial^2 \hat{\varphi}}{\partial x^2}+\frac{\partial^2 \hat{\varphi}}{\partial y^2}+k^2\hat{\varphi}=0 \tag{1.18}$$

Where $\hat{\varphi}(x, y, z)$ is the electric field envelope, x and y denote the transverse coordinates, and z is the longitudinal coordinate. Here, $k = k_0 n_0$ indicates the wavenumber, where k_0 is the vacuum wavenumber and n_0 is the refractive index. Solutions to Eq. (1.18) can be found in the Fourier regime, as:

$$\hat{\varphi}(x, y, z)=\frac{1}{4\pi^2}\iint_{-\infty}^{+\infty}\hat{\Phi}(k_x, k_y, 0)e^{\pm iz\sqrt{k^2-k_x{}^2-k_y{}^2}}\,e^{i\left(k_x x+k_y y\right)}dk_x dk_y . \tag{1.19}$$

where $\hat{\Phi}(k_x, k_y, 0)=\iint_{-\infty}^{+\infty}\hat{\varphi}(x, y, 0)e^{-i\left(k_x x+k_y y\right)}dxdy$ is the input spectrum. In Eq. (1.19), the positive sign of the first exponential term accounts for forward propagations, while a negative sign refers to backward propagations. Looking at the Fourier regime, the spatial frequencies in charge of the propagation are in the range $\sqrt{k^2-k_x^2-k_y^2}\geq 0$, while those out of this range are associated to the generation of evanescent waves. To obtain the paraxial wave equation from Eq. (1.19), the condition of a slowly-varying envelope must be satisfied, i.e. $|\partial^2\hat{\varphi}/\partial z^2|\ll 2k|\partial\hat{\varphi}/\partial z|$. In the Fourier regime, such condition means to consider optical beams whose spatial spectrum is confined in a small range of spatial frequencies so that $k >> k_x$ and $k >> k_y$. From a physical viewpoint, the paraxial wave equation can thus only describe the propagation of self-accelerating beams when the trajectory is limited to small angles. For larger angles, such beams are not anymore shape-preserving. For instance, in the paraxial regime, an ideal Airy beam preserves its amplitude for all distances. When propagating under non-paraxial condition, its trajectory tends to break after short propagation distances (or small angles), thus becoming no longer shape-preserving [69] [see Fig. 1.10(g)]. This constitutes a serious limitation as the propagation angle of a self-accelerating beam continuously increases, and after a given distance, the beam dynamics actually fall into the non-paraxial regime. Indeed, steeper angles involve more spatial frequencies to sustain the beam acceleration. Therefore, it is important to find self-accelerating beams capable of maintaining the bending propagation, even in the non-paraxial regime. Further research on this field has been undertaken to solve this problem. In the last five years, several non-diffractive self-accelerating beam solutions to the Helmholtz equation have been introduced and demonstrated [Fig. 1.10].

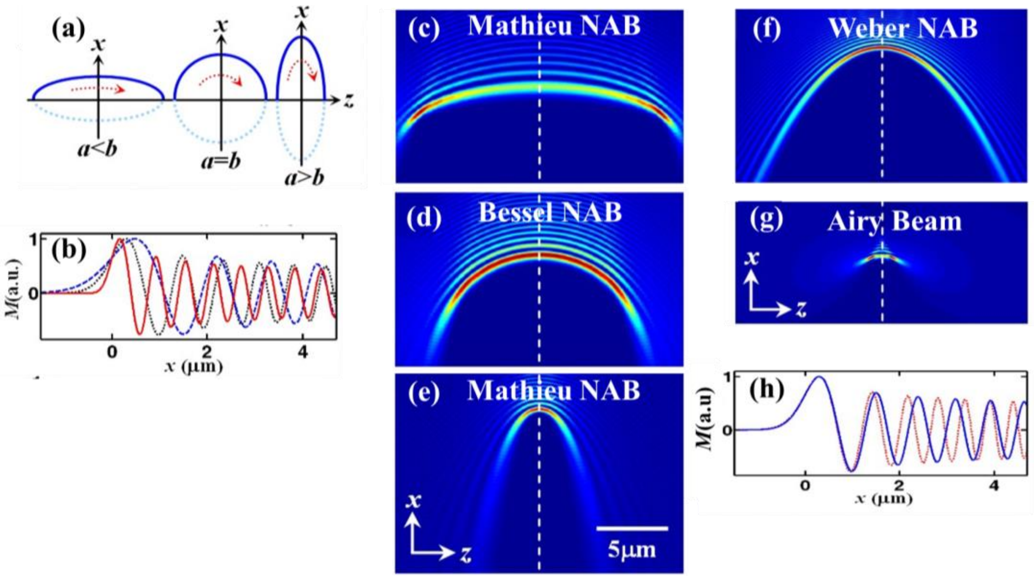

Figure 1.10: Non-paraxial self-accelerating beams obtained by solving the Helmholtz equation in different conical coordinate systems. (a) Schematic of different trajectories related to a Mathieu non-paraxial accelerating beam (NAB) for various ellipse parameters (i.e. semi-axes a and b) The case $a = b$ corresponds to a Bessel NAB. (b) Amplitude of NABs at $z = 0$ for $a < b$ (red solid line), $a = b$ (black dotted line) and $a > b$ (blue dashed line). Propagation dynamics of the Mathieu NABs for (c) $a < b$, (d) $a = b$ and (e) $a > b$. (f-g) Comparison between the propagation dynamics of (f) a Weber NAB and an (g) Airy beam. (h) Amplitude of Weber NAB (solid blue line) and Airy beam (red dotted line) at $z = 0$. The white dashed line in (c-g) marks the input distance $z = 0$. (Figure adapted from Ref. [21]).

I. Kaminer *et al.* [20] were the first to introduce the concept of non-paraxial accelerating beams. By solving the (1+1)D Helmholtz equation in polar coordinates, they found a family of shape-preserving non-paraxial accelerating beams showing a Bessel amplitude profile and a circular propagation trajectory. In particular, the electric field envelope is here defined in Cartesian coordinates yielding $\varphi(x,z) = J_a\left(k\sqrt{x^2+z^2}\right)\exp\left(ia\times\arctan(z/x)\right)$, where J_a indicates the Bessel function of order a. This beam is non-diffracting and accelerates along a closed circle trajectory, but requires both the forward and backward components as well as an infinite energy. The beam forms a longitudinal vortex of order a in the (x-z) plane. If only the forward (or backward) component is considered, the corresponding non-paraxial Bessel beam accelerates along a concave (or convex) semi-circular trajectory. In this case, the beam is not shape-preserving along the complete 180^{o} angle of propagation. P. Zhang *et al.* [19] reported the experimental demonstration of such Bessel non-paraxial beams. In this case, the authors introduced a shifted and truncated version of these beams [Fig. 1.10(d)] using both an exponential aperture and a Heaviside step function $\left(\varphi(x,z=0) = \exp\left(-\alpha x\right)\times H\left(x+a/k\right)J_a\left(kx+a\right)\right)$. Consequently, they retrieved the appropriate amplitude and phase modulations. In this case, the experimental technique was similar to the one used for the 1D Airy beam, but imprinting onto the SLM an off-axis hologram (produced by the interference between a plane wave with the spectral phase profile of the non-paraxial beam). In addition, a 4f spatial filtering system [1] has been placed between the SLM and the Fourier-transforming cylindrical lens, in order to reconstruct the encoded phase information after the incident Gaussian beam has been phase-modulated by the hologram on the SLM. Similarly, P. Zhang *et al.* [21] also demonstrated both theoretically and experimentally both Mathieu [Figs. 1.10(c, e)] and Weber [Fig. 1.10(f)] non-paraxial accelerating beams (NAB). They found two families of exacts shape-preserving solutions of the Helmholtz equation in the elliptic (Mathieu) and parabolic (Weber) coordinates systems. In the former case, non-paraxial self-accelerating beams travel along an elliptic trajectory, and the amplitude profile is determined by the radial and angular Mathieu functions [70] [Fig. 1.10(b)]. Akin to non-paraxial Bessel beams, an ideal non-paraxial Mathieu beam propagating along a closed elliptical trajectory requires infinite energy and both forward and backward components. In the latter case, non-paraxial parabolic beams propagate along a large-angle parabolic trajectory, whereas the amplitude profile is obtained by multiplying the eigensolutions of the Weber differential equation [6,70], but with opposite sign eigenvalues [Fig. 1.10(f)]. In contrast with the other two cases, an ideal non-paraxial Weber beam, although requiring infinite energy, only contains either the forward or backward beam propagation component.

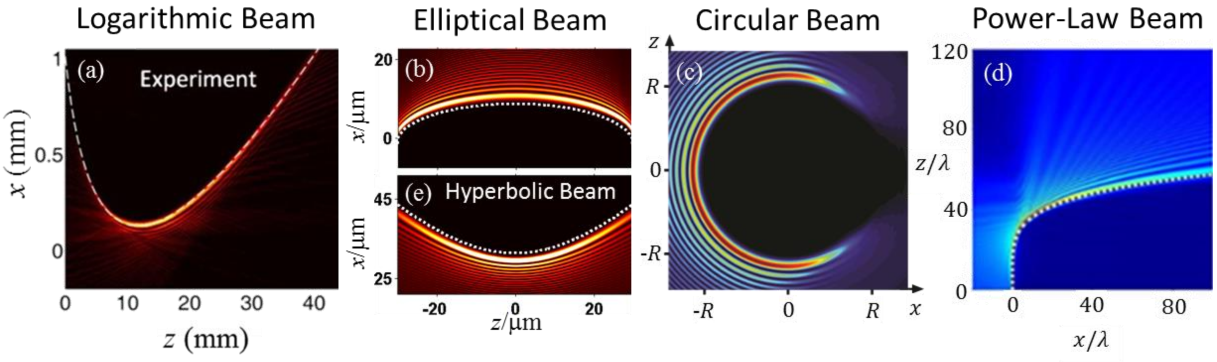

Figure 1.11: Generation of non-paraxial self-accelerating beams through caustic methods. (a) Measured intensity distributions of a non-paraxial logarithmic beam, obtained by designing the phase modulation in the real space. (Figure adapted from Ref. [17]). (b, e) Non-paraxial accelerating beams evolving along (b) an elliptical and (e) a hyperbolic trajectory, generated by a phase modulation in the Fourier domain. (Figures adapted from Ref. [18]). (c) Intensity distribution of a non-paraxial circular beam obtained from a properly-shaped mirror surface. (Figure adapted from Ref. [23]). (d) Amplitude profile of non-paraxial power-law beams, obtained from a closed-form expression of the phase modulation at the input plane. (Figure adapted from Ref. [22]).

In parallel, several research groups proposed alternative methods that are not based on solving the Helmholtz equation through complex angular functions. Most of these approaches use the caustic theory [71] for generating a variety of non-paraxial self-accelerating beams as illustrated in Fig. 1.11. For example, L. Froehly, *et al.* [17] used the geometrical properties of optical caustics and the Legendre transform (i.e. the parametrization of a convex curve in term of its tangents and axis intercepts) to estimate the appropriated spatial phase profiles to be applied to an incident Gaussian beam in order to generate 1D paraxial and non-paraxial self-accelerating beams along arbitrary convex trajectory. As illustrative examples, several cases of non-paraxial beams have been demonstrated theoretically and experimentally. In particular, the authors engineered the real-space phase masks to experimentally synthesize parabolic, quartic and logarithmic accelerating profiles [Fig. 1.11(a)]. Interestingly, applying such direct phase masks with a reflection or rotational symmetry leads to novel two- and three-dimensional self-accelerating beams, with localized high intensity profiles or optical spiral structures. In a related work, A. Mathis *et al.* demonstrated non-paraxial periodic accelerating beams, combining a binary amplitude and a phase modulation in real space [44]. The authors estimated the spatial phases to generate Circular and Weber self-accelerating beams using a similar approach to that reported in Ref. [17], and for which the authors directly encoded the binary amplitude modulation into the phase mask of the SLM and used a 4f system to filter the 0^{th}-order diffraction term. As demonstrated by J. Davis *et al.* [72], if a binary amplitude profile is encoded onto an only-phase structure, it spatially modifies the diffraction efficiency so that the light which is not diffracted into the 1^{st}-order is correspondingly remaining in the 0^{th}diffractive order. In this way, the effective phase and amplitude modulation profiles can be therefore reproduced in the 1^{st}-order of the diffracted light. As presented in Ref. [18] and later detailed in Chapter 2, we also proposed a straightforward method to generate 1D non-paraxial accelerating beams along arbitrary convex trajectories by only designing, through caustic theory, the spectral phase modulation to be implemented in the Fourier regime [Fig. 1.11(b) and 1.11(e)].

Alternatively, M. Alonso and M. Bandres introduced a ray-based description of non-paraxial self-accelerating beams in both the (1+1)D and (2+1)D regime [23-24]. The authors developed a geometric procedure for designing mirror shapes that convert collimated beams generated by a point source into self-accelerating beams propagating beyond a semicircle trajectory [Fig. 1.11(c)]. Recently, R. Penciu *et al.* [22] presented a real-space method for the generation of non-paraxial self-accelerating beams that follow arbitrary convex paths [Fig. 1.11(d)]. Their approach enables to find non-paraxial beams where the initial phase modulation is computed in a closed-form expression. Furthermore, the beams intensity contrast along the desired convex trajectories can be controlled by changing the initial amplitude profile. Indeed, depending on the initial amplitude profile, non-paraxial accelerating beams can show uniform intensity profiles along the caustic, as well as patterns where the beam intensity is different at various locations along the trajectory.

1.8 Nonlinear self-accelerating beams

In optics and photonics, it is important, for both fundamentals aspects and related applications, to study the dynamics of self-accelerating beams propagating in a nonlinear regime (i.e. when the effective medium refractive index depends on the beam intensity).

In general, the nonlinear propagation of a laser beam can be described by the nonlinear paraxial wave equation (NLPWE), according to the following equation:

$$i\frac{\partial A}{\partial z}+\frac{1}{2k}\left(\frac{\partial^2 A}{\partial x^2}+\frac{\partial^2 A}{\partial y^2}\right)+\frac{k\Delta n(I)}{n_0}A=0. \tag{1.20}$$

Here $A(x,y,z)$ is the slowly-varying electric field envelope in the physical coordinates x, y and z, $k=k_0 n_0$ is the wavenumber, k_0 is the vacuum wavenumber, n_0 the refractive index, and $\Delta n(I)$ the nonlinear refractive index change driven by the beam intensity I. During propagation, an optical beam undergoes a self-induced phase modulation (SPM) due to $\Delta n(I)$ which results in a reshaping of the beam wave front. In general, the specific form of $\Delta n(I)$ depends on the nonlinear medium and on the physical process involved. One of the most important nonlinear phenomenon is the optical Kerr effect, which is observable in centro-symmetric materials, such as silica glass. The beam intensity induces a linear change of the refractive index, according to $\Delta n(I) = n_2 I$ where n_2 is the Kerr coefficient. In such a medium, nonlinearity can lead an optical beam either to collapse into a singularity (self-focusing ($n_2 > 0$), or to broaden similarly to what happens for a diverging lens (self-defocusing ($n_2 < 0$)), both being unstable evolutions. Several studies concerning nonlinear optical wave manipulations with the main goal of achieving stationarity, stability and wave localization have been presented. For example, under certain conditions in the 1D regime, self-focusing can compensate diffraction, thus leading to shape-preserved light localizations named spatial solitons [73]. Nevertheless, in higher-dimension geometries, nonlinearity only drives the beam to instability. In this case, self-focusing can be counteracted by several stabilizing mechanisms based on higher nonlinear phenomena, such as Kerr saturation, plasma-induced defocusing, or stimulated Raman scattering [74].

Besides the Kerr effect, photorefractive nonlinearity is one of the most commonly used nonlinear effects. This is mainly because photorefractive (PR) materials (for example, ferroelectric crystals such as Strontium Barium Niobate (SBN)) can also show both self-focusing and -defocusing property, which can be used to compensate diffraction, as seen in self-trapped bright (or dark) solitons [75]. In a PR medium, the optical intensity induces an internal electric field, originating from different mechanisms, such as carrier diffusion, photovoltaic effect, and drift current driven by an external voltage. In turn, this internal electric field causes a nonlinear refractive index change ($\Delta n(I)$) via the electro-optic effect [76]. Furthermore, the type of the nonlinearity in PR media can be easily switched by reversing the sign of an applied external voltage.

In the context of self-accelerating beams, one of the most challenging issue is to preserve the bending trajectory (acceleration) inside the nonlinear medium, which can be seriously affected by the nonlinearity of the system. If an Airy beam propagates in the presence of a Kerr nonlinearity, both its amplitude profile and parabolic trajectory tend to be destroyed due to the action of self-focusing [25], in turn leading to the concentration of most of the beam energy into a self-trapped off-shooting soliton [77] (see also Fig. 1.16). Several research efforts have been pursued to solve this problem, some of which focused on finding stationary nonlinear accelerating solutions to Eq. (1.20). In particular, I. Kaminer *et al.* [31] demonstrated the existence of a family of shape-preserving self-trapped 1D accelerating beams in Kerr media. Such nonlinear accelerating beams are stable under self-defocusing and weak self-focusing, whereas under the influence of a strong self-focusing, the beam breaks up and emits a series of solitons, as shown in Fig.1.12. In a related work, A. Lotti *et al.* [32] also reported a family of shape-preserving self-trapped 1D self-accelerating beams existing even when considering the effects of Kerr nonlinearity and nonlinear losses in the propagation dynamics. The same authors also investigated the evolution of intense 2D Airy beams in air and water [78]. Under these conditions, they showed that the accelerating property of a 2D Airy beam is preserved if the power content in the main lobe remains below a certain threshold. Once this value is overcome, the 2D Airy beam breaks into a multi-filamentary pattern that affects its bending propagation.

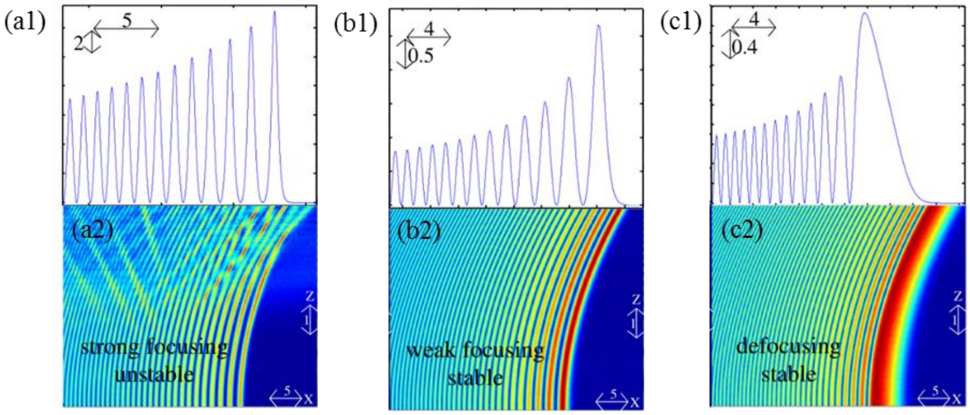

Figure 1.12: Examples of self-accelerating beams dynamics in Kerr media. (a1-c1) Intensity profiles at the input of the crystal (z = 0) and (a2-c2) intensity evolution of nonlinear self-accelerating beams propagating under (a1-a2) strong focusing, (b1-b2) weak focusing and (c1-c2) defocusing nonlinearity. (Figures adapted from Ref. [31]).

Interestingly, non-paraxial accelerating beams are less sensitive to the Kerr nonlinearity when compared to their paraxial counterparts. In particular, for the case of Bessel-like accelerating beam, P. Zhang *et al.* reported that such non-paraxial wave packet, instead of being broken up by the nonlinearity, maintains its circular trajectory even under self-focusing [19].

In a nonlinear PR medium, self-accelerating beams were firstly investigated by S. Lee *et al.* [79], which reported the experimental observation of self-trapped Airy beams in nonlinear PR media, under the effect of carrier diffusion only (i.e. without any external bias). As an Airy beam is a shape-preserving solution of the paraxial Helmholtz equation, such “nonlinear Airy beams” are stationary solutions of the nonlinear paraxial equation, governing the diffraction dynamics of an optical beam which propagates in an unbiased photorefractive medium.

Moreover, in an externally-biased photorefractive media, an Airy beam breaks up (i.e. looses both its invariant intensity pattern and its acceleration). As an illustrative example, the nonlinear evolution of a 2D Airy beam in a 1 cm-long SBN crystal is shown in Fig. 1.13 [26], where is also compared with the linear case (no bias applied) [Figs. 1.13(a1-a2)]. By applying a positive bias to the PR crystal, the 2D Airy beam experiences a self-focusing effect. The nonlinearity causes a stagnation of its acceleration and leads the intensity pattern to mostly concentrate onto the four lobes close to the main hump with shorter tails [Figs. 1.13(b1-b2)]. If the polarity of the bias is negative, the 2D Airy beam propagates under the action of a self-defocusing nonlinearity. In this case, the intensity pattern of the 2D Airy beam is expanded but nearly unchanged during propagation, and its acceleration is persisting more than in the self-focusing case [Figs. 1.13(c1-c2)].

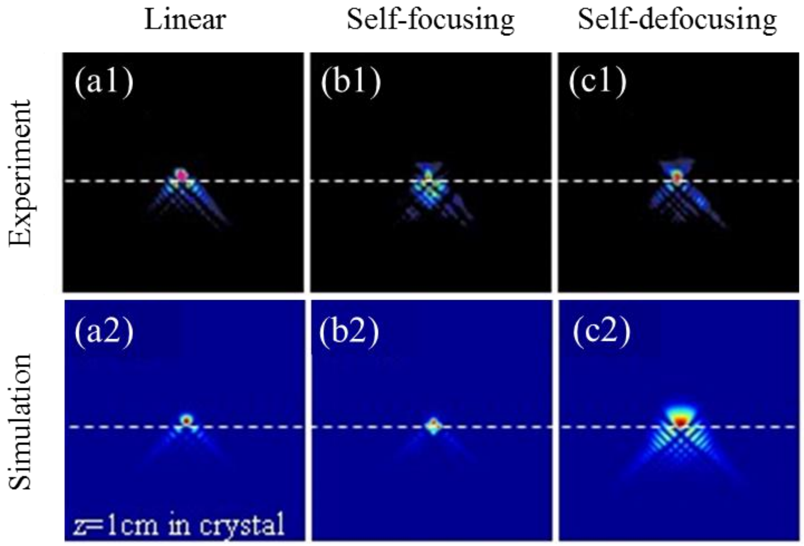

Figure 1.13: Nonlinear propagation of Airy beams in a biased photorefractive medium. Experimental transverse intensity distributions of nonlinear 2D self-accelerating beams after propagation into a 1cm-long SBN (Strontium Barium Niobate) crystal, with (a1) no nonlinearity, (b) self-focusing nonlinearity and (c1) self-defocusing nonlinearity. (a2-c2) are the corresponding numerical results. (Figures adapted from Ref. [26]).

It is worth to mention that under certain conditions, an Airy beam can also preserve its accelerating evolution in the presence of self-focusing. As it will be described in more details in the Chapter 4 of this dissertation, we demonstrate that by applying a transversal shift to the cubic phase mask in the Fourier regime, an Airy beam maintains its accelerating properties in both Kerr and photorefractive media, yielding a dramatic reshaping of the linear Gaussian spectrum [33,80].

1.9 Self-accelerating Airy pulses

In the temporal domain, self-accelerating pulses are analog to self-accelerating beams in space. From a physical viewpoint, self-accelerating beams exhibit bending propagation in space. On the other hand, for their temporal counterparts, the accelerating property manifest themselves as a change in the group velocity. The analogy origins from the fact that the paraxial Helmholtz equation (describing the linear propagation of optical spatial beams) has the same mathematical form as the linear dispersion equation (LDE), modelling the evolution of optical temporal pulses in a dispersive medium [81]. In the nonlinear regime, the spatio-temporal duality also remains valid because the nonlinear spatial beams and temporal pulses can be described by the same (1+1)D normalized nonlinear Schrödinger equation (NLSE) [73]. Noteworthy, almost all studies reported to date on self-accelerating pulses are restricted to Airy pulses and their dynamics in optical fiber propagation. The choice to deal with optical fiber applications is motivated by the fact that optical fibers offer a reproducible and convenient environment to experimentally study both the linear and nonlinear propagation dynamics of temporal optical pulse. Airy pulses are analog to Airy beams, and were the first self-accelerating pulses to be introduced and studied in the literature [11,13]. Like an Airy beam, an infinite-energy Airy pulse is resistant to dispersion and its dominant intensity peak (i.e. its main lobe) propagates along a parabolic trajectory so that the group velocity undergoes a parabolic change. They are also able to regenerate their profile after being selectively attenuated or distorted (“self-healing”). For instance, if an Airy pulse is apodized by truncating its oscillating tail, the wave packet exhibits the key characteristics as in the ideal case before the dispersion takes place. In what follows, we provide an overview of the studies related to both linear and nonlinear Airy pulses propagation in optical fibers.

1.9.a Airy pulses under linear propagation regimes

As mention above, the linear propagation of an optical pulse in a dispersive medium is described by the linear dispersion equation (LDE). If only group velocity dispersion (GVD) and third-order dispersion (TOD) are taken into account (i.e. by only retaining the dispersion coefficients up to the 3rd order term of the Taylor expansion propagation constant $\beta(\omega)$ around the carrier angular frequency ω_0), the LDE takes the following form:

$$i\frac{\partial A}{\partial z}-\frac{\beta_2}{2}\frac{\partial^2 A}{\partial \tau^2}-i\frac{\beta_3}{6}\frac{\partial^3 A}{\partial \tau^3}=0, \tag{1.21}$$

where in the Eq. (1.21) $A(z,\tau)$ is the slowly-varying pulse envelope at ω_0, $\tau = t - z/v_g$ is the time coordinate in the framework of the group velocity v_g, in which z and t are the physical distance and time. We also indicate the pulse duration as T_0, and the dispersion length $L_d = T_0^2/|\beta_2|$. β_2 and β_3 are, respectively, the GVD and TOD coefficients. Although higher order dispersion may be neglected (most of the time) to efficiently model such pulse dynamics, the inclusion of the TOD coefficient usually must be taken into account for optical pulses whose central wavelength is close to the zero-dispersion value of the fiber, or when considering the evolution of ultrashort pulses possessing a significantly large bandwidth. In general, Eq. (1.21) can be solved in the Fourier domain as:

$$A(\tau,z)=\frac{1}{2\pi}\int_{-\infty}^{+\infty}\tilde{A}(\omega,0)e^{\left(\frac{i}{2}\beta_2\omega^2 z-\frac{i}{6}\beta_3\omega^3 z\right)}e^{i\omega\tau}d\omega, \tag{1.22}$$

in which $\tilde{A}(\omega,0)=\int_{-\infty}^{+\infty}A(\tau,0)e^{-i\omega\tau}d\tau$ is the input spectrum. More specifically, we study the linear dynamics of finite-energy Airy pulses, whose input condition is given by $A(\tau,0)=Ai(\tau)e^{i\alpha\tau}$. Here, α is the truncation coefficient. In the linear case, the solution can be found in a close form [82], as:

$$A(\tau,Z)=\frac{1}{(1+bZ)^{1/3}}\exp\left(\frac{6\alpha\left(2\tau-Z^2\right)+iZ\left(-6\alpha^2-6\tau+Z^2\right)}{12(1+bZ)^2}\right)\times$$
$$\exp\left(b\frac{4Z\alpha\left(-\alpha^2+3\tau+\alpha^2 bZ\right)+i6Z^2\left(\alpha^2-\tau\right)}{12(1+bZ)^2}\right)Ai\left(\frac{\left(\tau-Z^2/4-i\alpha Z\right)+bZ\left(\tau-\alpha^2\right)}{(1+bZ)^{4/3}}\right), \tag{1.23}$$

where $b = -\beta_3 / (2\beta_2)$ and $Z = z\beta_2$. When neglecting the impact of TOD in the system so that $\beta_3 = 0$, Eq. (1.23) reduces to:

$$A(\tau,Z) = \exp\left(\alpha\tau - \frac{\alpha Z^2}{2}\right)\exp\left(-i\frac{\alpha^2 Z}{2} - i\frac{\tau Z}{2} + i\frac{Z^3}{12}\right) \times Ai\left(\tau - Z^2/4 - i\alpha Z\right). \qquad (1.24)$$

The solution described by Eq. (1.24) is analog to the finite-energy Airy beam [see Fig. 1.15(a)] [3]. In particular, when considering evolution in the anomalous dispersion regime ($\beta_2 < 0$), the linear propagation of an Airy pulse coincides with the Airy beam evolution described by Eq. (1.8).

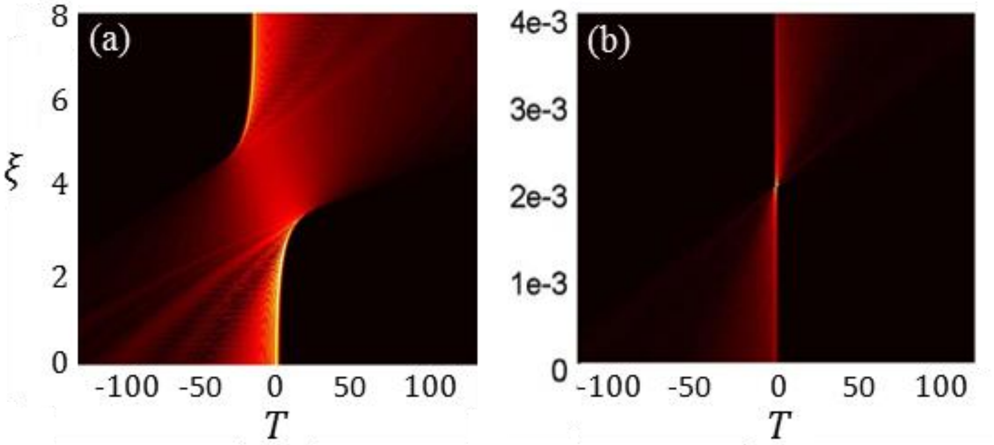

Figure 1.14: Dynamics of an Airy pulse propagating in optical fiber in presence of anomalous GVD dispersion with a positive TOD included. Absolute temporal amplitudes as a function of the normalized distance $\xi = z / L_d$ and time $T = \tau / T_0$ under (a) only the presence of TOD, and (b) the combined action of anomalous GVD and positive TOD with comparable strengths. (Figure adapted from Ref. [34]).

When the TOD is also taken into account ($\beta_3 \neq 0$), the Airy wave packet experiences different propagation dynamics, depending on the sign and strength of both the GVD and TOD [34,82-83]. An interesting case is illustrated in Fig. 1.14 (a), showing the dynamics of an Airy pulse under the influence of an anomalous GVD ($\beta_2 < 0$) and a positive TOD ($\beta_3 > 0$). During propagation, the Airy pulse presents a breaking area after which the wave packet shows an inversion in its acceleration [Fig. 1.14 (a)]. An explanation of such evolution has been provided by R. Driben *et al.* [34]. The authors investigated the dynamics of an Airy pulse launched into an optical fiber close to the zero-dispersion point, thus only considering the predominant effect of the TOD coefficient. Under this condition, the pulse reaches what they call "tight-focusing" distance, where the energy content concentrates into a very narrow and intense light spot. After that point, the pulse undergoes an acceleration inversion, as shown in Fig. 1.14(b). The compression ratio, i.e. the ratio between the peak intensity at the input and at the tight-focusing distance, depends on the truncation coefficient *α*. From a physical viewpoint, the TOD balances the spectral cubic phase modulation generating an Airy pulse at the tight-focusing distance. Beyond this point, the Airy pulse reverses its acceleration because the TOD overcomes the cubic phase modulation with an opposite sign. Instead, if GVD and TOD introduce comparable contributions, the focal point extends into a finite area, after which the wave packet reverses its acceleration. The extension of this area depend on the relative influence of the dispersions parameters [Fig. 1.14(a)].

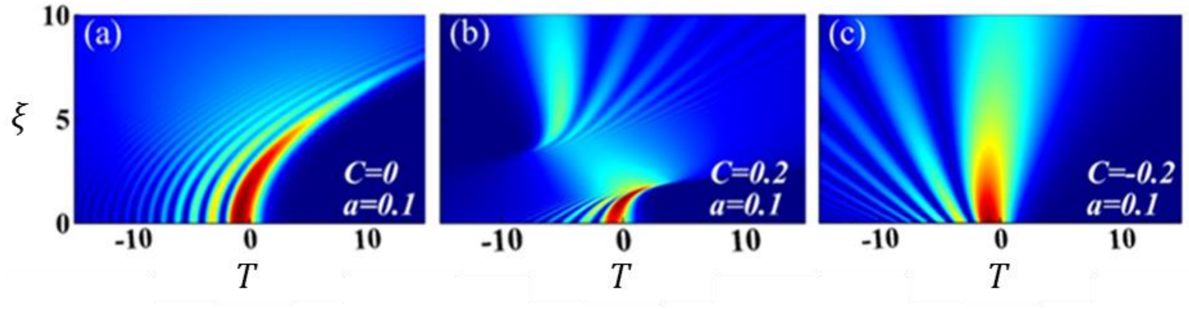

Figure 1.15: Linear evolution of chirped Airy pulses in optical fiber in anomalous dispersion regime. Evolutions of the absolute temporal amplitude as a function of the normalized distance $\xi = z / L_d$ and time $T = \tau / T_0$ for the case of an initial (a) un-chirped, (b) positively-chirped and (c1) negatively-chirped Airy pulse. (Figure adapted from Ref. [84]).

Recently, it has also been demonstrated that an initially chirped Airy pulse can experience an acceleration reversal without requiring the inclusion of TOD effects [84]. Initially chirped Airy pulses are defined as: $A(\tau,0) = Ai(\tau)e^{\alpha\tau}e^{-iC\tau^2}$, where *C* is the chirp parameter. The linear propagation dynamics in optical fibers of such an initially chirped Airy pulse depends considerably on the signs of the GVD and C [Fig. 1.15]. For $\beta_2 C < 0$, the chirped Airy pulse experiences an initial compression phase up to a breakup area, after which the pulse continues to travel with opposite acceleration [Fig. 1.15(b)]. On the other hand, for $\beta_2 C > 0$, the chirped Airy pulse always disperses during propagation [Fig. 1.15(c)].

1.9.b Airy pulses under a nonlinear propagation regimes

In general, the nonlinear evolution of an optical pulse in an optical fiber is described by the nonlinear Schrödinger equation (NLSE) [85]. When only GVD and TOD terms are taken into account, the NLSE reads:

$$i\frac{\partial A}{\partial z}-\frac{\beta_2}{2}\frac{\partial^2 A}{\partial \tau^2}-i\frac{\beta_3}{6}\frac{\partial^3 A}{\partial \tau^3}+\gamma\left|A\right|^2 A=0. \tag{1.25}$$

where, γ is the nonlinear parameter, responsible of the self-phase modulation (SPM) experienced by the pulse [85]. Such a nonlinear optical effect arises from the Kerr nonlinearity, which induces an intensity-dependent phase shift on the temporal pulse, similar to the above discussed spatial self-focusing effect. A direct consequence of SPM is a change on the pulse spectrum, due to an induced frequency modulation (or frequency chirp) of the pulse carrier frequency ω_0 [85]. Under certain conditions, SPM can compensate the effect of anomalous GVD, in such a way that the optical pulse propagates undistorted along the fibers, i.e. giving rise to the formation of so-called solitons [73,85].

Airy pulse propagation in a Kerr medium, under the combined influence of SPM effect and different types of dispersion, has been investigated in both the temporal and spectral domains. In particular, Y. Fattal *et al.* [27] described the nonlinear propagation of an Airy pulse in the presence of a Kerr nonlinearity and anomalous GVD ($\beta_2 < 0$). In such conditions, the launched Airy pulse leads to the shedding of various soliton pulses, depending on the truncation coefficient (α) [Fig. 1.16]. In this case, most of the energy is provided to the temporal solitons, thus affecting the acceleration of the Airy pulse. Instead, by reversing the dispersion sign (i.e. normal GVD, $\beta_2 > 0$), the Airy wave packet disperses, and no soliton formation occurs in this case [83]. Although the main part of the energy content supports the pulse acceleration, a certain amount of leakage is observed. As presented in Ref. [33] and later detailed in Chapter 4 of this thesis, we will also show that an Airy pulse can fully preserve its accelerating property under SPM effect for both sign of β_2.

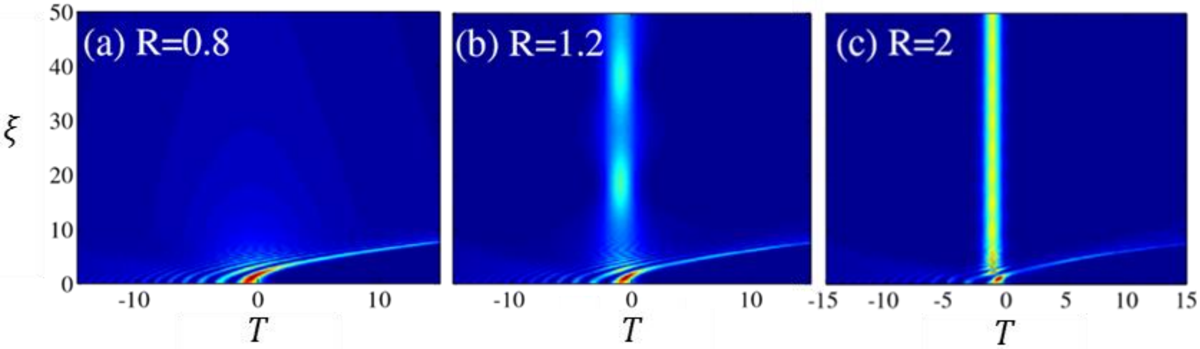

Figure 1.16: Nonlinear evolution of an Airy pulse in the presence of an anomalous GVD dispersion and SPM. Intensity distributions as a function of the normalized distance $\xi = z / L_d$ and time $T = \tau / T_0$ for (a) $R = 0.8$, (b) $R = 1.2$, and (c) $R = 2$. Here, R is a dimensionless parameter tuned to scale the Airy pulse power. (Figure adapted from Ref. [27]).

For the case considering a positive TOD, nonlinear self-focusing distorts the phase evolution typically associated with linear Airy pulse propagation. The consequence is a reduction of the previously mentioned tight-focusing effect [34].

In another relevant aspect of fiber propagation, the modulation instability (MI) of Airy wave packets has also been studied [86]. MI is a nonlinear phenomenon that originates from the interplay between nonlinearity and dispersion [87]. In optical fibers, MI can be due the interaction between SPM and anomalous GVD, leading to, e.g., a spontaneous break-up of an intense continuous wave (CW) radiation into a modulated light wave or a periodic pulse train, - see Ref. [85] for more details.

In the case of an Airy pulse, MI induces a modulation on the envelope of the various pulse lobes, followed by a splitting into multiple sub-pulses. If the truncation factor is small, the sub-lobe splitting precedes the one of the main lobe [Fig. 1.17(a)], while the opposite occurs for a larger truncation coefficient α [Fig. 1.17(b)] [86].

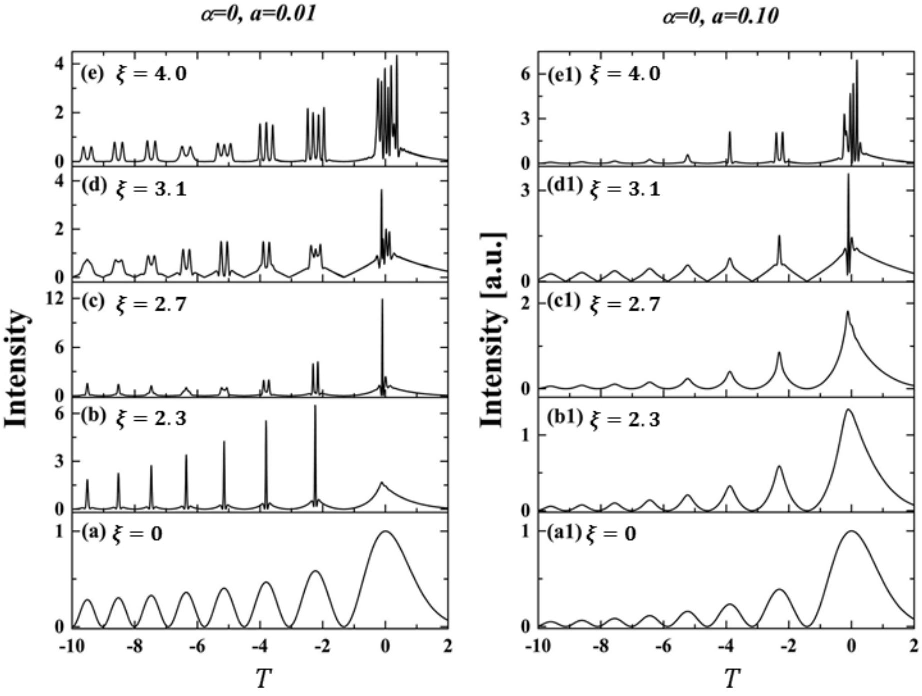

Figure 1.17: Modulation instability of an Airy pulse in the presence of an anomalous GVD and SPM. Intensity profile as a function of the normalized time $T = \tau / T_0$ at selected normalized distance $\xi = z / L_d$ for truncation coefficients (a-e) $\alpha = 0.01$ and (a1-e1) $\alpha = 0.1$, respectively. (Figure adapted from Ref. [86]).

Besides, the propagation dynamics of Airy pulses has also been investigated under the simultaneous influence of high-order dispersions and nonlinear effects. Such high-order contributions must be taken into account for nonlinear propagation of pulses with a duration typically shorter than 100fs [85]. The nonlinear evolution of such ultrashort pulses in fiber optics can be described by the generalized nonlinear Schrödinger equation (GNLSE) [88]:

$$\frac{\partial A}{\partial z} + \frac{\hat{\alpha}}{2} A - \sum_{k \geq 2} \frac{i^{k+1}}{k!} \beta_k \frac{\partial^k A}{\partial \tau^k} = i\gamma \left(1 + iT_{shock} \frac{\partial}{\partial \tau} \right) \left(A(z,\tau) \int_{-\infty}^{+\infty} R(\tau') \left| A\left(z, \tau - \tau'\right) \right|^2 d\tau' \right), \quad (1.26)$$

where the left- and right-hand terms account for the linear and nonlinear propagation effects, respectively. In Eq. (1.26), $\hat{\alpha}$ represents the linear loss, β_k the dispersion coefficients obtained from the Taylor expansion of $\beta(\omega)$ around ω_0, $R(\tau)$ the global nonlinear response function that includes instantaneous electronic (Kerr nonlinearity) and delayed Raman contributions. The delayed Raman response gives rise to the so-called Raman-induced frequency shift (RIFS), i.e. the shift of the spectrum associated to an ultrashort optical pulse toward longer wavelengths (red-shift). From the physical viewpoint, RIFS is attributed to intrapulse Raman scattering (IRS), a phenomenon where longer wavelength components of an optical pulse are amplified by the shorter wavelength components, thus providing energy to the red side of the spectrum through stimulated Raman scattering [89].

The time derivative term on the right-hand side models the dispersion of nonlinearity (or intensity-dependence of group velocity), characterized by the time scale $T_{shock}= 1/\omega_0$, and associated to the self-steepening (SS) effect. SS affects the propagation of an intense pulse by driving its peak at a lower speed than its wings, thus leading to shock formation in one of pulse edges [85].

Since Airy pulses are featured by an asymmetric temporal shape, they show a versatile behavior when experiencing such an “asymmetric” nonlinearity induced by the delayed Raman response.

L. Zhang *et al.* [90] investigated the role of IRS, SS and TOD on the dynamics of Airy pulses in optical fibers. In this study, several Airy pulses with different truncation coefficients (a) and input peak powers have been considered. In absence of IRS, the Airy pulse undergoes soliton shedding at high peak power, due to the interplay between SPM and anomalous GVD, as shown in Figs. 1.16 (b-c). When the effect of IRS is taken into accounts, the soliton generated from the Airy pulse captures a significant amount of the initial pulse energy and propagates, decelerating, along the fiber length, mainly due to the presence of IRS [Figs. 1.18 (a-d)]. In the Fourier domain, as expected, the Airy pulse spectrum undergoes a frequency red-shift induced by IRS [Figs. 1.18 (e-f)]. The RIFS can be tailored, not only by varying the peak power of the launched Airy pulse, but also acting on its truncation coefficient (a). Moreover, if the combined influence of Raman scattering and SS (or positive TOD) are taken into account, both TOD and SS effects slow down the RIFS during the nonlinear propagation of the Airy pulse. In particular, SS can suppress RIFS for long propagation distances. Furthermore, in addition to red-shifted frequency components, the simultaneous contributions of Raman, TOD, and SS effects produce a broadening spectrum that also extends toward blue-shifted components, when compared to symmetric input pulses [90].

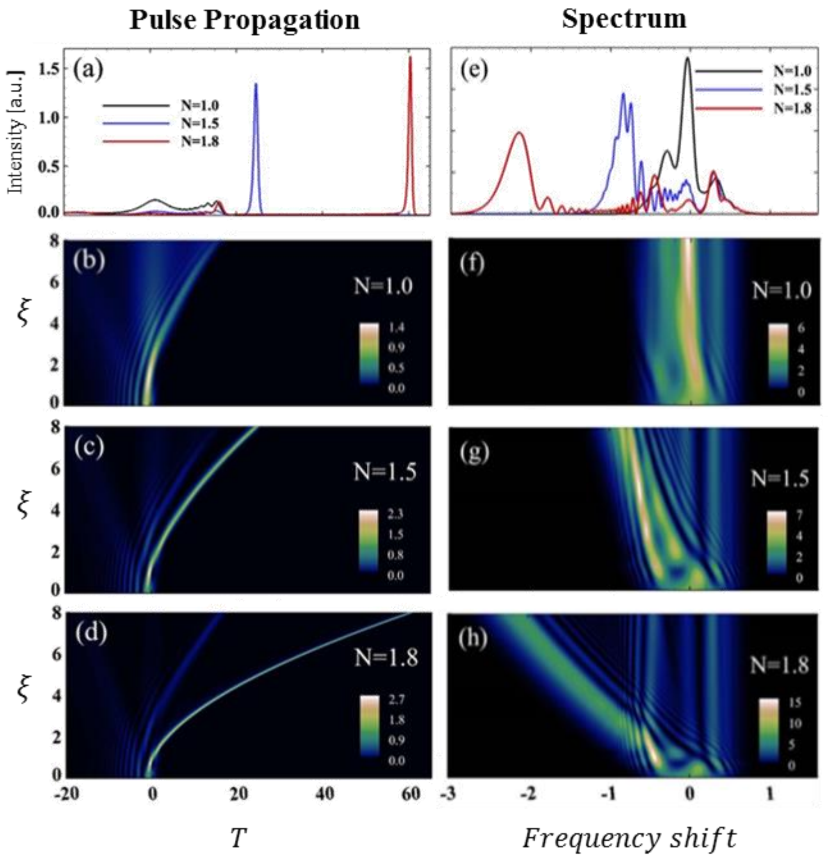

Figure 1.18: Nonlinear evolution of an Airy pulse in the presence of IRS, anomalous GVD dispersion and SPM. (a) Intensity and (e) spectral intensity profiles at $\xi = 8$, where $\xi = z / L_d$ is the normalized distance. (b-d) Intensity and (f-h) spectral distributions as a function of ξ and time $T = \tau / T_0$ for (b, f) $N = 1$, (c, g) $N = 1.5$, and (d, h) $N = 1.8$. Here, N is a dimensionless parameter tuned to scale the Airy pulse power. (Figure adapted from Ref. [90]).

Another way to control the RIFS was reported by Y. Hu *et al.* [36], who experimentally demonstrated the possibility of tuning the generation of solitons from an Airy pulse. A straightforward method to tune the RIFS is by using initially time-reversed Airy pulse.

Additionally, the authors also proposed how to control the RIFS by applying an offset to the initial cubic spectral phase structure used to generate the input Airy pulse.

Finally, Airy pulses have also been used in extreme nonlinear conditions for supercontinuum generation [91]. Such a nonlinear phenomenon is related to the spectral broadening experienced by optical pulses, due to the combined effects of dispersion and nonlinearity along the propagation medium [89]. Both experimental and numerical results of femtosecond Airy pulses sent in a highly nonlinear optical fiber typically shows the generation of distinctive features in the optical spectrum [91].

1.10 Optical Airy bullet

In the multi-dimensional (3+1)D regime, self-accelerating wave packets enable an easy and straightforward way to achieve optical light bullets, especially in the case of free-space propagation. Such localizations are spatio-temporal wave packets impervious to both dispersion and diffraction. Theoretically, the beam envelope in the spatio-temporal domain is described by the following normalized paraxial differential equation [10]:

$$i\frac{\partial\psi}{\partial Z}+\frac{1}{2}\left(\frac{\partial^2\psi}{\partial^2 X}+\frac{\partial^2\psi}{\partial^2 Y}+\frac{\partial^2\psi}{\partial^2 T}\right)=0. \tag{1.27}$$

In Eq. (1.27), $\psi(\vec{R},Z)$ is the electric field envelope, and $(\vec{R},Z)=(X,Y,T,Z)=$ $(x/w_0, y/w_0, \tau/\tau_0, z/L_{diff})$ are the dimensionless coordinates, in which w_0 and τ_0 are, respectively, the spatial width and the pulse duration of the wave packet. $L_{diff}= kw_0^2$ is the diffraction length, and k the wave vector. In particular, Eq. (1.27) is obtained by assuming anomalous dispersion. Here, a solution can be found using the separation of variables as: $\psi = \varphi(Z,T)U(Z,X,Y)$ [13]. In this case, to generate linear optical bullets, it is necessary to use non-diffractive beams in space and nondispersive pulses in time. Remarkably, an Airy pulse is the unique nondispersive wave packet existing in the (1+1)D regime, thus resulting the essential element required to synthesize linear optical bullets. For the spatial domain, the possibility of choice is multiple. In fact, any 2D non-diffractive configurations such as Bessel, Mathieu, 2D Airy beams, etc. can be employed [Fig. 1.19]. Nevertheless, since complete shape-preserving propagation intrinsically requires infinite energy, such optical bullets are only physically realizable by using finite energy non-broadening wave packets.

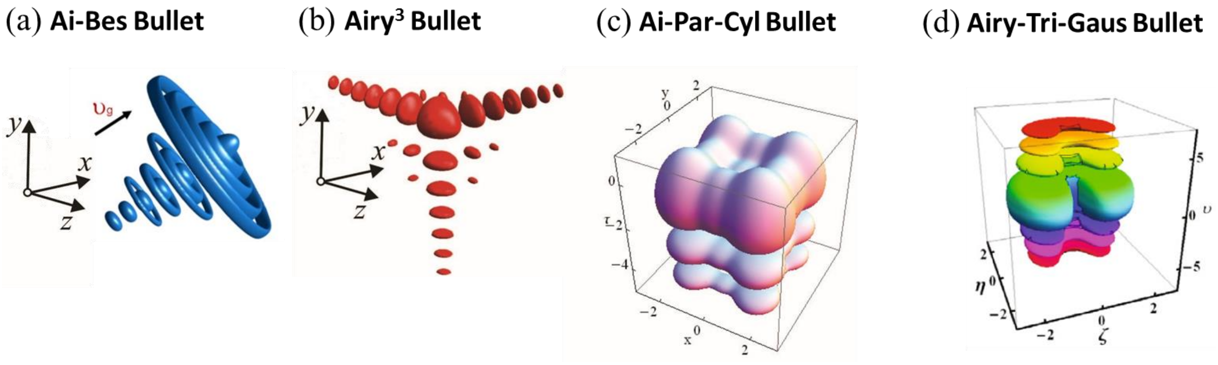

Figure 1.19: Linear three-dimensional (3D) spatio-temporal wave packets. (a-d) Examples of linear optical Airy bullets. (a) Airy-Bessel [37], (b) Airy^3 [38], (c) Airy-Parabolic-Cylinder [92] and (d) Airy-Tricomi-Gaussian [93] optical Airy bullets.

In this framework, A. Chong *et al.* [37] reported the first experimental demonstration of Airy-Bessel (Ai-Bes) bullets, formed by the combination of a Bessel beam in the transverse plane and an Airy pulse in time. The method is very general, being independent of the medium nonlinearity and material properties. Another work reported an analytical and numerical investigation of Airy Parabolic-Cylinder (Ai-Par-Cyl) light bullets, in which the spatial component is a parabolic-cylinder function, while the temporal counterpart is an Airy pulse [92]. Airy Tricomi-Gauss (Ai-Tri-Gau) light bullets have been also proposed and investigated [93]. In this case, the temporal part is given by the superposition of two counter-accelerating Airy functions, while the spatial part is formed by Tricomi-Gauss polynomials. One of most relevant works was performed by D. Abdollahpour *et al.* [38], who demonstrated experimentally the first realization of Airy^3 light bullets. Such linear spatio-temporal wave packets are formed by the combination of a spatial 2D Airy beam and an Airy pulse. Differently from all previously cases, in which the optical Airy bullets propagate along a straight path, an Airy^3 bullet evolves along a parabolic trajectory. In particular, an optical Airy^3 bullet extends to the spatio-temporal regime all the intriguing properties seen for its 2D counterpart, such as a bending propagation and self-healing. Interestingly, the authors also showed that this wave packet is robust in the high intensity regime. This research has been motivated by the fact that, due to the Airy wave packet self-healing property, the bullet is capable of counteracting the nonlinear-induced distortions and thus restore its initial spatio-temporal profile.

More interestingly, optical Airy^3 and Bessel-Airy bullets have been synthesized by separately shaping the temporal or spatial profiles, thus providing a straightforward way of experimentally realizing such spatio-temporal wave packets.

Finally, optical Airy bullets can also be realized in nonlinear media as demonstrated by P. Panagiotopoulos *et al.* [94], who investigated the nonlinear propagation, in fused silica, of intense radially-symmetric Airy waves (or abruptly autofocusing beams (AABs)). Under strong nonlinear conditions, the authors experimentally demonstrated that AABs reshape into nonlinear intense light bullets propagating over extended distances.

1.11 Selected self-accelerating beam applications

Over the last few years, several applications employing self-accelerating beams have been proposed and demonstrated. Most of them are related to the use of the Airy beam, even though several applications using non-paraxial configurations of self-accelerating beams have been recently introduced. In this section, we provide a brief overview of the most important works reported to date.

1.11.a Laser-assisted guiding of electric discharges by Airy beams

Electric discharges in air occur when a voltage is applied between two electrodes in order to establish an electric field exceeding a typical threshold value of about 34kV/cm. The large current arising from the electric breakdown usually follows an unpredictable path. Recently, M. Clerici et *al.* [42] have shown that electric discharges can be manipulated by means of shaped beams, thus sending the electric charges along pre-defined paths [Fig. 1.20]. From a physical viewpoint, shaped beams such as Airy beams induce an air ionization favoring the electric discharge due to the decrease of the breakdown voltage over the laser path [95-97]. In this work, the authors generated an electric discharge along a parabolic line using an Airy beam [Fig. 1.20(b)], while bypassing an obstacle placed along two wire electrodes. For completeness, they also induced discharges along more complex paths including an S-shaped trajectory - formed by concatenating two Airy beams generated from a binary cubic phase mask [Fig. 1.20(c)]. More interesting, the self-healing property of an Airy beam can be transferred directly from the laser to the flow of charges. Placing an obstacle at a given distance, the authors also demonstrated that the electric discharge resumed its original trajectory after being disrupted by the obstacle.

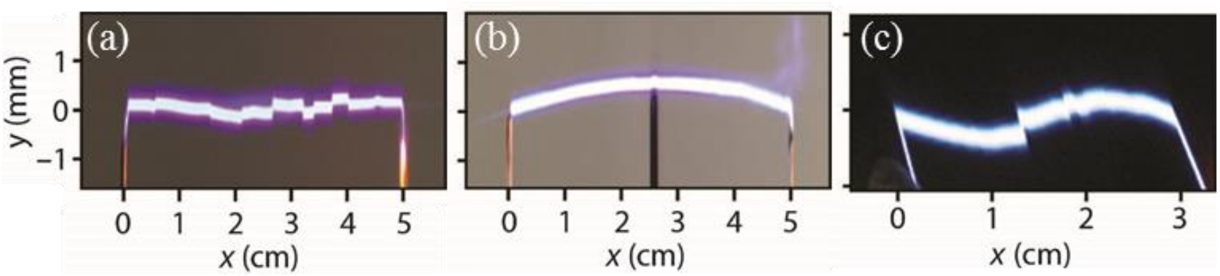

Figure 1.20: Laser-assisted curved electric discharges. (a-b) show different electric discharge paths induced by different optical beams, in the presence of a high voltage between two electrodes. (a) Gaussian beam case. (b) Airy beam case. (c) S-shaped beam case. Such an S-shaped path can be obtained by properly combining two Airy beams. (Figures adapted from Ref. [42]).

1.11.b Optical-induced particles cleaning using Airy beam

Another exciting application of self-accelerating beams was proposed for optical micromanipulation by J. Baumgartl et *al.* [98]. By using a 2D Airy beam, the authors reported the first demonstration of particle guiding along a curved path [Fig. 1.21(a)]. In their experiment, a 2D Airy beam was used as “snowblower”. As shown in Fig. 1.21(b), the curved beam entraps the colloidal particles from one section of a cuvette and ‘blows’ them towards the neighbor section [Fig. 1.21(b)]. Physically, micrometers-sized particles such as biological and colloidal objects respond to gradient and scattering forces, influencing the flow direction of these particles. If a 2D Airy beam is used, the optical gradient forces exerted by the Airy pattern drag these micrometers-sized particles towards the (high intensity) main lobe, which in turn guides the particles vertically along the parabolic trajectory. The particles are then dropped out from the beam-induced trapping when diffraction takes over. Moreover, self-healing in Airy beams makes this optically-induced particle sorting more robust compared to other light-based configurations. Additionally, the same group reported “optical path cleaning (OPC)” induced by Airy beams [99]. In this work, the authors showed the cleaning of large regions in a sample by using rotating multiple 2D Airy beams, acting in a synchronized fashion.

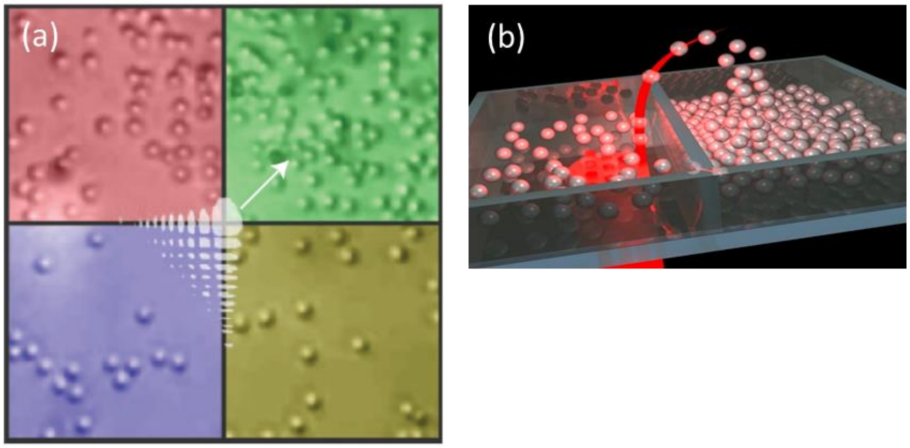

Figure 1.21: Optical micromanipulation using Airy beams. (a) Recorded micrograph of the sample after colloidal particles were exposed to an Airy beam. The white overlay highlights the Airy beam pattern, while the white arrow indicates its propagation direction. (b) 3D schematic view highlighting the ‘snowblowing’ effect produced by an Airy beam. (Figures adapted from Ref. [98]).

1.11.c Generation of curved plasma channels using Airy beams

Self-accelerating beams can also be employed to generate curved plasma channels. From a physical viewpoint, femtosecond laser pulses propagating in air can generate plasma by multiphoton absorption. Once formed, the defocusing effect of the plasma prevents the beam from collapsing (due to a strong self-focusing effect) into a singularity, thus forming submillimeter plasma channels (or filaments). In previous studies, plasma channels were generated by axially symmetric beams characterized by straight line propagations [45,100]. The emission of broadband conical light is also associated to laser-induced plasma channels, occurring at different longitudinal sections. The so generated contributions to such a radiation lead to mutual interference, thus affecting its frequency content. To address this issue,

P. Polynkin *et al.* [39] have demonstrated that by shaping an input femtosecond pulse with a Gaussian profile into a transversal 2D Airy profile [Fig. 1.22], it is possible to induce curved plasma channels in air, evolving along a parabolic path. In this way, the parabolic propagation of this Airy pump has been used to angularly resolve the generated broadband conical radiation in the far field [Fig. 1.22(a)]. In another related work, the same authors also reported the experimental observation of curved filaments in water. In this case, the predominant mechanism responsible for the beam collapse arrest is the group velocity dispersion in the medium [101].

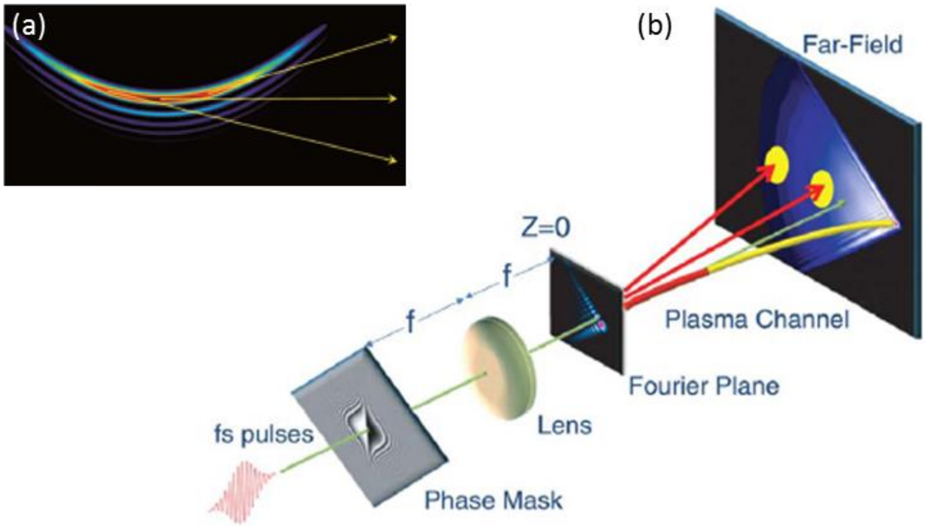

Figure 1.22: Curved-plasma channels generation from Airy beams. (a) Angularly-resolved radiation emission from a curved plasma. (b) Schematic of the experimental setup. The location in the plane at which the emission is observed allows to determinate the origin of the emission along the parabolic plasma. (Figures adapted from Ref. [39]).

1.11.d Generation of electron Airy beams

Almost all the applications involving self-accelerating beams rely directly on the evolution of optical fields. However, due to the mathematical analogy between the paraxial Helmholtz equation and the Schrödinger equation, the temporal evolution of the wave packet of a massive particle is similar to the propagation dynamics of a zero mass photon. In this contest, N. Voloch-Bloch *et al.* reported the first generation and observation of an Airy wave packet made of free electrons (thus referred as "electron Airy beam") [102]. Similar to their optical counterparts, electron Airy beams are shape-preserving matter waves exhibiting self-acceleration in the absence of an external force [Fig. 1.23(a)], as well as self-healing of their original shape when the initial electron beam profile deteriorates.

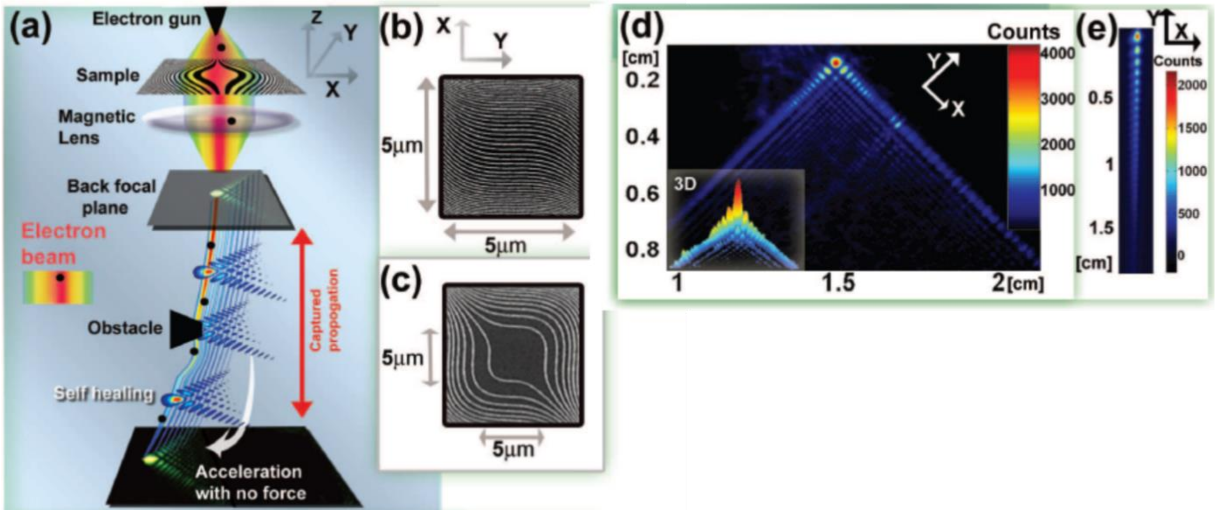

Figure 1.23: Experimental generation of electron Airy beams. (a) Schematic experimental setup. (b-c) TEM micrographs of the nano-scale holograms used to impress a cubic phase structure to the input electron gun with (b) and without (c) a spatial frequency carrier. (d-e) Micrographs of the experimentally generated (d) 2D and (e) 1D electron Airy beams. (Figures adapted from Ref. [102]).

The experimental realization of electron Airy beams was based on the same technique used to generate optical Airy beams. Firstly, the authors induced a cubic phase modulation in the Fourier domain of an initial electron beam through a nano-scale hologram, shown in Fig. 1.23(b). In particular, they imposed an additional spatial carrier frequency to the typical cubic phase structure [Fig. 1.23(c)]. Then, the electron Airy beam was generated by Fourier transforming the phase-modulated electron beam through a magnetic lens. The entire characterization was carried out inside a transmission electron microscope. Since the electronic beam shaping technique is similar to those exploited in optics, it enables the possibility of readily extending the advances obtained in optical systems to matter waves in both the paraxial and non-paraxial regime.

1.11.e Micromachining

Since an Airy beam was the first self-accelerating beam to be introduced in optics, it is natural to expect that most of applications actually refer to this wave packet. However, since it accelerates along a parabolic trajectory in the paraxial regime, it cannot be exploited in applications where different beam paths and/or large angles are required. To overcome this serious limitation, researchers are trying to extend the range of possible applications even to more arbitrary beams. For example, J. M. Dudley's group demonstrated the realization of arbitrary convex accelerating beams by engineering (in the real space) the appropriate phase mask to be imprinted to an indent Gaussian beam [17]. Such phase profiles, for both paraxial and non-paraxial accelerating beams, were estimated by using the caustic theory approach. As a proof of principle, the authors synthesized femtosecond accelerating beams with the desired trajectories, showing the ability of writing curved region of refractive index modification in glass, as shown in Fig. 1.24.

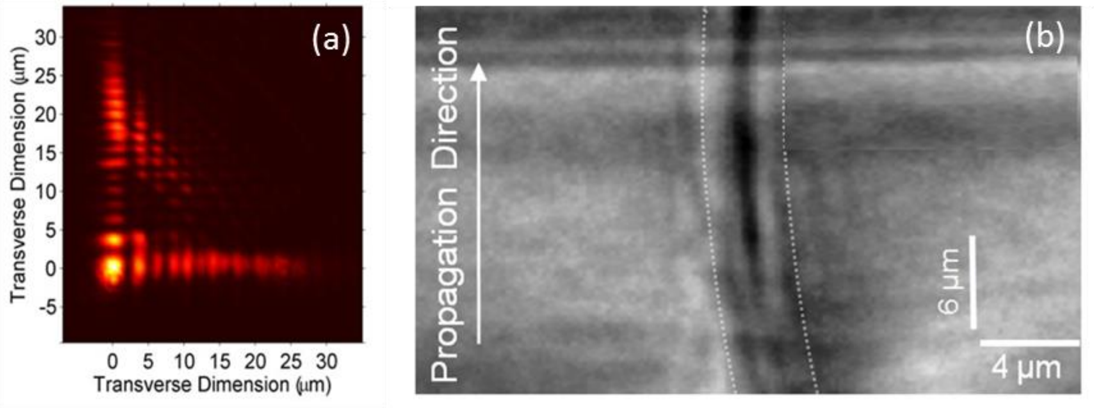

Figure 1.24: Femtosecond waveguide writing. (a) Transversal intensity distribution of the synthesized 2D Airy beam. (b) Curved region of refractive index modification. (Figure adapted from Ref. [17]).

To increase the beam intensity in the main lobe, the estimated phase profile has been applied along the two orthogonal directions of the SLM, thus creating a 2D beam profile, with an energy mostly confined in the beam main lobe [Fig. 1.24(a)]. In this experiment, a parabolic accelerating beam has been used, but the method is readily applicable for any arbitrary trajectory, even in the non-paraxial regime.

In related works, this group also reported laser micromachining of micron-sized curved surface and trenches with circular profiles, using tailored femtosecond accelerating beams [103-104]. For this application, the authors not only demonstrated the ablation in materials such as silicon and diamond using femtosecond accelerating beams, but also showed how efficiently a control of the depth of the trenches, as well as of the curvature of the surface could be achieved - as shown in Fig. 1.25.

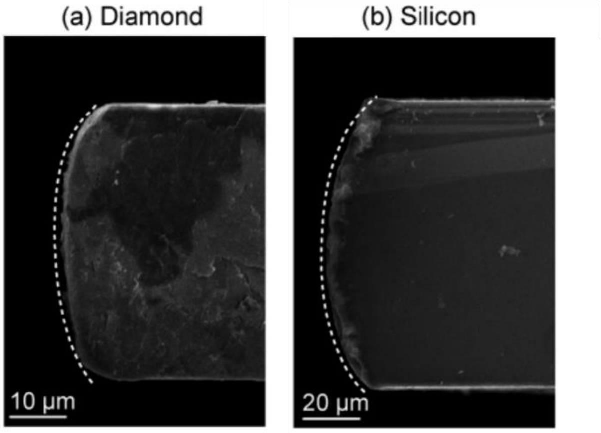

Figure 1.25: Micromachining using circular self-accelerating beams. (a) Curved machined surface obtained by ablating a 50μm-thick diamond sample with a bending radius of 70μm. (b) Machined surface for a 100μm-thick silicon sample using a beam circular trajectory with a 120μm-long bending radius. Dotted white line in (a-b) are the calculated ablation profiles. (Figure adapted from Ref. [103]).

1.11.f Other self-accelerating beams applications

Apart from the examples described above, the number of potential applications for self-accelerating beams has been growing rapidly in the last few years. For instance, G. Porat *et al.* [105] proposed a method to realize a solid-state laser emitting Airy beams. In such a laser, a diffraction grating imposing a transverse cubic phase to the diffractive light was used as the output-coupler. The Airy beam profile was obtained by adding to the laser system an external lens to compute the Fourier transform of the output beam. P. Rose *et al.* [106] introduced an all-optical routing scheme based on Airy beams capable to address as much as 16 individually output channels. For imaging applications, T. Vettenburg *et al.* [107] reported light-sheet microscopy using Airy beams. In this application, the authors demonstrated that an Airy beam not only produces high contrast and resolutions up to a tenfold larger field of view (FOV), but that its transverse asymmetric beam structure improves the imaging method. Using nonlinear optical phenomena, T. Ellenbogen *et al.* [28] demonstrated a new way of generating Airy beams. In particular, the authors experimentally generated a second-harmonic Airy beam by using three-wave mixing processes in asymmetric nonlinear photonic crystals. In related works, I. Dolev *et al.* also reported Airy beam generation and control from three-wave mixing processes [108-110]. In the field of plasmonics, A. Saladrino and D. Christodoulides [111] reported the existence of a 1D Airy solution in the planar system of a metal interface. Later on, several groups have provided experimental realization and control of plasmonic Airy beams [112-115]. Other applications of particular interests are those involving abruptly autofocusing beams (AABs). D. Papazoglou et *al.* [116] showed the advantage of AABs in laser processing of thick samples (e.g. 10mm fused silica) compared to a traditional Gaussian beam. Due to an abrupt enhancement in the intensity of these beams at the focal point, AABs combine short focal volume with a long working distance, thus making them ideal for nanosurgery and biomedical applications. P. Zhang *et al.* [117] also explored the possibility of trapping and guiding dielectric microparticles using AABs. In this work, the authors sent an AAB into an optical tweezers-like setting where the microparticles were trapped and transported along the AAB, which therefore behaved as a tapered channel guide for the microparticles.

Chapter 2

Trajectory prediction and designing of self-accelerating beams

In this chapter, we propose and demonstrate a method to control and design the propagation trajectories of one-dimensional (1D) single- and multi-path self-accelerating beams by way of a spectrum-to-distance mapping. Such mapping not only allows for a Fourier-space prediction of the propagation trajectory based on the a priori knowledge of the imposed spectral phase configuration, but also enables the possibility to engineer the beam initial spectral phase so to generate a beam propagating along an arbitrary convex trajectory. Furthermore, our approach gives an alternative physical justification to the self-healing property shown by this type of beams [15]. Non-paraxial accelerating beams characterized by large-angle convex trajectories can also be described by this method in both the scalar and vectorial context. Moreover, we also demonstrate the generation of periodic or zigzag self-accelerating beams in both the paraxial and non-paraxial regimes.

2.1. Introduction

In the last few years, the field of self-accelerating beams has attracted growing attention, mainly due to their fascinating propagation along a transversely bending trajectory. Airy beams, propagating along a parabolic trajectory in the paraxial condition, were the first wave packets to exhibit bending or self-accelerating trajectories (see Chapter 1 and reviews [118-119]). Potential applications, as well as the intriguing properties of these optical beams, have driven the research efforts to go beyond the paraxial approximation limit, and extend Airy parabolic paths towards the generation of more arbitrary convex trajectories. A great variety of self-accelerating beams exhibiting different trajectories has been suggested and demonstrated [17-21,44,47,51-52,120], in both the paraxial and non-paraxial regime. In these settings, the generation of these beams is obtained by imposing a phase modulation in the real space. Some works also showing the Fourier-generation of self-accelerating beams have already been recently reported in the literature. In particular, under the non-paraxial condition, both amplitude and spectral phase configurations for main humps following circular (Bessel-like), parabolic (Weber) and elliptic (Mathieu) trajectories, are found as solutions of complex separable coordinate systems, derived from the wave equation [19,21]. Nevertheless, all of them dealt with light localizations in which the main lobe moves along a convex smooth trajectory. Furthermore, all the progresses accomplished in this field rely on the application of a specific monotonic phase modulation which leads to single-path self-accelerating beams. The effect of a non-monotonic phase which can lead to multi-path beam localizations has not, surprisingly, been investigated to the best of our knowledge. Besides, a smooth trajectory is not the only possible way in which a self-accelerating beam can evolve. Light localizations with periodic or snake-like optical paths have been also introduced and experimentally observed through different approaches [121]. In particular, periodic self-accelerating beams can be realized by applying both a phase and an amplitude modulation in the Fourier regime, but they lack a general and detailed explanation. Such knowledge may pave the way to the design of beams with any desired profiles [43-44].

In this chapter, we introduce the concept of spatial spectral phase gradient which enables to map spatial frequencies to propagation distances. We will show theoretically and experimentally that such a spectrum-to-distance mapping can be employed to predict and manage the trajectories of single- or multi-paths self-accelerating beams by means of analyzing the Fourier-space phase. With reference to previous works, we notice that the spectrum of a self-accelerating beam is composed of different spatial frequencies whose phases have a special relationship. This resembles non-stationary signals in the time domain, which cannot be decomposed in sinusoidal signals of the same frequency. To analyze these signals in the framework of signal processing, the spectral phase gradient has been successfully introduced to describe the group delay [122]. Since the concept of group delay in time can be analogous to the position in the spatial domain, the spatial spectral phase gradient can be used to describe positions in space, so giving us the opportunity to control the trajectories of self-accelerating beams by analyzing the spatial spectral phase. In particular, we will show that for self-accelerating beams with a single smooth trajectory, different propagation distances are linked to different key spatial frequencies in the spectrum. Instead, for multi-path light localizations, different portions of the spectrum are mapped to different trajectories and each of them behaves in the same way as a single-path beam does. Several properties, including self-healing and curved trajectories, descent from such principle. Through this scheme, the path of a self-accelerating beam can be predicted from the knowledge of the phase modulation applied to the Fourier space. Conversely, the spectral phase structure can be also engineered in order to restrict the main hump propagation along any desired convex trajectory. Another important point to highlight is the fact that this method is not limited to the description of convex trajectories generated by phase-only spectral modulation, but also applies to beam paths produced by the combination of both spectral phase and amplitude modulation. Additionally, the generation of periodic accelerating beams will be also discussed. Such light localization patterns can be obtained by imposing both phase and amplitude modulations in the Fourier domain. We will show that when a homogenous or small amplitude modulation is impressed in the Fourier domain, a self-accelerating beam follows a smooth convex trajectory that can be traced by only analyzing the initially imposed spectral phase. Larger amplitude modulations, such as a Heaviside-shape profile with zero amplitude values, greatly affect the beam path, thus leading to the co-existence of straight-lines and convex trajectories. A “spectral well” structure yields to a reshaping of the convex trajectory into a “V”-shaped path. Periodic accelerating beams can be generated by employing appropriate arrays of “spectral wells”.

Beside the paraxial limit, we will also show that such a mapping is also applicable for generating large-angle multi-path periodic/smooth self-accelerating beams, only achievable under non-paraxial condition. Remarkably, our approach can explain from another perspective why an Airy beam breaks down the acceleration in the non-paraxial regime. Finally, we will analyze vectorial self-accelerating beams, whose intensity patterns are shared by the two polarized components. Similarly to the scalar case, we can apply our method to predict or engineering the whole beam pattern that will be followed by the sum of the two components.

2.2 Theory of spectrum to space mapping

We start our analysis by considering the 1D paraxial diffraction equation, which describes the propagation dynamics of the electric field envelope in the linear regime [1]:

$$i\frac{\partial\phi}{\partial z}+\frac{1}{2k}\frac{\partial\phi^2}{\partial x^2}=0, \tag{2.1}$$

Here $\phi(x,z)$ is the electric field envelope and k is the wave number. As shown in the sketch of Fig. 2.1, self-accelerating beams are generated in the real space (x-y-z), after shaping the spectrum in the Fourier plane. In this case, an initial plane wave is modulated in both amplitude and phase at the x'-y' plane (left side of Fig. 2.1) corresponding with the focal plane of a lens of focal length f. Since we here only deal with 1D self-accelerating beams, we apply a y'-independent amplitude and phase modulation in the spectrum. Additionally, the 1D Fourier transform of the modulated plane wave is spatially achieved through the use of a cylindrical lens (assumed to be ideal), thus forming a self-accelerating beam in the real space (x-y-z), right side of Fig. 2.1).

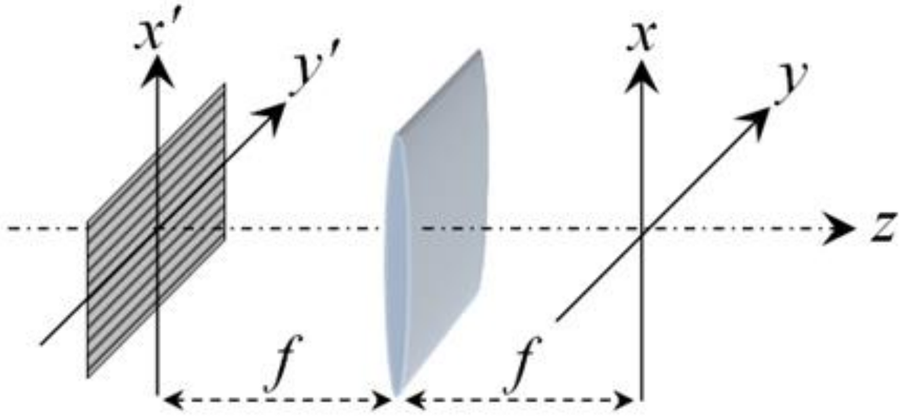

Figure 2.1: Sketch of the experimental setup employed for generating 1D self-accelerating beams, in which both a phase and an amplitude modulation is imprinted in the Fourier space (*x'*-*y'*).

The polarization of the input beam (i.e. the direction of the electric field oscillation) is set along the *y'*-axis. In such a case, no change of the polarization is involved throughout the propagation of self-accelerating beams, and the scalar description is therefore valid. On the other hand, if the initial beam is at least partially polarized along the *x'*-axis, a vectorial analysis must be considered as a bending propagation induces a change of polarization to the electric field. This case will be treated in further details in the next sections.

Under the paraxial condition, the electric field envelope can be described by this simple expression:

$$\phi(x,z)=\frac{1}{2\pi}\int_{-\infty}^{\infty}\tilde{E}(k_x,z)e^{ixk_x}dk_x. \tag{2.2}$$

In Eq. (2.2) $k_x = x'k/f$ is the spatial angular frequency, where x'/f is a scaling factor. $\tilde{E}(k_x,z)=A(k_x)\exp[i\mu(k_x,z)]$ is the Fourier spectrum, for which $\mu(k_x,z)=-{k_x}^2 z/(2k)+$ $+\rho(k_x)$ corresponds to the spectral phase. $A(k_x)\geq 0$ and $\rho(k_x)$ are respectively the amplitude and phase modulations set at the x'-y' plane. In analogy to the time domain, where the spectral phase gradient can be related to the group velocity [122], the spectral phase gradient in the spatial domain is related to the local position so that:

$$x=-\frac{\partial\mu(k_x,z)}{\partial k_x}=\frac{k_x}{k}z-\rho'(k_x). \tag{2.3}$$

In a local range Δx, the spatial frequencies $\Delta k_x \partial^2\mu(k_x,z)/\partial {k_x}^2$ are mainly responsible for aggregating the light, as these nearly-in-phase waves generate constructive interference. Since each spatial frequency component is weighted by $A(k_x)$, the spectral density $D(k_x)=\frac{dk_x}{dx}$ takes the form:

$$D(k_x)=\frac{A(k_x)}{\left|\partial^2\mu(k_x,z)/\partial {k_x}^2\right|} \tag{2.4}$$

At first, we will focus on self-accelerating beams generated by phase-only modulation in the Fourier space, without considering any effect due to an amplitude modulation. $A(k_x)$ is assumed to be homogenous and unitary $(A(k_x)=1)$. Since we only deal with phase variations, the amplitude of each k_x component in the Eq. (2.2) is thus equal and the spectral density $D(k_x)$ reduces to $1/\left|\partial^2\mu(k_x,z)/\partial k_x{}^2\right|$. The beam can reach the maximum intensity (MI) when the singularity condition $\partial^2\mu(k_x,z)/\partial k_x{}^2=0$ is satisfied. This spectral density singularity determines the beam caustic, strictly related to the trajectory followed by the self-accelerating beam. It can also be expressed as:

$$\rho''(k_x)=\frac{z}{k}, \tag{2.5}$$

thus relating spatial frequencies to propagation distance z. By solving Eq. (2.5), the key spatial frequencies (k_{xc}) determining the propagation trajectory can be expressed as a function of z. Furthermore, Eq. (2.5) together with the following:

$$\frac{dx}{dz}=\frac{k_{xc}(z)}{k}, \tag{2.6}$$

which is derived from Eq. (2.3) and (2.5), readily leads to the convex trajectory followed by the maximum intensity of the beam. A simple case can be illustrated by assuming $\rho''(k_x)$ to be a smooth monotonic function of the spectral angular frequency k_x. By solving Eqs. (2.5) and (2.6) the key spatial frequency k_{xc} is found to be a single-valued function of the propagation distance z so that the corresponding beam localization consists of a single convex trajectory. This allows us to define a spectrum-to-distance mapping, since different propagation distances z are related to different key spatial frequencies.

If the spectral amplitude components $A(k_x)$ are no longer uniform, the analysis must include further considerations. However, as will be shown in section 2.4, our method can still be applied to describe the dynamics of self-accelerating beams.

2.3 Phase-only modulation

In this section, we apply our analytical method to some particular cases of single- and multi-path beams. Herein, in particular, we deal with phase-only modulation, which leads to a light localization showing smooth single- and multi-trajectory paths. Under this condition, the beam evolution is given by:

$$\tilde{E}\left(k_x, z\right) = \exp[i\mu\left(k_x, z\right)]. \tag{2.7}$$

From the knowledge of the spectral phase modulation $\rho(k_x)$, the beam path of a self-accelerating beam can be predicted by calculating the key spatial frequency $k_{xc}(z)$ from Eq. (2.5), and then substituting it into Eq. (2.6). On the other hand, the phase structure $\rho(k_x)$ can be also engineered for any desired convex trajectory through the determination of $k_{xc}(z)$ from Eq. (2.6) and then inserting it into Eq. (2.5).

2.3.a Single-path self-accelerating beams

At first, a single-path self-accelerating beam is considered. As mentioned above, the phase modulation must have a second derivative which behaves as a smooth monotonic function of the spectral frequency k_x. A well-known case of single-path self-accelerating beam is the Airy beam, which bends along a parabolic trajectory, and is generated by a cubic phase modulation, as e.g. $\rho\left(k_x\right) = \left(\alpha k_x / k\right)^3$ ($a = 200$ and $k = 633\text{nm}$). Starting from this phase distribution, as expected from Eq. (2.5), the key spatial frequency is a linear function of the propagation distance z, according to $k_{xc} = k^2 z / (6\alpha^3)$ [dotted white line in Fig. 2.2(a)]. Inserting this estimated k_{xc} in Eq. (2.6), the convex trajectory followed by the MI is found to be the parabolic curve so that $T_r(z) = kz^2 / (12\alpha^3)$ [dotted white line in Fig. 2.2(b)]. The analytical prediction is further confirmed by numerical simulations of the beam propagation obtained by a Fourier transform of Eq. (2.2), as shown in the Fig. 2.2(b). Additionally, if all the sub-lobes in the intensity path illustrated in the Fig. 2.2(b) are then discarded, in order to only consider the main lobe of the beam, the spectrum corresponding to the residual intense hump will follow the linear evolution of the key spatial frequency described above [Fig. 2.2(a)].

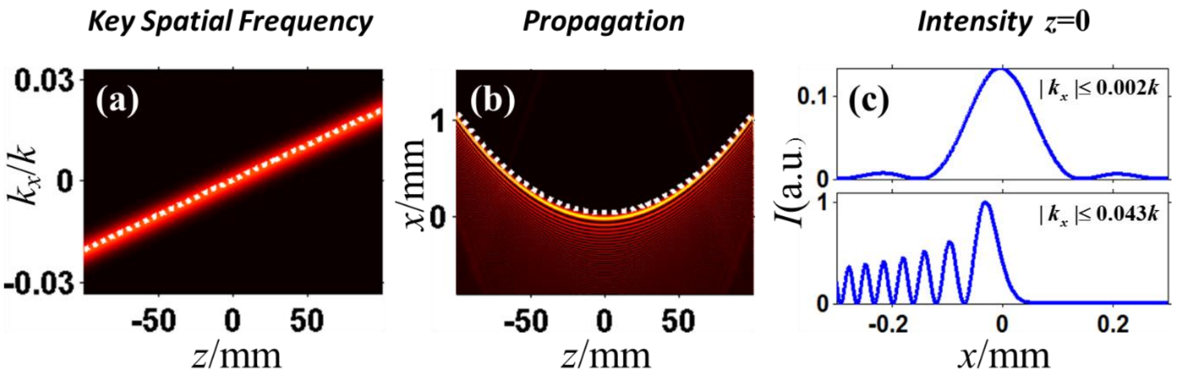

Figure 2.2: Single-path self-accelerating beam generated by a spectral cubic phase modulation under the paraxial approximation. (a) Estimated key spatial frequency (dashed white line) and residual spectrum (false color) corresponding to the main hump of (b); (b) predicted propagation trajectory (dashed white line) and numerical intensity beam evolution (false color); (c) intensity pattern at $z = 0$ calculated by considering a small $|k_x| \leq 0.002k$ (upper) and a large $|k_x| \leq 0.043k$ (bottom) interval of spatial frequencies k_x filtered around the key frequency k_{xc}. All the trajectories calculated analytically are slightly shifted with the purpose of better visual clarity when comparing the beam evolutions. This also applies to all the following figures.

A deeper understanding of the beam dynamics is also achieved by studying the influence of the spatial frequencies k_x around the key spatial frequency k_{xc}. As shown in the upper panel in Fig. 2.2(c), if we limit our study to the spectral components located within a small range around the key spatial frequency, the MI of the corresponding beam at $z = 0$ matches the spectral density singularity, estimated to be localized at $x = 0$. If we consider more spectral components, i.e. a larger frequency range surrounding the key spatial frequency, one can observe the deviation of the location of the MI with respect to the spectral density singularity position [bottom panel of Fig. 2.2(c)]. Neglecting this minor mismatch, the trajectory predicted by Eq. (2.5) and (2.6) perfectly agrees with the path of the main hump shown in Fig. 2.2(c).

The self-healing property, characteristic of self-accelerating beams, can thus be fully understood by this "uncorrelated" propagation of the main hump [18]. Indeed, since the main humps at different distances z are determined by different key spatial frequencies, even if the main lobe at a certain position is filtered out (or blocked – in more physical terms), the main hump at subsequent propagation distances, further away from the obstacle, is not influenced, as its position is mapped to a different key spatial frequency.

Although we limited our study to the particular example of a spectral cubic phase, our approach can be also used to describe a more general class of beams. In particular, the spectrum-to-distance mapping can be defined for any self-accelerating beam generated by an arbitrary phase modulation $(\rho(k_x))$ whose second derivative $(\rho''(k_x))$ is a monotonic function. As mentioned in the end of section (2.2), the key spatial frequency calculated from Eq. (2.5) remains, in this case, a single-valued function of z. Indeed, the beam path retrieved via Eq. (2.6) is composed by a single convex trajectory. Due to this mapping, the main hump of the beam at different propagation distances is linked to different key spatial frequencies. Furthermore, while for a spectral cubic phase the key spatial frequency varies linearly with the propagation distance [Fig. 2.2(a)], such evolution is generally curvilinear for an arbitrary spectral phase modulation.

2.3.b Multi-path self-accelerating beams

Next, we consider the case of an arbitrary spectral phase modulation. Since $\rho''(k_x)$ may not be a monotonic function, two or more key spatial frequencies could be involved in this case, in order to determine multiple beam localizations. The results for a typical example of non-monotonic function $\rho''(k_x)$ are shown in Figs. 2.3(a, b), obtained by analyzing the sinusoidal spectral phase modulation $\rho(k_x) = 130\sin(80k_x / k)$. By inserting this phase structure in Eq.(2.5), the propagation distance z is linked to the key spatial frequency through the relation:

$$z(k_{xc}) = -8.32\times 10^5 \sin(80k_{xc} / k) / k \tag{2.8}$$

Unlike single-path beams, in this case the key spatial frequency (k_{xc} (z)) is expressed as a multi-valued function of z and is numerically evaluated from Eq. (2.8). This is achieved by restricting the domain of k_{xc} to the portions of the spectrum [highlighted by the numbers 1, 2, 3 in Fig. 2.3(a)] where Eq. (2.8) results to be a single value of k_{xc}. If the monotonic portions of the key spatial frequency are then inserted into Eq. (2.6), we can predict the beam path to be composed by three trajectories (or branches). Each of these trajectories is associated to different spectral components, due to the fact that the key spatial frequency is still monotonic in that spectral range. This correspondence is illustrated in Figs. 2.3(a, b), where for clarity, we labeled with the same number each key spatial frequency and its related trajectory.

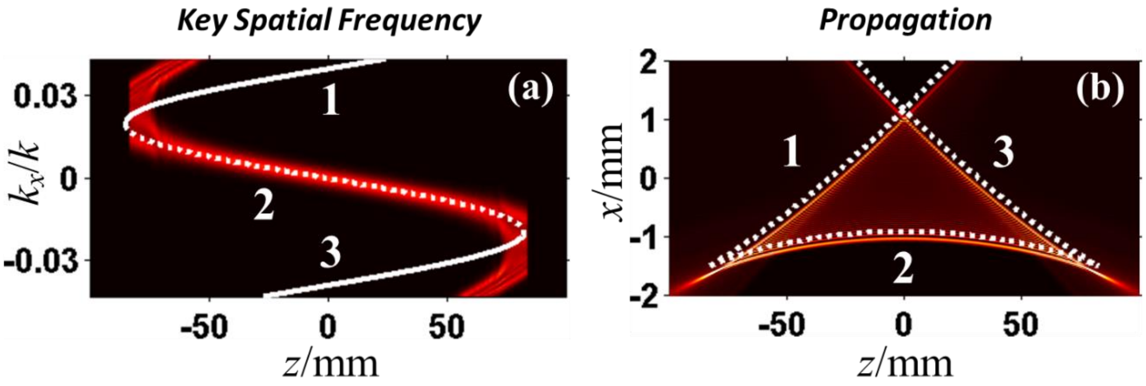

Figure 2.3: Multi-path self-accelerating beams generated by a spectral sinusoidal phase modulation under the paraxial approximation. (a) Multi-valued key spatial frequency (dashed white line) and the residual spectrum corresponding to the three main humps paths in (b); (b) predicted beam path (dashed white curves) and numerical beam evolution. The numbers indicate the correspondence between the trajectory and the related key frequency.

As shown in Fig. 2.3(b), our analytical approach is further confirmed by numerical simulations of the beam evolution based on the Fourier transforms of Eq. (2.2). In addition, when the beam path is filtered in order to only retain the main hump of the 2nd trajectory, the residual spectrum tends to evolve as expected from the corresponding key spatial frequency [white dotted line in Fig. 2.3(a)]. If the same filtering is carried out for the 1st and 3rd trajectories, the spectra associated to their main lobes evolve, respectively, almost as the corresponding key spatial frequencies [white solid lines in Fig. 2.3(a)]. Indeed, it is worth noting that the imperfect overlap is due to the unoptimized filtering procedure employed in the numerical simulations. This mismatch is expected to be efficiently reduced by blocking the beam path (i.e. filtering) in a more accurate way.

Going back to the general case, the same analysis carried out for the above example of a spectral sinusoidal phase can be directly applied to any arbitrary non-monotonic key spatial frequency. Different trajectories composing the beam path can be therefore linked to different portions of spectrum where the remaining key spatial frequency has a monotonic trend. In this way, all typologies of multi-trajectory beams can be described by using our approach.

In the next section, we provide experimental observations attesting the validity of such a spectrum-to-distance mapping approach.

2.3.c Experimental results

To verify the above analysis, we perform an experimental characterization using the setup shown in Fig. 2.4. A 2D Gaussian beam obtained by means of a He-Ne laser (CW at $\lambda = 633$ nm), horizontally-polarized (along the y'-axis) is initially truncated by two metallic blades, so as to approximate the circular Gaussian distribution to a 1D Gaussian beam. Then, the beam is phase modulated at the rear focal plane of a cylindrical lens (f=100 mm) using a phase mask, that is numerically uploaded into phase-only spatial light modulator (SLM) produced by Holoeye (Pluto – 1920×1080 pixels of 8×8 µm area, with 256 phase levels). The lens computes the Fourier transform of the phase-modulated Gaussian beam at the front focal plane. A CCD camera moving on a translation stage is then employed after the lens (i.e. in the real space), to record the beam evolution and the corresponding spatial spectrum. The latter are imaged by means of an additional cylindrical lens ($f = 100$ mm), while spectral filtering of the beam main hump is obtained using an adjustable slit made of two metallic blades.

We initially considered an Airy beam propagating along the parabolic trajectory shown in Fig. 2.2(b). The Airy beam is generated by uploading, into the SLM, a wrapped shifted 1D cubic phase mask [62], whose profile is plotted in the upper panel of Fig. 2.5(a). The beam evolution [Fig. 2.5(b)] follows the parabolic trajectory predicted by our model (dashed white line in Fig. 2.5(b)). More interestingly, as shown in Fig. 2.5(c), if the sub-lobes are filtered out, the main hump's spectrum shifts linearly with the propagation distance *z*, similarly to the simulation presented in Fig. 2.2(a), thus providing a direct proof that beam localizations at different propagation distances *z* are mapped to different spatial frequencies.

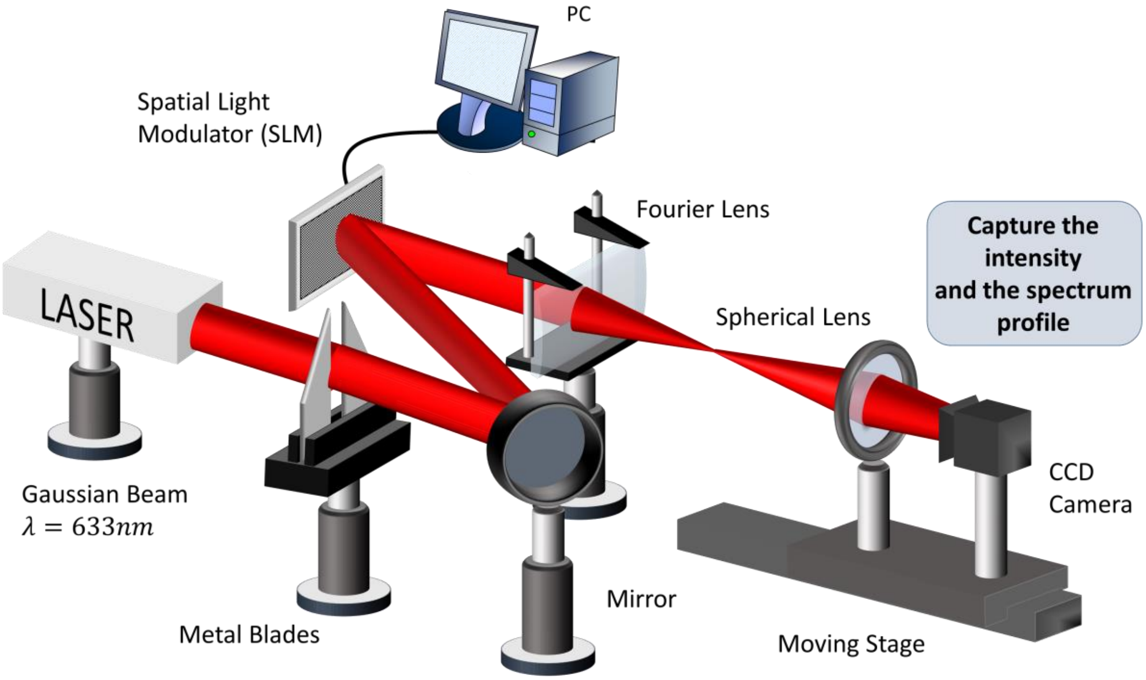

Figure 2.4: Experimental Setup

In a second experiment aiming to generate multi-path beam localizations, we employed two examples of phase modulation shown in Figs. 2.5(d, g), for which beam patterns exhibit two and three main humps, respectively. As illustrated in Figs. 2.5(e, h), the measured propagation patterns are in good agreement with the analytical predictions obtained via the spectrum-to-distance mapping (dashed white line in Figs. 2.5(e, h)). Furthermore, by blocking alternately the beam path(s) in the real space, each residual branch is shown to be linked to different parts of the spectrum, as presented in Figs. 2.5(f, i). Indeed, for the beam path constituted by two main trajectories [Fig. 2.5(e)], we can readily observe that two different spectral parts are linked to the two branches.

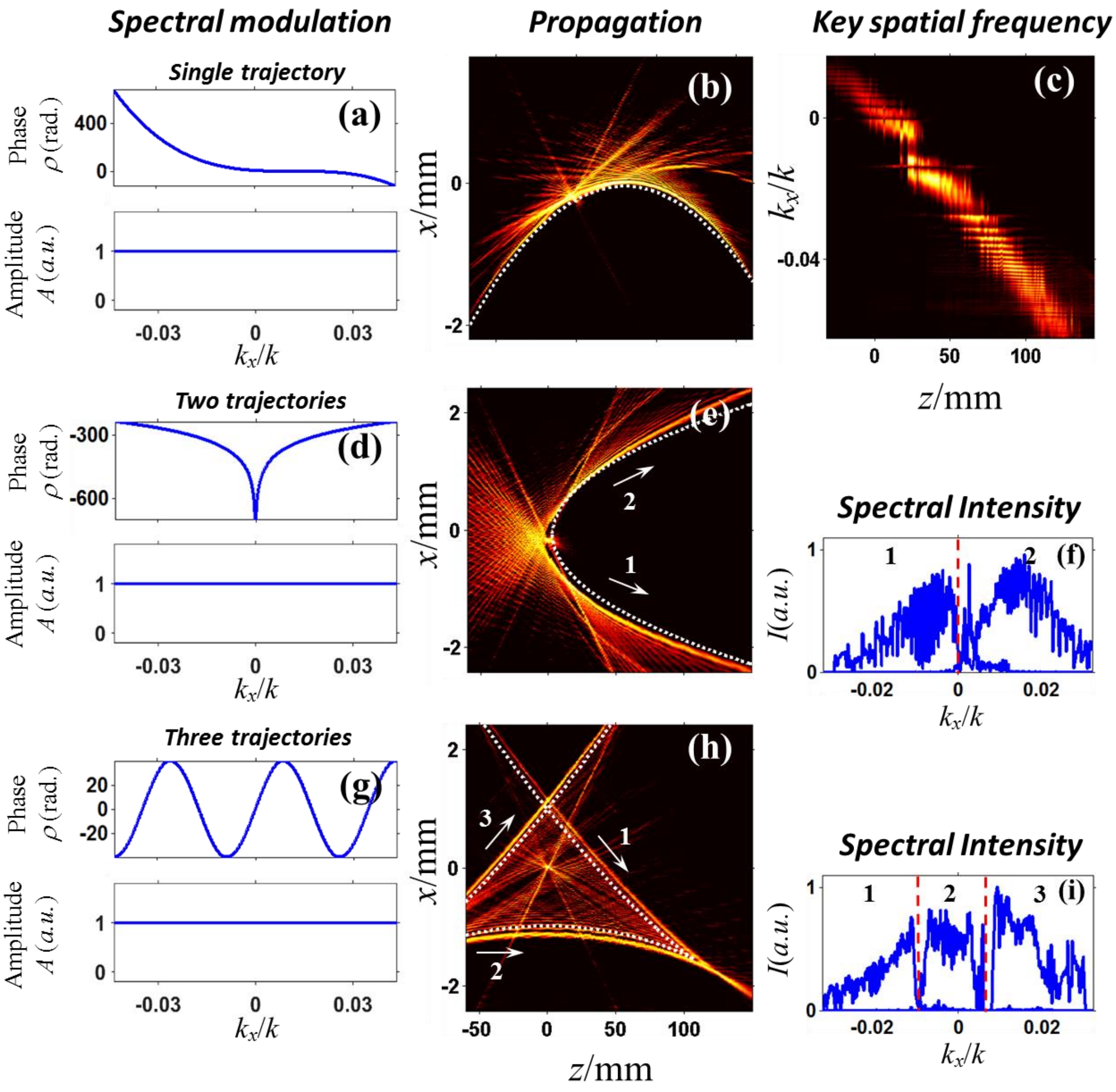

Figure 2.5: Experimental observation of self-accelerating beams with single- and multi-trajectory paths. (a, d and g) k-space phase and amplitude modulations imposed on the SLM, respectively corresponding to the beams evolution in (b, e and h). Note that in (b, e and h), the analytically predicted trajectories are shown as white dashed lines; Panels (a, b) depict a case of self-accelerating beam with a single-path related to the Airy beam; the associated (c) key spatial frequency distribution (c) is obtained by plotting the residual spectrum of the main hump as a function of the propagation distance after spatial filtering. Panels (d, e) and (g, h) show two cases of multi-path self-accelerating beams with two and three trajectories, respectively. For each of these cases, (f) and (i) respectively represent the spectral intensity of the multi-path self-accelerating beams extracted at z = 50 mm. Furthermore, in panels (f) and (i), the portions of the spectrum associated to the different trajectories in (e) and (h) are, respectively, labeled with the same numbers in (e) and (h).

Our measurements experimentally confirm the existence of a spectrum-to-distance mapping even for multi-path light localizations. Moreover, by alternatively blocking one of the two main branches and further filtering out the sub-lobes of the remaining trajectory (so leaving only its main hump), we can also image the different spatial frequencies associated to different positions of the main hump. As expected, this key spatial frequency is only localized in the portion of spectrum associated to the unblocked trajectory. The same behavior is also observed for the pattern exhibiting three main trajectories. [Fig. 2.5(h)].

Although all the analysis and experimental observations shown here are related to the trajectory prediction from a known spectral phase, it can be conjectured that, conversely, the phase structure to be implemented for any desired beam trajectory can be designed using the results shown above. Several examples of this approach are shown in section 2.5a, where the spectral phases for various trajectories of non-paraxial self-accelerating beams are engineered (see Fig. 2.11). Paraxial examples of similar beam designs are also shown in the third chapter, for which we extend our previous analysis to the two-dimensional regime in order to calculate the spectral distributions to be used for generating the desired trajectories.

2.4 Spectral phase and amplitude modulation

When the spectral modulation in Eq. (2.2) does not exhibit a constant amplitude anymore, meaning that $A(k_x)$ is now a function of the spatial frequency, the theoretical analysis shown previously may require further considerations. Assuming that the spectral amplitude is strictly positive (i.e. $A(k_x) > 0$), with relatively small variations, the spectral density $D(k_x)$ = $A(k_x)/\ |\mu''(k_x)|$ still shows a singularity for $|\mu''(k_x)| = 0$. Therefore, the previous analysis used to predict the beam path still remains valid. Nevertheless, when the amplitude modulation depth is very high, i.e. $A(k_x) \approx 0$, this approach is not valid anymore and the analysis must be revisited. To analyze the influence of a spectral amplitude modulation on the dynamics of self-accelerating beams, we will study three particular examples of amplitude distributions: a Heaviside-shape, a so-called "spectral well" and an array of multiple "spectral wells".

2.4.a Heaviside spectral amplitude modulation

The simplest case of spectral amplitude modulation to be considered corresponds to a Heaviside shape whose profile is given as:

$$A(k_x) = \begin{cases} 1 & k_x \le k_{x0} \\ 0 & k_x > k_{x0} \end{cases} \tag{2.9}$$

We illustrate this example in Fig. 2.6, where we show the dynamics of a Fourier-generated self-accelerating beam [Fig. 2.6(a)] obtained by combining an arbitrary phase modulation $\rho(k_x)$ with a Heaviside amplitude modulation $A(k_x)$ (illustrated as a grey shaded rectangle in Fig. 2.6(b). The phase modulation $\rho(k_x)$ is assumed to be monotonic, with a second derivative $\rho''(k_x)$ also increasing monotonically, for which our method predicts the beam to propagate along a smooth convex trajectory. Here, the presence of a Heaviside amplitude modulation strongly alters the curved propagation: For ranges of propagation distances z up to $z_0 = k\rho''(k_{x0})$, Eqs. (2.3) and (2.4) can be still used to estimate the convex trajectory, since these distances are mapped to key spatial frequencies whose amplitude is unitary ($A(k_x) = 1$). Nevertheless, for distances z larger than z_0 (i.e. where $A(k_x) = 0$), the beam path deviates from the predicted convex trajectory and our approach must be re-examined. Indeed, according to Eq. (2.3), such distances should be mapped to key spatial frequencies larger than k_{x0}, for which the spectral density $D(k_x)$ is actually equal to zero - rather than exhibiting a singularity that enables the calculation of the beam path seen above. In this case $D(k_x)$ can only reach a maximum in the range $k_x \le k_{x0}$, associated to a minimum of $|\mu''(k_x)|$). The underlying question here is related to the behavior of $|\mu''(k_x)|$ outside this propagation range. Since we assume that $\rho''(k_x)$ is a monotonically growing function, $\mu''(k_x)$ not only increases monotonically, but also remains negative for propagation distances $z > z_0$. Conversely, $|\mu''(k_x)|$ has a monotonic decreasing trend (black solid line in Fig. 2.6(b)) reaching the minimum at the jump point of the Heaviside-shape spectrum $k_x = k_{x0}$. For spatial frequencies

$k_x > k_{x0}$, $|\mu''(k_x)|$ continues decreasing, but the spectral density $D(k_x)$ is null in this case. As a result, the spectral density $D(k_x)$ does not show a singularity when $|\mu''(k_x)| \to 0$, because it is null for $z > z_0$. For these distances, $D(k_x)$ only reaches a maximum value appearing at $k_x = k_{x0}$. As a consequence, the key spatial frequency k_{xc} is constant over this range and coincides with the spatial frequency at the jump point of the Heaviside spectrum k_{x0}.

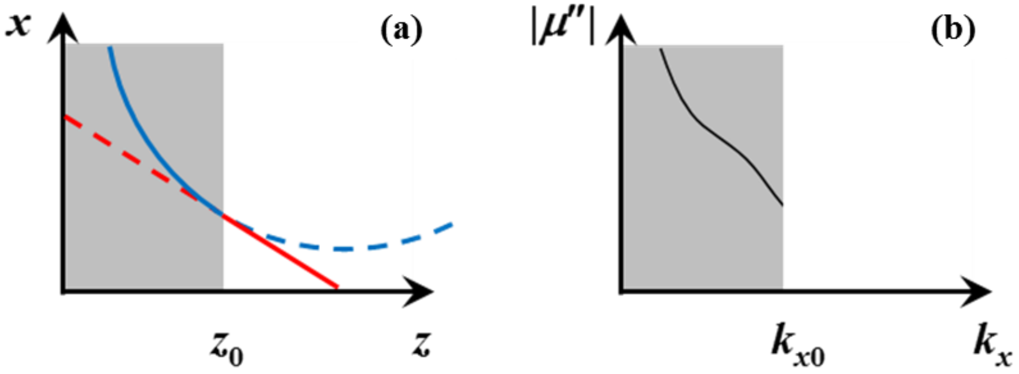

Figure 2.6: Schematic dynamics of a self-accelerating beam obtained from a spectral amplitude modulation having a Heaviside shape. Panel (a) shows the composed path followed by the beam during propagation. Solid blue and red lines highlight the convex and straight-line components, associated to spatial frequencies in which the Heaviside amplitude modulation is unitary and zero, respectively. Panel (b) shows a plot of the evolution of $|\mu''(k_x)|$ for propagation distances $z > z_0$. The shaded grey rectangle in (b) indicates the Heaviside amplitude spectral distribution.

According to this argument, we can infer that our analytical scheme still provides a correct description of the beam path, even in the presence of a larger spectral amplitude modulation, but Eq. (2.2) must be first modified so that:

$$x = \frac{k_{x0}}{k} z - \rho'(k_{x0}). \tag{2.10}$$

Eq. (2.10) points out that the beam path is not a convex trajectory anymore, but the MI undergoes a linear shift with distance. Such a linear evolution is schematically described by the red line plotted in Fig. 2.6, which is tangent to the convex trajectory (blue line) at $z = z_0$.

In particular, Eq. (2.10) is obtained analytically from Eqs. (2.6) and (2.3) by substituting $k_{xc} = k_{x0}$ for every $z \geq z_0$. Indeed, from Eq. (2.6), we find that $dx/dz\,|_{z\geq z_0} = k_{xc}\left(z\right)/k = k_{x0}/k$. From this expression, the beam trajectory for $z \geq z_0$ is calculated to be the tangent line to the convex trajectory at z_0, given by:

$$x(z) = x(z_0) + \frac{k_{x0}}{k}\left(z - z_0\right). \tag{2.11}$$

Moreover, from Eq. (2.3), we can find out that the local positon at $z = z_0$ is related to the spectral phase gradient as: $x\left(k_{xc}(z_0), z_0\right) = k_{x0} z_0 / k - \rho'\left(k_{x0}\right)$. Finally, Eq. (2.10) results by replacing the term $x(z_0)$ on the right-hand side of Eq. (2.11) with $x\left(k_{xc}(z_0), z_0\right)$.

Therefore, if a spectral amplitude with a Heaviside shape is impressed in the frequency domain, the beam path can still be predicted via our approach as a composite trajectory made of the curved and straight paths respectively corresponding to propagation distances before and after the distance $z = z_0$. The MI of beam follows a convex trajectory for $z < z_0$ and then it evolves along the straight path tangent to the convex trajectory at z_0. All our considerations are based on a monotonically increasing $\rho''(k_x)$, but a similar behavior can be readily retrieved assuming a monotonically decreasing case. It is also worth mentioning that the path followed by a self-accelerating beam generated by a Heaviside-like amplitude modulation with non-zero values at $k_x > k_{x0}$ (e.g., by adding a constant offset to the previous Heaviside spectral distribution) is similar to the one obtained by a complete modulation.

2.4.b Airy beam generated by a Heaviside spectral amplitude modulation

To validate the above analyses, we now take in consideration a specific example of self-accelerating beam, generated by applying both a phase $\rho(k_x)$ and a Heaviside amplitude $A(k_x)$ modulation at the Fourier space. As spectral phase, we consider the cubic function $\rho(k_x) = [a\,(k_x - b)/k]^3$ $(a^3 = -4\times10^6, b = 0.033k)$ [upper panel in Fig. 2.7(a)], widely-used to generate Airy beams. In this case, both $\rho(k_x)$ and its second derivative $\rho''(k_x) = 6a^3(k_x - b)/k^3$ are monotonically increasing functions. The numerical simulation shown in Fig. 2.7(c) illustrate the parabolic trajectory $T_r(z) = kz^2/(12a^3) + bz/k$ followed by the Airy beam in the absence of a spectral amplitude modulation (see Fig. 2.7(a)). If now the cubic phase modulation is combined with a spectral Heaviside amplitude modulation (for which $k_{x0} = 0.005k$) [see lower panel in Fig. 2.7(b)], our method estimates the beam path to be composed by a parabolic curve up to $z = z_0 = 6a^3(k_{x0} - b)/k^2$, and a straight line tangent to this curve at z_0 for propagation distances larger than z_0 (white dashed line in Fig. 2.7(d)). This analytical prediction is confirmed by the beam evolution computed from Eq. (2.2), in which one can also notice that the main hump of the beam experiences a dramatic increase in terms of width when propagating along the straight-line portion (thus attesting for the loss of non-diffraction behavior over this propagation range – see Fig. 2.7(d)). In addition, if the sub-lobes in Fig. 2.7(d) are filtered out, thus only leaving the main lobe, the residual spectrum shifts linearly with the propagation distance z up to z_0, and then remains constant for $z > z_0$ [Fig. 2.7(e)], in good agreement with our theoretical predictions. To complement numerical simulations, we also carried out an experimental demonstration employing the setup used described in the first section. The spectral amplitude modulation was performed by placing a transparent film right in front of the SLM, on which the designed (opaque) amplitude pattern was printed. The amplitude modulation have been drawn through scaling the spectral and real coordinates with the focal lens (f = 100 mm), as $x = k_x/f$. In order to readily compare our experimental results with the numerical simulations illustrated in Figs. 2.7(c-e), we generated an Airy beam using the same parameters. As shown in Figs. 2.7(f-h), the measured beam propagations and main lobe spectral distributions show excellent qualitative agreement with our numerical results.

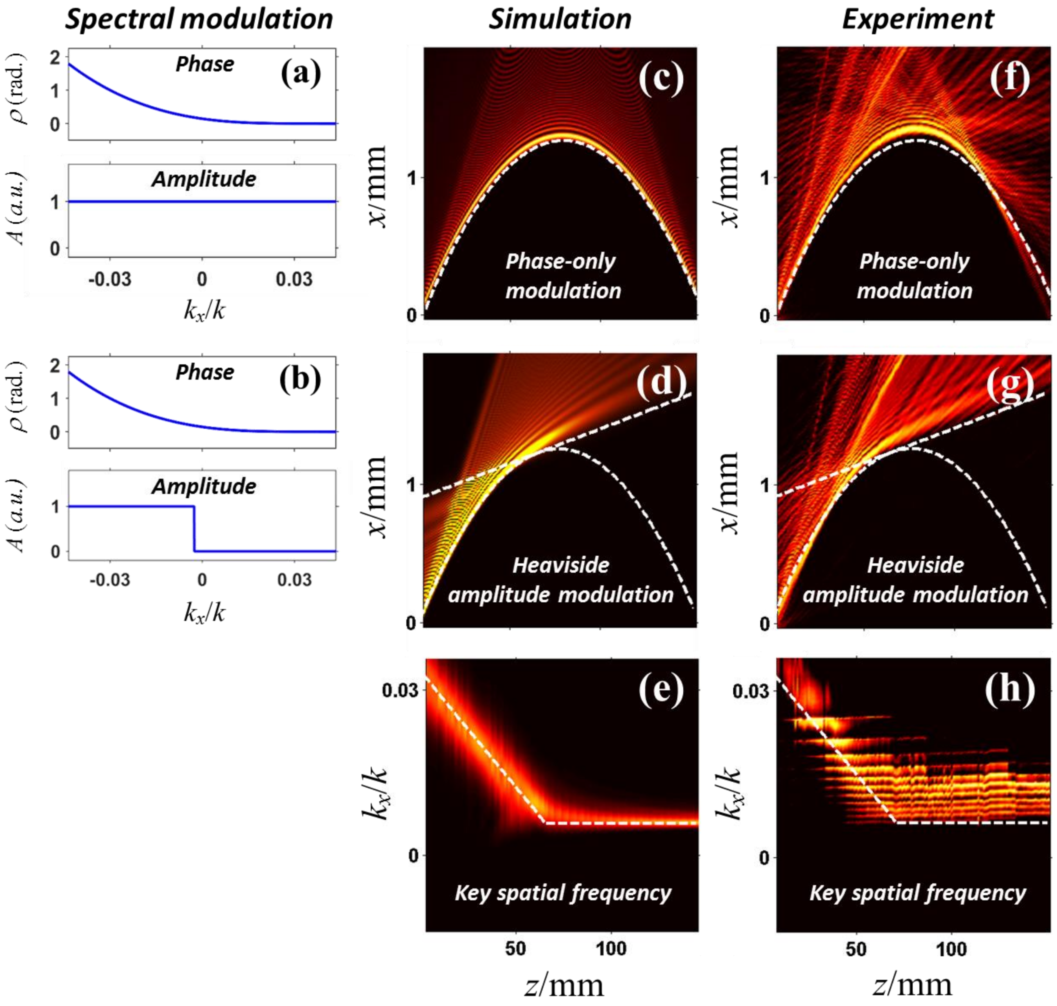

Figure 2.7: Experimental observation of an Airy beam generated using a cubic phase modulation and different amplitude modulations in the spectral domain. In the 1st column we plot the spectral cubic phase (upper panel) and amplitude (lower panel) distributions imposed in the SLM; the 2nd and 3rd columns illustrate the numerical evolutions and experimental observations, respectively. (a) Plots of the spectral phase and an homogenous amplitude modulation corresponding to an Airy beam propagating along the smooth parabolic trajectory shown in (c) and (f); (b) plots of the phase and a Heaviside-shape amplitude modulations for an Airy beam propagating along a path composed by a smooth parabolic trajectory and straight line in (d) and (g). (e) Numerical and (h) experimental key spatial frequency distributions obtained by filtering the main-lobes in (d) and (g), respectively. In all the panels, dashed white lines represent the analytical predictions of either the beam trajectory or key spatial frequencies, obtained via the spectral-to-space mapping.

2.4.c “Spectral well” amplitude modulation

Before, we analyze the effect of a Heaviside-shape amplitude modulation on the dynamics of the Airy beam. Here, we extend our study towards the effect of more complex spectral amplitude structures on the Airy beam propagation dynamics (whose phase modulation is here $\rho(k_x)=\left[a(k_x-b)/k\right]^3$ – where $a^3=-6\times10^6$, $b=$ 0.043k – as seen in Fig. 2.8(a)). A straightforward case consists in modulating the amplitude through a “spectral well”, in which the spectral amplitude $A(k_x)$ is null within the range $k_{x1} \leq k \leq k_{x2}$, and 1 otherwise [see Fig. 2.8(b)].

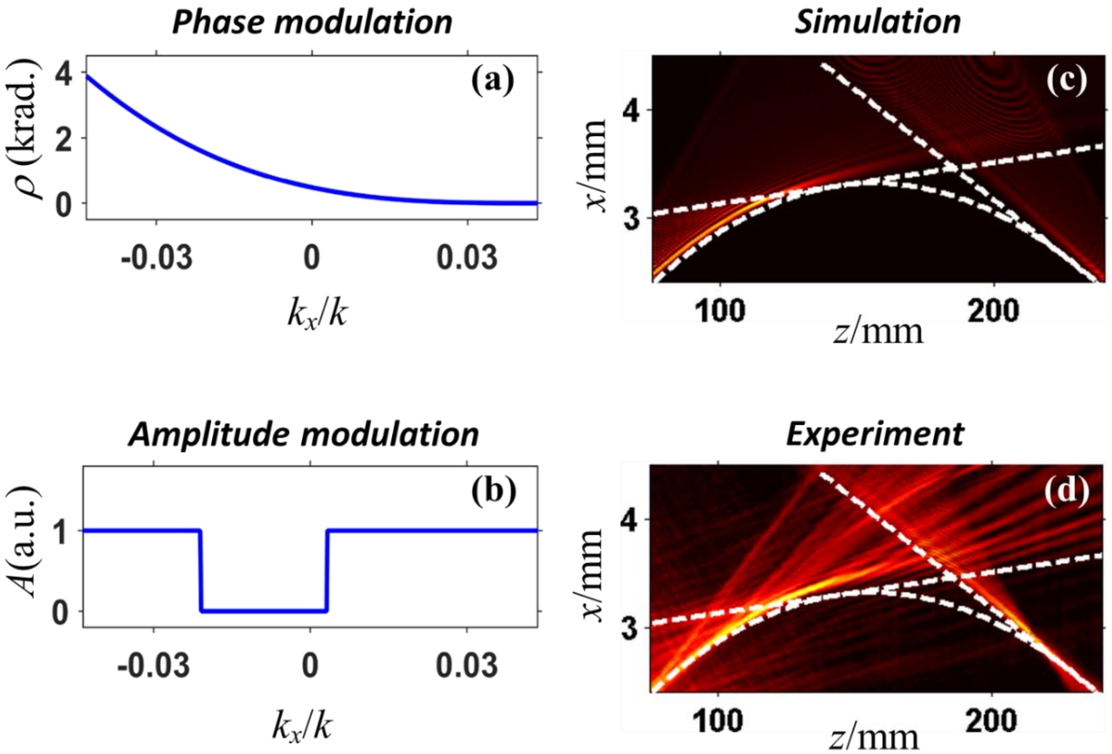

Figure 2.8: V-shaped path of a self-accelerating beam along a parabolic trajectory, generated by modulating the amplitude through a single spectral “well”, and the phase through a spectral cubic distribution. Panels (a) and (b) represent the spectral phase and amplitude modulation, respectively. Panels (c) and (d) show the numerical and experimental results of the propagation intensity distributions. Dashed white lines in (c,d) represent analytical predictions of the various trajectory components (ideal parabolic and tangential lines) via both the spectral-to-space mapping for the combination of the phase and amplitude modulation shown in (a) and (b).

In this case, the beam path predicted through the spectrum-to-distance mapping is found by joining together two straight lines, appearing in the range $6a^3\left(k_{x2}-b\right)/k^2 < z < 6a^3\left(k_{x1}-b\right)/k^2$, with a parabolic trajectory elsewhere (dashed white line in Fig. 2.8(b)). Such linear propagation range Δz is bounded by $z_1 = k\rho''\left(k_{x1}\right)$ and $z_2 = k\rho''\left(k_{x2}\right)$, and is correlated to the spectral distance between the jump points present in the "spectral well" $\Delta k_x = \left|k_{x2}-k_{x1}\right|$, similar to what is seen for the case of a Heaviside-shape distribution. If Δk_x is small enough, the parabolic trajectory evolves into a "V"-shaped beam path formed by the two straight lines tangent to z_1 and z_2. We mention that the "V"-shaped path matches the parabolic trajectory asymptotically, i.e. for $\Delta k_x \to 0$. As Δk_x increases, the "V"-shaped path vanishes, thus causing a severe distortion at the convex trajectory.

The results shown in Fig. 2.8 further confirm the analytical prediction of a "V"-shaped beam path, highlighting the good agreement between numerical simulations [Fig. 2.8(c)] and the experimental observations seen in Fig. 2.8(d).

2.4.d Periodic self-accelerating beams

An interesting feature of the above-mentioned "V"-shaped paths lies in their ability to be used as elementary cells for the construction of periodic (or "zigzag") self-accelerating beams. Since a "spectral well" amplitude modulation produces a light interference leading to a beam propagation along two straight lines (when the corresponding spectral amplitude modulation is null), one can envision the generation of periodic self-accelerating beams composed of several "V"-shaped paths, employing an array of wells for the initially imprinted spectral amplitude modulation. As an illustrative example, we here focus our attention to the case of a beam whose spectral phase modulation possesses the same characteristics of the "spectral well case" shown in Fig. 2.8, and also reported in Fig. 2.9(a) for clarity. Through numerical simulations, we first optimized the periodicity of the amplitude modulation to be used for generating an appropriate "zigzag" accelerating beam. Imposing such a periodic amplitude modulation, as illustrated in Fig. 2.9(b) the beam exhibits a path in which the main lobe still accelerates along a parabolic trajectory, but experimenting several local and periodic "zigzag" oscillations.

These oscillations are matched by the series of "V"-shaped straight lines, and our simulation results as well as experimental observations are both in excellent agreement with the predictions of our approach. In order to observe a proper periodic beam path generated by the light interference pattern, both the period and the relative duty cycle of the spectral well array should be adequately tuned to achieve a symmetric zigzag. Otherwise, the absence of a properly adjusted amplitude modulation can lead to the disappearance of such oscillations.

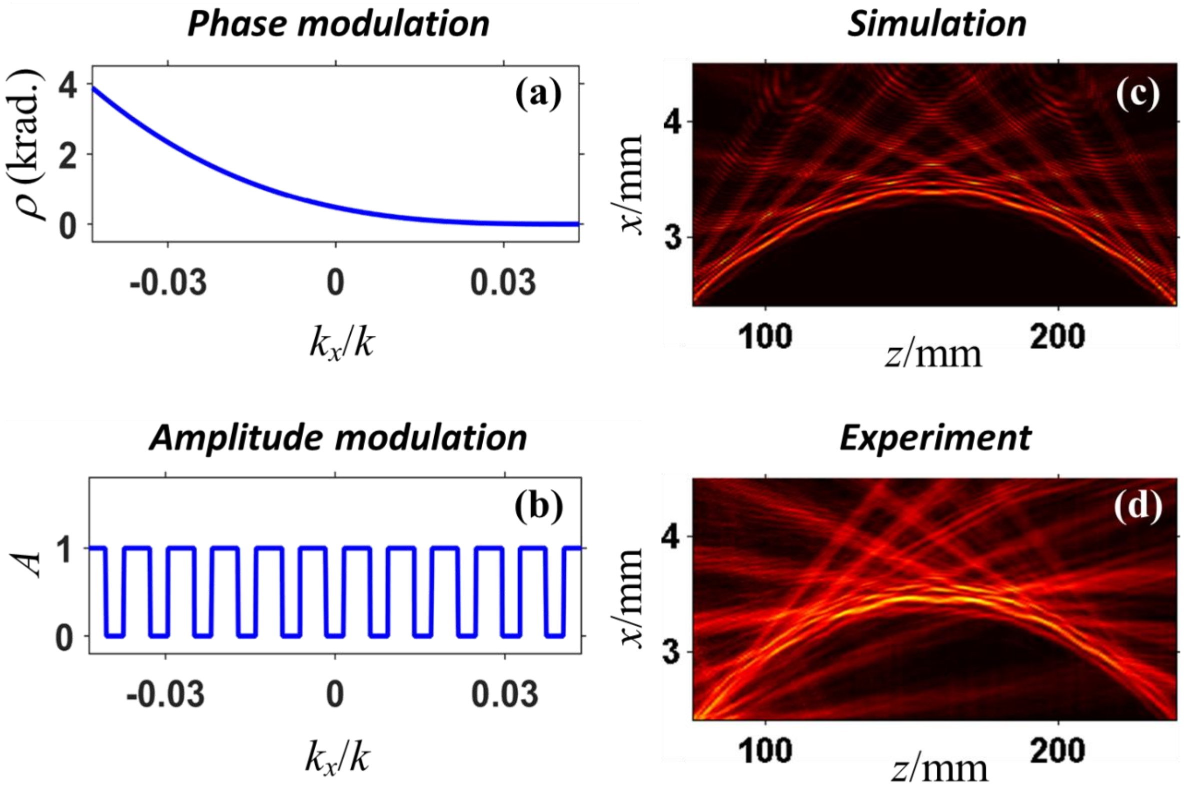

Figure 2.9: Periodic (or zigzag) self-accelerating beam along a parabolic trajectory, generated by modulating the beam spectral amplitude through an array of spectral "wells", and the spectral phase through a cubic distribution. Panels (a) and (b) show the applied spectral phase and amplitude modulation, respectively. (c) depicts the numerically-calculated intensity distribution and (d) the corresponding experimental observation of the beam profile.

2.5 Non-paraxial self-accelerating beams

Besides the paraxial approximation, the previous analysis is also applicable to the non-paraxial regime, i.e. for beams propagating along a large bending angle. In this case, 1D non-paraxial self-accelerating beams are described by the Helmholtz equation [1] as:

$$\frac{\partial \phi^2}{\partial z^2}+\frac{\partial \phi^2}{\partial x^2}+k^2\phi=0. \tag{2.12}$$

By neglecting the backward propagating component, the spectrum evolution of a beam takes the form:

$$\tilde{E}\left(k_x,z\right)=A\left(k_x\right)\exp\left(i\sqrt{k^2-{k_x}^2}z+i\rho\left(k_x\right)\right) \tag{2.13}$$

Although the calculation here exhibit a slightly higher complexity, due to the presence of a square root in Eq. (2.13), the beam trajectory is still predicable from a given phase modulation $\rho(k_x)$, even when propagating in the non-paraxial regime. In this case, the theoretical approach is similar to what has been done for Eq. (2.2) – i.e. only replacing in $\mu\left(k_x,z\right)$ the paraxial term $-{k_x}^2z/(2k)$ with the non-paraxial one $\sqrt{k^2-{k_x}^2}z$ - and for which such beams basically manifest the same behaviors as those seen under the paraxial approximation.

2.5.a Scalar non-paraxial self-accelerating beams

Let us start by the simple case of a non-paraxial accelerating beam generated though spectral phase modulation only (so that the spectral amplitude modulation $A(k_x)$ is assumed uniform). In this case, the spectrum evolution reduces to:

$$\tilde{E}\left(k_x,z\right)=\exp\left(i\sqrt{k^2-{k_x}^2}z+i\rho\left(k_x\right)\right). \tag{2.14}$$

By carrying out an analysis similar to the one for the paraxial regime, the spectral density singularity determining the beam caustic is expressed as:

$$\frac{\partial^2 \rho(k_x)}{\partial {k_x}^2} = \frac{k^2}{\left(k^2 - {k_x}^2\right)^{3/2}} z. \tag{2.15}$$

The spatial key frequency ($k_{sc}(z)$) is found by solving the Eq. (2.15), while the propagation trajectory is obtained by means of the following expression:

$$\frac{\partial x}{\partial z} = \frac{k_{xsc}(z)}{\sqrt{k^2 - k_{xsc}(z)^2}}. \tag{2.16}$$

To study the validity of our approach to the non-paraxial regime, we apply our analysis to predict the trajectory of two typical non-paraxial beams generated by the spectral modulations shown in Figs. 2.10(a, b).

The first case corresponds to a the circular self-accelerating beam [19-20] generated by a spectral inverse sinusoidal function $\rho(k_x) = rk\sin^{-1}(k_x/k)$ (with r = 40×10^{-6} – see dotted blue line in in Fig. 2.10(a)), while the other case corresponds to a cubic phase structure $\rho(k_x) = (5k_x/k)^3$ (solid blue line in in Fig. 2.10(a)). Applying our method, the spectrum-to-distance mapping can still predict the propagation of a Bessel-like (or circular) beam along a smooth circular trajectory $T_r(z) = -\sqrt{r^2/k^2 - z^2}$ [dashed white line in Fig. 2.10(c)], as attested by the propagation simulation shown in Fig. 2.10(c). In opposition to the work reported in [19], where the circular accelerating beam is generated by imposing both a spectral phase and an amplitude modulation, our method only relies on a spectral phase modulation, thus greatly simplifying the experimental synthesis of such non-paraxial beams.

In a second example, the cubic phase structure, associated to a non-diffractive Airy beam [11,13] in the paraxial approximation, leads to a beam localization with three main trajectories in the non-paraxial regime [see white dotted line in Fig. 2.10(d)]. Our predictions are once again in good agreement with the beam evolution computed numerically from Eq. (2.13) [see Fig. 2.10(d)]. Moreover, such a beam pattern explains why the multi-path Airy beam cannot propagate in the non-paraxial regime [20]. In contrast to the paraxial case where an Airy beam has a single trajectory, a non-paraxial Airy beam is associated with a multi-path localization composed of three main trajectories whose interference deforms the beam over a small scale [19-20,47], thus destroying the ideal parabolic propagation seen in the paraxial regime.

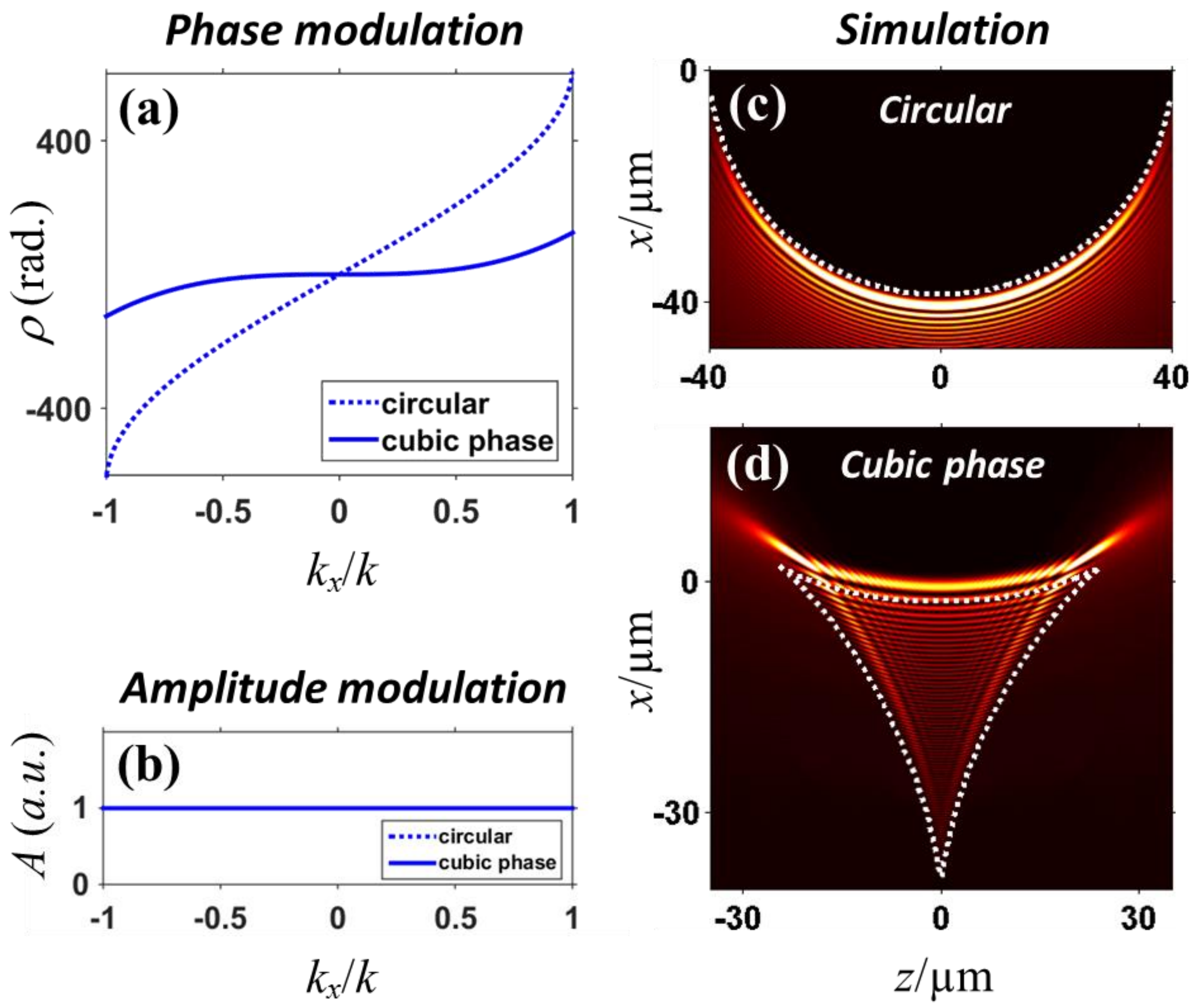

Figure 2.10: Trajectory prediction of self-accelerating beams under non-paraxial conditions. Panels (a) and (b) show the initial spectral phase and amplitude modulations, respectively. The dotted blue line in (a) refers to the inverse sinusoidal phase used to generate a circular (or Bessel-like) beam, while the solid blue lines in (a) correspond to the cubic phase used to realize a non-paraxial Airy beam. Note that both cases exhibit a constant (unitary) spectral amplitude modulation as illustrated in (b). The intensity distributions in (c) and (d) are the beam evolutions obtained numerically - based on the two corresponding cases of spectral modulations shown in (a). Dashed white lines in (c) and (d) correspond to the analytical beam trajectories predicted via the spectral-to-space mapping.

Furthermore, this example of spectral cubic phase clearly highlights that the phase modulations $\rho(k_x)$, whose second derivative $\rho''(k_x)$ is a monotonic function of the spatial frequency, do not generally lead to self-accelerating beams with a smooth single trajectory under non-paraxial conditions. An example of a multiple non-paraxial beam generated by a not monotonic $\rho''(k_x)$ is also shown in the section 2.5c. Herein, we investigate the particular case of a spectral sinusoidal phase to explain the vectorial nature of self-accelerating beams. As seen for their paraxial counterparts, even for multi-path non-paraxial beams, we found that different parts of the spectrum are responsible for different trajectories, and for each single trajectory the key frequency is a monotonic function of the propagation distance z [see Fig. 2.14(a)].

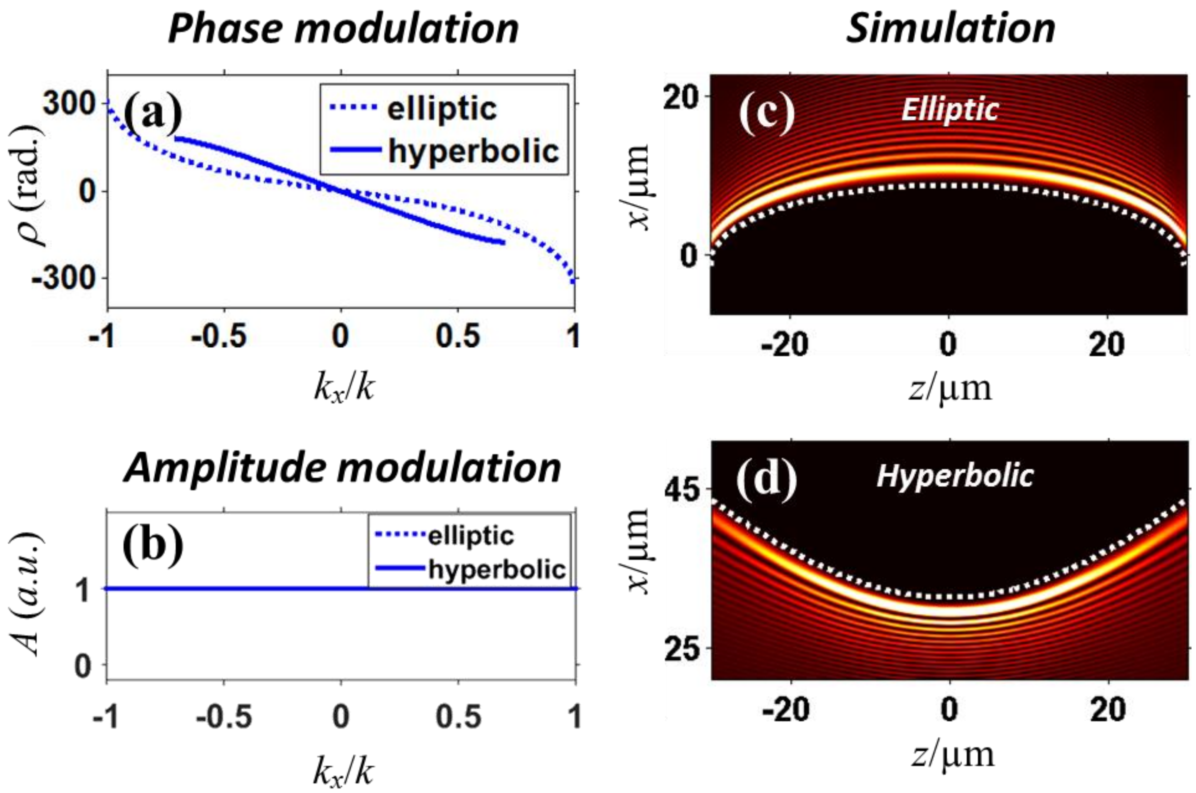
Phase modulation

Simulation

Amplitude modulation

Figure 2.11: Spectral phase design of self-accelerating beams in the non-paraxial regime. Spectral phase (a) and amplitude (b) distributions (estimated numerically to generate self-accelerating beams propagating along either a smooth elliptic (c) or a hyperbolic (d) trajectory. Dashed white lines in (c) and (d) are the desired beam trajectories used as "a priori" information to engineer the phase structure in (a) via the spectral-to-space mapping technique.

For the particular cases of non-paraxial accelerating beams discussed above, we have used the spectrum-to-distance mapping method to verify that the various beams generated from a known spectral phase modulation yielded to a beam path in agreement with analytical predictions of the trajectory. Now, we propose to use an inverse approach by selecting an arbitrary convex trajectory as an a priori information to retrieve the ideal spectral modulation to be applied on the initial beam. As a typical example, we apply our method to engineer the phase structure of an elliptical and a hyperbolic trajectory, respectively described by $T_r\left(z\right)=a\sqrt{b^2-z^2}/b$ and $T_r\left(z\right)=c\sqrt{d^2+z^2}/d$. Using the parameters b = 30 μm and $c = d$ = 30 μm, the phase shapes retrieved numerically are respectively plotted in Fig. 2.11(a). The most noticeable difference between the two retrieved phases in Fig. 2.11(a) is that, while all the spatial frequencies $\left(k_x \leq |k|\right)$ contributes to form an elliptical accelerating beam, only a certain range of frequencies $\left(k_x \leq k\left|c/\sqrt{c^2+d^2}\right|\right)$ is involved for the formation of the hyperbolic accelerating beam. To verify that the main humps of the beams propagate along the desired trajectories, numerical simulations of the beam propagation are performed based on imposing the estimated phases in the frequency domain. As shown in Figs. 2.11(c, d), the beam evolutions calculated through Eq. (2.13) show propagations in which their main hump follows the targeted convex trajectories. For the non-paraxial regime, the approach shown here provides an easier and more straightforward way of manipulating the trajectories of self-accelerating beams in comparison with alternative techniques reported in the literature [21,47] (e.g. where elliptical non-paraxial beams are found by solving the Helmholtz equation using complex angular Mathieu functions).

In this framework, it is worth mentioning that additional numerical studies highlight the fact that our method remains applicable when generate multiple self-accelerating beams along two or more different trajectories, as long as different spectral parts associated to different trajectories are non-overlapping.

2.5.b Non-paraxial periodic self-accelerating beams

In the non-paraxial regime, our previous analytical study is still applicable for generating non-paraxial periodic accelerating beams by modulating, at the same time, both amplitude and phase in the Fourier domain. In this case, the spectral evolution has the following form:

$$\tilde{E}\left(k_x, z\right) = A\left(k_x\right)\exp\left(i\sqrt{k^2 - {k_x}^2}\,z + i\rho\left(k_x\right)\right). \tag{2.17}$$

In Fig. 2.11(a), we show the retrieved spectral phase structures used to generate non-paraxial self-accelerating beams propagating along a circular, an elliptical and a parabolic trajectory, respectively described by $T_r\left(z\right) = \sqrt{r^2 / k^2 - z^2}$ (with $r = 40\times10^{-6}$), $T_r\left(z\right) = a\sqrt{b^2 - z^2} / b$ (with $a = 20\times10^{-6}$ and $b = 40\times10^{-6}$), and $T_r(z) = \sigma z^2$ (with $\sigma = 9.93\times10^{3}$). For the sake of clarity, we mention that at this stage no amplitude modulation has been considered.

In a second step, by imposing the amplitude modulations shown in Figs. 2.12(b1-d1), the intense main lobes of the circular, the elliptic and the parabolic self-accelerating beams undergo an oscillating (periodic) propagation while still maintaining their targeted curved trajectories [Figs. 2.12(b2-d2)].

Unlike the case of periodic self-accelerating beams propagating in the paraxial regime, both the depths and widths of the “spectral wells” composing the periodic spectral amplitude distributions in Fig. 2.12 are also modulated (i.e. a sinusoidal like modulation rather than a “creneau” shape in this case). Such a requirement is due to the larger curvature associated to non-paraxial beams when compared to paraxial ones. Indeed, as the beam curvature increases, the spectral well period has to be reduced adequately, in order to ensure a constructive interference and achieving a zigzag path.

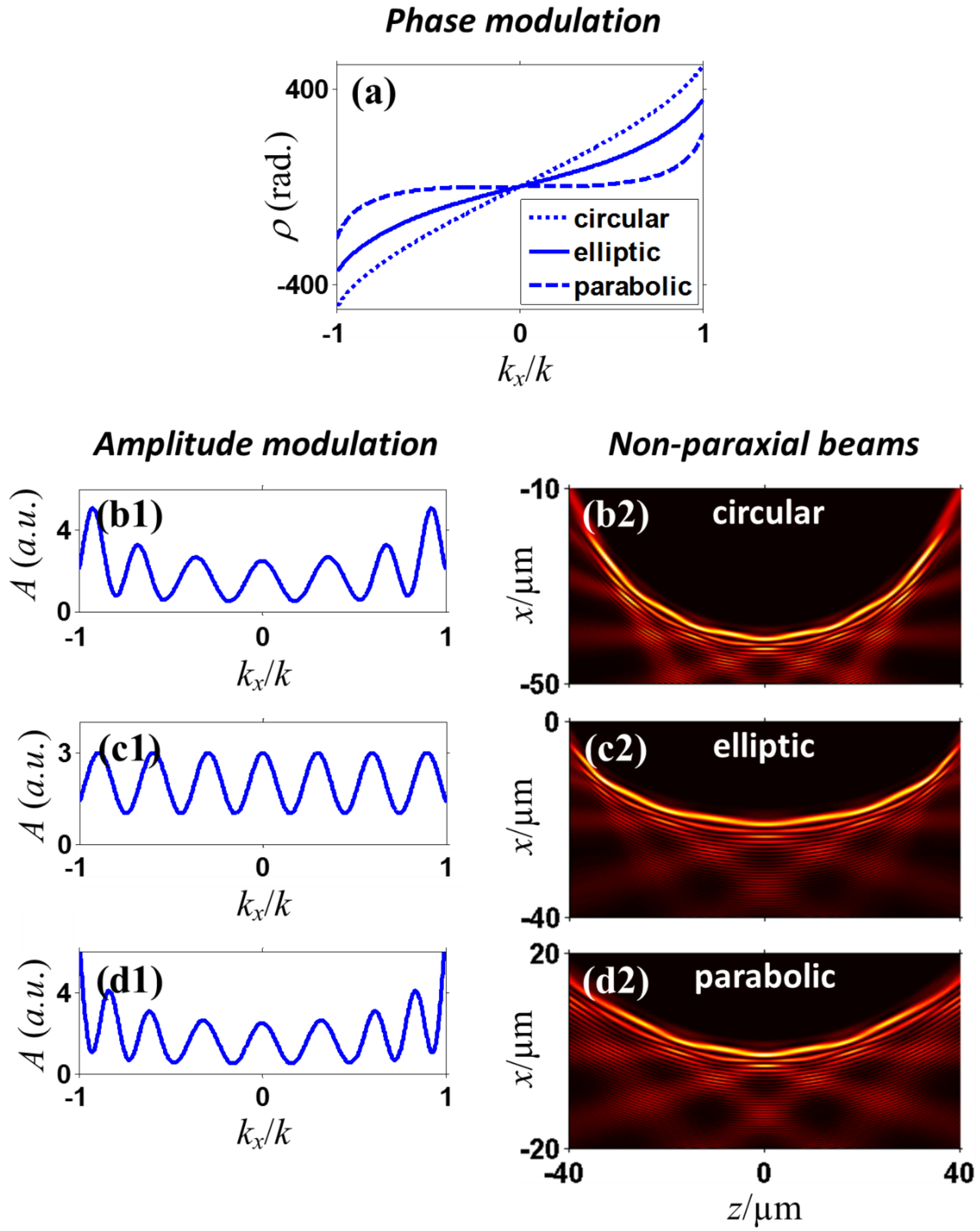

Figure 2.12: Non-paraxial periodic self-accelerating beams. (a) Estimated spectral phase and amplitude modulations (b1-d1) for generating periodic (or zigzag) beams along circular, elliptic and parabolic trajectories, respectively. The corresponding longitudinal intensity beam patterns estimated numerically are shown in (b2), (c2) and (d2).

2.5.c Vectorial non-paraxial self-accelerating beams

In the previous sections, we only discussed the case of scalar self-accelerating beams. According to the scheme in Fig. 2.1, those were generated by setting the polarization of the input light incident onto the SLM along an y'-axis (see also Fig. 2.13(a)). From a physical viewpoint, the phase front of the initial light beam is tilted due to the modulation mask and the cylindrical lens, regardless of the polarization of the electric field. Assuming that the phase modulation only changes along the x'-axis, such phase tilt does not alter the polarization direction for a y'-polarized electric field [Fig. 2.13(a)] [120]. However, by setting the initial beam polarization along the x'-axis, the change of polarization throughout propagation must be taken into consideration. Indeed, because of the above-mentioned rotation of the wave vector, the electric field vector acquires a component along the propagation direction z, as shown in Fig. 2.13(b).

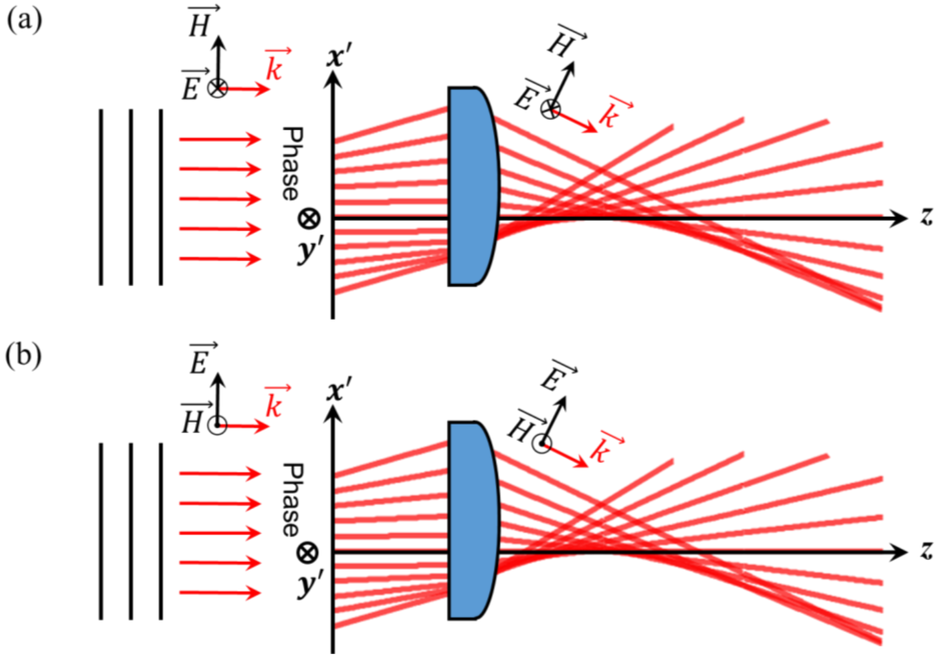

Figure 2.13: Schematic illustration highlighting the electric field polarization of the Fourier-generated self-accelerating beams obtained by input beams which were linearly-polarized along the (a) *y'*-axis and (b) *x'*-axis. In particular, the black arrows labeled with $\vec{E}$ and $\vec{H}$ indicate, respectively, the directions of the electric and magnetic fields. The red arrow labeled with $\vec{k}$ indicates the corresponding wave vectors.

We can account for the vectorial nature of polarization by means of the Jones matrix [56]. Therefore, the spectral evolution of the beam is separated into its *x*- and *z*- components, which thus read as:

$$\tilde{E}_x\left(k_x, z\right) = \frac{\sqrt{k^2 - k_x{}^2}}{k} \exp\left(ik_x x + i\sqrt{k^2 - k_x{}^2} z + i\rho\left(k_x\right)\right) \tag{2.18}$$

$$\tilde{E}_z\left(k_x, z\right) = \frac{k_x}{k} \exp\left(ik_x x + i\sqrt{k^2 - k_x{}^2} z + i\rho\left(k_x\right)\right) \tag{2.19}$$

In Eqs. (2.18) and (2.19), both the *x*- and *z*- components of the spectral evolution are featured by the same phase term as for non-paraxial beams, and an additional amplitude modulation term, showing an intrinsic complementarity between the two spectral components. Such complementarity is revealed by noting that the amplitude modulation associated to total spectral evolution $\tilde{E}\left(k_x, z\right) = \sqrt{\tilde{E}_x{}^2 + \tilde{E}_z{}^2} = \exp\left(ik_x x + i\sqrt{k^2 - k_x{}^2} z + i\rho\left(k_x\right)\right)$ is homogenous and unitary. For each spectral component, we can therefore use the previous analysis concerning non-paraxial accelerating beams.

Now, we apply now our approach to predict the beam path associated to specific example of vectorial accelerating beams. In particular, we specifically consider the vectorial beams generated by the sinusoidal phase $\rho\left(k_x\right) = 100\sin(2\pi k_x / k)$. Since the phase terms of the spectral evolutions in Eqs. (2.18) and (2.19) are the same, the key spatial frequencies estimated through Eq. (2.18) for both the two components are obviously identical. As illustrated in Fig. 2.14(a), the key frequency is a monotonic function in five different portions of the spectrum. Such spectral regions are highlighted by alternating solid and dotted lines in Fig. 2.1(a). As a consequence, the beam path predicted by our approach for either the two components results to be composed by five main trajectories [see white dotted line in Fig. 2.14(b)]. The analytical prediction is further confirmed by the calculated beam evolution obtained by numerically Fourier transforming Eqs. (2.18) and (2.19) as well as the total spectral evolution $\tilde{E}\left(k_x, z\right)$. As expected, the estimated trajectories have a good matching with the beam evolutions of the total intensity [Fig. 2.14(b)]. Nevertheless, the method can only partially predict the beam path for each component due to the influence of the inhomogeneous spectral amplitude.

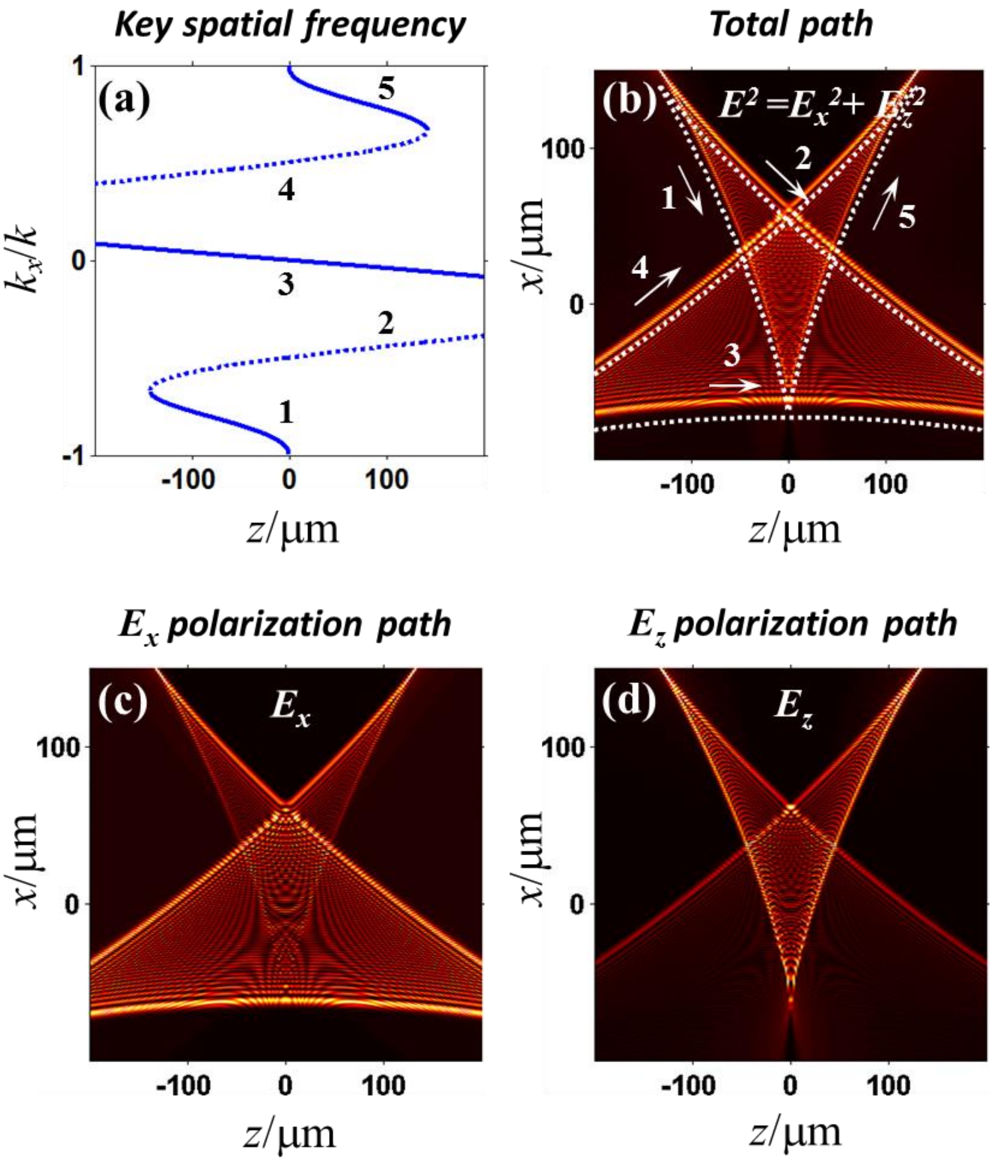

Figure 2.14: Beam evolution dynamics of a vectorial self-accelerating beam related to a sinusoidal phase under the non-paraxial condition. Panel (a) shows the calculated key spatial frequencies, (b) the total intensity pattern, (c) and (d) the intensity distributions for the (c) *x*- and (d) *z*-component. The numbers in (a) and (b) mark the correspondence between the beam trajectories and the related key spatial frequency segments. Note that the sum of intensity distributions in (c) and (d) provides the total intensity pattern in (b).

For the x-component field, the beam along trajectories 1 and 5 fades away as the amplitude approaches zero or $|k_x|$ approaches k [Fig. 2.14(c)]. Instead, for the z-component, the beam along trajectory 3 totally disappears since the spectral amplitude reaches zero around the corresponding key frequencies [Fig. 2.14(d)]. The intensity patterns of the two components are nevertheless complementary, and their sum hence follows the predicted trajectories.

From the results in Fig. 2.14, we can state that our approach is still applicable for vectorial self-accelerating beams, and the scheme shown here can be successfully applied to the analysis of non-paraxial three-dimensional (3D) cases whose polarization always needs to be accounted for.

2.6 Final remarks

In this chapter, we reported a method to generate and control single- or multi-path self-accelerating beams through Fourier-space phase engineering. In the spatial domain, the beam localization is related to the gradient of the spatial spectral phase. If a phase-only modulation is applied in the Fourier regime, we found that different parts of the spectrum are in charge of different parts of the beam trajectory. For each single trajectory, the key frequency monotonously varies along the propagation, being mapped to various main hump position of the beam. The properties of the self-accelerating beams, such as self-bending and self-healing, are well explained with a deeper understanding in term of frequency correspondence. Via our method, the beam trajectories under the paraxial approximation can be predicted from a known spectral phase, while the phase to be used for a given (single or multiple) beam trajectory can be retrieved analytically.

We also studied the dynamics of self-accelerating beams generated by the combined effect of a spectral phase and an amplitude modulation. In particular, we extended the spectrum-to-distance mapping method to the case of an amplitude modulation superimposed to a phase structure in the Fourier regime. While small amplitude modulations only slightly affect the trajectory generated by a suitable spectral phase modulation [123], large amplitude modulations, such as a Heaviside-shape amplitude distribution, greatly modify the beam path, adding to the global convex path some portions where the propagation trajectory is both linear and tangent to the overall convex path. A “spectral well” amplitude structure yields to the generation of a convex trajectory including a “V”-shaped path structure, which can be further exploited as an elementary cell for constructing periodic self-accelerating beams. In both the paraxial and non-paraxial regime, periodic or zigzag beam paths are readily generated by employing an array of spectral wells. In contrast with the works reported by other groups (for which periodic self-accelerating beams have been observed in the non-paraxial regime by applying both spectral amplitude and phase modulations) [43-44], our scheme also offers a detailed explanation about the formation of periodic paths via a spectrum-to-distance mapping.

In the non-paraxial regime, our approach can also be extended to generate any large-angle (smooth or periodic) convex self-accelerating beam or employed to predict their paths from a known modulation. In addition, we have shown that a non-paraxial Airy beam is a multi-path beam composed by three main trajectories, thus providing a physical explanation on the underlying reasons for which the parabolic propagation of an Airy beam breaks under non-paraxial condition. Moreover, our method is readily applicable to the case of vectorial self-accelerating beams.

There are several promising directions for future investigations, such as developing beam localizations for incoherent light [124], manipulating spatio-temporal self-accelerating beams [37-38], extending our scheme to the nonlinear regime [33,80], and so on. On a broader note, it is worth mentioning that any progress made in optics can be beneficial and give insights for the study and exploitation of any other self-accelerating ondulatory phenomenon found in nature.

Chapter 3

Energy confinement enhancement of self-accelerating wavepackets

In this chapter, we introduce a practical method to increase the energy confinement of self-accelerating wave packets. Our approach is based on a generalization of the concept of the spatial spectral phase gradient to the (2+1) and (3+1)D regimes. We show that the trajectories of these self-accelerating wave packets can be determined by a spectrum-to-distance mapping, and the frequencies associated to such wave packets' main lobes are limited to a certain range of the Fourier spectra. In particular, we demonstrate that an appropriate shaping of the Fourier spectra that does not affect the main lobes evolution, leading instead to a dramatic enhancement of their peak intensity, as well as a significant decrease of their spatial or spatio-temporal footprint. Remarkably, such self-accelerating beams retain both the expected acceleration profiles and intrinsic self-healing properties.

3.1 Introduction

In most of the applications reported in literature using either (2+1) or (3+1)D self-accelerating wave packets, the patterns associated with these wave packets occupies a large area filled by several sub-lobes [37-40,102,104,125-126]. In most of them, the energy contained in their long tails could be considered wasted, or even undesirable, because of their minor interest in comparison with the higher intensity portion of the main lobes. In this framework, some works have been focusing on ways to obtain accelerating beams with a reduced sub-lobes expansion by directly solving the related wave functions. Nevertheless, these studies have actually been restricted to only a few special trajectories in both the paraxial and non-paraxial regime [45-47,127]. Particularly in the context of arbitrary trajectories, the issue of optimal energy confinement has not been directly addressed. Although not unexpected, the peak intensity enhancements of these confined accelerating beams have not been quantitatively evaluated so far. In this chapter, we will show that an appropriate shaping of the initial spectra is able to increase the energy confinement of both (2+1) and (3+1)D self-accelerating wave packets. Furthermore, the concept of spatial spectral phase gradient is generalized to both the (2+1) and (3+1)D regimes, thus showing that even in these scenarios the accelerating trajectory can be determinate by a spectrum-to-distance mapping where the various frequencies in the spectrum are mapped to different propagation distances. As seen for 1D self-accelerating beams, the trajectory of such wave packets can be predicted from the knowledge of an applied phase modulation. Conversely, we note that the phase structure imprinted in the Fourier regime to obtain any desired convex propagation can be engineered by using this mapping. Interestingly, we will also illustrate that only some frequencies in the Fourier regime are responsible for the evolution of the wave packet main lobe over the entire range of propagation distances. Motivated by this consideration, we introduce a method for improving the optical bullet energy confinement by transferring the energy from the spectral region associated to the sub-lobes to its main lobe. The first part of this chapter will focus on self-accelerating beams in the (2+1)D regime. We will show, both theoretically and experimentally, that by appropriately shaping the spatial spectra, we are capable of generating optimized versions of 2D accelerating beams. The optimized beams exhibit more compact transversal patterns as well as enhanced peak intensities without significantly degrading either the propagation characteristics or the intrinsic properties of their unshaped counterparts. In the second part of this chapter, our spectral shaping method will be extended to the (3+1)D regime. In particular, we report a numerical investigation aimed at optimizing the energy efficiency of an Airy^3 bullet propagating under anomalous dispersion condition. The approach is based on an appropriate compression of the initial Gaussian spatio-temporal spectrum leading to the generation of a “short-tail” version of the Airy^3 bullet, which exhibits a significant enhancement of the bullet peak power as well as the overall energy confinement. Similar to the (2+1)D case, we also illustrate that the newly-optimized Airy^3 bullet is not subject to significant degradations of the Airy^3 bullet characteristics, such as parabolic trajectory and self-healing.

3.2 Two-dimensional spatial phase gradient

Let us consider a two-dimensional (2D) optical beam propagating in free-space along the *z*-axis, and linearly polarized along the *x*-axis. In this case, the 2D optical beam is experiencing diffraction in the transversal plane (*x*,*y*). Under this condition, the propagation dynamics of a linearly-polarized electromagnetic wave $\mathbf{E}(\vec{r},t)=E_x(\vec{r},t)\boldsymbol{x}$ can be described by the scalar wave equation [2]:

$$\nabla^2 E_x - \frac{1}{c^2}\frac{\partial^2 E_x}{\partial t^2} = 0. \tag{3.1}$$

In the Eq. (3.1), ∇^2 is the Laplacian operator, $E_x(\vec{r},t)$ the *x*-component of the electric field, *t* is the time coordinate, and $\vec{r}=(x,y,z)$ is the spatial vector. Solutions to Eq. (3.1) can be found by defining $E_x(\vec{r},t)$ as:

$$E_x(\vec{r},t) = E(\vec{r})e^{i(kz-\omega_0 t)}, \tag{3.2}$$

where $E(\vec{r})$ and $k=\omega_0/c$ refer to the complex envelope and the vacuum wavenumber, respectively, while ω_0 is the angular frequency and *c* the light velocity. By substituting the latter expression into Eq. (3.1), the complex envelope $E(\vec{r})$ of the *x*-component of the electric field obeys to the Helmholtz equation, explicitly expressed as:

$$2ik\frac{\partial E}{\partial z} + \frac{\partial^2 E}{\partial z^2} + \nabla_\perp{}^2 E = 0. \tag{3.3}$$

Under the paraxial condition, the approximation $|\partial^2 E/\partial z^2| << 2k|\partial E/\partial z|$ is valid, hence propagation dynamics can be described by the 2D paraxial wave equation of diffraction so that:

$$i\frac{\partial E}{\partial z} + \frac{1}{2k}\nabla_\perp{}^2 E = 0, \tag{3.4}$$

where $\nabla_\perp{}^2 = \left(\frac{\partial^2}{\partial x^2}, \frac{\partial^2}{\partial y^2}\right)$. Solutions of Eq. (3.4) can be found in the Fourier domain as:

$$E(x,y,z)=\frac{1}{4\pi^2}\int_{-\infty}^{+\infty}\int_{-\infty}^{+\infty}\tilde{E}(k_x,k_y 0)e^{-\frac{i}{2k}\left(k_x{}^2+k_y{}^2\right)z}e^{ik_xx+ik_yy}dk_xdk_y, \tag{3.5}$$

where $\tilde{E}(k_x,k_y 0)=\int_{-\infty}^{+\infty}\int_{-\infty}^{+\infty}E(x,y,0)e^{-ik_xx-ik_yy}dxdy,$ is the Fourier transform of the input beam, while k_x, and k_y are the corresponding spatial angular frequencies.

3.2.a Theory of (2+1)D spectrum-to-space mapping

As input condition, we consider a phase-modulated Gaussian spectral profile. Such input spectrum can be obtained by applying an arbitrary transverse (spectral) phase modulation $\rho(k_x,k_y)$ to an incident Gaussian beam at the Fourier plane of a spherical lens. Using such a modulation, the input spectrum can be expressed as:

$$\tilde{E}(k_x,k_y,0)=\exp\left[-(\alpha k_x{}^2+\alpha k_y{}^2)\right]\exp\left[i\rho(k_x,k_y)\right], \tag{3.6}$$

where α is related to the beam waist of the input Gaussian beam. If we insert Eq. (3.6) into Eq. (3.5), the Fourier spectrum is:

$$\tilde{E}(k_x,k_y,z)=\exp\left[-(\alpha k_x{}^2+\alpha k_y{}^2)\right]\exp\left[i\mu(k_x,k_y,z)\right], \tag{3.7}$$

where $\mu(k_x,k_y,z)=-(k_x{}^2+k_y{}^2)\ \dfrac{z}{2k}+\rho(k_x,k_y)$ is the spectral phase. Similar to the approach undertaken in Chapter 2 for 1D self-accelerating beams, the concept of spatial spectral phase gradient can also be extended to self-accelerating beams in the 2D regime. In this case, the transverse positions x and y are related to the gradient of $\mu(k_x,k_y,z)$ by means of the expressions:

$$x=-\frac{\partial\mu(k_x,k_y,z)}{\partial k_x};\ \ y=-\frac{\partial\mu(k_x,k_y,z)}{\partial k_y}. \tag{3.8}$$

The spectral density $D(k_x,k_y,z)=\left|\mu''(k_x,k_y,z)\right|^{-1}$ within the infinitesimal area $dA = dxdy$ is calculated from the inverse determinant of the Hessian matrix $H(\mu)$ [128]. At each propagation distance z, $D(k_x, k_y,z)$ is singular when the determinant of the Hessian matrix $H(\mu)$ is zero, so that the following condition is satisfied:

$$\left(\frac{z}{k}-\frac{\partial^2\rho\left(k_x,k_y,z\right)}{\partial {k_x}^2}\right)\left(\frac{z}{k}-\frac{\partial^2\rho\left(k_x,k_y,z\right)}{\partial {k_y}^2}\right)-\frac{\partial^2\rho\left(k_x,k_y,z\right)}{\partial k_x\partial k_y}\frac{\partial^2\rho\left(k_x,k_y,z\right)}{\partial k_y\partial k_x}=0\ . \quad (3.9)$$

The complex form of Eq. (3.9) can be greatly simplified by assuming the imposed transverse phase modulation to be a separable function, i.e., $\rho(k_x,k_y)\ =\rho_x(k_x)+\rho_y(k_y)$. By inserting the latter expression into Eq. (3.9), it reduces to:

$$\left(\frac{\partial^2\rho}{\partial {k_x}^2},\ \frac{\partial^2\rho}{\partial {k_y}^2}\right)=\left(\frac{z}{k},\ \frac{z}{k}\right). \quad (3.10)$$

Akin to 1D self-accelerating beams, Eq. (3.10) links spatial frequencies to propagation distances z. Starting from the spectral phase structure $\rho(k_x,k_y)$, the key spatial frequencies (indicated as $k_{xc}(z)$ and $k_{yc}(z)$) can be estimated by Eq. (3.10), thus offering the possibility of building a mapping between distance and spatial frequency. Once $k_{xc}(z)$ and $k_{yc}(z)$ are estimated, the beam trajectory can be therefore predicted as a parametric representation of the propagation distance z using the following expression:

$$\left(\frac{\partial x}{\partial z},\ \frac{\partial y}{\partial z}\right)=\left(\frac{k_{xc}(z)}{k},\ \frac{k_{yc}(z)}{k}\right), \quad (3.11)$$

Alternatively, the spectrum-to-distance mapping also allows us to engineer any desired convex beam trajectory. The required convex paths are engineered by firstly retrieving the key spatial frequencies from the Eq. (3.11), and then finding the initial spectral phase mask structures to be implemented from Eq. (3.10).

3.2.b 2D self-accelerating beams via spectrum-to-space mapping

In this section, the validity of the previous analytical method is confirmed by applying the theory to two typical classes of 2D self-accelerating beams. In particular, we consider curved beams that are characterized by the following convex paths: nth-order polynomial and an exponential trajectory. In contrast with Chapter 2, for which the beam trajectories of 1D self-accelerating beams and associated key spatial frequencies were found from the initial spectral phase structures, we here use the spectrum-to-space mapping to engineer the initial spectral phase profiles retrieved from the desired beam paths. The phase distributions are designed by choosing the same acceleration profiles along the *x* and *y* directions in order to obtain beam paths with accelerating trajectories localized exclusively on a single plane. Such a plane orthogonally intersects the $(x-y)$ plane along the 45° radial direction, so that the projections of the beam trajectories lie on the 45° diagonal line only. Likewise, the related key spatial frequencies are projected on the 45° diagonal line of the $(k_x - k_y)$ plane. In this way, we can study the beam propagation characteristics by solely analyzing the evolution along this 45° line. When the accelerations along the *x* and *y* directions are different, the beam trajectory is localized in the 3D space (and not only on one plane), making the description of the beam dynamics more complex, thus requiring further analytic considerations. Since the beam acceleration along the *x* and *y* directions are chosen to be the same, for convenience we define the radial position of the main hump as $s=\sqrt{x^2+y^2}$ in the real space and $k_s=\sqrt{k_x{}^2+k_y{}^2}$ in the spectral domain. First, we analyze an nth-order polynomial trajectory given as: $(x,y,z)=(bz^n,bz^n,z)$. The beam path is expressed as a parametric representation of the propagation distances *z*, with *b* indicating a scaling factor. Substituting this expression into Eq. (3.11), the key spatial frequencies are $(k_{xc}(z),k_{yc}(z))$ = $(nbkz^{n-1},nbkz^{n-1})$ being therefore a monotonic function of the propagation distance *z*. The spectral phase modulation is estimated by inverting these key spatial frequencies in order to express the propagation distance *z* as function of k_{xc} and k_{yc}, i.e. $(z(k_{xc}), z(k_{yc}))$, and then inserted into Eq. (3.10).

If *n* is even, the spectral phase mask from Eq. (3.10) has the following form:

$$\rho\left(k_x,k_y\right)=\frac{\left(n-1\right)^2}{n\left(2n-1\right)}\left(\frac{1}{nb}\right)^{\frac{1}{n-1}}\left(\frac{1}{k}\right)^{\frac{n}{n-1}}\left[\left(k_x\right)^{\frac{2n-1}{n-1}}+\left(k_y\right)^{\frac{2n-1}{n-1}}\right]. \tag{3.12}$$

Conversely, if *n* is odd, the phase profile reads as:

$$\rho\left(k_x \geq 0, k_y \geq 0\right) = \begin{cases} \dfrac{(n-1)^2}{n(2n-1)}\left(\dfrac{1}{nb}\right)^{\frac{1}{n-1}}\left(\dfrac{1}{k}\right)^{\frac{n}{n-1}}\left[\left(k_x\right)^{\frac{2n-1}{n-1}} + \left(k_y\right)^{\frac{2n-1}{n-1}}\right] & z \geq 0 \\ -\dfrac{(n-1)^2}{n(2n-1)}\left(\dfrac{1}{nb}\right)^{\frac{1}{n-1}}\left(\dfrac{1}{k}\right)^{\frac{n}{n-1}}\left[\left(k_x\right)^{\frac{2n-1}{n-1}} + \left(k_x\right)^{\frac{2n-1}{n-1}}\right] & z \leq 0 \end{cases} . \tag{3.13}$$

Whenever *n* is even, all spatial frequencies contribute to form the polynomial accelerating beam [see Eq. (3.12)], and, therefore, different distances *z* are mapped to different key spatial frequencies. On the contrary, when *n* is odd, only the non-negative spatial frequencies play a role in forming the polynomial accelerating beam [see Eq. (3.13)]. This means that only the non-negative spatial key frequencies are linked to different propagation distances *z*. In particular, each positive key spatial frequency is related to two values of *z*, corresponding to either forward ($z \geq 0$) or backward ($z \leq 0$) propagations, for which the spectrum-to-space mapping is respectively valid. Both estimated spectral phases have the same profiles, with the exception of an opposite (negative) sign when negative propagation distances are considered.

In a second case, we focus on a general class of 2D exponential self-accelerating beams. Here, the convex trajectory is described as: $(x, y, z) = (F(e^{bz}-1), F(e^{bz}-1), z),$ where *b* and *F* are arbitrary distance and amplitude scaling factors, respectively. Substituting this expression in Eq. (3.11), the corresponding monotonic key spatial frequencies are: $(k_{xsc}(z), k_{ysc}(z)) = (Fbke^{bz}, Fbke^{bz}).$ The phase mask structure retrieved from Eq. (3.10) is therefore:

$$\rho\left(k_x > 0, k_y > 0\right) = \frac{k_x^{\ 2}}{2bk}\left[\ln\left(\frac{k_x}{Fbk}\right) - \frac{3}{2}\right] + \frac{k_y^{\ 2}}{2bk}\left[\ln\left(\frac{k_y}{Fbk}\right) - \frac{3}{2}\right] + F\left(k_x + k_y\right). \tag{3.14}$$

Eq. (3.14) shows that only the positive spatial frequencies contribute to form an exponential accelerating beam, being those mapped into different propagation distances *z*.

3.2.c Numerical results

In what follows, we perform numerical simulations in order to analyze in more details three specific cases of the above described convex trajectories: for instance, a parabolic, a cubic polynomial and an exponential trajectory. The trajectory parameters F and b are chosen to obtain beam trajectories that can be represented on the same scale (i.e. with qualitatively similar dimensions). The characteristics and parameters of these beams (calculated numerically) are presented in Tab. 1.

Type of trajectory	**Trajectory** $(x, y, z) = f(z)$	**Key Spatial Frequency** $(k_{xc} = k_{yc})$
Parabolic	$0.1\,z^2, 0.1\,z^2, z$	$0.2\,kz$
Cubic polynomial	$1.13\,z^3, 1.13\,z^3, z$	$3.39\,kz^2$
Exponential	$4.10^{-4}\,(e^{20z}-1), 4.10^{-4}\,(e^{20z}-1), z$	$8.10^{-3}\,ke^{20z}$

Table 3.1: 2D self-accelerating beams under study and corresponding parameters.

In Fig. 3.1(a), we show the phase structure used for generating a 2D self-accelerating beam with the parabolic trajectory presented in Tab 1. Such phase mask, designed from the Eq. (3.12) using the parameters $n = 2$ and $b = 0.1$, exhibits the typical cubic profile associated to the well-known 2D Airy beam. By imposing this phase modulation in the Fourier domain, we can numerically simulate the evolution of the beam using Eq. (3.5). As an illustrative example, we show in Fig 3.1(b) the corresponding beam intensity pattern at $z = 8.1$cm. As expected, the intensity distribution is a 2D Airy beam showing an intense main lobe and two long tails of sub-lobes (along the x and y directions). The 2D Airy beam moves along the radial direction s in the $(x-y)$ transverse plane [see dashed line in Fig. 3.1(b)], while in the $(s-z)$ longitudinal plane, the main lobe of the beam follows the desired parabolic trajectory shown in Fig. 3.1(c).

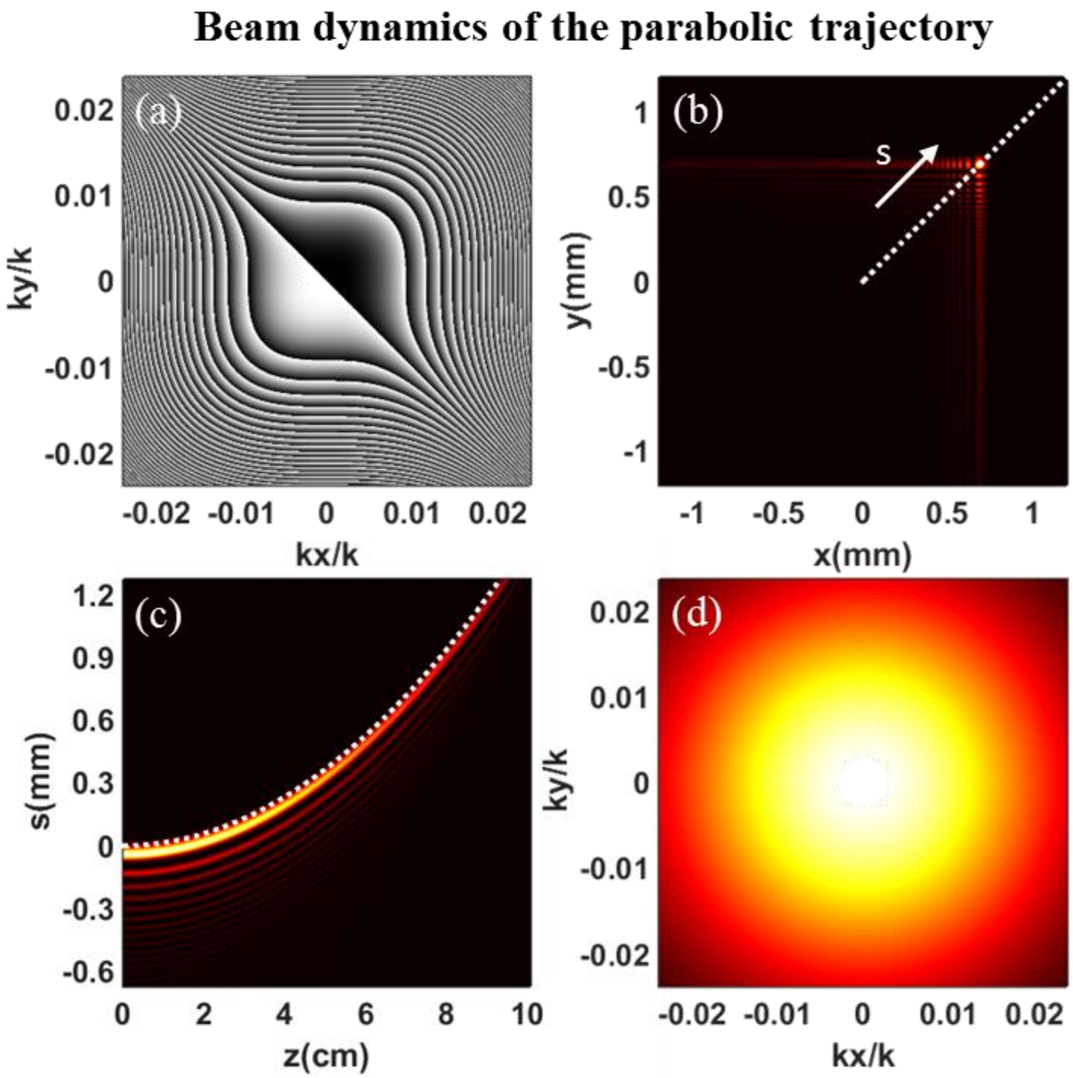

Figure 3.1: Beam features of a 2D self-accelerating beam propagating along a parabolic trajectory (Airy beam) using a circular Gaussian beam. (a) Wrapped cubic phase mask designed for the parabolic trajectory whose parameters are given in Tab 1. (b) Intensity pattern of the Airy beam at z = 8.1cm. (c) Longitudinal intensity pattern along the radial direction s as a function of the distance z. (d) Spatial spectrum corresponding to the beam pattern in (b). Dotted white lines in (b) and (c) mark the corresponding parabolic trajectory predicted analytically.

Now, if we look at the Fourier domain, the beam spectrum has a Gaussian profile [Fig. 3.1(d)]. In our numerical investigations, we also observed that such a spectral profile does not change along the propagation distance *z*. Nevertheless, if we filter out the sub-lobes from the

2D Airy beam, (as shown in the inset in Fig. 3.2(a) for the Airy beam at z = 8.1cm), the spatial frequencies associated with the residual main lobe are located in a spot of drastically reduced size [Fig. 3.2(a)]. During propagation, such spectral spot shifts along the radial direction k_s on the $\left(k_x - k_y\right)$ plane, as illustrated in Fig. 3.2(b), while its longitudinal evolution follows the linear key frequency predicted by the mapping [see Fig. 3.2(c)]. As result, we found that the entire spectrum associated with the main lobe remains confined only into a spectral stripe delimited by the white lines shown in Fig. 3.2(b-c). This feature also illustrates that the spectral content located outside this stripe is actually associated with the wide sub-lobes of the Airy beam.

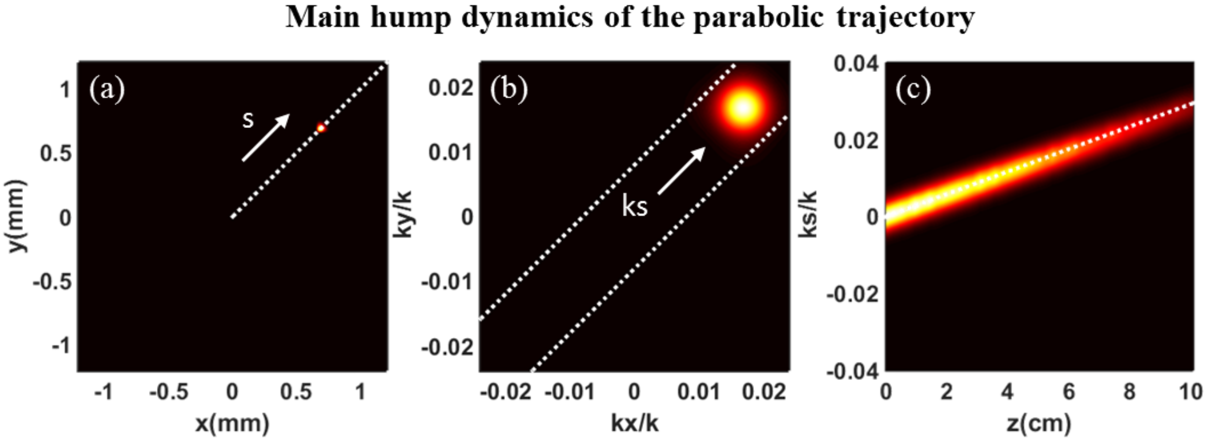

Figure 3.2: Main hump characteristics of the 2D self-accelerating beam shown in Fig. 3.1. (a) Intensity pattern corresponding to the main lobe of the Airy beam in Fig. 3.1(b), obtained by filtering out its sub-lobes. (b) Spatial spectrum associated to the main lobe in (a). (c) Longitudinal evolution of the main lobe spectrum along the radial direction k_s as a function of the propagation distance z. The dotted white line in (b) delimits the spectral area of the main lobe spectrum for all propagation distances z, while the white line in (c) marks the key spatial frequency obtained from theory.

Similarly to the above presented parabolic case, we also engineered the spectral phases for the two other convex paths presented in Tab. 1. For the cubic polynomial trajectory, the appropriated phase structure was estimated from Eq. (3.13) assuming positive distances $z \geq 0$ and n = 3 [Fig. 3.3(a)], whereas, for the exponential trajectory, the spectral modulation was retrieved from Eq. (3.14) [Fig. 3.4(a)]. In contrast with the Airy beam case, only positive spatial frequencies are involved in forming such 2D self-accelerating beams.

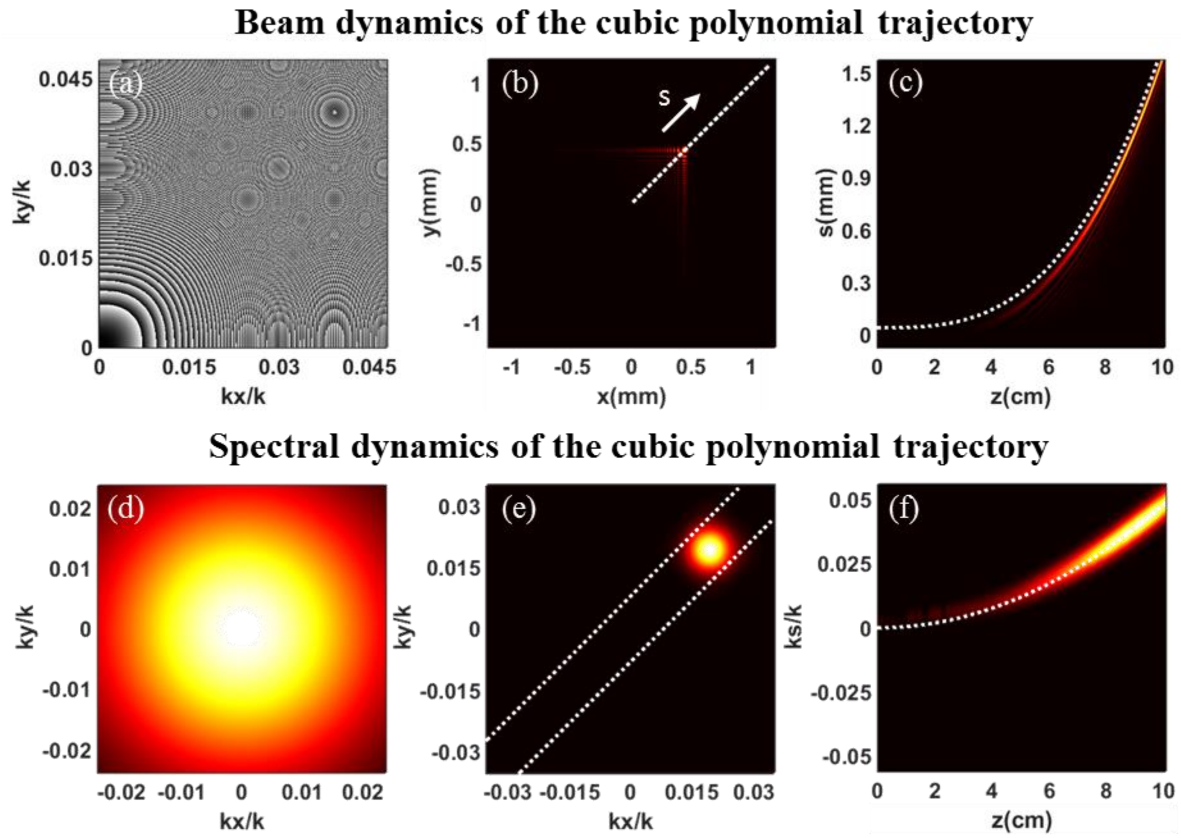

Figure 3.3: Beam and spectral characteristics of a 2D self-accelerating beam propagating along a cubic polynomial trajectory using a circular Gaussian beam. (a) Wrapped cubic phase mask designed for the cubic polynomial trajectory whose parameters are given in Tab 1. (b) Intensity distribution at *z* = 7.4 cm. (c) Longitudinal intensity pattern along the radial direction s as a function of the distance *z*. (d) Spatial spectrum corresponding to the beam pattern in (b). (e) Spatial spectrum associated to the main lobe in (b) when the sub-lobes are filtered out. (f) Longitudinal evolution of the main lobe spectrum along the radial direction k_s as a function of the propagation distance *z*. Dotted white lines in (b) and (c) mark the corresponding cubic polynomial trajectory predicted analytically. In particular, the trajectory in (c) is intentionally shifted upwards for a better illustration. The dotted white lines in (e) delimit the spectral area of the main lobe spectrum for all propagation distances *z*, while the white line in (f) marks the key spatial frequency obtained from theory.

In Figs. 3.3(b) and 3.4(b) we show the intensity patterns at two selected distances, z = 7.4 and 2.8cm respectively. Those were obtained by numerically simulating the beam evolutions after applying the estimated phase modulations in the Fourier domain. For both these intensity distributions, 2D Airy-like profiles are observed, both moving along the radial direction s in the (x-y) plane during propagation [see Figs. 3.3(b) and 3.4(b)]. The corresponding longitudinal evolutions of the beams are presented in Figs. 3.3(c) and 3.4(c), clearly showing that the main lobes accelerate along different propagation trajectories, being both in excellent agreement with theoretical predictions. With respect to the Airy beam, the most distinctive feature is that the peak intensities appear far away from the onset distance z = 0. Furthermore, while the exponential beam follows the analytical prediction even for small propagation distances close to z = 0, the theory fails to properly describe the cubic polynomial beam in such a range.

In the Fourier domain, the spectra of the two input beams have the same Gaussian shape as in Fig. 3.1(d). As for the Airy beam case, we also checked numerically that these other two spectral profiles remain invariants throughout propagation [Figs. 3.3(d) and 3.4(d)]. Nevertheless, the spectra associated with the main lobes also take the form of two small-sized spots [Figs. 3.3(e) and 3.4(e)]. During propagation, the spectral spots tend to move along the k_s direction in the $\left(k_x - k_y\right)$ plane [Figs. 3.3(e) and 3.4(e)]. Similar to the 2D Airy beam, the main lobes spectra are confined within a stripe on the spatial frequency plane [Figs. 3.3(e) and 3.4(e)] but evolve, in the longitudinal plane, along different key spatial frequencies - in agreement with their respective analytical predictions [Figs. 3.3(f) and 3.4(f)]. In particular, the main lobe spectrum of the cubic polynomial beam follows a parabolic key spatial frequency [Fig. 3.3(f)], while the one associated to the exponential beam evolves as an exponential key spatial frequency during propagation [Fig. 3.4(f)]. It is worth noting that the numerical simulation in Fig. 3.3(f) shows that the main lobe spectrum tends to slightly deviate from the key spatial frequency prediction (dotted white line) near z = 0, i.e. where the slope of the cubic polynomial trajectory is very small or null. This discrepancy indicates that the validity of our analytical method is limited when describing the evolution of the cubic polynomial beam in this region. Although not explicitly shown here, we have found through additional numerical investigations that a similar limitation is also observed for other convex beams, and was attributed to the vanishing value of the slope of the trajectory under investigation.

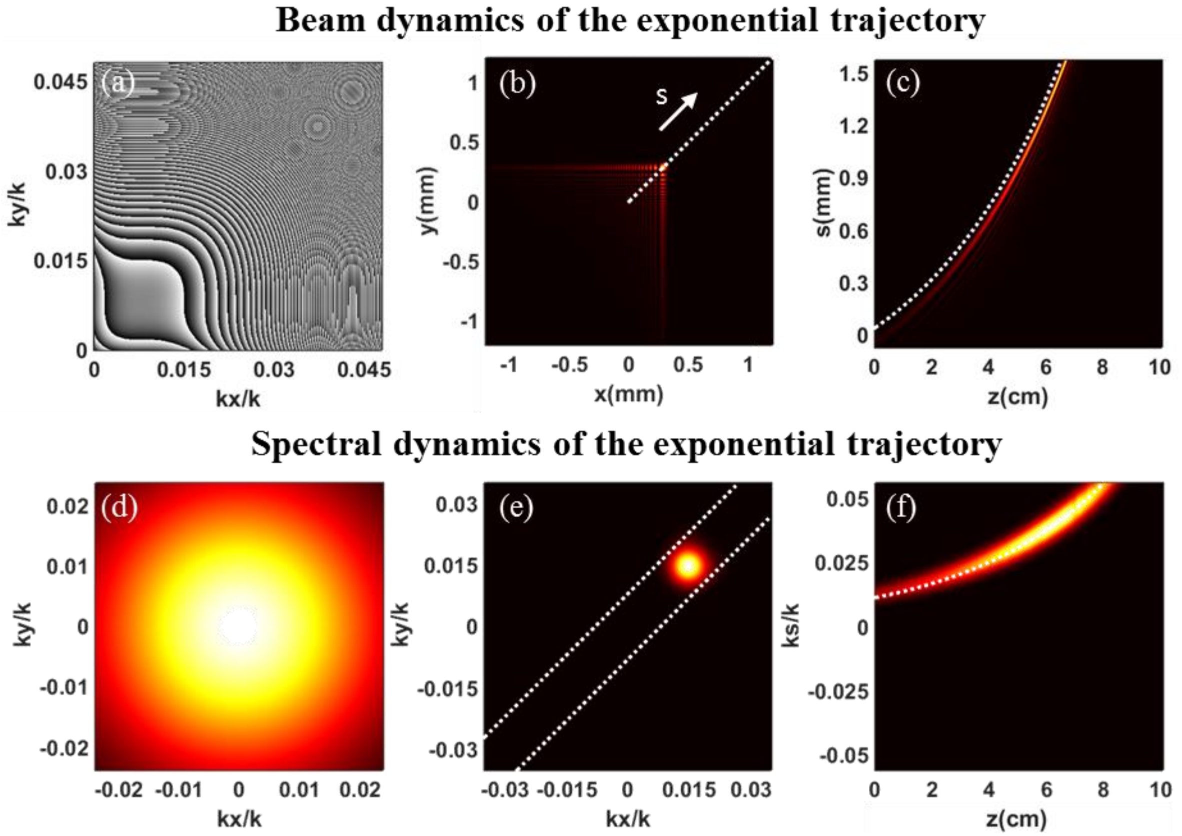

Figure 3.4: Beam and spectral characteristics of a 2D self-accelerating beam propagating along an exponential trajectory using a circular Gaussian beam. (a) Wrapped cubic phase mask designed for the exponential trajectory whose parameters are given in the Tab 1. (b) Intensity distribution at z = 28 cm. (c) Longitudinal intensity pattern along the radial direction s as a function of the distance z. (d) Spatial spectrum corresponding to the beam pattern in (b). (e) Spatial spectrum associated to the main lobe in (b) when the sub-lobes are filtered out. (f) Longitudinal evolution of the main lobe spectrum along the radial direction k_s as a function of the propagation distance z. Dotted white lines in (b) and (c) mark the corresponding exponential trajectory predicted analytically. In particular, the trajectory in (c) is intentionally shifted upwards for a better illustration. The dotted white lines in (e) delimit the spectral area of the main lobe spectrum for all propagation distances z, while the white line in (f) marks the key spatial frequency obtained from theory.

3.2.d Experimental results

Besides the theoretical and the numerical study, we also performed experimental measurements to confirm our predictions using a setup similar to the one employed for 1D self-accelerating beams. A broad-sized Gaussian beam (CW at λ = 633 nm, w_0 = 2.45 mm) was used to illuminate a phase-only Pluto Spatial Light Modulator (SLM) produced by Holoeye (Pluto - 1920 x 1080 pixels of 8x8 μm area, 8-bit grey phase levels). The SLM modulates the phase of the incident Gaussian beam by means of an applied grey-scale hologram reproducing the appropriate phase mask $\rho\left(k_x,k_y\right)$.

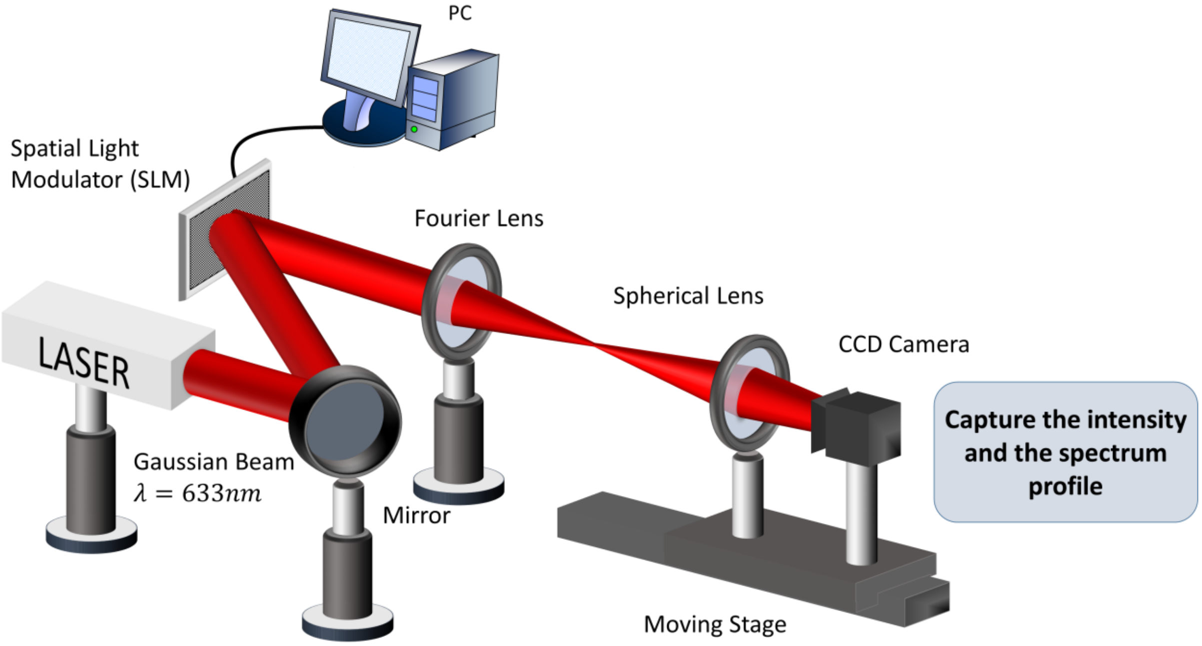

Figure 3.5: Experimental setup used for 2D self-accelerating beams characterization.

As shown in Fig. 3.5, the SLM was used to impress a phase modulation in the Fourier domain and placed at the back focal plane of a spherical lens (f = 150 mm – noted as Fourier lens), which is used to compute the 2D Fourier transform of the initial phase-modulated Gaussian beam. The transverse patterns at the front focal plane of the lens are the 2D self-accelerating beams, whose main intensity lobes are expected to follow the desired trajectories after the lens-induced Fourier transform. By means of a CCD camera (Sony XC-ST50 - 640x480 pixels of 8.4 x 9.8 μm area, 8-bit dynamic range) mounted on a translation stage, the intensity distributions of the beams and their corresponding spectra were imaged at selected (longitudinal) propagation distances. In particular, the spectral intensity distributions were retrieved by imaging the beam in the Fourier plane of a second spherical lens (*f* = 100mm), which was also mounted on the translation stage. The main lobe spectra were measured by means of an additional adjustable aperture slit placed on the translation stage, in correspondence with the back focal plane of the second lens. The aperture slit filters out the contributions of the beam side-lobes, thus only leaving the contribution of main lobe to be analyzed at selected longitudinal distances.

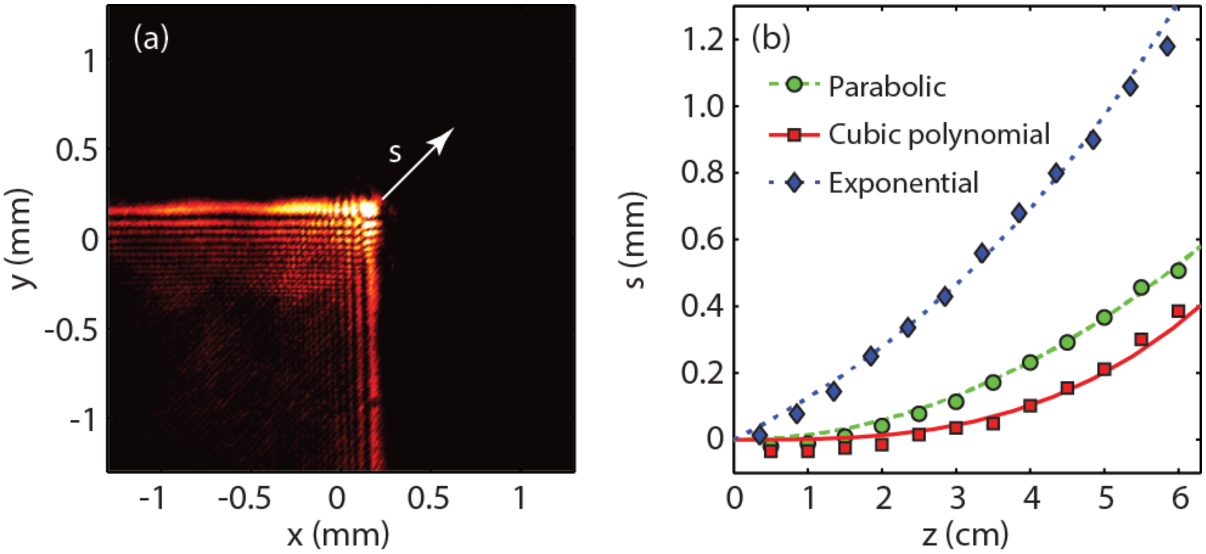

Figure 3.6: Propagation features of self-accelerating beams generated by a circular Gaussian beam. (a) Intensity beam pattern obtained experimentally at z = 4.2cm for the parabolic trajectory (Airy beam). (b) Main hump displacements as a function of the propagation distance measured along the radial direction s for the three trajectories given in Tab. 1. The curves refer to the analytical prediction while the markers are the corresponding experimental results for the 3 selected trajectories, as seen in the legend.

In a first set of measurements, both propagation and spectral characteristics of the three considered beams have been measured. Typical experimental results are shown in Fig. 3.6. In particular, as an illustrative example, Fig. 3.6(a) presents the measured intensity distribution at *z* = 4.2 cm for the typical case of a parabolic trajectory. Such intensity pattern presents a high intensity lobe surrounded by decreasing intensity side-lobes. Although not reported here, similar Airy-like intensity patterns were observed for a cubic polynomial and an exponential path, in good agreement with the numerical simulations shown in Figs. 3.3(b) and 3.4(b). To confirm the reliability of our setup, we also evaluated the beam trajectories of these three accelerating beams by measuring the main lobe displacements at selected propagation distances. Results are summarized in Fig. 3.6(b). The experimental convex trajectories (markers) are in excellent agreement with the analytically- expected evolutions (lines).

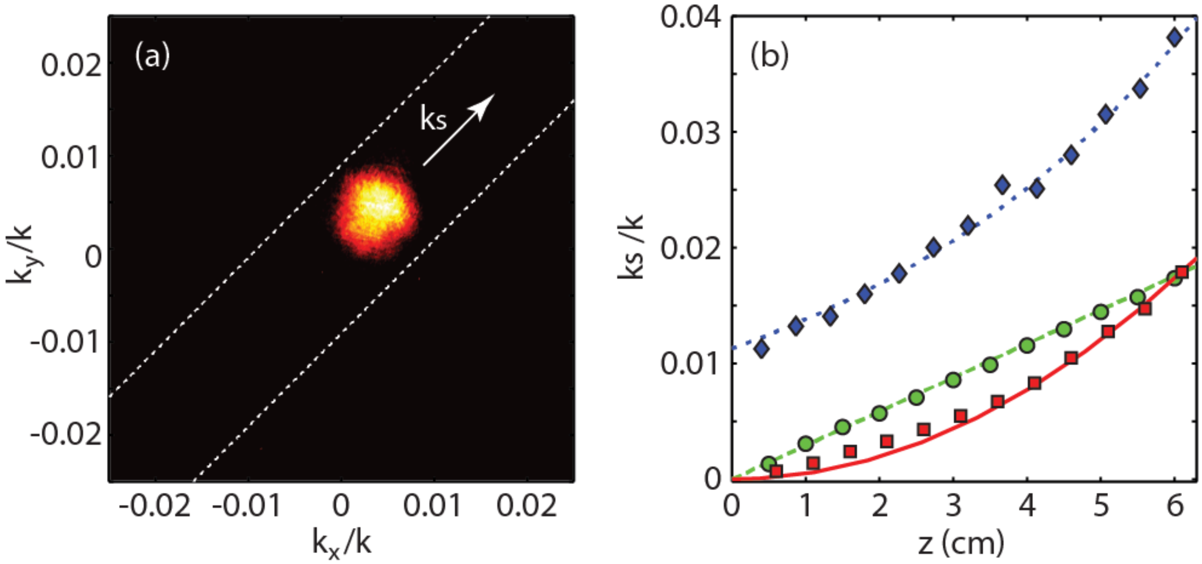

Figure 3.7: Spectral characteristics of self-accelerating beams generated by a circular Gaussian beam. (a) Spectral intensity pattern associated with the main hump of the Airy beam in Figs. 3.6(a). (b) Radial positions of main hump spectra (marker) as a function of propagation distance *z* measured for the three trajectories given in Tab. 1, and corresponding key spatial frequencies deduced from theory (curves). The color code is the same as in Fig. 3.6.

In the Fourier domain, the spectrum of the 2D Airy beam exhibits a Gaussian shape remaining invariant over the whole range of propagation distances. For the other two beam cases, the same spectral feature was also observed. Nevertheless, by filtering out the side-lobes from the intensity pattern, the spectral content associated to the residual main hump for those case self-accelerating beams reduces to a small-sized spot. As an illustrative example, Fig. 3.7(a) shows the main lobe spectrum associated to a 2D Airy beam at $z = 4.2\mathrm{cm}$. As expected from simulations, we observed experimentally that the main lobe spectra not only exhibits a reduced spot size, but also moves along the radial direction k_s as the beam propagates in real space. Therefore, the overall energy associated with the spectral spots is confined within a diagonal stripe, oriented along the radial direction k_s in the Fourier plane. In Fig. 3.7(a), such spectral stripe is bounded by the two white dashed lines. In particular, we estimated the width of such a spectral stripe using a 95% intensity cut-off (i.e. twice the standard deviation of a Gaussian function).

Besides, we also measured the displacements of these spectral spots as a function of the propagation distance z. The side-lobes were filtered out from the beams by placing the aperture slit at the same distances where the beam trajectories in Fig. 3.6(b) were measured. As expected from numerical simulations, the shifts of the main lobe spectra follow both the longitudinal and transversal evolutions of their corresponding key spatial frequencies. The results reported in Fig. 3.7(b) clearly highlight this excellent agreement between the experimentally-measured spot shifts (markers) and the longitudinal evolutions of the key spatial frequencies (lines) predicted by Eq. (3.11).

From a physical viewpoint, our experimental observations further confirm that the spectral component surrounding the key spatial frequencies only contributes to the main lobes intensity, and most of them are localized in the spectral stripe highlighted in Fig. 3.7(a).

3.3 Transverse energy confinement through spectral reshaping

Since the spectral components surrounding the key spatial frequencies (i.e. localized within the stripe shown above) are associated with the main lobe of the 2D self-accelerating beams, the spectral components outside such spectral stripe are connected to the remaining sub-lobes. Numerous applications involving curved beams are predominantly dealing with the optical intensity and the accelerating feature of these beams, so that the exact beam shape might have limited importance. Therefore, the energy stored in the sub-lobes is usually considered as unwanted or wasted. Furthermore, an optimal spatial confinement of the beam intensity may also be required in applications such as optical mapping or pump-probe measurements, in which several experimental factors can constrain or limit the applicability of these light localizations. For example, experimental constraints might be caused by the spatial resolutions or the numerical apertures of the optical elements used in the experimental setting. A way to address these issues directly might be to increase the spatial confinement of the beam itself. In this framework, we introduce a practical and straightforward method suitable to achieve the energy confinement of a 2D self-accelerating beam, i.e. by illuminating the SLM phase mask with an elliptical Gaussian beam (rather than a circular Gaussian beam) whose major axis is oriented along the spectral stripe bounded by the two white dashed lines in Fig. 3.7(a).

In our setup - shown in Fig. 3.8, an elliptical Gaussian beam was obtained by reshaping the incident circular Gaussian beam through a cylindrical telescope. Such optical system was formed by means of two conjugated cylindrical lenses of focal lengths f_1 = 200 mm and f_2 = 50 mm, respectively. The telescope system was rotated 45° around the z axis, in order to align the major axis of the elliptical beam with the radial direction k_s. From a physical viewpoint, since the SLM is placed at the front focal plane of a lens (responsible for performing a Fourier transform of the beam), the presence of the cylindrical telescope affects the spatial spectrum of the circular Gaussian beam by squeezing its spatial frequencies along the direction orthogonal to k_s (i.e. the axis noted ds'), thus preserving the overall energy content of the initial beam.

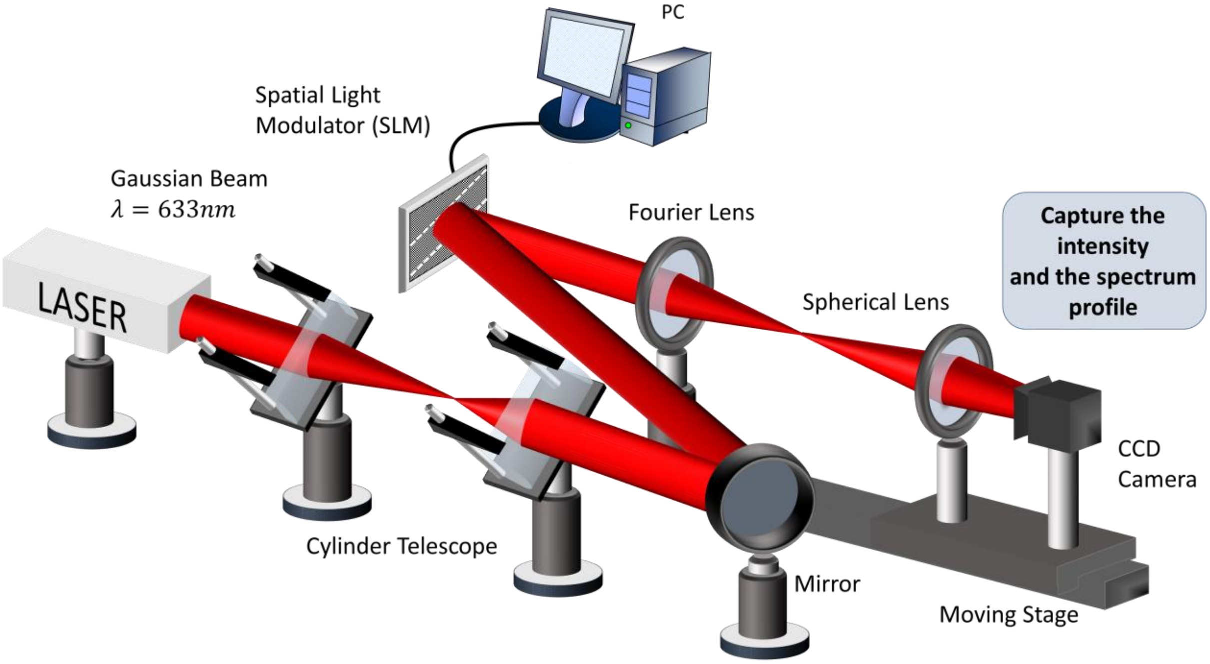

Figure 3.8: Experimental setup for the generation and characterization of 2D self-accelerating beams initiated from an elliptical Gaussian beam.

As illustrated in Fig. 3.9(a), this approach allows the illumination of the SLM phase mask with an elliptical Gaussian beam (red shading ellipse) rather than a circular Gaussian beam (blue shading disc). As an outcome of such a compression, almost all the energy of the incident circular Gaussian beam is focused on the spectral region of the SLM phase mask corresponding to the stripe associated with the main lobe spectral location of a 2D self-accelerating beam (see white dashed lines in 3.9 (a)).

In our experiment, we recorded the accelerating trajectories for the three cases of convex path previously generated (see Tab. 1). However, here we illuminate the SLM with the elliptical Gaussian beam described above [Fig. 3.9(a)]. Besides this spectral compression obtained by the addition of a rotated cylindrical telescope in the setup, the measurements have been carried out using the same parameters and experimental conditions as those reported in Figs. 3.6 and 3.7.

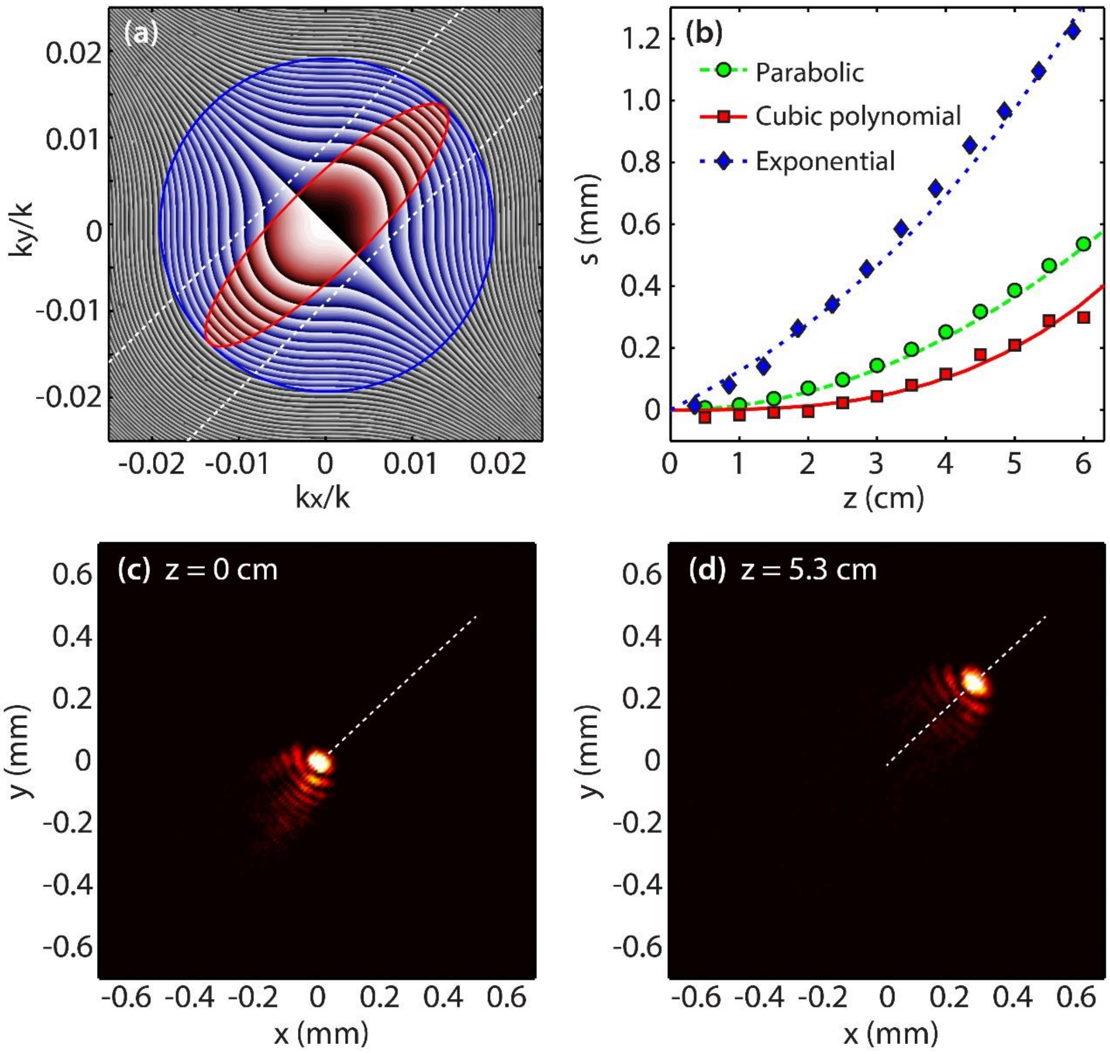

Figure 3.9: Self-accelerating beams properties after spectral compression, for the case in which they were initiated from an elliptical Gaussian beam. (a) Wrapped cubic phase mask applied on the SLM for the case of a parabolic trajectory superimposed to the beam intensity profiles (95% cutoff) of the incident elliptical (red shading – after spectral compression) and circular Gaussian beam (blue shading – before spectral compression). (b) Main hump position along the radial direction *s* as a function of the propagation distance *z*, measured for the three convex trajectories of Tab. 1. The lines refer to the analytical predictions, while the markers show the experimental results. (c, d) Transverse intensity pattern of a “short-tail” beam measured experimentally at *z* = 0 and *z* = 5.3 cm for the case of a parabolic trajectory. Note that for the sake of clarity, the color scale is normalized here to the maximal intensity value of each measurement.

As illustrated in Fig. 3.9(b), the measured trajectories (markers) are in excellent agreement with the numerical predictions (lines). These results confirm that the propagation trajectories remain almost unaffected by the spectral compression of the beam, as we would expect from theory. To provide a visual illustration of the self-accelerating beams obtained from the elliptical Gaussian beam, we have measured the corresponding transverse intensity distributions of the beams after spectral compression. As an illustrative example, we show in Figs. 3.9(c, d) two transverse intensity maps corresponding to the case of the parabolic trajectory, recorded at two different propagation distances ($z = 0$ and $z = 5.3$ cm). Compared to the uncompressed case of Fig. 3.6(a), the transverse intensity patterns of the newly-obtained beams exhibit tails (i.e. the temporal side lobes) characteristic of a greatly reduced spatial expansion, and whose intensity profiles have a similar shape to those of the zero-order accelerating parabolic beams reported in ref. [45-46]. Interestingly, as the energy is conserved with our method, the peak intensity of the beam is expected to be significantly enhanced in comparison with the "uncompressed" case. This aspect will be quantitatively discussed in the next sections. Finally, it is worth mentioning that the spatial confinement obtained by reshaping the circular Gaussian beam only preserves the initial curved trajectory if the major axis of the elliptical Gaussian beams is aligned with k_s . Otherwise, the short-tail beam tends to be destroyed, with a "speed" increasing proportionally with the "misalignment" of those two axes.

3.4 Characterization of the peak intensity enhancement

So far, we have demonstrated that the spectral "squeezing" of a 2D self-accelerating beam is associated with an increase of the beam spatial confinement without affecting its convex propagation. Additionally, the beam peak intensity is expected to increase while the overall energy remains constant. To investigate the effect of such a spectral compression applied to a circular Gaussian spectrum over the resulting peak intensity enhancement, numerical simulations have been performed for the case of the parabolic trajectory under investigation. In Fig. 3.10, we show the peak intensity enhancement as a function of the minor diameter of the elliptical Gaussian beam, whose width is varying along the ds' direction (orthogonal to k_s).

According to this result, the experimental elliptical beam (red circle) would provide a peak intensity of the short-tail beam approximately 60% higher than the corresponding Airy beam obtained from the initial circular beam (blue square). The expected peak intensity is determined by the amount of "squeezing" of the input circular spectrum, intrinsically related to the associated numerical aperture of the cylindrical telescope. For our experimental conditions, the optimal values of energy harvesting are expected for a beam minor diameter of 2 mm. In this case, the spectrum of an elliptical Gaussian beam exhibits a maximal overlap with the main lobe spectral components of the 2D Airy beam. When further increasing the eccentricity of the elliptical beam shape (i.e. for values of ds below 2 mm), the peak intensity starts to decrease drastically.

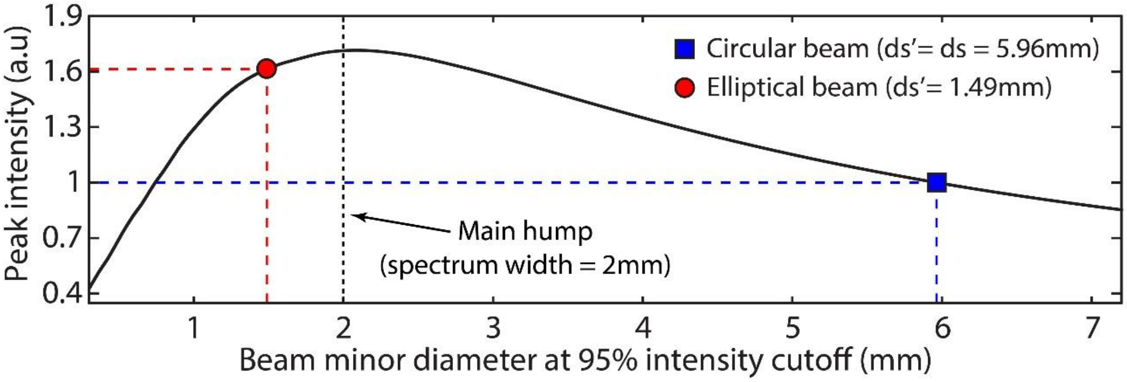

Figure 3.10: Peak intensity enhancement for the case of a parabolic trajectory as a function of the elliptical Gaussian beam minor diameter (ds'). The major diameter is constrained to the circular Gaussian beam diameter, whose experimental value is ds = 5.96 mm. The plot shows that the highest peak intensity enhancement is obtained when the minor diameter approximates 2mm.

Physically, the plot illustrated in Fig. 3.10 highlights the most relevant findings of our study. To optimize the energy confinement, the minor diameter of the elliptical Gaussian beam must closely match the width of the spectral stripe associated with the beam main lobe, as shown in Fig. 3.9(a). When the minor diameter of the elliptical Gaussian spectrum is wider or narrower than the stripe width, both the spatial confinement and peak intensity tend to drift away from their optimal values. Indeed, a broadening of the beam minor diameter tends to involve more and more sub-lobes within the overall beam shape. Instead, a narrowing of its width affects the beam main lobe by (excessively) increasing its transverse size, according to the Fourier limit. Additionally, it is worth mentioning that the spectrum of the main lobe does not possess, strictly speaking, a Gaussian shape. In fact, our approach based on using an elliptical Gaussian shape represents only an approximation of main lobe ideal spectral shape. One would expect that an ideal optimization would be achieved by using an input beam not only matching the stripe width of main lobe spectrum, but also its spectral profile.

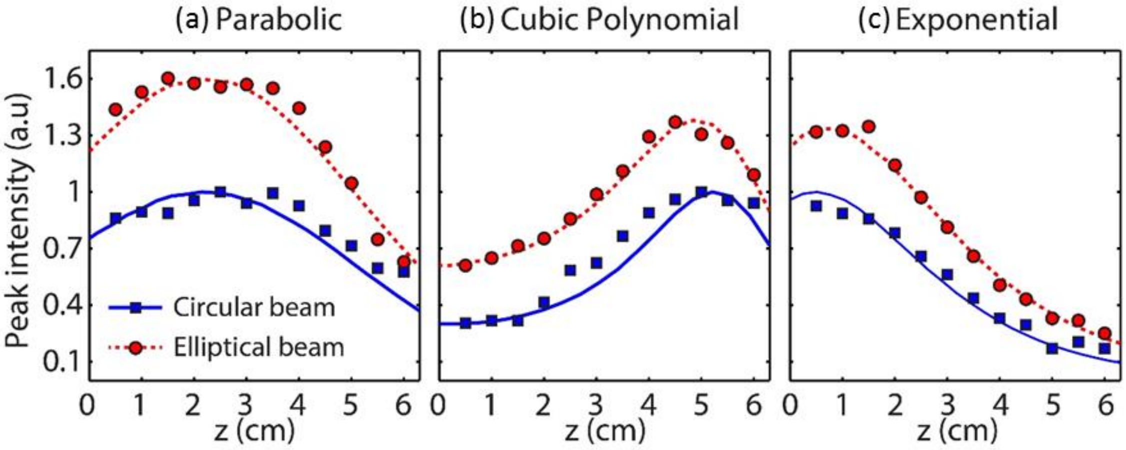

Figure 3.11: Peak intensity enhancement along the propagation distance range. Measured peak intensity values as a function of the longitudinal distance *z* for the case of a (a) parabolic, (b) cubic polynomial and (c) exponential trajectory. Rounded red and squared blue markers are, respectively, the experimental results obtained from an incident elliptical and circular Gaussian beam, while the dotted red and solid blue lines show the corresponding simulation results.

To confirm the validity of our numerical simulation, we have experimentally measured the evolution of the beam peak intensity throughout the propagation range for the three trajectories given in Tab. 1. As illustrated in Figs. 3.11(a-c), these results provide a comparison between the peak intensity values of the beam when either a circular (blue squares) or an elliptical (red circles) incident beam is used. In both cases, the peak intensity evolutions show a similar trend over of the longitudinal propagation. For the case of a parabolic trajectory [Fig. 3.11(a)], we can observe a very good agreement with the 60% intensity enhancement expected from the simulations. For the cubic and exponential trajectories, respectively shown in Figs. 3.11(b, c), the measurements still provide an excellent agreement with simulations, yielding peak intensities values 30% higher than the ones of the uncompressed case.

To perform a proper comparison of our measurements (for each of the cases presented in Fig. 3.11), we have carefully characterized the overall power of both the input circular and elliptical Gaussian beams, in order to equalize them at the input and output of the imaging system. The characterization has been carried out by both power measurements and transverse spatial integration of the CCD images, allowing for a straightforward measurement of the peak intensity enhancement. Furthermore, for each beam trajectory, the comparison between the peak intensity evolutions from both the circular and elliptical Gaussian beams have been plotted by normalizing the curves to the maximal peak intensity detected on the CCD camera for the input circular Gaussian beam case, and similar normalization was done for numerical results.

3.5 Self-healing of short-tail beams

Due to a reduced expansion of the tails of sub-lobes, one may intuitively infer that the self-healing property of newly generated accelerating beams might be entirely affected or, however, limited, over a small longitudinal range only. To clarify this point, we also experimentally verified the self-healing behavior of all considered cases of accelerating beams. The experiments have been carried out by blocking the main lobes at the propagation onset ($z = 0$), and then recording the intensity patterns at selected distances z. As an illustrative example, Fig. 3.12 show the intensity distributions associated to the case of a parabolic trajectory. The results provide a direct observation of the self-healing property for this specific case. Similarly, for the other two paths, no significant changes of the self-healing features with or without compression of the input spatial spectrum have been observed, thus highlighting that the short-tail beams obtained by squeezing the initial spectrum retain the self-healing property of their “classic” 2D self-accelerating beam counterparts.

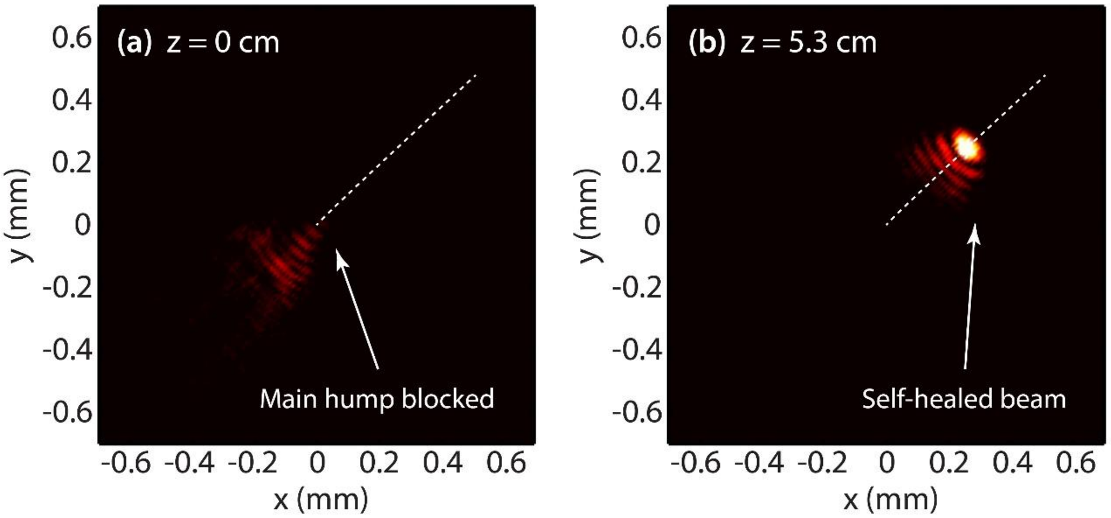

Figure 3.12: Example of self-healing of a 2D accelerating beam initiated from an elliptical beam propagating along a parabolic trajectory. Experimental transverse intensity maps at (a) z = 0 cm and (b) z = 5.3 cm, respectively. The measures have been performed by blocking the main hump of the beam at the onset of propagation (z = 0).

These self-healing measurements further confirm the capability of our practical method to not only to provide energetically confined beam patterns, but also to retain all the peculiar properties of 2D accelerating beams. We have in fact shown, both theoretically and experimentally, that by appropriately shaping the spatial spectra, 2D self-accelerating beams exhibiting significantly reduced tails and enhanced peak intensity can be generated. These beams follow the originally predicted trajectories and, most importantly, they retain their self-healing properties.

Interestingly, our approach based on shaping the initial spectrum is expected to be directly applicable also to the (3+1)D regime, in order to increase the energy confinement of so-called optical light bullets. Such optical bullets can be seen as the spatio-temporal version of 2D self-accelerating beams, which exhibit a self-preserving shape propagation in all spatial directions, i.e. along (x, y, z). The next sections of this chapter will be devoted to investigate the possibility of applying the manipulation of the initial wave packet spectrum also in the case of a spatio-temporal propagation regime.

3.6 Optical light bullets

Until now, we only considered the case of a spatial beam propagating in vacuum, without considering the temporal evolution dynamics of the wave packet. Nevertheless, during propagation in a homogenous dielectric medium, an optical (no CW) wave packet naturally tends to spread in both space and time due to the combined effects of diffraction and dispersion. Over the last few years, tremendous efforts have been deployed by the community to avoid the detrimental effects occurring during light propagation in both the linear and nonlinear regimes, in order to achieve the generation of so-called “optical light bullets” [129-132].

When considering an optical wave packet of large instantaneous power (i.e. intensity), nonlinear effects can compensate both dispersion/diffraction when the appropriate propagation parameters are used. In turn, this allows maintaining the pulse temporal/spatial envelope throughout propagation, leading to what are commonly referred as temporal/spatial solitons [73]. Although of high interest for numerous applications, the use of nonlinearity to mitigate such spreading is limited to special combinations of optical wave packet parameters and propagation media, which both need to be perfectly characterized and therefore cannot be usually tuned over a wide range of parameters. Additionally, such nonlinear optical bullets, due to their high-power requirements, cannot be implemented for applications requiring non-disruptive and non-invasive techniques including, for example, biomedical imaging or optical probing, where the propagation medium should not be significantly impacted by the incident electromagnetic wave.

In the linear regime, optical bullet solutions propagating with a straight trajectory can exhibit either an X-wave or O-wave structure, respectively obtained when considering propagation in either a normal or anomalous dispersion regime [131-132]. On the other hand, self-accelerating solutions (such as Airy beams/pulses) offer the opportunity to generate linear optical bullets in a rather straightforward fashion by taking advantage of the potential separation between the spatial and the temporal components of the solution [37-38]. Similarly to the above studied analog in the spatial domain, an optical pulse featured by an Airy temporal profile is not affected, in the temporal domain , by dispersion during its propagation (i.e., its temporal shape remains unchanged) [133].

Interestingly, Airy wave packets have been demonstrated to be unique non-diffractive solutions existing in a one dimensional regime [11,55] and have thus been exploited as a key building block for the generation of (3+1)D linear optical bullets. This is particularly true when considering the temporal component of such optical bullets, where structures combining an Airy pulse with different typologies of two dimensional non-diffractive beams, such as Airy-Bessel [37], Airy-Airy (i.e. Airy^3) [38], and Airy Parabolic-Cylinder [92] bullets have been extensively reported in literature. Among them, Airy^3 bullets are of particular interest as they maintain all properties of their one or two dimensional beams counterpart: i.e. self-healing, parabolic trajectory and non-diffracting/dispersive propagation. Nevertheless, such bullets have the intrinsic disadvantage of occupying a large (spatio-temporal) volume filled by the numerous sub-lobes typical of Airy functions, as already discussed extensively in the first sections of this chapter. This large-area pattern is thus expected to strongly limit the range of the targeted applications, especially in the framework where low energy but high confinement of the bullet is required, such as, for example, spatio-temporally resolved and non-disruptive optical probing, microscopy and biomedical applications [107,134-135]. Interestingly, few (or perhaps no) studies have addressed the possibility of reshaping Airy bullets to improve the re-distribution of energy in the beam pattern while still preserving the beneficial properties of self-accelerating beams (bullets) [45-46,127,136].

In the second part of this chapter, we report a numerical investigation related to the realization of an optimized version of Airy^3 bullets propagating under anomalous dispersion. In particular, we provide a method to generate a spatio-temporally confined bullet by reshaping both the temporal and the spatial frequency domain of the initial pulse, as a straightforward expansion of the beam optimization already reported above. We show that, in a similar fashion, an appropriate compression of the spatio-temporal input spectrum leads to the generation of a “short-tail” version of the Airy^3 bullet, exhibiting a significant enhancement of the bullet main lobe intensity, paired with a confinement of its spatio-temporal footprint. Remarkably, this is matched by the absence of a significant degradation in the propagation characteristics (i.e. parabolic trajectory and self-healing properties).

3.7 Theory of (3+1)D accelerating optical bullets

In the linear regime, the spatio-temporal propagation of an optical wave packet in a dispersive medium can be described by the (3+1)D paraxial differential equation [73]:

$$i\frac{\partial E(\vec{r},\tau)}{\partial z}+\frac{1}{2\beta(\omega_0)}\nabla_\perp{}^2E(\vec{r},\tau)=\frac{\beta_2(\omega_0)}{2}\frac{\partial^2E(\vec{r},\tau)}{\partial\tau^2}, \tag{3.15}$$

where $E(\vec{r},\tau)=E(x,y,z,\tau)$ is the electric field slowly-varying envelope. Here, x and y are the transverse coordinates, z refers to the longitudinal propagation distance, and $\tau=t-z/v_g$ represents the time coordinate in a frame moving with the group velocity v_g.

The transverse Laplacian operator $\nabla_\perp{}^2=\frac{\partial^2}{\partial x^2}+\frac{\partial^2}{\partial y^2}$ in Eq. (3.15) describes the diffraction effect and the right hand side term accounts for dispersion, where the wave number $\beta(\omega_0)=\omega_0 n(\omega_0)/c$ and group velocity dispersion $\beta_2(\omega_0)=\left.\frac{\partial^2\beta}{\partial\omega^2}\right|_{\omega_0}$ are evaluated at the carrier frequency ω_0. Using the dimensionless coordinates $(\vec{R},Z)=(X,Y,T,Z)=\left(\frac{x}{w_0},\frac{y}{w_0},\frac{\tau}{\tau_0},\frac{z}{L_{diff}}\right)$, where w_0 is the beam spatial width and τ_0 the duration of the wave packet, Eq. (3.15) can be recasted in a normalized form by introducing the diffraction length $L_{diff}=\beta(\omega_0)w_0{}^2$ and the dispersion length $L_{disp}=\frac{\tau_0{}^2}{|\beta_2(\omega_0)|}$ so that:

$$i\frac{\partial\phi(\vec{R},Z)}{\partial Z}+\frac{1}{2}\left[\frac{\partial^2\phi(\vec{R},Z)}{\partial X^2}+\frac{\partial^2\phi(\vec{R},Z)}{\partial Y^2}-sign[\beta_2]\frac{L_{diff}}{L_{disp}}\frac{\partial^2\phi(\vec{R},Z)}{\partial T^2}\right]=0, \tag{3.16}$$

where in Eq. (3.16), $\phi(\vec{R},Z)=E(\vec{R},Z)$ is the normalized electric field envelope. In the following, we consider propagation in an anomalous dispersion regime ($\beta_2<0$) where, for simplicity, dispersion and diffraction are assumed to have the same quantitative effect along propagation so that $L_{diff} = L_{disp}$. Although arbitrary, such an assumption can be easily discarded and the propagation properties readily scaled from the normalized form of Eq. (3.16). Nevertheless, in this particular case, the spatio-temporal evolution of an optical bullet can be drastically simplified for analytic purpose yielding:

$$i\frac{\partial\phi\left(\vec{R},Z\right)}{\partial Z}+\frac{1}{2}\nabla^2\phi\left(\vec{R},Z\right)=0, \tag{3.17}$$

where $\nabla^2=\frac{\partial^2}{\partial X^2}+\frac{\partial^2}{\partial Y^2}+\frac{\partial^2}{\partial T^2}$ is the Laplacian operator. In the normalized Fourier space, i.e. where the spectrum has the spatio-temporal coordinates $\left(\vec{K},Z\right)=\left(K_X,K_Y,\omega,Z\right)$, a solution of Eq. (3.17) can be found as:

$$\phi\left(\vec{R},Z\right)=\frac{1}{8\pi^3}\iiint\limits_{-\infty}^{+\infty}\Phi\left(\vec{K},Z\right)e^{i\vec{K}\bullet\vec{R}}d\vec{K}=\frac{1}{8\pi^3}\iiint\limits_{-\infty}^{+\infty}\Phi\left(\vec{K},0\right)e^{-i\frac{\left\|\vec{K}\right\|^2}{2}Z}e^{i\vec{K}\bullet\vec{R}}d\vec{K} \quad , \tag{3.18}$$

where $d\vec{K}=dK_YdK_Xd\omega$, $d\vec{R}=dXdYdT$ and $\left\|\vec{K}\right\|^2=K_X{}^2+K_Y{}^2+\omega^2$, while the initial spatio-temporal spectrum is given by the relation $\Phi\left(\vec{K},0\right)=\iiint\limits_{-\infty}^{+\infty}\phi\left(\vec{R},0\right)e^{-i\vec{K}\bullet\vec{R}}d\vec{R}$.

Considering an initial spectrum formed by a phase term only, i.e. $\Phi\left(\vec{K},0\right)=e^{i\rho\left(\vec{K}\right)}$, a mapping between spectrum and propagation distance can be obtained in the (3+1)D paraxial regime by an analysis similar to those conducted in the first part of this chapter. Indeed, by defining the phase term in the Fourier domain of Eq. (3.18) so that:

$$\mu\left(\vec{K},Z\right)=\frac{\left\|\vec{K}\right\|^2}{2}Z-\rho\left(\vec{K}\right), \tag{3.19}$$

one can readily extend the concept of spatial phase gradient to the (3+1)D case, where the spatio-temporal coordinates $\left(X,Y,T\right)$ are directly related to the gradient of $\mu\left(\vec{K},Z\right)$ through the relation:

$$\vec{R}=-\nabla_{\vec{K}}\mu\left(\vec{K},Z\right). \tag{3.20}$$

The spectral density within the volume $dXdYdT$ (i.e. the inverse determinant of the matrix $\nabla_{\vec{K}}\nabla_{\vec{K}}\mu(\vec{K},Z)$) shows a singularity at each propagation distance Z, associated with the bullet trajectory, when the following condition is satisfied:

$$Det\left[\nabla_{\vec{K}}\nabla_{\vec{K}}\mu\left(\vec{K},Z\right)\right]=\left|\ \nabla_{\vec{K}}\left[-\vec{K}\,Z+\nabla_{\vec{K}}\rho\left(\vec{K}\right)\right]\ \right|=0\,. \tag{3.21}$$

The expansion of the Eq. (3.21) yields:

$$\left(-Z+\frac{\partial^2\rho\left(\vec{K}\right)}{\partial {K_X}^2}\right)\left(-Z+\frac{\partial^2\rho\left(\vec{K}\right)}{\partial {K_Y}^2}\right)\left(-Z+\frac{\partial^2\rho\left(\vec{K}\right)}{\partial\omega^2}\right)+2\frac{\partial^2\rho\left(\vec{K}\right)}{\partial K_X\partial K_Y}\frac{\partial^2\rho\left(\vec{K}\right)}{\partial K_Y\partial\omega}\frac{\partial^2\rho\left(\vec{K}\right)}{\partial K_X\partial\omega}+ \tag{3.22}$$

$$\left(Z-\frac{\partial^2\rho\left(\vec{K}\right)}{\partial {K_Y}^2}\right)\left[\frac{\partial^2\rho\left(\vec{K}\right)}{\partial K_X\partial\omega}\right]^2+\left(Z-\frac{\partial^2\rho\left(\vec{K}\right)}{\partial {K_X}^2}\right)\left[\frac{\partial^2\rho\left(\vec{K}\right)}{\partial K_Y\partial\omega}\right]^2+\left(Z-\frac{\partial^2\rho\left(\vec{K}\right)}{\partial {K_T}^2}\right)\left[\frac{\partial^2\rho\left(\vec{K}\right)}{\partial K_X\partial K_Y}\right]^2=0.$$

Eq. (3.22) exhibits a complex form that can be greatly simplified considering the imposed phase modulation to be a separable function, i.e. $\rho\left(\vec{K}\right)=\rho_X\left(K_X\right)+\rho_Y\left(K_Y\right)+\rho_T\left(\omega\right)$, yielding a relation:

$$\left(\frac{\partial^2\rho\left(\vec{K}\right)}{\partial {K_X}^2},\frac{\partial^2\rho\left(\vec{K}\right)}{\partial {K_Y}^2},\frac{\partial^2\rho\left(\vec{K}\right)}{\partial\omega^2}\right)=\left(Z,Z,Z\right)\,, \tag{3.23}$$

By solving Eq. (3.23) in an analogous way to the (2+1) case, a mapping between the Fourier and direct space can be found by estimating the key frequencies $\vec{K}_c=\left(K_{X_c}\left(Z\right),K_{Y_c}\left(Z\right),\omega\left(Z\right)\right)$, so that the propagation trajectory of the bullet can be predicted by:

$$\frac{\partial\vec{R}}{\partial Z}=\vec{K}_c \tag{3.24}$$

The analysis reported here is general and can be applied to optical bullets with an arbitrary convex trajectory, which can be directly retrieved from the initially imposed phase mask. From a practical viewpoint, a straightforward approach lies on selecting a desired trajectory, evaluating the corresponding key frequencies from Eq. (3.24) and, finally, calculating the initial phase mask $\rho\left(\vec{K}\right)$ to be applied (retrieved from Eq. (3.23)).

3.8 The Airy^3 bullets

Although the approach is rather general, we here focus on optical bullets following a parabolic trajectory, which is described by the well-known Airy wave packet.

In what follows, we consider the particular case of an ideal Airy^3 bullet [13] whose initial amplitude takes the form of $\phi\left(\vec{R},0\right)=Ai\left(X\right)Ai\left(Y\right)Ai\left(T\right)$, where Ai refers here to the Airy function [12]. In the Fourier space, the corresponding spatio-temporal spectrum is characterized by a 3D cubic spectral phase $\Phi\left(\vec{K},0\right)=e^{i\rho\left(\vec{K}\right)}=e^{i\frac{\left(k_X{}^3+k_Y{}^3+\omega^3\right)}{3}}$, yielding a solution to Eq. (3.17) of the form [11,13]:

$$\phi\left(\vec{R},Z\right)=Ai\left(X-\frac{Z^2}{4}\right)Ai\left(Y-\frac{Z^2}{4}\right)Ai\left(T-\frac{Z^2}{4}\right)e^{i\left(X+Y+T\right)\frac{Z}{2}}e^{-i\frac{Z^3}{4}} \tag{3.25}$$

Such a wave packet is constituted of a 2D Airy beam in the *X* and *Y* plane and an Airy pulse along the time axis *T* (or, correspondingly, in the longitudinal propagation direction *Z*, as time and longitudinal propagation are related here by the bullet group velocity v_g).

An ideal Airy^3 bullet moves freely along the parabolic trajectory defined as $\left(X,Y,T\right)=\left(\frac{Z^2}{4},\frac{Z^2}{4},\frac{Z^2}{4}\right)$, for which the bullet intensity profile remains invariant over a longitudinal propagation (i.e. being non-diffractive and non-dispersive). Correspondingly, in the Fourier domain, the key frequencies of the bullet can be directly mapped as a function of distance so that $\vec{K}_S=\left(\frac{Z}{2},\frac{Z}{2},\frac{Z}{2}\right)$.

In the dimensionless space $\left(X,Y,Z\right)$, the intensity distribution evolves along the parabolic trajectory $\left(\frac{Z^2}{4},\frac{Z^2}{4},Z\right)$, while the temporal shift in the longitudinal direction exhibit the temporal trajectory $T = Z^2/4$. Physically, this corresponds to a modification of the propagation velocity of the Airy wave packet $v_z = \frac{dz}{dt} = \frac{v_g}{1+\frac{v_g\,\tau_0}{2\,L_{diff}{}^2}\,z}$, where a maximum is obtained at $z = 0$ so that $v_z\,(z = 0) = v_g$.

3.9 Finite-energy Airy^3 bullets

From a physical viewpoint, the generation of an ideal Airy^3 bullet is not realizable as it would require the generation of infinite energy bullets (due to the fact that an Airy function is not square integrable). In a practical scenario, one can consider the case where the spatio-temporal spectrum exhibits a 3D Gaussian amplitude profile, on top of which is applied a cubic phase. This in turn yields, in the Fourier domain, to the initial condition $\Phi\left(\vec{K},0\right)=e^{i\rho\left(\vec{K}\right)}\,e^{-\left(\alpha_X k_X{}^2+\alpha_Y k_Y{}^2+\alpha_T k_T{}^2\right)}$, where the truncation coefficients $\alpha_i << 1$ ($i = X,Y,T$) are positive and constant**.** Mathematically, such Gaussian apodization in the Fourier domain is a close approximation of an exponential windowing function in direct space, so that $\phi\left(\vec{R},0\right)\approx Ai\left(X\right)Ai\left(Y\right)Ai\left(T\right)e^{\left(\alpha_X X+\alpha_Y Y+\alpha_T T\right)}$. Rigorously speaking, an input spectrum featured by a Gaussian amplitude leads to the physical synthesis of a finite-energy Airy wave packet whose solution of Eq. (3.18) takes the form:

$$\begin{aligned}\phi\left(\vec{R},Z\right)=&Ai\left[X-\frac{Z^2}{4}+i\alpha Z+\alpha^2\right]Ai\left[Y-\frac{Z^2}{4}+i\alpha Z+\alpha^2\right]Ai\left[T-\frac{Z^2}{4}+i\alpha Z+\alpha^2\right]\\ &\exp\left[\alpha\left(2\alpha^2+X+Y+T-\frac{3}{2}Z^2\right)\right]\exp\left[i\left(X+Y+T+6\alpha^2-\frac{Z^2}{2}\right)\frac{Z}{2}\right]\end{aligned} \tag{3.26}$$

Note that, in Eq. (3.26), the truncation parameters of each component are assumed equal for the sake of simplicity, so that $\alpha = \alpha_X = \alpha_Y = \alpha_T$. In our simulations, we considered a small truncation factor of $\alpha = 0.04$ in order to obtain a bullet of sufficient expansion (i.e. maintaining the main properties of an ideal Airy^3 bullet) while ensuring that the numerical grid span was sufficiently discretized to encompass properly the whole bullet and, at the same time, accurately resolve the fine bullet characteristics (taking into account the computational memory limitation of our system).

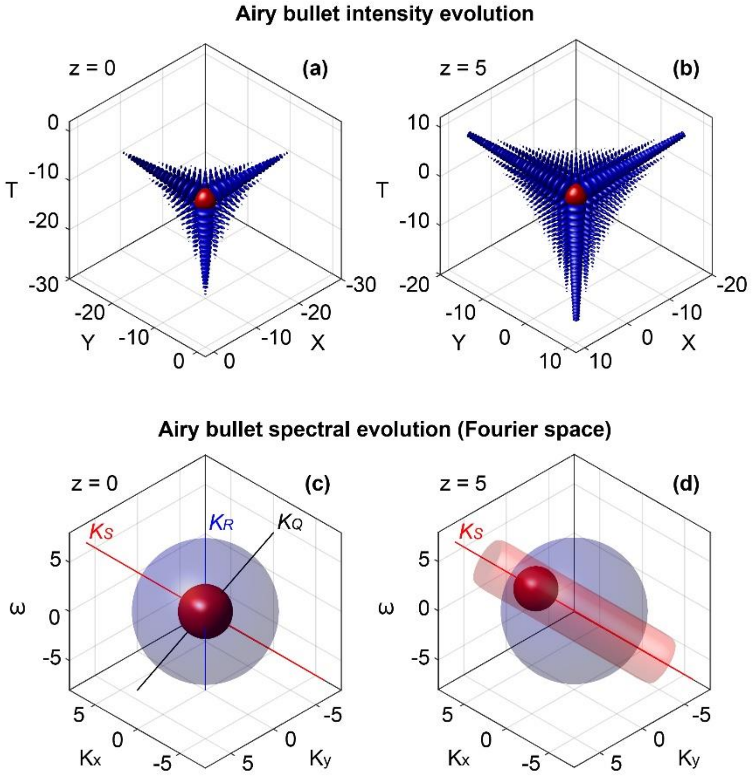

Figure 3.13: Spatio-temporal evolution of an Airy bullet. (a,b) Spatio-temporal and (c,d) spectral intensity isosurfaces of a (finite-energy) Airy^3 bullet shown in blue, and obtained at $Z = 0$ and $Z = 5$, respectively. Red isosurfaces highlight the bullet main lobe in (a,b), and its spectral counterpart in the Fourier space (shown in (c,d)). The isosurfaces are extracted using a 95% intensity cutoff. The red line in (c,d) corresponds to the key spatial frequency trajectory $\vec{K}_s$ followed by the main lobe spectral components, whose location in the Fourier space (throughout the entire range of propagation) is represented by the red shaded cylinder in (d).

Fig. 3.13 shows the direct and Fourier space intensities (95% cutoff isosurfaces) of the corresponding bullet at two different propagation distances (for instance $Z = 0$ and $Z = 5$). In the spatio-temporal space (X, Y, T), depicted in Figs. 3.13(a, b), the Airy wave packet is characterized by an intense main lobe (highlighted in red), as well as three main (long) tails formed of numerous sub-lobes. Although one may identify non negligible spreading when approaching $Z = 5$ (i.e. the increase of the bullet expansion due to its finite energy), we verified that the Airy^3 bullet maintains its shape over a significant propagation range and follows closely the predicted parabolic trajectory along the direction $\vec{S} = \left(X, Y, T\right) = \left(\frac{Z^2}{4}, \frac{Z^2}{4}, \frac{Z^2}{4}\right)$.

In the Fourier space, the spectral intensity isosurfaces shown in Figs. 3.13(c, d) exhibit a spherical shape (blue isosurface), invariant over propagation and intrinsically associated to the spherical symmetry set by the 3D Gaussian amplitude of the input spectrum. In contrast, the spectral content associated with the bullet main lobe (smaller red isosurface) is located in the central part of the input spectrum [Fig. 3.13(c)], but its location moves within the main spectrum to follow the trajectory defined by the key spatio-temporal frequency $\vec{K}_S = \left(K_X, K_Y, \omega\right) = \left(\frac{Z}{2}, \frac{Z}{2}, \frac{Z}{2}\right)$, as illustrated in Fig. 3.13(d). Over the whole propagation range, the main lobe spectral content moves along the axis $\vec{K}_S$ similarly to the cases studied in the (2+1)D regime, however defined here as the diagonals of the cube $[K_X, K_Y, \omega]$. In such a case, the main lobe spectral intensity remains confined within an elliptic cylinder (red shading) with half-axis defined along the (orthogonal) directions $\vec{K}_Q = (K_X, -K_Y, 0)$ and $\vec{K}_R = (-K_X, -K_Y, 2\omega)$.

3.10 Compressed Airy^3 bullets

The fact that the spectral components associated with the main lobe of the Airy^3 bullet are found within a specific spectral location is of paramount importance for the targeted optimization of such an Airy^3 bullet. Indeed, by reshaping the spatio-temporal spectral intensity in an efficient way, we foresee that a significant enhancement of the bullet main lobe intensity associated with a reduced overall spatio-temporal can be readily obtained. This can be achieved in a similar way as what we reported above for the cases of 2D self-accelerating beams, i.e. by confining the initial Gaussian spectrum of the Airy^3 bullet along the key spatial frequency K_S . This leads in turn to the compression of the spatio-temporal spectral intensity along both the directions $\vec{K}_Q = (K_X, -K_Y, 0)$ and $\vec{K}_R = (-K_X, -K_Y, 2\omega)$.

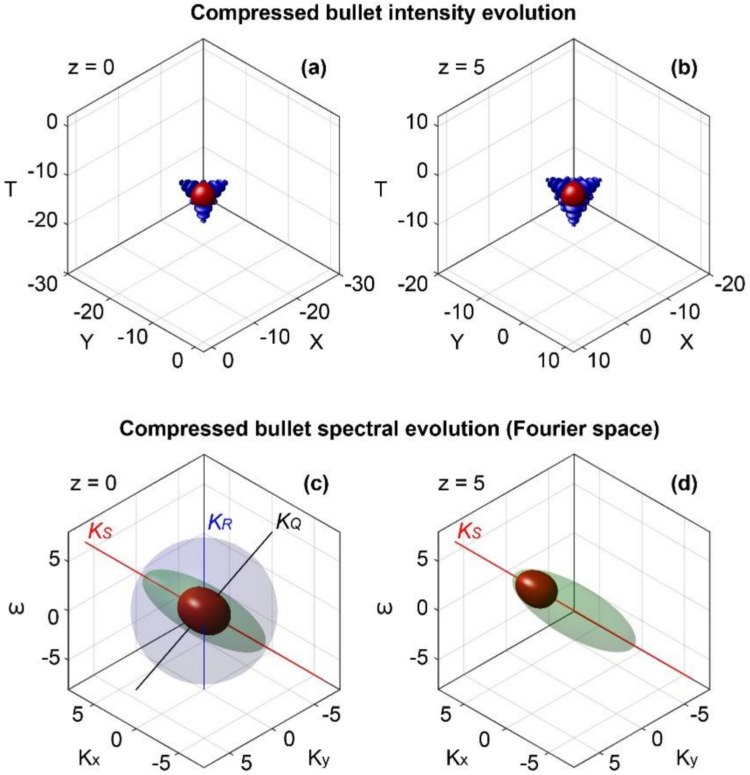

Figure 3.14: Spatio-temporal evolution of a "Short-tail bullet". (a-d) Isosurfaces plots as shown in Fig. 3.13, considering a compressed bullet with a spectrum "squeezed" along $\vec{K}_Q$ and $\vec{K}_R$. With a compression factor $C_Q = C_R = 8$, the initial Gaussian spectrum (blue sphere) shown in (c) is reshaped into an ellipsoid (green shading) closely matching the displacement of the main lobe spectral components throughout propagation [see Fig. 3.13(d)].

Here, to avoid losses of generality, we perform a normalized numerical analysis to assess the effect of such a "spectral squeezing" on the dynamics of a finite-energy Airy^3 bullet. In this framework, we define the squeezing (or compression) parameters as the ratio between the Gaussian waist α_Q obtained after spectral compression along $\vec{K}_Q$ with the initial waist of the spectrum α given in Eq. (3.26) so that $C_Q = \alpha_Q / \alpha$. Correspondingly, a spectral compression along $\vec{K}_R$ is associated to the parameter $C_R = \alpha_R / \alpha$.

In Fig. 3.14, we show numerical results considering the same bullet parameters, but with a symmetric compression of the spatio-temporal spectrum along $\vec{K}_Q$ and $\vec{K}_R$ so that $C_Q = C_R = 8$. Physically, this corresponds to a decrease of the spectral intensity FWHM by a factor $\sqrt{C_Q} = \sqrt{C_R} = 2.83$, as can be seen in Figs. 3.14(c, d), where the compressed spectrum is shown as green isosurfaces, and compared with the initial Gaussian spectrum (blue shading). In the direct space, presented in Figs. 3.14(a, b), the overall compressed bullet (blue) exhibit a reduced expansion compared to the previous case but the shape of the main lobe (red) remains almost unaffected at both propagation distances.

3.11 Impact of Airy^3 bullet compression

Although Fig. 3.14 already illustrates qualitatively the effect of the spectral compression on the bullet shape, a more qualitative study regarding the impact of the spectral compression on the bullets is provided in Fig. 3.15, comparing the properties of the bullets shown in Fig. 3.13 and 3.14 as a function of propagation. As seen in Fig. 3.15(a), both the trajectories of the Airy^3 (blue dots) and compressed (red circles) bullets are in excellent agreement with the analytically predicted parabolic trajectory over the range $Z = [-5:5]$ (black line). Additionally, the compressed bullet peak power shown in Fig. 3.15(b) exhibits a significant enhancement (i.e. by a factor > 3) compared to the bullet of Fig. 3.13 which is here used as normalized reference. In comparison with the 2D beams optimization reported above, what we find to probably be the most striking feature is illustrated in Fig. 3.15(c). Here we extracted and compared the volume of the bullet in the "classic" and compressed case.

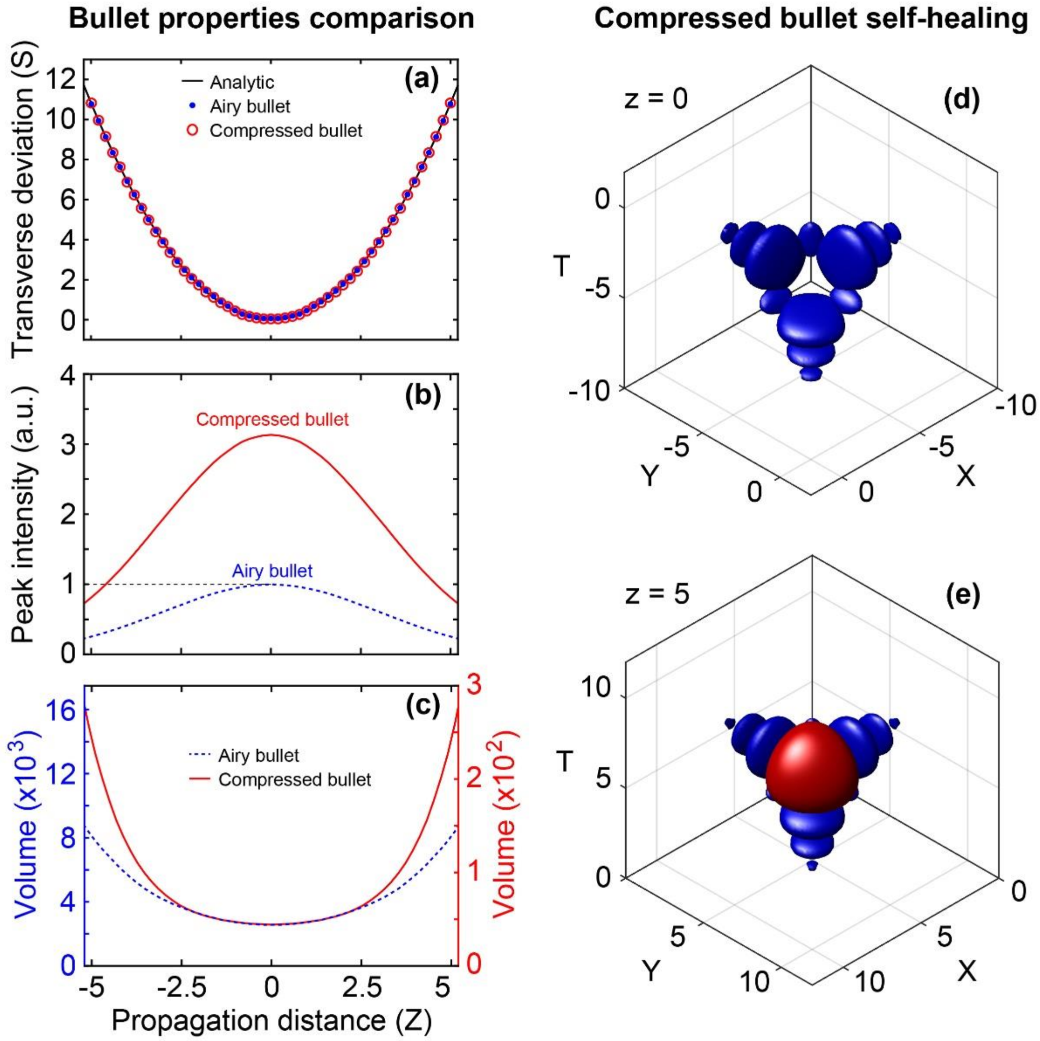

Figure 3.15: Comparison between the fundamental properties of an Airy bullet and a "Short-tail bullet" obtained by an appropriate compression of the Airy bullet spectrum. (a) Spatio-temporal trajectories, (b) peak intensities, and (c) volumes along the propagation Z, considering the Airy^3 bullet of Fig. 3.13 (dashed blue) and the compressed bullet shown in Fig. 3.14 (red). (d-e) Illustration of the self-healing property of a compressed bullet (i.e. $C_Q = C_R = 8$). The main lobe of the bullet is blocked at $Z = 0$, as seen in (d), and regenerated after propagation, as illustrated in (e) for $Z = 5$.

In particular, such volumes are extracted as the smaller cube ($V = \Delta X\,\Delta Y\,\Delta T$) where components above 0.1% of the bullet peak intensity could be found (so that at least 95% of the overall bullet energy is enclosed within this region), and normalized with respect to the volume of the bullet main lobe shown in Fig. 3.13(a). Although slightly larger spatio-temporal expansion can be observed at the edges of the propagation range, one can clearly assess the drastic volume reduction of the compressed bullet over almost two orders of magnitude (see left/right axis scale) when compared to the Gaussian spectrum case of Fig. 3.13. This confirms the potential of this approach in efficiently confining the Airy^3 bullet spatio-temporal expansion while maintaining its propagation characteristics almost unaffected. This is further attested by the ability of the compressed bullet to "self-heal", as illustrated in Figs. 3.15(d, e). Specifically, we numerically "suppressed" the spectral components associated with the bullet main lobe at $Z = 0$ which corresponds to the red isosurface shown in Fig. 3.14(c). At this propagation distance, illustrated in Fig. 3.15(d), the main bullet lobe is thus absent but is still regenerated through propagation, as shown for instance at $Z = 5$ in Fig. 3.15(e). Indeed, the fact that the reshaped spectrum seen in Figs. 3.14(c, d) closely overlaps the spectral content of the main lobe (i.e. the 'red shaded' cylinder in Fig. 3.13(d)) allows the bullet to maintain (and eventually "self-heal") its compressed shape over a significant propagation range, which could not be reached otherwise (e.g. by only using a Gaussian shape with a higher truncation parameter).

3.12 Effect of the spectral compression

As previously seen, the bullet spectral compression can greatly affect its intensity and expansion without significantly deteriorating the overall propagation dynamics. In Fig. 3.16, we report a more detailed and quantitative study of the impact of the spectral compression on the bullet properties recorded on the onset of propagation (i.e. $Z = 0$). In these cases, the truncation factor is kept constant with the same value as shown in Figs. 3.13 - 3.15 so that $\alpha = 0.04$. Fig. 3.16(a) depicts a colorplot of the peak intensity, obtained at $Z = 0$, as a function of both compression factors C_Q and C_R. In this case, one can readily see that a significant intensity enhancement can be obtained even for low (and eventually asymmetric) compression factors. Optimal intensity enhancement is achieved for symmetric compression so that $C_Q = C_R$ (white dashed line diagonal) and, in this case, the relevant bullet properties are extracted and illustrated in Figs. 3.16(b-d). We can observe a significant and monotonic peak intensity enhancement for compression factors below ~10, as seen in Fig. 3.16(b). For higher values, further spectral compression starts to become detrimental, as the bullet does not overlap anymore with the key frequency components shown in Fig. 3.13(d) and 3.14(d) [136] – i.e. in a similar fashion as observed for 2D self-accelerating beams.

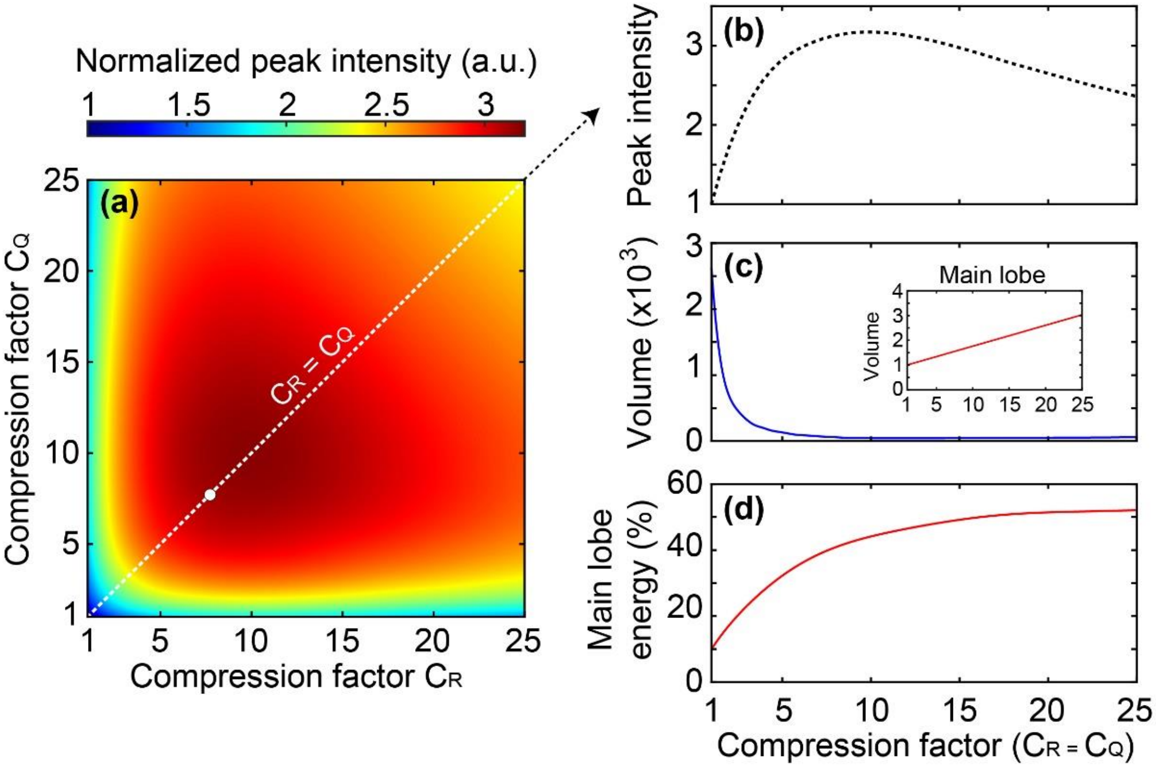

Figure 3.16: Peak intensity and spatio-temporal volume of the "Short-tail bullet" as a function of the spectral compression. (a) Peak intensity distribution as a function of the spectral compression factors C_Q and C_R (the case shown previously is illustrated with a white dot in the plot). For symmetric squeezing (dashed white line, i.e. $C_Q = C_R$), we extracted the bullet (b) peak intensity, (c) volume and (d) energy ratio present in the main lobe as a function of the spectral compression factor. The inset in Fig. 3.16(c) illustrates the effect of spectral compression on the main lobe volume.

As a consequence, the extracted peak intensity starts to decrease from this optimal value and the bullet propagation dynamics is expected to exhibit some deterioration. The impact of spectral compression on the overall bullet volume is shown in Fig. 3.16(c), where one can observe an exponential-like decay of the volume as the bullet spectrum is compressed, until reaching quasi-saturation for compressions greater than ~10. In the inset, we report the corresponding variation of the bullet main lobe volume as a function of spectral squeezing. In this case, we can see a small but steady increase of the main lobe volume, attesting for the energy transfer of the bullet power from its wings to the main lobe as we increase the compression of the bullet spectrum. This phenomenon is even better illustrated when computing the ratio of the bullet energy contained in the main lobe as a function of spectral squeezing, see Fig. 3.16(d). Indeed, one can see that a clear increase of the main lobe energy is obtained when the bullet spectrum is compressed around its key frequency components. For instance, the main lobe contains about 10% of the total bullet energy without spectral compression (as in the case shown in Fig. 3.13) while the compressed bullet of Fig. 3.14 (i.e. $C_Q = C_R = 8$) possesses more than 40% of its energy concentrated in its main lobe. In fact, our numerical results predict the possibility to concentrate more than half of the bullet energy in the main lobe - when considering this truncation factor and an optimal spectral compression (corresponding to $C_Q = C_R \approx 10$) .

Our approach clearly has a twofold advantage. Not only it increases the bullet main lobe intensity/energy, but also reduces the overall spatio-temporal bullet expansion. Evidently, both of these aspects are associated with an improvement of the bullet energy confinement (here calculated as the ratio between energy and volume), whose impact is summarized in Fig. 3.17. We can thus observe that the energy confinement of the bullet main lobe (red line) is indeed enhanced by a factor of approximately 3 for an optimal compression factor of ~10 before decreasing upon further spectral squeezing. The main significant aspect of such compression is nevertheless associated with the overall bullet energy confinement, which can be improved by a factor above 50 for a similar spectral squeezing.

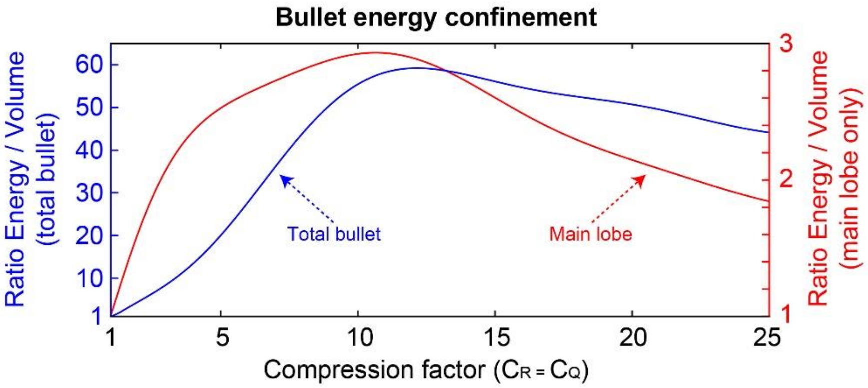

Figure 3.17: Energy spatio-temporal confinement of the total bullet (blue line) and its main lobe (red line) as a function of spectral compression. Energy confinement is calculated as the average ratio between energy and volume shown in Figs. 3.16(c-d), and normalized to unity with respect to the (uncompressed) Airy^3 bullet case.

It is worth noting that the impact of spectral squeezing depends clearly on the initial truncation parameter, which fixes the energy content of the Airy bullet. Here we focused on the case where α = 0.04 (for numerical grid limitations), which corresponds to scenarios that can be typically obtained experimentally. Although not presented here, we conducted additional numerical simulations using both lower and upper values of α. For instance, by considering α = 0.02, the spectral compression provides a more dramatic impact on the bullet energy confinement. The bullet will maintain its shape over longer distances, while exhibiting a higher energy confinement. The optimal spectral compression can yield to a bullet confinement improved by a factor up to 150. One the other hand, when fixing α = 0.08, the improvement of spectral compression on the bullet energy confinement is reduced as the bullet spectral expansion is already closely matching the key frequency components, but the bullet do not maintain its shape over such a long propagation range.

Finally, we also mention that the technique discussed above can be directly generalized to optical linear bullets propagating along arbitrary convex trajectories. As seen for 2D self-accelerating beams, we can engineer the spatio-temporal phase structure to generate optical linear Airy-like bullets with the desired convex trajectory. Since the main-lobe associated to these optical bullets show the same spectral features as the Airy bullet, energy confinement can be directly achieved by squeezing the input spectrum in an appropriate (yet similar) way.

3.13 Potential experimental implementations

By looking at the approach discussed above to improve the bullet energy confinement, one may wonder about its viability in a realistic and suitable experimental setting. Despite this being out of the scope of this thesis, we can briefly mention that this exact approach might not be trivial to implement (first of all because a compression of the temporal spectrum is not really feasible in the linear regime). However, we foresee that a similar technique may be implemented without requiring a compression of the spectral components, but rather their spectral redistribution. The scheme in Fig. 3.18 shows a potential way to experimentally achieve such a bullet energy confinement. First, an input Gaussian pulse undergoes a temporal shaping in order to modify its temporal profile into an Airy pulse. This can be obtained by spreading its spectral (temporal) components through an optical system, formed by a diffraction grating and a lens. At the Fourier plane of this lens, we can perform the 1D cubic phase modulation using, for example, an SLM. Then, the Airy pulse is obtained by recombining the spectral (temporal) components using a second system of lens and a grating, which is placed specularly to the first one. Before carrying out the recombination, the circular (spatial) profile of the beam is reshaped into an ellipse shape by means of a cylindrical telescope. In this way, the spherical spectrum of the input Gaussian pulse (blue isosurface in Fig. 3.13(c)) is reshaped into an ellipsoid before the application of a "spatial" 2D cubic phase modulation. As shown in Fig. 3.14(c), an appropriate spectral tilt of the ellipsoidal spectrum has to be introduced in order to project K_S onto the plane $[K_X\ , K_Y\ ]$ of the SLM. Such tilting could be tuned by rotating the reflection angle of a third grating. This grating, along with another lens, is also responsible of distributing the spectral (temporal) components at the Fourier plane, where the spatial phase modulation is performed. In order to orient the ellipsoidal spectrum along the K_S direction, the spatial modulation can be carried out by rotating the 2D cubic phase mask of 45-degree. Finally, the fourth lens is used to obtain, in the real space, a compressed Airy bullet analog to the one numerically investigated here.

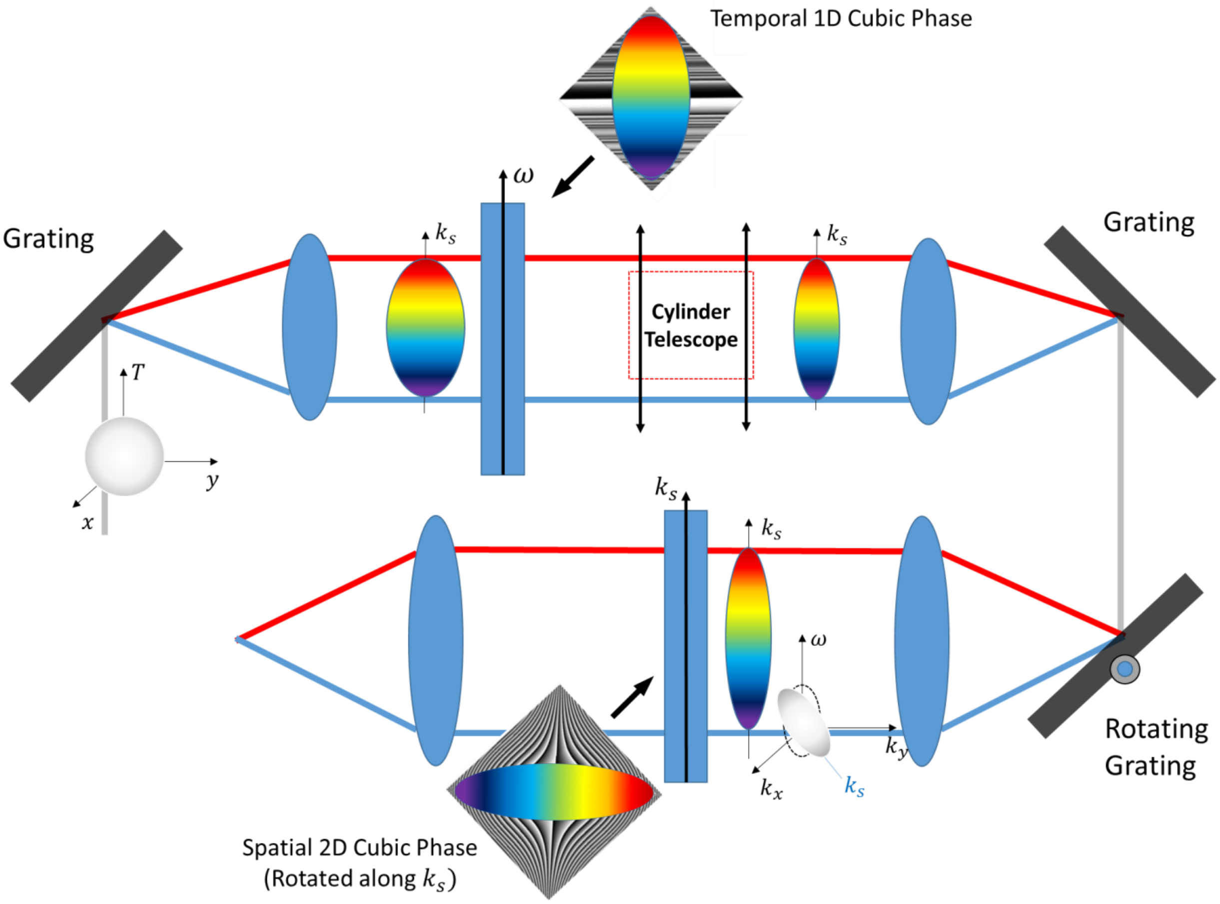

Figure 3.18: Proposed experimental implementation

The actual set-up is expected to require additional adjustments that will be the subject of further investigation, taking into account the numerical apertures and physical parameters of the system as well as the potential deteriorations of the beam/pulse quality due to this implementation (e.g. astigmatism, lens dispersion, viability of spectral tilting, etc.). Nevertheless, we foresee that such a spectral intensity reshaping could be easily obtained through the joint use of widely available dispersive and focusing optical elements (e.g. gratings, lenses), as previously discussed.

3.14 Final remarks

In conclusion, we have demonstrated the possibility to significantly enhance the energy confinement of 2D self-accelerating beams and optical Airy bullets, both propagating in a linear regime. This energy confinement can be readily obtained by reshaping the input spectra in order to properly match the spatial frequency content associated with the main lobes over propagation. The initial spectral reshaping gives rise to a short-tail version of the associated optical wave packets, showing a significant increase of the peak intensity of its main lobes, while maintaining the same peculiar features of their "classical" counterparts.

In the first part of this chapter, we dealt with the energy confinement of 2D self-accelerating beams. At first, we extended the spectral-to-space mapping to the (2+1)D regime, highlighting that the spectra associated with the main lobe of these beams is mapped into the propagation distance. To prove our analysis, three different convex trajectories have been studied: a parabolic, a cubic polynomial and an exponential trajectory. Starting from the convex paths, for which we assumed to have the same acceleration along the *x* and *y* directions, we retrieved the appropriate phase structures to be applied in the Fourier domain to generate the desired beam patterns. For each case, we studied the propagation and spectral characteristics of these 2D self-accelerating beams. Then, we introduced a practical method to significantly and efficiently enhance the energy confinement of these 2D self-accelerating beams. This is easily reached experimentally by reshaping the circular Gaussian beam (incident to the SLM) into an elliptical Gaussian beam matching the spectral stripe associated to the main lobe spectrum during propagation. A notable enhancement of the main lobe peak intensity along several convex trajectories was observed in experiments, and a reduction of their equivalent transverse expansion was obtained. When an optimal shaping of the initial beam is realized, the intensity localized in the main lobe can be increased up to about 60%. Furthermore, we also verified that the newly generated short-tail beam preserves the intrinsic characteristics of the beams initiated by the circular Gaussian beams.

In the second part of this chapter, the spectrum-to-space mapping has been also extended to the (3+1)D regime. We proposed a numerical method to enhance the spatio-temporal energy confinement of an Airy^3 bullet by an appropriate spectral reshaping of the bullet amplitude in the Fourier space. The spectral compression proposed here – analogous to the one studied experimentally for the (2+1)D case - has the potential to generate an Airy^3 bullet of reduced spatio-temporal expansion – also exhibiting an enhanced energy confinement. For instance, we observed that the overall bullet energy confinement can be improved by a factor above 50, while the energy confinement of the bullet main lobe can be enhanced by a factor of approximately 3 in comparison with a “classical” Airy^3 bullet featured by the same characteristics. Additionally, the compressed bullet peak power exhibits a significant enhancement by a factor > 3. We also demonstrated numerically that the bullet peculiar properties (i.e. non-diffractive, non-dispersive, self-healing) are, similarly to the case of 2D beams, conserved for the desired trajectory.

We expect that the results reported in this chapter will have a significant impact towards the implementation of curved trajectories wave packets for applications requiring non-destructive and non-invasive techniques including, for example, biomedical imaging and highly localized optical probing. Here, the propagation medium should not be significantly impacted by the electromagnetic wave. Additionally, future work will focus on extending this approach to the case of accelerating wave packets propagating in a nonlinear medium, for typical applications requiring higher powers, as for example micro-machining.

Chapter 4

Acceleration and spectral reshaping of nonlinear Airy wavepackets

In this chapter, the nonlinear behavior of Airy beams and pulses is investigated. In the first part, spatial Airy beams are studied, both theoretically and experimentally, by considering their propagation in a biased photorefractive (PR) material, under either a self-focusing or self-defocusing nonlinearity. We found that a finite-energy Airy beam can preserve its acceleration properties in nonlinear photorefractive media, with a slight change of the beam path with respect to the linear parabolic trajectory. Additionally, throughout the nonlinear propagation, the spatial spectrum undergoes a dramatic reshaping initiated from a Gaussian spectral distribution. A positive or negative defect appears under the self-focusing or -defocusing nonlinearity, respectively. In the second part, the nonlinear propagation of Airy pulses in optical fiber are studied theoretically and experimentally under the combined effect of the both self-phase modulation (SPM) and GVD dispersion. We observe that most spectra content concentrates into one or two position-dependent self-shifting peaks under normal or anomalous dispersion, respectively. Furthermore, we also propose a practical method to proportionally control frequency shifts, by acting on the central frequency of a spectral cubic phase structure without the need to alter the fiber length.

4.1 Introduction

Optical Airy beams/pulses are self-accelerating wave packets having, respectively, a better resistance to diffraction and dispersion comparing to Gaussian beams/pulses. Since they were introduced and experimentally observed in optics [13-14], many intriguing phenomena and potential applications associated with these wave packets have been proposed and demonstrated [118]. As we saw in the previous chapter, one of the most remarkable applications for Airy wave packets is the realization of linear optical bullets, where an Airy pulse is combined with a non-diffractive 2D beam, hence suppressing the broadening of the spatio-temporal wave packet - both in spatial and temporal domains without the need of using nonlinear phenomena [37-38,92-93,137]. In the nonlinear regime, one of the most challenging issue for Airy wave packets is to preserve their self-accelerating property. Along this direction, many research efforts have been devoted to control and maintain the parabolic acceleration under the action of nonlinearities [25-26,28,31,79,108-109]. In space, nonlinear Airy beams have been studied theoretically and explored experimentally in different nonlinear environments, such as in Kerr, saturable Kerr, and quadratic nonlinear media [32,78,138-139]. In particular, an Airy beam breakdowns and loses its acceleration under a self-focusing nonlinearity that seriously alters the optical phase [25-26,78]. Nevertheless, the acceleration is better kept for in a self-defocusing medium, yet it is still affected by the presence of the nonlinearity [26]. To understand how a parabolic trajectory can be also followed by an optical beam in nonlinear media, the formation of 1D self-accelerating nonlinear modes have been proposed [31,78]. These self-trapped optical beams are found as self-accelerating solutions of the nonlinear wave equation (NLWE), including either self-focusing or -defocusing nonlinearities [31]. Temporal Airy pulses share analogous nonlinear behaviors with 1D Airy beams in space [13-14]. In nonlinear environments, such as nonlinear optical fibers, their propagation is described by the generalized nonlinear Schrödinger equation (GNLSE) [85]. Airy pulses have been employed to control super-continuous generation in photonic crystal fibers [91] and to improve the intra-pulse Raman scattering [36]. For a simply and realistic case where only the Kerr effect is considered, Airy pulses tend to shed self-trapped solitons [27].

In this chapter, we investigate numerically and experimentally the nonlinear propagation of optical Airy beams and pulses. We propose a scheme to preserve their self-accelerating properties in the nonlinear regime, as well as control both trajectories and spectral features. In the first part, we will deal with spatial Airy beams propagating in a biased PR crystal under self-focusing and -defocusing nonlinearities. When a finite-energy Airy beam is delivered into a nonlinear PR medium, the nonlinearity, especially the self-focusing type, is able to greatly affect the self-accelerating properties [25-26,78]. In most cases, finite-energy Airy beams (called from now Airy beams) are generated in the Fourier regime by modulating an input Gaussian beam with a cubic phase mask coded into a spatial light modulator (SLM). We will show that if the central frequency of the cubic phase modulation is shifted, the Airy beam tends to maintain its acceleration under photorefractive nonlinearity, albeit with a slight change on the propagation trajectory with respect to the linear parabolic path. Accordingly, their Fourier spectra reshape into some interesting configurations. Under a self-focusing (self-defocusing) nonlinearity, such spectrum is featured by a notch (spectral peak) that can shift during the pulse propagation.

The second part of the chapter will be focused on the nonlinear propagation of optical Airy pulses, described by the nonlinear Schrödinger equation (NLSE). In particular, we will investigate the self-phase modulation (SPM) of Airy pulses under normal and anomalous dispersion in single mode fibers, and will consider their behavior in the presence of Kerr nonlinear effects. Similar to the spatial counterpart, Airy pulses are generated by imposing a a cubic phase modulation to an input Gaussian pulse in the Fourier domain. Such phase modulation is performed by employing a pulse shaper that is based on the space-time pulse conversion technique. In time, we will demonstrate that Airy pulses can also preserve their self-acceleration property in a Kerr medium under normal and anomalous dispersion. This can be achieved by shifting the central frequency of the applied cubic phase modulation, as done for the spatial case. During nonlinear propagation under normal dispersion, most of the spectrum concentrates to one self-shifting peak (or positive defect). Instead, under anomalous dispersion, the spectrum reshapes into two self-shifting peaks (or negative defect). Moreover, the shifts of the spectral defects at the output side of a single-mode fiber (SMF) can be proportionally controlled solely by shifting the cubic phase structures, without the need of any change in terms of fiber length. Therefore, we can readily realize wavelength selection by employing Airy pulses. Finally, these nonlinear spectral reshaping occurring in both spatial and temporal domains may find applications in laser filamentation and plasma guidance, as well as in beam/pulse shaping.

4.2 Nonlinear effects in a dielectric medium

In the first two chapters, we only studied self-accelerating beams and Airy bullets in the linear regime. The unique physical phenomena taken in consideration were diffraction and dispersion. In the spatial domain, diffraction causes the waist of a finite-energy optical beam to spread along propagation in a dielectric medium. In a similar fashion, dispersion affects a finite-energy optical pulse propagating inside a dielectric medium in the temporal domain. Under normal or anomalous dispersion, the pulse undergoes a broadening or narrowing of its pulse duration, respectively. Since the refractive index is a function of the frequency, the different components of an optical pulse will travel with different phase velocities, affecting the pulse width. Nonlinearity is another property that can affect the propagation of both optical beams and pulses. It consists in the change of the refractive index due to the optical intensity. Many nonlinear phenomena have been demonstrated in optics [89]. In this section, we only limit our discussion to consider two important nonlinear effects: Kerr and PR saturable nonlinearities. Under a Kerr nonlinearity, the optical intensity induces a nonlinear change of the polarization density which in turn induces a refractive index change in the material. On the other hand, in the presence of PR nonlinearity, the optical intensity induces an internal electric field which modifies the refractive index of the material via the electro-optic effect. These two nonlinearities are analyzed more in the details in the following sections. In particular, the refractive index changes as function of the optical intensity will be derived and investigated.

4.2.a Kerr nonlinearity

Kerr nonlinearity can induce a change in the refractive index originating from a light-induced nonlinear change of the polarization density. Here, we briefly review the physical mechanism, limiting the analysis to the specific cases used in the next sections. More details on this topic can be found in Ref. [89].

When an electromagnetic wave propagates inside a dielectric medium, light-matter interactions are described by the vector relationship between the polarization density **P** and the electric field **E**. Polarization effects originate from the motion of the bound electrons inside the material, induced by the applied electromagnetic field. If this motion is harmonic, the total polarization is linear and the medium is also called linear. On the other hand, an intense electric fields **E** produces an anharmonic motion and, as a consequence, the total polarization density **P** becomes nonlinear. If the electric field only varies along one dimension, for example, **E** = $E\boldsymbol{x}$, the polarization density is also induced along the same direction, i.e. **P** = P $\boldsymbol{x}$. Since we will deal with linearly-polarized laser beams, the analysis can be reduced to the scalar case.

Under the above conditions and assuming the nonlinearity weak when compared to the intra-atomic forces inside the medium, the relationship between P and E is expressed via a Tailor series as:

$$P(t)=\varepsilon_0\chi^{(1)}E(t)+\varepsilon_0\chi^{(2)}E^2(t)+\varepsilon_0\chi^{(3)}E^3(t)+\ldots \tag{4.1}$$

Where $\varepsilon_\mathbf{0}$ is the free-space dielectric permeability and $\chi^{(n)}$ is the n$^{\text{th}}$-order dielectric susceptibility. For the sake of simplicity, we assume the dielectric medium to be isotropic, homogeneous and dispersiveless. In general, susceptibility terms $\chi^{(n)}$ higher than the third order are (n=3) not taken into account because they provide a negligible effect.

If light is monochromatic, the electric field is expressed as: $E(t)=\Re[E_0 e^{i\omega t}]=E_0\cos(\omega t)$. Therefore, the induced polarization density takes the following form:

$$\begin{aligned}P(t)=\varepsilon_0\Bigg[&\frac{1}{2}\chi^{(2)}E_0^2+\left(\chi^{(1)}+\frac{3}{4}\chi^{(3)}E_0^2\right)E_0\cos(\omega t)+\\&\frac{1}{2}\chi^{(2)}E_0^2\cos(2\omega t)+\frac{1}{2}\chi^{(3)}E_0^3\cos(3\omega t)\Bigg].\end{aligned} \tag{4.2}$$

Eq. (4.2) shows that the nonlinear polarization density generates new terms whose angular frequencies are different from those carried by the input electric field. These components are responsible for well-known nonlinear phenomena, such as optical rectification, second- and third-harmonic generation, the Kerr effect etc. [89]. In particular, the second term in Eq. (4.2) represents indeed such Kerr effect. In non-centrosymmetric materials where $\chi^{(2)}$ is not zero, the Kerr effect is usually negligible with respect to other nonlinear effects because $\chi^{(2)}$ is much larger than $\chi^{(3)}$.

However in centrosymmetric materials, such as silica in optical fibers, $\chi^{(2)}$ is zero and the Eq. (4.2) reduces to:

$$P(t)=\varepsilon_0\left(\chi^{(1)}+\frac{3}{4}\chi^{(3)}E_0^2\right)E_0\cos(\omega t)+\frac{1}{2}\varepsilon_0\chi^{(3)}E_0^3\cos(3\omega t), \tag{4.3}$$

in which only the components of polarization at frequencies ω and 3ω are preserved. The 3ω term corresponds to third harmonic generation, but in most practical cases the energy conversion efficiency is low. Therefore, we can also neglect this term. Finally, the polarization density induced by a monochromatic pump reads as (in complex form):

$$P(t)=\Re\left[\varepsilon_0\chi^{(1)}E_0e^{i\omega t}\right]+\Re\left[\frac{3}{4}\varepsilon_0\chi^{(3)}|E|^2E_0e^{i\omega t}\right]=\Re\left[P_Le^{i\omega t}\right]+\Re\left[P_{NL}e^{i\omega t}\right], \tag{4.4}$$

Where $P_L=\varepsilon_{\mathbf{0}}\chi^{(1)}E_0$ and $P_{NL}=\varepsilon_{\mathbf{0}}\Delta\chi E_0$ (with $\Delta\chi = 3/4\ \chi^{(3)}|E|^2$) are the linear and nonlinear polarization densities, respectively. To connect the nonlinear polarization to a nonlinear change in the refractive index, we consider now the displacement vector:

$$D=\varepsilon_0E+P=\varepsilon_0(1+\chi+\Delta\chi)E \tag{4.5}$$

Since the refractive index n is related to the relative permittivity $\varepsilon_{\mathbf{r}}$ through $n^2=\varepsilon_{\mathbf{r}}=1+\chi+\Delta\chi$ we can find the refractive index n as:

$$n^2=(n_0+\Delta n)^2\approx n_0+2n_0\Delta n=1+\chi+\Delta\chi. \tag{4.6}$$

From Eq. (4.6), the nonlinear change in the refractive index is derived as:

$$\Delta n(I)=\frac{\Delta\chi}{2n_0}=\frac{3}{8n_0}\chi^{(3)}|E|^2=n_2I, \tag{4.7}$$

Where $n_2=3\eta_0/(4n_0^2)\chi^{(3)}$ is the nonlinear refractive index coefficient, $I=n_0|E|^2/(2\eta_0)$ is the optical intensity and $\eta_0\approx 380\Omega$ is the free-space impedance. In conclusion, the refractive index in Kerr media can be modified by the light intensity due to the Kerr effect:

$$n=n_0+\Delta n(I)=n_0+n_2I \tag{4.8}$$

4.2.b Propagation of light in anisotropic media and electro-optics effect

To better understand the physics of light propagating inside a PR crystal, it is worth to recap very briefly two important concepts in optics: optical anisotropy, and the electro-optics effect. As known from both theory and experiments, differently polarized plane waves propagating in isotropic media will travel at the same phase velocity. However, in an anisotropic medium, the phase velocity depends on the polarization of light. This can be intuitively explained observing that electric fields along different directions experience dissimilar refractive indexes. Birefringence is the most appreciable phenomenon caused by anisotropy in crystals. Physically, an elliptically polarized light beam travelling through an anisotropic crystal is split into two orthogonal linearly-polarized components, eventually emerging from the crystal as two separated light beams [2]. In particular, the most used crystals in both experimental settings and applications are uniaxial ones, where ordinary refractive index n_0 appears along two orthogonal directions (ordinary axis), e.g. the y-and z-axis, and extraordinary refractive index n_e along the other dimension, i.e. the x-axis (extraordinary axis and also called optical c-axis). In such crystals, when a plane wave is linearly-polarized along the c-axis (or alternatively along the y-/z-axis), it will travel at an extraordinary phase velocity $v_\mathrm{e}= c / n_\mathrm{e}$ (or at an ordinary phase velocity $v_0= c / n_0$, respectively). In general, the refractive index along three axes could be completely different, which corresponds to the so called biaxial crystals.

Another property that is inherent to the anisotropy of a crystal is the electro-optic effect. Here, a change of the refractive index is caused by an applied or induced electric field. In the most common electro-optic effect, the refractive index change is linearly-dependent of the applied electric field - so-called electro-optic Pockels'effect. The relationship between the refractive index change and the applied electric field is described by a 6×3 matrix $[r_{ij}]$, $i = 1 \dots 6$ and $j = 1 \dots 3$, known as linear *electro optics tensor,* providing that the electro-optic coefficients r_{ij} is related to the crystallographic composition and symmetry of the electro-optic material [1]. We would like to mention that the electro-optic effect could be also of Kerr type, which has a quadratic dependence on the electric field and mainly appears in centrosymmetric electro-optics materials. However, in the case of PR crystals, the induced internal electric field modifies the refractive index via the electro-optic Pockel's effect only.

4.2.c Photorefractive nonlinearity

In PR media, the change of the refractive index is caused by the combination of both the photoconductive and the electro-optic effects exhibited by these materials. Photorefractivity was first observed in a $LiNbO_3$ (Lithium Niobate) crystal by Ashkin and his collaborators [140]. In literature, a variety of materials are reported to manifest PR properties. Among others, the most used are: ferroelectric crystals such as $LiNbO_3$, SBN (Strontium Barium Niobate), $BaTiO_3$ (Barium Titanate), $KNbO_3$ (Potassium Niobate), KTN (Potassium Tantalate Niobate) and KLTN (Potassium Lithium Tantalate Niobate); paraelectric crystals such as BSO (Bismuth Silicon Oxide), BTO (Bismuth Titanate Oxide) and BGO (Bismuth Germanium Oxide); semiconductors such as GaAs (Gallium Arsenide).

The PR effect is commonly explained by using a simple band-transport model, named Kukhtarev model [141]. In the following, we will limit to analyze more detail only the 1D case associated to our study. For more general cases, in which 2D modeling is required, the interested readers can refer to the excellent available literature [142-145].

Figure 4.1 illustrates a simplified scheme describing the physical mechanisms associated with the PR effect. If an optical beam illuminates a PR medium, free charge carriers, electrons or holes, are generated from impurity energy levels (e.g. Fe^{2+} in $LiNbO_3$) in the forbidden band, at a generation rate that is proportional to the light intensity $I = I(x, z)$. In addition to the optical excitation, free charge carriers can also be thermally generated. This phenomenon is taken into account by introducing the so-called dark irradiance I_D. Upon excitation, free carriers move away from the high intensity locations, thus leaving ions with opposite signs. Charge transport is mainly due to a diffusion current produced by the concentration gradient of the charge carriers, and a drift current arises when an external electric field is applied. An additional contribution can come from a photovoltaic current, originating from the anisotropic photoexcitation of carriers in piezoelectric media. Once moving, these free charge carriers can recombine at other ionized impurities (e.g. Fe^{3+} in $LiNbO_3$), thus creating an excess of charges with the same sign in these locations. In this way, an inhomogeneous space-charge distribution in the PR medium is created, which in turn induces an internal electric field $\mathbf{E}_{sc}(x)$, known as a *space charge field*. As a result, such field modulates the refractive index of the PR medium via the electro-optic Pockel's effect.

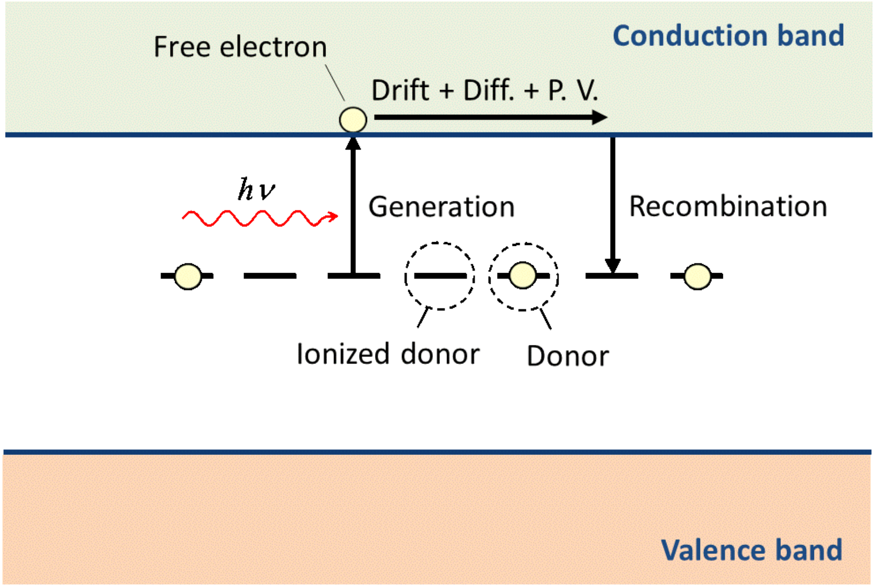

Figure 4.1: Kukhtarev's band transport model.

For illustrative purposes, we will now derivate quantitatively the change of the refractive index due to the induced space-charge field inside a PR medium. At first, we need to calculate the screening electric field $\mathbf{E}_{sc}(x)$ via the Kukhtarev transport model. Let us consider a scenario in which an external bias electric field E_0 is applied to a PR crystal along its optical *c*-axis (*x* direction). The optical beam is linearly-polarized along the *x* direction and propagates in the biased PR medium along the *z*-direction. Moreover, the beam is only permitted to diffract along the *x*-direction with an intensity profile $I = I(x, z)$. Under these assumptions, the induced electric field $E_{sc}(x)$ will be also oriented along the *c*-axis: $\mathbf{E}_{sc}(x) = E_{sc}(x)\ \boldsymbol{x}$. Therefore, the Kukhtarev's model reduces to the one-dimensional case. The crystal under test here is SBN that is uniaxial and widely-used, especially when large nonlinear optical coefficients are required. The electro-optic coefficient r_{33} along the optical *c*-axis can reach values larger than 200 pm/V [146]. The photovoltaic effect in this material is low enough to make the photovoltaic current basically neglectable. Although our analysis is limited to the particular case of SBN crystals [75,147], it can be similarly applied to others PR media, such as $LiNbO_3$. However, in this case, the photovoltaic contribution should also be taken into account [148].

Another reasonable approximation is to consider electrons as the only free charge carriers in the SBN crystal. Under the conditions above, the time-independent response through the one-dimensional Kukharev's model is governed by a set of equations describing the different involved processes [75]:

$$s_i\left(I+I_D\right)\left(N_D-N_D^+\right)=\gamma_R \mathrm{n}_e N_D{}^+. \tag{4.9}$$

$$J=e\mu\left(\mathrm{n}_e E_{SC}+\frac{K_B T}{e}\frac{\partial \mathrm{n}_e}{\partial x}\right), \tag{4.10}$$

$$\frac{\partial J}{\partial x}=0 \text{ and } J=\mathrm{cost} \tag{4.11}$$

$$\frac{\partial E_{SC}}{\partial x}=\frac{e}{\varepsilon_0\varepsilon_r}\left(N_D^+-N_A-\mathrm{n}_e\right). \tag{4.12}$$

Where s_i is the photoexcitation cross section, γ_{R} is the carrier recombination rate, N_D, N_A, N_D^+, and n_e are the volume density of donors, acceptors or traps, ionized donors, and free-electrons, respectively. I_D is the dark irradiance, $I = I(x, z)$ is the light intensity, ε_0 and ε_r are the static free-space and relative permittivity, respectively. Furthermore, $E_{sc}(x)$ is the induced spatial-charge electric field, J is the current density, K_B is Boltzmann's constant, T is the temperature, μ and e are the electron mobility and the charge, respectively.

The overall rate of generation, i.e. $G(x) = s_i(I + I_D)(N_D - N_D^+)$, and recombination, i.e. $R(x) = \gamma_{\mathrm{R}}\mathrm{n}_{\mathrm{e}}N_D^+$, for free charge carriers must be equal. The generation rate $G(x)$ is contributed by both the optical, i.e. $G_{op}(x) = s_i I(N_D - N_D^+)$, and thermal, i.e. $G_{th}(x) = s_i I_D(N_D - N_D^+)$ processes. The redistribution of the electrical charges and the creation of a space charge field obey the Poisson's equation. The total current density J is contributed from both the drift current, i.e. $J_{Esc} = e\mu\mathrm{n}_e E_{sc}$, and the diffusion current, i.e. $J_{\mathrm{D}} = \mu K_B T\, \partial\mathrm{n}_e/\partial x$. The electric field $E_{sc}(x)$, due to the nonuniform space-charge distribution (resulting from the electrons transport in the PR crystal), can be therefore calculated by solving the set of equations presented above.

An easy way to estimate $E_{sc}(x)$ is to consider further simplifications which are physically valid in most PR media, including SBN. In particular, we assume that the light intensity $I = I(x, z)$ is slowly varying respect to x, and $N_A \gg \mathrm{n}_e$ and $N_D^+ \gg \mathrm{n}_e$. Using these approximations, Eq. (4.9) and (4.12) can be reduced to a simpler form [148]:

$$N_D^+ = N_A \tag{4.13}$$

$$\mathrm{n}_e = \frac{s_i\left(N_D - N_A\right)}{\gamma_R N_A}\left(I + I_D\right) \tag{4.14}$$

Let us also assume that the optical intensity $I = I(x, z)$ asymptotically tends to a constant value at $x \to \pm\infty$, i.e. $I(x \to \pm\infty, z) = I_\infty$. In these regions, the induced space-charge field is independent of x, i.e. $E_{sc}(x \to \pm\infty, z) = E_0$. If the width W of the PR crystal is much larger than the spatial extension of the optical wave, and a constant voltage bias V is applied, E_0 is approximately $\pm V/W$. In such case, the Eq. (4.14) asymptotically reads:

$$\mathrm{n}_e\left(x \to \pm\infty\right) = \frac{s_i\left(N_D - N_A\right)}{\gamma_R N_A}\left(I_\infty + I_D\right) \tag{4.15}$$

Since the current density is constant respect to x: $J = J_\infty$, one can obtain from Eq. (4.11):

$$\mathrm{n}_e E_{SC} + \frac{K_B T}{e}\frac{\partial \mathrm{n}_e}{\partial x} = \mathrm{n}_e\left(x \to +\infty\right)E_0 + \frac{K_B T}{e}\frac{\partial \mathrm{n}_e\left(x \to +\infty\right)}{\partial x} \tag{4.16}$$

Substituting Eq. (4.15) into Eq. (4.16), the induced space-charge field is estimated to be:

$$E_{SC} = E_0\frac{I_\infty + I_D}{I + I_D} - \frac{K_B T}{e}\frac{1}{I + I_D}\frac{\partial I}{\partial x} \tag{4.17}$$

Generally speaking, the bias electric field E_0 can reach appreciable values. As a result, the drift component of the current will be dominant when compared to the diffusion term. In this case, the second term in Eq. (4.17) can be neglected. Furthermore, if the width W of the crystal is larger than the spatial extension of the optical beam, I_D can also be considered much larger than I_∞. Therefore, the induced space-charge electric field $E_{sc}(x)$ can be simplified as:

$$E_{SC} = E_0 \frac{I_D}{I + I_D}. \tag{4.18}$$

As previously mentioned, the internal electric field $E_{sc}(x)$ locally perturbs the refractive index of the SBN crystal by virtue of the electro-optic Pockel's effect. Since the optical beam is linearly-polarized along the *c*-axis, only the extraordinary refractive index is taken into account. The index change $\Delta n_e(x)$ of the extraordinary refractive index n_e caused by $E_{sc}(x)$ via the electro-optic effect, is given as [76]:

$$\Delta n = -\frac{1}{2} n_e^3 r_{33} E_{SC}, \tag{4.19}$$

Where n_e and r_{33} are the unperturbed extraordinary refractive index and the electro-optic coefficient of the SBN crystal, respectively. The relationship between the incident beam intensity $I(x, z)$ and the resultant refractive index change $\Delta n_e(x)$ can be readily obtained by substituting Eq. (4.14) into Eq. (4.16):

$$\Delta n = -\frac{1}{2} n_e^3 r_{33} E_0 \frac{I_D}{I + I_D}. \tag{4.20}$$

The most notable characteristic is that, differently from the Kerr effect, the PR nonlinearity manifests a refractive index change $\Delta n_e(x)$ that has a saturable evolution with the optical intensity. For this reason, it is called saturable PR nonlinearity.

4.3 Nonlinear propagation of an optical beam

In the previous section, we have demonstrated that the optical intensity produces a change of the refractive index in a dielectric medium. In what follows, we will derive the nonlinear paraxial wave equation (NLPWE) describing the spatial propagation of an optical beam under the nonlinear regime. To simplify the analysis, we assume that the wave packet propagates along the z-axis and diffracts along the transversal direction (x-axis). Additionally, we also assume the optical beam being linearly-polarized along the x-axis direction. Starting from Maxwell's equations, the electric field expressed via $\mathbf{E}(x, z,t) = E_x(x, z,t)\boldsymbol{x}$ obeys to the relation:

$$\frac{\partial^2 E_x}{\partial z^2} + \frac{\partial^2 E_x}{\partial x^2} - \frac{1}{v^2}\frac{\partial^2 E_x}{\partial t^2} = 0. \tag{4.21}$$

In Eq. (4.21), $E_x(x, z,t)$ is the x-component of the electric field, x is the transversal coordinate, z is the propagation coordinate, t is the time coordinate and $v = \mathrm{c}/n$ is the propagation velocity Here, c is the speed of light in vacuum and n is the nonlinear refractive index. n follows the formula $n^2 = \left(n_0 + \Delta n(I)\right)^2 \approx n_0^2 + 2n_0\Delta n(I)$, where n_0 is the linear refractive index and $\Delta n(I)$ is the small index change induced by the nonlinearity. For monochromatic beams, a typical way to solve the wave equation is by separating the x-component of the electric field into its spatial and time-harmonic solutions:

$$E_x\left(x,z,t\right) = E\left(x,z\right)\exp\left(-i\omega_0 t\right), \tag{4.22}$$

in which $E(x, z)$ denotes the spatial-varying component of the electric field, and ω_0 is the carrier frequency. Substituting this expression into Eq. (4.21), the spatial component satisfies the nonlinear Helmholtz equation:

$$\frac{\partial^2 E}{\partial z^2} + \frac{\partial^2 E}{\partial x^2} + \left(k_0 n\right)^2 E = 0, \tag{4.23}$$

Where $k_0 = \omega_0 /c$ is the free-space wave number. The electric field can be expressed via $E(x,z) = A(x,z)\exp(ikz)$, where $A(x,z)$ is the slowly-varying electric field envelope, and $k = \omega_0 n_0 /c$ is the wave number. By substituting those terms into Eq. (4.23), the NLPWE under the slowly-varying envelope approximation $\left|2k\partial A/\partial z\ \right| << \left|\partial^2 A/\partial z^2\right|$ reaches its final form:

$$i\frac{\partial A}{\partial z} + \frac{1}{2k}\frac{\partial^2 A}{\partial x^2} + \frac{k\Delta n\left(I\right)}{n_0}A = 0 \tag{4.24}$$

For a Kerr nonlinearity $\Delta n(I) = n_2 I$, while in the presence of a PR nonlinearity we have instead $\Delta n(I) = -0.5 n_0^3 r_{33} E_0 \, I_D / (I + I_D)$. Here n_0 is the unperturbed extraordinary refractive index n_e and $I = |A|^2 / (2\eta)$.

After deriving the NLPWE, we will now introduce two nonlinear effects related to a change in the refractive index: the so-called *self-focusing* and *self-defocusing* nonlinearities.

4.3.a Self-focusing and self-defocusing nonlinear effect

Assuming that the beam diffraction is vanishingly small, or alternatively that the material is very thin, we can neglect diffraction and consider only the nonlinear contribution in Eq. (4.24), thus obtaining:

$$i\frac{\partial A}{\partial z} + \frac{k\Delta n(I)}{n_0} A = 0 \tag{4.25}$$

Defining $A(x,z) = |A(x,z)| \exp[i\Phi(x,z)]$, Eq. (4.25) contains real and imaginary parts, i.e.

$$\begin{aligned} \frac{\partial |A(x,z)|}{\partial z} &= 0 \\ \frac{\partial \Phi(x,z)}{\partial z} &= \frac{k\Delta n(I)}{n_0} \end{aligned} \tag{4.26}$$

Then the solution to Eq. (4.25) is found to be:

$$A(z,x) = |A(0,x)| \exp\left(i\frac{k}{n_0} \Delta n\big(I(0,x)\big) z \right) \tag{4.27}$$

As a result of nonlinearity, the optical wave experiences a spatial self-phase modulation (SPM) during propagation. Two interesting effects that are associated with SPM are self-focusing and –defocusing nonlinearities. In Fig. 4.2 we show the propagation of a Gaussian beam in both Kerr and PR saturable media under a self-focusing and -defocusing nonlinearity, respectively, when no diffraction is considered. If a Gaussian beam is transmitted through a Kerr material, the induced refractive index change, i.e. $\Delta n(I) = n_2 I$, reproduces its optical intensity profile. If the Kerr parameter n_2 is positive [Fig. 4.2(a)], SPM changes the wave front of the Gaussian beam similarly to what a converging lens will do, causing self-focusing. Likewise, SPM can also induce self-focusing in PR saturable media, i.e. $\Delta n(I) = -1/2n_0^3 r_{33} E_0 I_D/(I+I_D)$. In particular, a self-focusing nonlinearity is obtained when a positive bias electric field ($E_0 > 0$) is applied on the PR material [Fig. 4.2(b)]. On the other hand, in Kerr media with $n_2 < 0$ [Fig. 4.2(c)], SPM can impose to the wave front of the Gaussian beam a change of the curvature similar to what a diverging lens will do, therefore causing self-defocusing. Interestingly, in PR media the self-defocusing nonlinearity can be easily turned on by reversing the applied static voltage ($E_0 < 0$) [Fig. 4.2(d)]. Nevertheless, diffraction cannot be generally ignored, so both SPM and diffractive effects must be taken into account together. Under certain conditions, SPM can compensate diffraction and the optical beam propagates without changing its spatial distribution, forming a so-called spatial soliton [73].

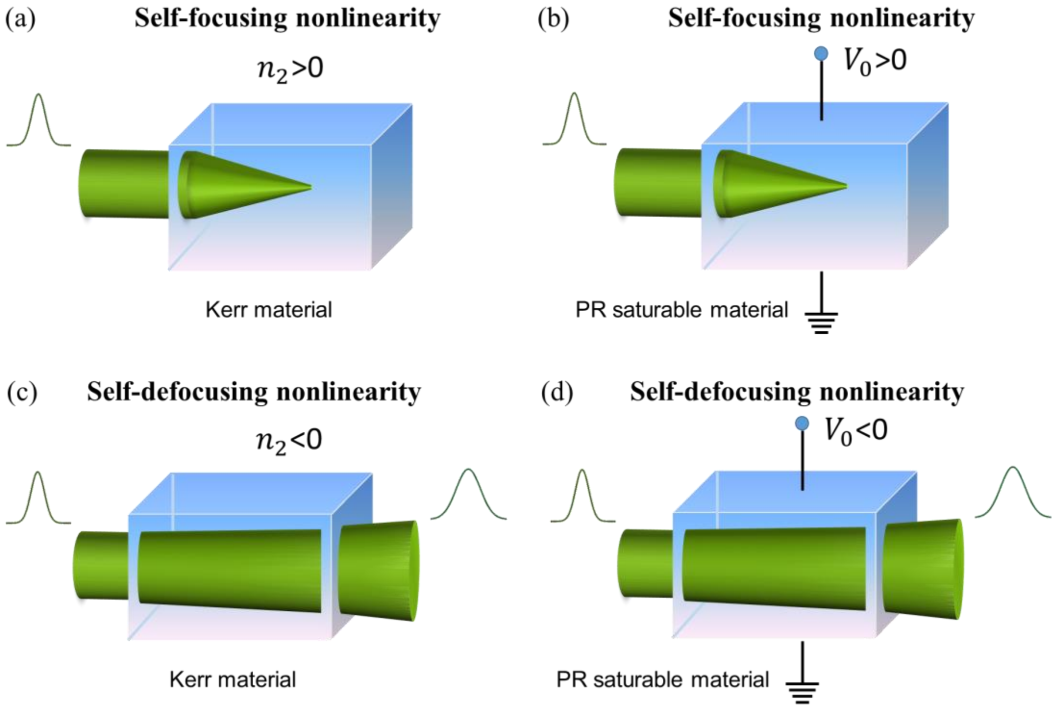

Figure 4.2: Pictorial representation of the effect of (a-b) self-focusing and (c-d) -defocusing nonlinearity on the dynamics of a Gaussian beam. The left-hand column shows (a) self-focusing and (c) -defocusing nonlinearity in a Kerr material. The right-hand column shows (b) self-focusing and (d) -defocusing nonlinearity in a biased PR saturable material.

We end by summarizing what have been discussed so far. In the previous sections, we introduced two types of nonlinear effects related to the optical intensity: PR saturable and Kerr nonlinearity. In both cases, the intensity-induced refractive index change is inserted into the NLPWE, modelling the nonlinear propagation of waves. We also pointed out that this nonlinear refractive index change affects the beam propagation through self-phase modulation. Additionally, we discussed self-focusing and –defocusing nonlinear effect associated with this modulation.

In the next sections, we will study the nonlinear propagation of Airy beams and Airy pulses. Notably, nonlinear Airy beams will be analyzed in PR saturable materials under both self-focusing and -defocusing nonlinearities. Airy pulses will be studied in Kerr materials (optical fibers) under both normal and anomalous dispersion. In the temporal domain, the nonlinear pulse evolution is described by the nonlinear Schrödinger equation analogous to the NLPWE in the spatial domain. Nevertheless, we will still introduce the Schrödinger equation in time before analyzing the nonlinear Airy pulse propagation. We will also prove that nonlinear phenomena are analogous in the spatial and temporal regimes.

4.4 Nonlinear dynamics of Airy beams

The propagation of optical beams in PR crystals has been recently a subject of intense research efforts. Compared with other nonlinear media such as those featured by a strong nonlinear Kerr response, PR media offer the possibility to observe self-action of a laser beam such as self-focusing and –defocusing effects, at very low power level (about μW). Kerr media would require much higher power level (about W) to observe such type of nonlinear processes. Moreover, since the electro-optical effect modifies the refractive index under optical illumination and in presence of an external electric field, another advantage offered by PR crystals is the possibility to switch the nonlinearity by means of simply reversing the external-applied electric field. Here, the propagation of a (1D) Airy beam in a nonlinear saturable PR medium is investigated. Under the slowly-varying amplitude approximation, the theoretical model to study the nonlinear propagation of an Airy beam is described by Eq. (4.24). For convenience, we transform this envelope equation into its normalized form. In dimensionless variables, Eq. (4.24) is reshaped as:

$$\frac{\partial \Psi}{\partial \xi} = \frac{i}{2}\frac{\partial^2 \Psi}{\partial s^2} - \frac{i\gamma}{1+|\Psi|^2}\Psi \tag{4.28}$$

where $\Psi(s,\xi) = A(s,\xi)/\sqrt{2\eta I_D}$ is the normalized complex amplitude of the optical field, η is the medium impedance, and I_D is the dark irradiance. $s = x/x_0$ and $\xi = z/(k_0 n_0 x_0^2)$ denote the normalized transverse and longitudinal coordinates, k_0 is the vacuum wave number, n_0 is the unperturbed extraordinary refractive index of the PR crystal, and x_0 is an arbitrary length scale. In Eq. (1.7), $\gamma = 0.5 k_0^2 n_0^4 x_0^2 r_{33} E_0$ represents the normalized nonlinear coefficient, in which E_0 is the external bias field, and r_{33} is the electro-optics coefficient for the extraordinarily polarized beams. The sign of the external-applied electric field determines the type of nonlinearity: $E_0 > 0$ (thus $\gamma > 0$) leads to a self-focusing nonlinearity, while $E_0 < 0$ (thus $\gamma < 0$) corresponds to a self-defocusing nonlinearity. When no bias field is present ($\gamma = 0$), the analysis is the same as in the linear regime. Although PR diffusion effect still exists, they can be neglected for a beam of sufficient large size.

4.4.a Linear Airy beam propagation

In the linear regime ($\gamma = 0$), the propagation of an Airy beam is studied by reducing Eq. (4.28) to the normalized paraxial differential equation of diffraction [13]:

$$\frac{\partial \Psi}{\partial \xi} = \frac{i}{2}\frac{\partial^2 \Psi}{\partial s^2} \tag{4.29}$$

Solutions to Eq. (4.29) can be found in the Fourier domain as:

$$\Psi(\xi, s) = \frac{1}{2\pi}\int_{-\infty}^{+\infty} \Phi(k_x, 0) e^{-\frac{i}{2}k_x{}^2\xi} e^{ik_x s} dk_x, \tag{4.30}$$

where $\Phi(k_x, 0) = \int_{-\infty}^{+\infty} \Psi(s,0) e^{-ik_x s} ds$ is the input spectrum. We consider a truncated Airy beam as the input: $\Psi(s,0) = \sqrt{I_0}\, Ai(s) e^{\alpha s}$, where $Ai(\cdot)$ denotes the Airy function, I_0 is the input peak intensity and $\alpha << 1$ is the truncation factor [13-14]. The spectrum associated to the finite Airy beam is:

$$\Phi\left(k_x,0\right)=\exp\left[i\frac{\left(k_x+ia\right)^3}{3}\right]\approx e^{-ak_x{}^2}e^{ik_x{}^3/3}. \tag{4.31}$$

One can infer from the above equation that this truncated Airy beam can be experimentally generated by Fourier transforming a Gaussian beam modulated with a cubic phase mask. The configuration corresponds to the case in which the Gaussian beam and the spectral mask are perfectly aligned, so that the linear Airy beam propagates along a parabolic trajectory [13-14]. However, further studies on this topic have shown that the evolution of an Airy beam can be easily altered by slightly 'misaligning' the Gaussian beam and the cubic phase structure in the Fourier space [54,62], thus inducing a ballistic propagation trajectory. This is realized by adding an offset to the phase modulation. In this case, the input condition in the k-space assumes the form:

$$\Phi\left(k_x,0\right)=\exp\left(-ak_x{}^2\right)\exp\left[i\frac{\left(k_x-\ \omega_m\right)^3}{3}\right] \tag{4.32}$$

where (ω_m) is the shift parameter of the cubic phase mask. The ballistic evolution of the Airy beam is analytically described by [62]:

$$\begin{gathered}\Psi\left(s,\xi\right)=\sqrt{I_0}\,f\left(s,\xi\right)Ai\left[s-\omega_m\xi-\frac{\xi^2}{4}+i\alpha\left(\xi+2\omega_m\right)\right]e^{i\omega_m s}\ ,\\ f\left(s,\xi\right)=\exp\left[\alpha s+is\frac{\xi}{2}+\xi\left(i\frac{\alpha^2}{2}-i\frac{\omega_m{}^2}{2}-2\alpha\omega_m\right)\right]\exp\left[-i\frac{\xi^3}{12}+\xi^2\left(-\frac{\alpha}{2}-i\frac{\omega_m}{2}\right)\right]\end{gathered} \tag{4.33}$$

From Eq. (4.33), it can be seen that the Airy beam accelerates following the ballistic trajectory $s = \omega_m\xi + \xi^2/4$, with the peak intensity I_0 appearing at $\xi = 2\omega_m$. Setting $\xi = 0$, the input beam $\Psi(s,0)$ reads:

$$\Psi\left(s,0\right)=\sqrt{I_0}\exp\left(\alpha s\right)Ai\left(s+i2\alpha\omega_m\right)e^{i\omega_m s}\ , \tag{4.34}$$

In Figs. 4.3(a1-c1) are the intensity distributions corresponding to three examples of numerically generated Airy beams in the linear regime ($\gamma = 0$), which are obtained by launching the input condition at $\omega_m = 0, -1$ and -6, and using $I_0 = 4.08$ and $\alpha = 0.08$ as parameter values.

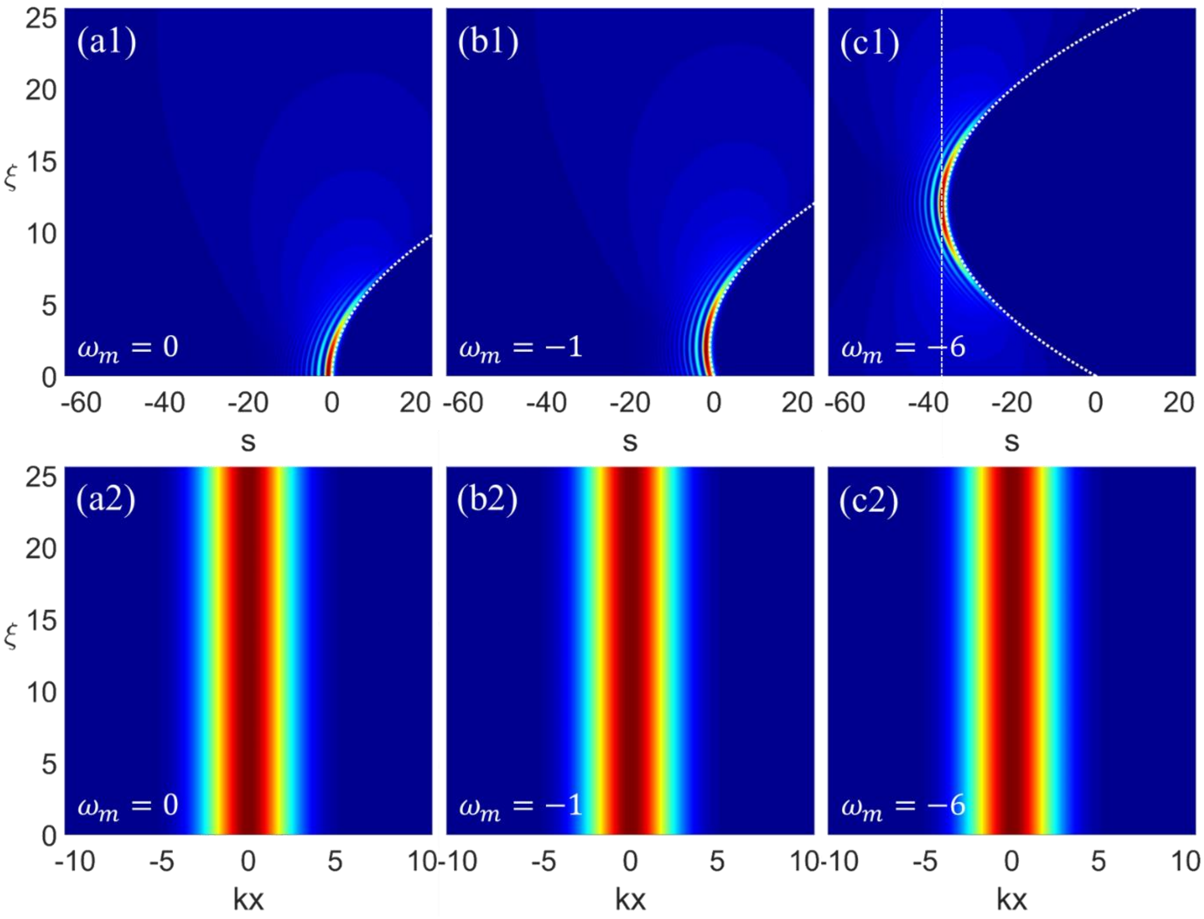

Figure 4.3: Linear propagation of an Airy beam. Intensity distributions of the Airy beam (a1-c1) and corresponding spectral intensity distributions (a2-c2), obtained for three different shifting values $\omega_m = 0, -1$ and -6 of the cubic phase mask, respectively.

In this study, simulations are carried out by means of the split-step Fourier method (SSFM) that is a common and efficient numerical algorithm to approximate nonlinear solutions of the paraxial differential equations [85]. Numerical solutions are found by applying separately diffraction and nonlinear response. In reality, both physical processes act simultaneously. However, for a very small distance, they can be approximately treated as independent effects.

As expected from the analytical solution in Eq. (4.34), the Airy beam evolves along a parabolic curve for ($\omega_m=0$) [Fig. 4.3(a)], while a shift of the cubic phase mask leads the Airy beam to move along a ballistic trajectory [Figs. 4.3(b, c)]. For such offset values, i.e., the peak intensities appear at $\xi = 0$, 2 and 12, respectively. Furthermore, the Fourier spectrum assumes a Gaussian profile for each offset value, maintaining unchanged for all propagation distances [Figs. 4.3(a2-c3)].

4.4.b Airy beams dynamics under a self-focusing nonlinearity

Once turning on the nonlinearity, Airy beams behave in a considerably different way. The intensity distributions in Figs. 4.4(a1-c1) illustrate the nonlinear propagation of Airy beams under a self-focusing ($\gamma > 0$) nonlinearity, obtained by launching the input condition $\Psi(s,0)$ at $\omega_m = 0, -1$ and -6, and setting $\gamma = \pm 2.72$, $I_0 = 4.08$ and $\alpha = 0.08$. The values of the latter three parameters are chosen in order to match the experimental conditions that will be discussed in detail in the next sections.

If no shift of the cubic phase mask ($\omega_m = 0$) is taken into con sideration, most energy of the Airy beam reshapes into an “off-shooting” soliton [77,139], thus destroying the self-accelerating properties [Fig. 4.4(a1)]. When a small shift is considered ($\omega_m = -1$), the acceleration property tends to survive [Fig. 4.4(b1)], and less energy of Airy beam is transfer to “off-shooting” solitons. At a larger shift value ($\omega_m = -6$), both the Airy profile and the accelerating properties are fully preserved, as shown in Fig. 4.4(c1). However, if the nonlinear evolution of the Airy beam is compared to the associated linear propagation [Fig. 4.4(a1)], the overall transverse width shrinks, while the propagation trajectory deviates slightly from the linear parabolic trajectory, rightwards along the transversal s directions. In addition, a nonlinear Airy beam under the action of a self-focusing nonlinearity accelerates faster than the linear Airy beam in the propagation region. This can be seen by noting the larger curvature of its trajectory with respect to the linear one.

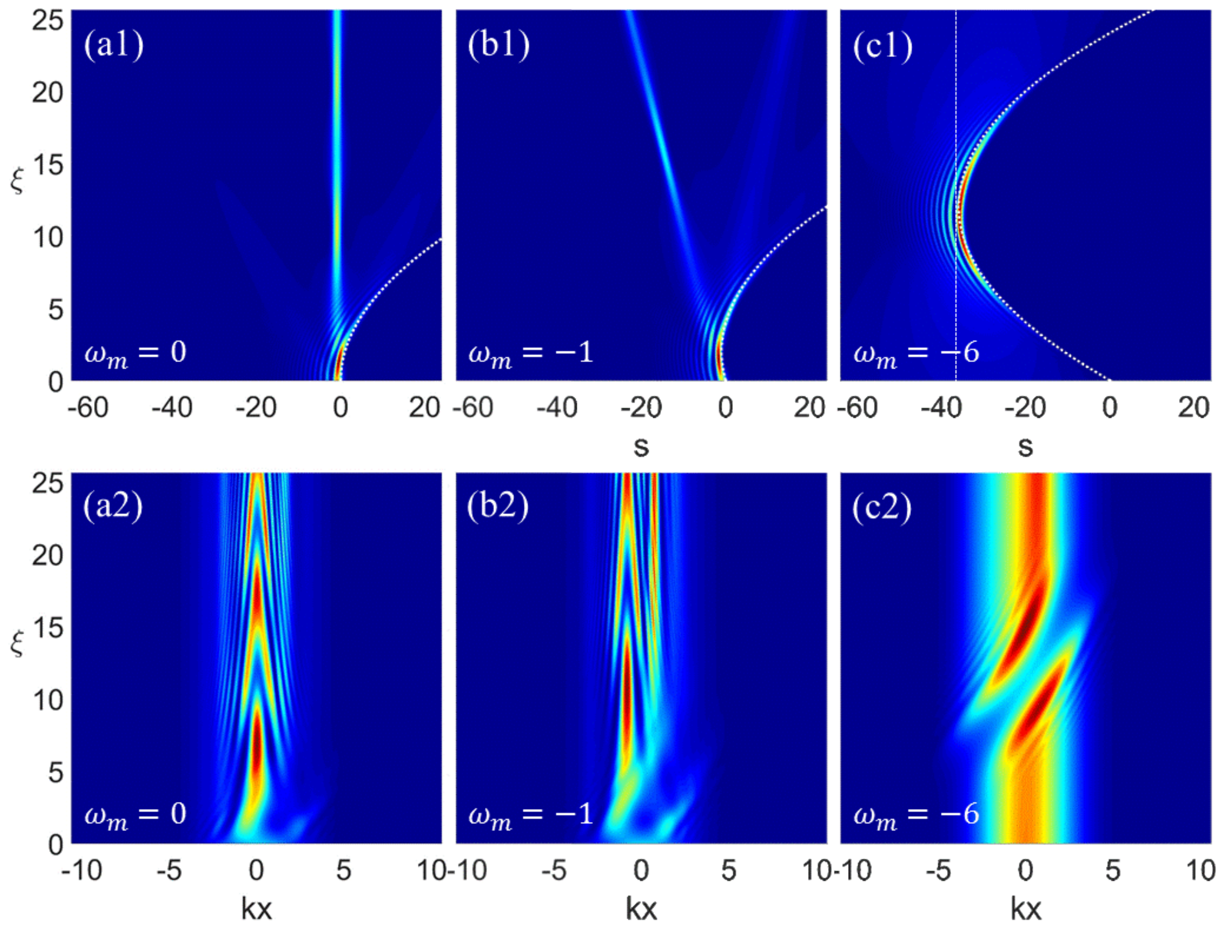

Figure 4.4: Nonlinear propagation of an Airy beam under a self-focusing nonlinearity. Intensity distributions of the Airy beam (a1-c1) and corresponding spectral intensity distributions (a2-c2), obtained for three different shifting values $\omega_m = 0$, -1 and -6 of the cubic phase mask, respectively.

We note that the scheme described in Fig. 4.4(c1) seems to be an efficient and easy way to maintain the acceleration property of a nonlinear Airy beam under a self-focusing nonlinearity. Several research works reported detailed simulation results indicating that when $\omega_m = 0$, even a weak self-focusing nonlinearity would affect the trajectory of the Airy beam [32,78,138]. On the contrary, our method shows that the acceleration can also be preserved under a self-focusing nonlinearity by simply shifting the center of the phase mask. A possible explanation can be that by shifting the mask, the peak intensity of the Airy beam moves far away from the input facet of the PR crystal, avoiding the soliton formation. Additionally, further elucidations on why an Airy beam can preserve its acceleration properties under a self-focusing nonlinearity can be also found by studying the evolution of nonlinear Airy beams in the Fourier regime.

As shown in Figs. 4.4(a2-c2), the spectra reshape completely from the initial linear Gaussian profile for each offset value ω_m. Considering $\omega_m = 0$ or -1, the spectra break into many parts, and the energy localizes at different positions along the propagation distance. Especially at a long distance ξ, the spectrum tends to have a Λ-shaped periodic structure, mainly because of the “off-shooting” solitons [Figs. 4.4(a2, b2)]. Particularly interesting is the case with $\omega_m = -6$, where the spectral content concentrates in a position-dependent self-shifting spectral notch, or negative defect [Fig. 4.4(c2)]. This negative defect appears at propagation distances ranging from $\xi = 7$ to 17, and most of the energy is transferred in the vicinity of it. Nonlinear spectral reshaping takes place near the location of peak beam intensity. Outside the spectral gap, the spectrum keeps a Gaussian distribution, due to the fact that in this region the beam intensity is low enough to make the influence of the nonlinearity weak or even negligible. It is worth noting that the spectral notches are noticeable even in the other two shifting cases. As shown in Figs. 4.4(a2, b2), the defects start forming when the Airy beam enters in the crystal, but the onset of self-trapped solitons interrupts their formation, thus affecting the acceleration properties.

4.4.c Dynamics of Airy beams under a self-defocusing nonlinearity

When reversing the external bias, the input beam $\Psi(s,0)$ experiences a self-defocusing nonlinearity ($\gamma > 0$). As shown in Figs. 4.5 (a1-c1), Airy beams under a self-defocusing nonlinearity perform much better than for the self-focusing case, due to the fact that most of the energy content supports their acceleration. For all shifting cases the acceleration properties are much better preserved, even when $\omega_m = 0$ [Fig. 4.5(a1)]. The beam widths tend to broaden slightly, when compared to the associated linear propagation. Similar to the self-focusing case, not only the beam width changes, but also the propagation trajectory differs slightly from the linear parabolic curve, which is more perceptible at $\omega_m = -6$. As shown in Fig. 4.5(c1), an Airy beam under self-defocusing nonlinearity tends to deviate leftwards along the *s* direction, with respect to the parabolic curve (dashed white line). It also preserves a reduced acceleration as inferred from the smaller curvature of its trajectory.

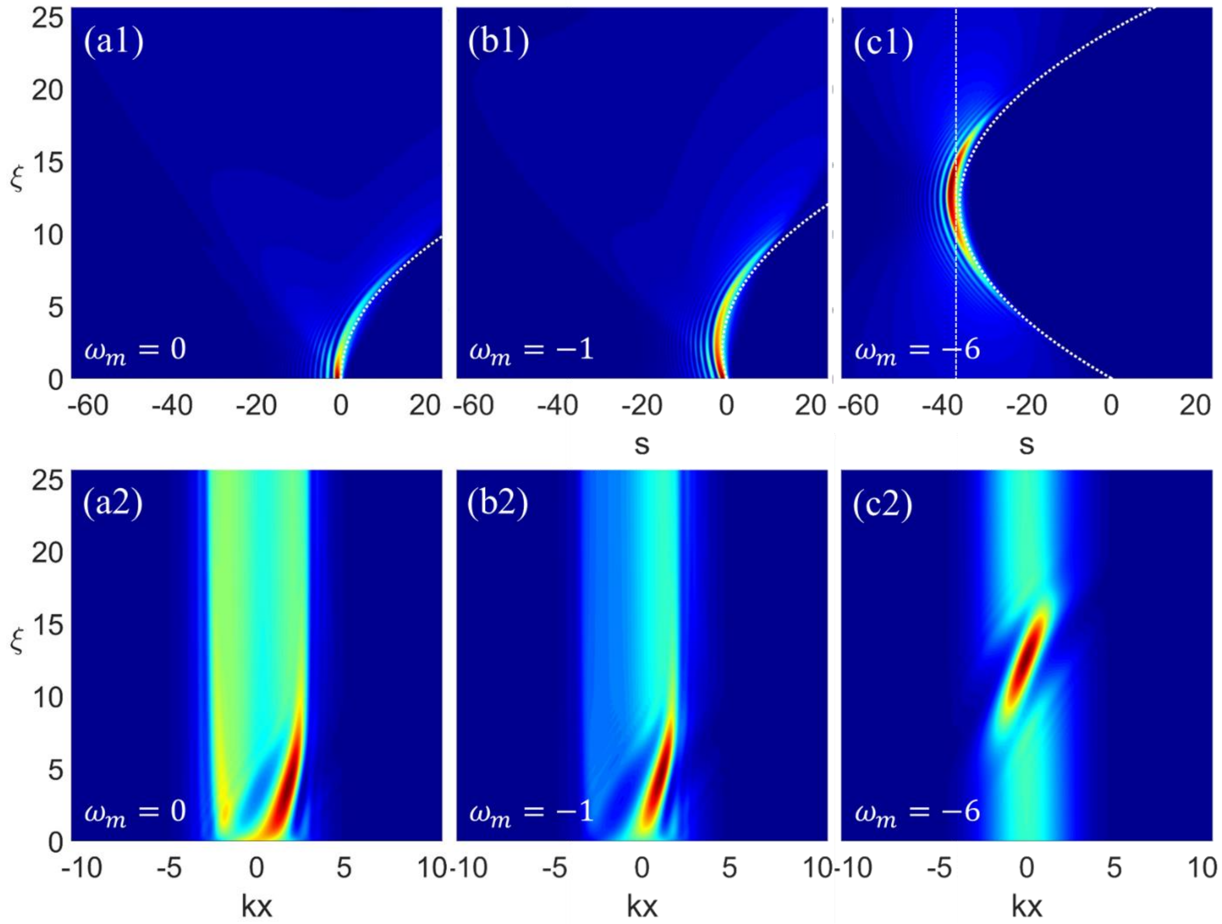

Figure 4.5: Nonlinear propagation of an Airy beam under a self-defocusing nonlinearity. Intensity distributions of the Airy beam (a1-c1) and corresponding spectral intensity distributions (a2-c2), obtained for three different shifting values ω_m = 0, -1 and -6 of the cubic phase mask, respectively.

In the Fourier space, the nonlinear spectra for each shifting parameter change dramatically, similarly to what happened in the self-focusing case. In the presence of a self-defocusing nonlinearity, the spectrum of nonlinear Airy beams reshapes into a position-dependent self-shifting spectral peak (positive defect). The positive defect forms wherever the beam intensity is sufficient strong. When the cubic mask is not shifted ($\omega_m = 0$), the positive defect appears from the input ($\xi = 0$) of the crystal up to $\xi = 7$, being a significant part of spectrum localized around this peak [Fig. 4.5(a2)]. Nevertheless, the defect shape is strongly deformed and stretched, indicating that part of the energy constituting the nonlinear Airy beam is dispersed and does not contribute to maintain its accelerating properties. By slightly shifting the cubic phase mask ($\omega_m = -1$), more and more spectral content tends to localize in the defect region from $\xi = 1$ to $\xi = 7$ [Fig. 4.5(a2)]. However, the positive defect is not fully-shaped yet, since some (small) part of the energy is still dispersed by the nonlinear Airy beam. At $\omega_m = -6$, the energy is completely transferred to the nonlinear Airy beam to preserve its acceleration properties, as shown in Fig. 4.5(c2). A full-shaped spectral peak appears at propagation distances ranging from $\xi = 7$ to $\xi = 15$ [Fig. 4.5(c2)], when most of the spectral content concentrates in the vicinity of the peak with a small surrounding ripple. Outside the positive defect the spectrum assumes a Gaussian profile. Similar to the self-focusing case, in this area the intensity is low enough to make nonlinearity weak or negligible. This spectral feature could find experimental applications such as frequency selection. Further simulations show that this spectrum reshaping is robust even in presence of high-level noise.

4.5 Spectral reshaping of nonlinear Airy beams

In the previous section, we have shown that when the cubic phase modulation is shifted to $\omega_m = -6$, Airy beams preserve their accelerating properties under both self-focusing and -defocusing nonlinearity in a saturable PR media. Since this is the most valuable result of our argument, hereafter we will only focus on studying these special cases of nonlinear Airy beams. For the sake of clarity, we review the spatial and spectral features of linear and nonlinear Airy beams with $\omega_m = -6$ and summarize the associated results in Fig 4.6. The beam dynamics for linear and nonlinear Airy beams appear to be similar [Figs. 4.6(a1-c1)], while the corresponding spectral features are quite different [Figs. 4.6(a2-c3)]. When comparing to the linear case [Fig. 4.6(a1)], the Airy beam exhibits a small shift towards positive s directions as well as a slightly width shrinking during propagation under a self-focusing nonlinearity

[Fig. 4.6(b1)]. On the other hand, a self-defocusing nonlinearity shifts the Airy beam towards negative *s* directions, while broadening the beam width [Fig. 4.6(c1)].

Such a transversal shift of nonlinear Airy beams along the *s* axis can be the reason of the spectral phase structures at ω_m = -6, see Figs. 4.6(a3-c3). The nonlinear phase distributions [Figs. 4.6(b3, c3)] are similar to the linear case [Fig. 4.6(a3)]. The main difference occurs along the defect regions. A self-focusing nonlinearity tends to tilt the phase stripes rightwards, while a self-defocusing nonlinearity tends to tilt them leftwards. According to the Fourier theory, these tiltings indicate that the nonlinear Airy beam in the real space can have a translation along either a positive (self-focusing) or negative (self-defocusing) *s* scale. In the linear Airy beam, the spectral stripes have not tilting and therefore any shift along *s* is induced. Although the spectral phase structures are similar in the linear and nonlinear regime, the corresponding intensity spectra have completely different characteristics. The spectrum of a finite-energy Airy beam in the linear regime assumes a Gaussian profile, which maintains unchanged for all propagation distances ξ, as shown in Fig. 4.6(a2). Conversely, the Gaussian spectrum reshapes into a position-dependent self-shifting spectral notch (peak) under a self-focusing (-defocusing) nonlinearity [Figs. 4.6(b2-c2)]. The spectral defects appear in the higher intensity region, and most of the spectral contents concentrate in the vicinity of defects. Outside these regions, since the beam intensity is sufficiently low, the spectra still keep their Gaussian distributions.

In the following, we will give a qualitatively explanation about the nonlinear propagation of Airy beams and their spectral reshaping, by numerically finding the self-accelerating eigenvalue solutions to Eq. (4.28). After that, we will provide an experimental demonstration of these nonlinear Airy beams in both the spatial and the spectral domains.

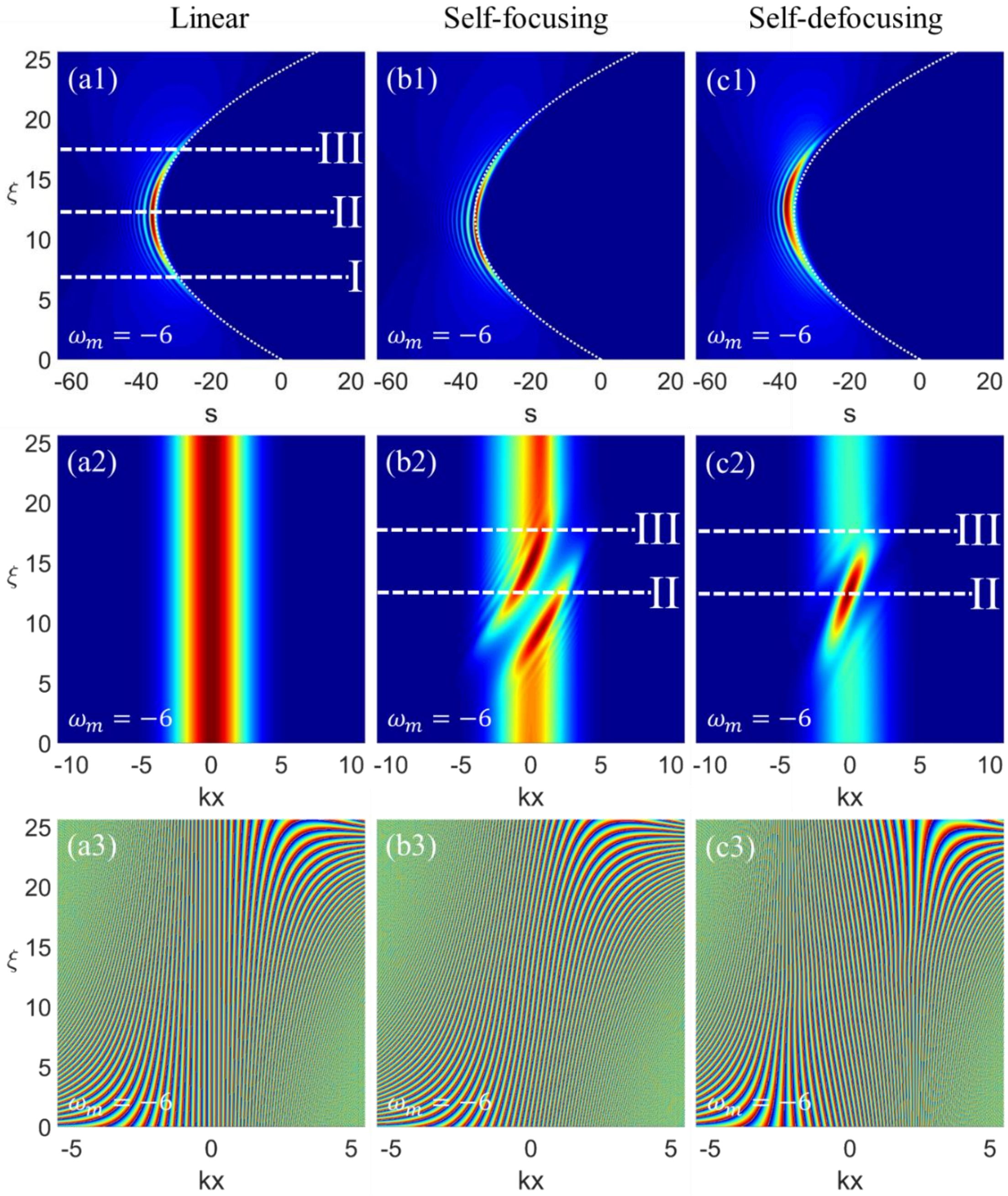

Figure 4.6: Spectral reshaping of nonlinear Airy beams. Top panels from left to right show the intensity distributions corresponding to a shifting parameter ω_m = -6 of the cubic phase mask under (a1) linear, (b1) nonlinear self-focusing, and (c2) nonlinear self-defocusing conditions. Middle and bottom panels from left to right show spectral (a2-c2) intensity and (a3-c3) phase distributions, corresponding to the intensity distributions in (a1-c1), respectively. Dashed white lines mark the (I) input, (II) the middle and (III) the output of the PR crystal.

4.6 Nonlinear self-accelerating modes

Based on our simulations, a finite-energy Airy beam can therefore preserve the accelerating propagation in the presence of a self-focusing and –defocusing nonlinearity in a saturable PR medium. This is accomplished by shifting the cubic phase mask in the Fourier space. As a consequence, the nonlinear Airy beam experiences a dramatic reshaping of its spectrum with respect to the linear regime. Yet, what is the mechanism behind these spectral features? In the literature, several works have demonstrated the existence of infinite-energy nonlinear self-accelerating modes for different nonlinear effects [31-32,138]. From these studies, one could infer that the acceleration persistence of a finite-energy Airy beam under a saturable nonlinearity might originate from the existence of ideal infinite-energy nonlinear self-accelerating modes. To solve such modes, we seek the solutions of Eq. (4.28) in the form:

$$\Psi\left(s,\xi\right)=u\left(s-h\frac{\xi^2}{2}\right)\exp\left(ih^2\frac{\xi^3}{6}+ih\xi s-ish^2\frac{\xi^3}{2}\right), \tag{4.35}$$

where h is the rate of acceleration and $u(s)$ is a real function. By defining $\varsigma=s-h\xi^2/2$, Eq. (4.35) is converted to:

$$\frac{\partial\Psi}{\partial\xi}-h\xi\frac{\partial\Psi}{\partial\varsigma}=\frac{i}{2}\frac{\partial^2\Psi}{\partial\varsigma^2}-\frac{i\gamma}{1+\left|\Psi\right|^2}\Psi. \tag{4.36}$$

Since we are concerned with solutions that accelerates along a parabolic trajectory, the rate of acceleration h is set to 1/2. Then Eq. (4.36) becomes:

$$\frac{d^2u}{d\varsigma^2}-u\varsigma-\frac{2\gamma}{1+u^2}u=0. \tag{4.37}$$

The above equation can be easily solved numerically. We note that for $\varsigma\to\infty$, the amplitude of u tends to become small, so to make the nonlinear term negligible. In this case, the boundary condition for $\varsigma\to\infty$ can be obtained from its linear solution ($\gamma = 0$), which follows an Airy function. The other values can be integrated from the initial condition. In addition, an α degree of freedom is also introduced in order to obtain a family of solutions for Eq.(4.37). This α parameter corresponds to nonlinear mode amplitudes. Therefore, we solve numerically

Eq.(4.37) through setting the asymptotic values as $u(\varsigma) = \alpha Ai(\varsigma)$ and $u'(\varsigma) = \alpha Ai'(\varsigma)$ for $\varsigma \to \infty$, to obtain a family of solutions with different peak intensities.

A comparison between the linear infinite-energy Airy beam and the typical nonlinear modes is shown in Fig. 4.7. A self-focusing (-defocusing) nonlinearity brings the main lobe of the nonlinear mode to slightly shrink (broaden) when compared to the ideal Airy beam [Figs. 4.7(a, d)]. These results are in a good agreement with numerical beam propagation, see section 4.3.

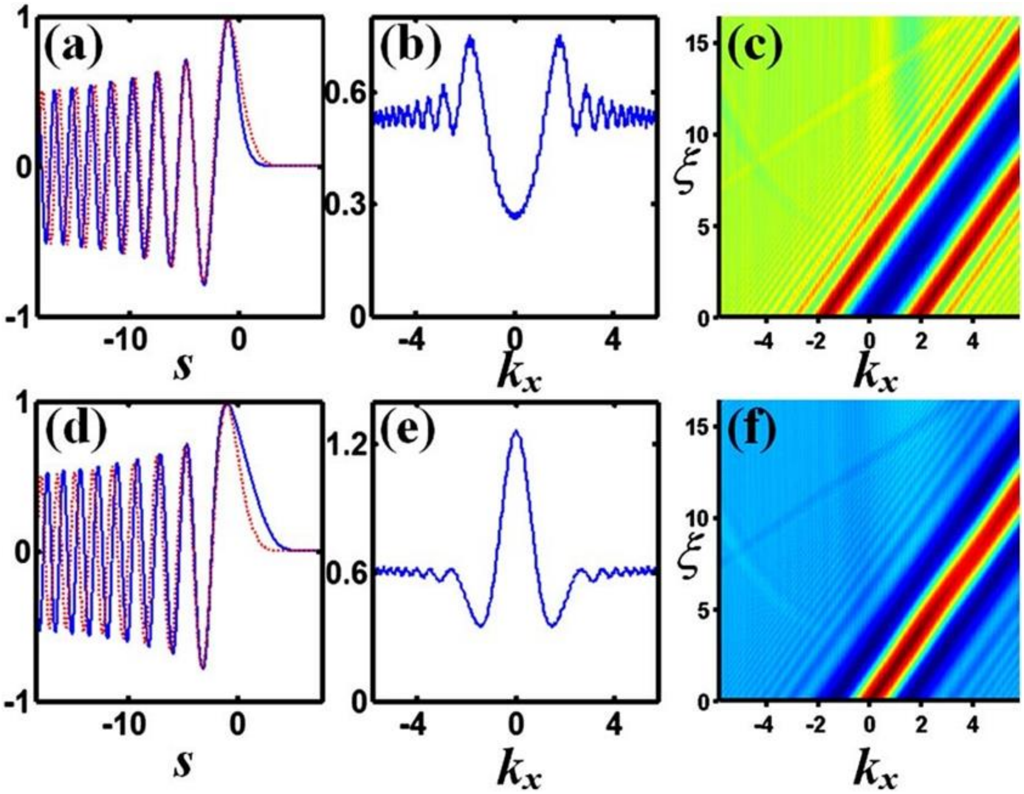

Figure 4.7: Nonlinear self-accelerating solutions under a saturable PR nonlinearity. (a) and (d) self-accelerating modes (blue solid curve) under self-focusing and -defocusing nonlinearities, respectively. The red dashed curves correspond to an ideal, linear Airy beam. (b) and (e) spectra corresponding to (a) and (d). (c) and (f) spectral distributions of the self-accelerating modes in (a) and (d), respectively.

In Fourier space, the corresponding spectra plotted in Figs. 4.7(b, e) present the formation of a spectral notch or peak defect similar to the spectral evolution in Figs. 4.4(c2) and 4.5(c2). In addition, the spectrum in Fig. 4.7(b) shows a more noticeable ripple outside the range where the spectral defect appears with respect to the spectral peak in Fig. 4.7(e), which confirms our previous numerical simulations. More interestingly, the power spectrum distribution [Figs. 4.7(c, f)] undergoes a linear shift during the beam propagation for both type of nonlinearities. This linear shift can be estimated analytically by Fourier transforming the nonlinear modes. To determinate it, let us start from:

$$\Psi\left(\varsigma,\xi\right)=u\left(\varsigma\right)\exp\left(ih^{2}\frac{\xi^{3}}{6}+ih\xi\varsigma\right). \tag{4.38}$$

By performing the Fourier transform of Eq. (4.38), the spectral profile can be expressed as:

$$\Phi\left(\omega,\xi\right)=\mathcal{F}\left[\Psi\left(\varsigma,\xi\right)\right]\left(\omega,\xi\right)=\exp\left(ih^{2}\frac{\xi^{3}}{6}\right)U\left(\omega-h\xi\right), \tag{4.39}$$

where $U(\omega)=\mathcal{F}[\mathrm{u}(\varsigma)](\omega)$ and $F(\cdot)$ stands for the Fourier transform. The power spectrum $I_{\Phi}(\omega, \xi) = |\mathrm{U}(\omega - h\xi)|^{2}$ demonstrates that the spectra have a linear shift at a rate given by, $h=1/2$ thus proving the spectral features in Figs. 4.7(c, f).

Our numerical investigations point out to the fact that the nonlinear modes under a saturable PR nonlinearity have both real and spectral characteristics similar to nonlinear Airy beam propagating in Figs. 4.4(c1) and 4.5(c1). In particular, their spectral features indicate that Airy beams are able to evolve into nonlinear self-acceleration modes under the action of self-focusing and –defocusing nonlinearities, thus preserving their acceleration (Figs. 4.4(c2) and 4.5(c2)). Differently from other approaches [149], our physical picture offers a new way to test the formation of nonlinear modes. The initial shift of a cubic phase mask is crucial in this framework because, by delivering the peak intensity inside the PR medium, it allows the Airy beam to evolve into a nonlinear mode, thus fully-maintaining its self-accelerating properties. Without shifting, the peak intensity appears at the input of the crystal, causing the strong nonlinearity to destroy the beam properties.

4.7 Experimental observation

To observe experimentally the phenomena obtained numerically, we use a set-up that is shown in Fig.4.8. A truncated Airy beam is created by phase-modulating a linearly-polarized Gaussian beam ($\lambda = 532$ nm) through a 1D cubic phase mask, uploaded into a spatial light modulator (SLM). The SLM is placed at the focal plane of a cylinder lens ($f = 40$ mm) which performs a Fourier transform. The polarization of the electric field is oriented along the x-direction, parallel to the optical c-axis of a biased Strontium Borate Nitrate (SBN: 60) PR crystal (5×5(c)×10mm). After the generation, the finite-energy Airy beam is coupled into the SBN crystal, and both output intensity and spectral profiles are recorded by CCD cameras.

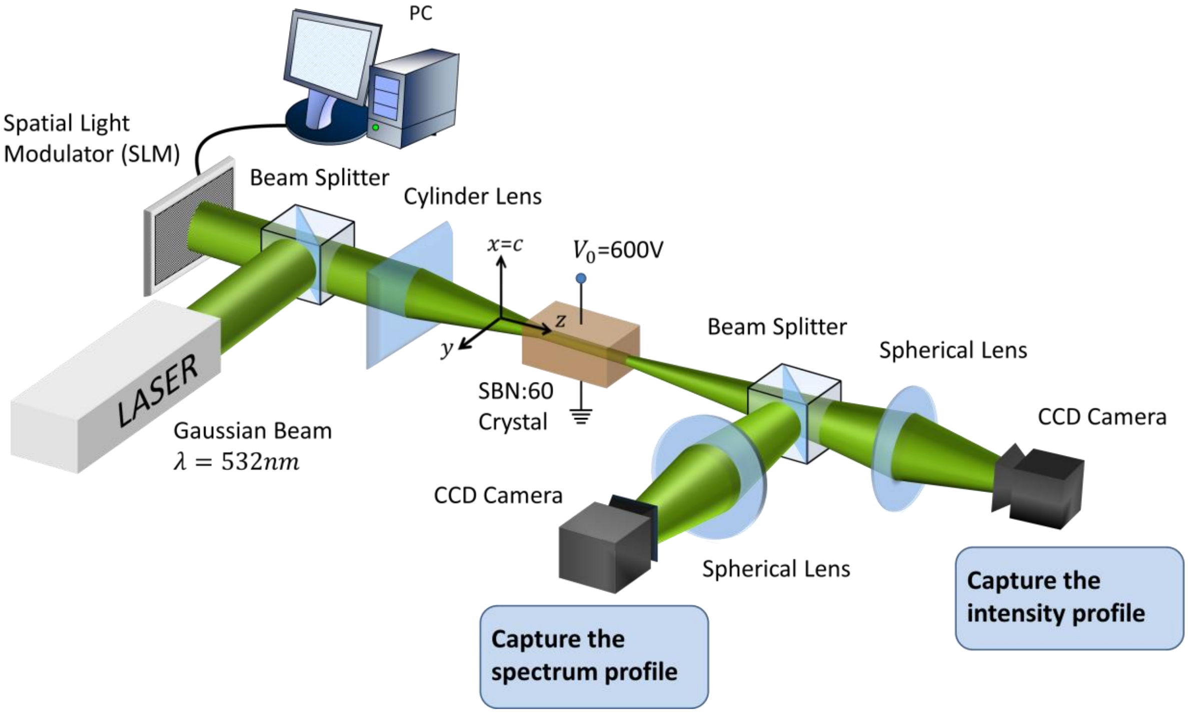

Figure 4.8: Experimental setup for measuring the nonlinear propagation of a finite-energy Airy beam in a saturable PR medium (SBN: 60) underboth a self-focusing and -defocusing nonlinearity.

To obtain a nonlinear coefficient $|\gamma| = 2.72$, a static voltage of 600 V ($|E| = 1.2\text{x}10^5$ V/m) is applied to the PR crystal along the optical c-axis. The absolute values of the bias voltage is kept fixed throughout the experimental measurement. The detection is accomplished by capturing the Airy beam patterns and the *k*-space spectra by means of two imaging systems composed of two spherical lenses and two CCD cameras. The cubic phase mask is ‘electronically’ shifted through the graphic interface of the software driving the SLM.

4.7.a Peak intensity of the Airy beam at the middle of the SBN crystal

In the first set of measurements, the experiments have been carried out by conveniently shifting the cubic phase mask with the purpose of bringing the peak intensity into the middle of the crystal along the propagation direction ξ, as indicated by the dashed white line II in Fig. 4.6(a1), where the other two dashed white lines, I and III, mark the spectral defect area localized in the region $\xi \approx 7$ to 17. Outside this range, the propagation can be basically considered linear and, therefore, of lower interest. With this in mind, the cubic phase mask has been scaled intentionally in order to match the concerned area with the longitudinal scale of the crystal.

Figure 4.9 presents the Airy beam patterns imaged at the output facet of the SBN crystal. In the linear regime, the output intensity pattern has a main hump localized at the same transverse position of te initial input beam [Fig. 4.9(a1)]. As in Fig 4.3(c1), and even in Fig. 4.7, this vertical line marks the transversal position of the peak intensity along the *s* direction for the linear Airy beam. In the presence of a self-focusing nonlinearity, Fig. 4.9(b1) shows an output pattern whose main hump is not self-trapped and, therefore, keeps its self-accelerating property. However, the main lobe shrinks and shifts to the right when compared to the linear case. Conversely, a self-defocusing nonlinearity expands the main hump of the output pattern and causes a leftwards shift with respect to the linear output [Fig. 4.9(c1)]. In the Fourier regime, the corresponding imaged *k*-spectra present a Gaussian profile for the linear Airy beam [Fig. 4.9(a2)], and the appearance of a spectral gap and peak defect under both self-focusing and -defocusing nonlinearities, respectively [Figs. 4.9(b2, c2)]. These spectral defects, whose positons are indicated by the downward pointing red arrows, reside at the right side of the *k*-space center.

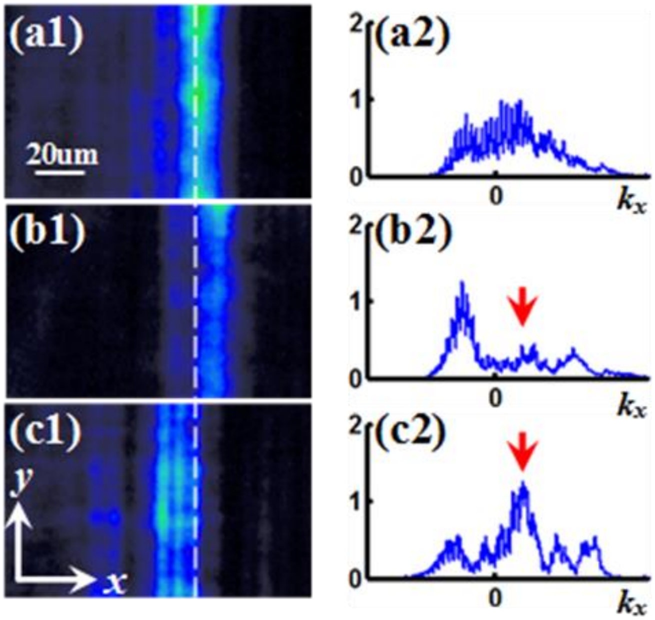

Figure 4.9: Experimental observations of Airy beams propagating in a biased PR crystal, after setting its peak intensity at the middle of the crystal. From top to bottom the panels correspond to beam propagation under (a) linear, nonlinear (b) self-focusing and (c) -defocusing conditions. (a1-c1) show the imagined Airy beam patterns at the output of the crystal. (a2-c2) show the spectra at the outputs in (a1-c1). The red arrows in (a2-c2) indicate the position of the spectral defects in the *k*-space.

4.7.b Peak intensity of the Airy beam at the output of the SBN crystal

In a second set of measurements, with the goal of further confirming the first observation of this spectral defect, we shifted the output facet of the crystal along the ξ-direction to the peak intensity position indicated by the white dashed line II in Fig. 4.6(a1). Output Airy beam patterns in Figs. 4.10(a1-c1) present a similar behavior as those shown in Figs. 4.9(a1-c1). In the *k*-space, the Gaussian profile is still kept for the linear regime [Fig. 4.10(a2)], while under nonlinear conditions, the spectral defect shifts to the center of the Fourier space [Fig. 4.10(b2) and 4.10(c2)]. This nonlinear behavior is expected because the beam experiences a half-shortened propagation distance when compared to the first set of measurements.

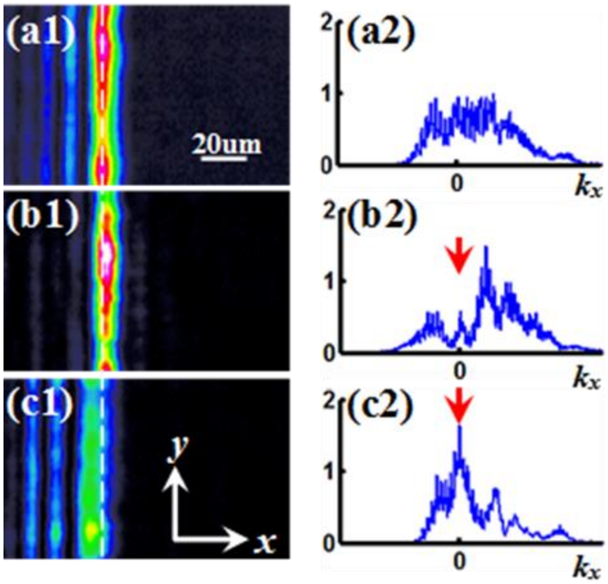

Figure 4.10: Experimental observations of Airy beams propagating in a biased PR crystal by setting its peak intensity at the output of the crystal. From top to bottom the panels correspond to beam propagation under (a) linear, nonlinear (b) self-focusing and (c) -defocusing conditions. (a1-c1) show the imagined Airy beam patterns at the output of the crystal. (a2-c2) show the spectra at the outputs, corresponding to (a1-c1). The red arrows in (a2-c2) indicate the position of the spectral defects in the *k*-space.

In conclusion, the experimental observations presented in Figs. 4.9 and 4.10 are in a good agreement with the numerical simulations discussed in Figs. 4.6(a1-c1) and Figs. 4.6(a2-c2).

4.8 Nonlinear Schrödinger equation

From now on, the chapter will be devoted to describe the nonlinear propagation of optical Airy pulses. In temporal domain, the evolution of optical pulses in the nonlinear regime is descripted by the nonlinear Schrödinger equation (NLSE) [85]. Our interest in studying the properties of nonlinear Airy pulses is inspired by the fact that the NLSE describing pulse propagation in time and the NLPWE describing beam evolution in space are featured by a similar mathematical form. Because of this analogy, Airy pulses in the nonlinear regime are expected to behave similarly to nonlinear Airy beams in PR materials. Under a Kerr nonlinearity, Airy pulses tend to shed solitons, thus affecting their acceleration properties [27]. Such a self-accelerating propagation could be preserved by applying a similar approach to that proposed for nonlinear Airy beams in the spatial domain. In light of these motivations, we will investigate the nonlinear Airy pulse propagation. We will restrict our study to fiber optics where the NLSE can be applied, even though Airy pulses could as well be investigated in bulk nonlinear media. More specifically, we will study here the dynamics of an Airy pulse under the combined influence of both dispersion and nonlinear effects in a single-mode optical fiber. A detailed derivation of the NLSE in a single mode nonlinear optical fiber can be found in Ref. [85]. Based on this derivation, the NLSE assumes the form:

$$\frac{\partial A}{\partial z}+\frac{\beta_1}{2}\frac{\partial A}{\partial t}+\frac{i\beta_2}{2}\frac{\partial^2 A}{\partial t^2}-\frac{\beta_3}{2}\frac{\partial^3 A}{\partial t^3}+\frac{\hat{\alpha}}{2}A-i\gamma\left|A\right|^2 A=0. \tag{4.40}$$

In Eq. (4.40) $A(z,t)$ is the pulse envelope, γ is the Kerr nonlinear parameter, $\hat{\alpha}$ is the fiber losses parameter. $\beta_1 = 1/v_g$, β_2 and β_3 are the first-, second-and third-order dispersion coefficients, in which v_g is the group velocity. Finally, z and t are the physical distance and time, respectively.

4.9 Nonlinear propagation of Gaussian pulses

In many practical applications, third-order dispersion can be generally neglected and Eq. (4.40) can be simplified by including the second order dispersion β_2 only. Additionally, for short length fibers, the losses are not generally taken into account. Under these conditions, the pulse propagation in the presence of a Kerr effect can be described by the normalized nonlinear Schrödinger equation (NNLSE):

$$\frac{\partial\varphi}{\partial\xi} = -\frac{i}{2}\operatorname{sgn}\left(\beta_2\right)\frac{\partial^2\varphi}{\partial T^2} + i\eta\left|\varphi\right|^2\varphi. \tag{4.41}$$

where $\varphi\left(\xi,T\right) = A\left(\xi,T\right)$ is the pulse envelope in normalized units $\xi = z\,|\,\beta_2\,|\,/t_0{}^2$ and $T = (t - z\,/\,v_g)\,/\,t_0$ are the normalized distance and time in the framework of the group velocity v_g. Here, z and t are the physical distance and time, and t_0 is a time scaling factor. The symbol *sgn*(·) is the sign operator, while $\eta = \gamma\,/\,(t_0{}^2\,|\,\beta_2\,|)$ is the normalized nonlinear coefficient. In the Eq. (4.41), the first term on the right-hand side of the NNLSE accounts for the group velocity dispersion (GVD), while the second term relates to the Kerr nonlinearity.

4.9.a Temporal self-phase modulation

As analyzed previously in space, we assume the single-mode fiber to be weakly dispersive. Therefore, we neglect the GVD term and consider solely the Kerr nonlinearity. Eq. (4.41) reduces to:

$$\frac{\partial\varphi}{\partial\xi} = i\eta\left|\varphi\right|^2\varphi. \tag{4.42}$$

Defining $\varphi(T,\xi) = \left|\varphi(T,\xi)\right|\exp\left[i\phi_{NL}(T,\xi)\right]$, Eq. (4.41) separates in the real and imaginary part as:

$$\begin{aligned}\frac{\partial\left|\varphi(T,\xi)\right|}{\partial\xi} &= 0\\ \frac{\partial\phi_{NL}}{\partial\xi} &= \eta\left|\varphi(T,\xi)\right|^2\end{aligned} \tag{4.43}$$

The solution to Eq. (4.43) is found to be:

$$\varphi(T,\xi) = \left|\varphi(0,T)\right|\exp\left(i\eta\left|\varphi(T,0)\right|^2\xi\right) \tag{4.44}$$

Similar to the spatial case, the Kerr nonlinearity introduces an intensity-dependence phase shift in the optical pulse due to self-phase modulation (SPM). Such nonlinear phase shift increases with distance. Its amplitude is not affected by SPM, hence the pulse-shape is maintained. Additionally, because of the time-dependence of $\phi_{NL}\left(T,\xi\right)$, a spectral change is induced by SPM. Such spectral change implies that the instantaneous frequency across the optical pulse deviates from the carrier frequency ω_0 (temporal chirping). The instantaneous frequency change is given by:

$$\Delta\omega\left(T,\xi\right)=-\frac{\partial\phi_{NL}}{\partial T}=-\eta\xi\frac{\partial\left|\varphi\left(T,0\right)\right|^2}{\partial T} \tag{4.45}$$

Fig. 4.11 shows the SPM effect on a Gaussian pulse propagating in a nonlinear optical fiber (which is featured by a positive Kerr nonlinearity). Due to SPM, the instantaneous frequency of the Gaussian pulse changes following the slope of the optical intensity. Since in fiber $n_2 > 0$ ($\eta > 0$), the frequency of the trailing edge (B) is increased, whereas the frequency in the leading edge (R) is decreased. Near the peak intensity, the instantaneous frequency experiences linear increasing (up-chirping).

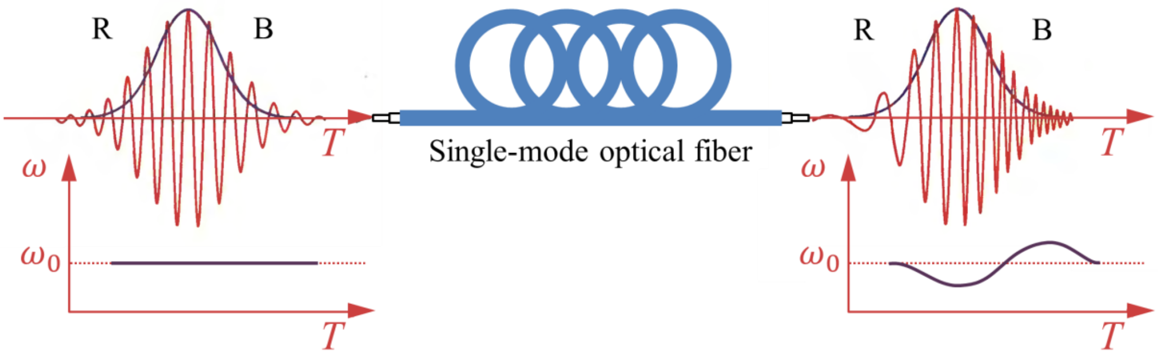

Figure 4.11: Scheme of self-phase modulation of a Gaussian pulse propagating in a single mode optical fiber.

In general, dispersion cannot be ignored, so SPM and dispersion must be considered together. In the normal dispersion regime (recalling that the Kerr response is positive in fibers), SPM accelerates the spreading of the pulse duration. Under the condition of anomalous dispersion, SPM may compensate dispersion and under certain conditions, an optical pulse propagates without changing its temporal profile, therefore forming a so-called temporal soliton [130].

4.9.b Nonlinear propagation of a Gaussian pulse

Similar to an Airy beam in the spatial domain, the spectrum associated to a finite-energy Airy pulse consists of a Gaussian amplitude chirped by cubic phase, in the form [1]:

$$\Phi\left(v\right) \approx exp(-\alpha v^2)exp\left[i\frac{v^3}{3}\right]. \tag{4.46}$$

The term $exp(-\alpha v^2)$ is the amplitude, while $exp(iv^3/3)$ is the cubic phase. Here $v = \omega/\omega_s$ is the normalized angular frequency, in which ω is the angular frequency, $\omega_s = 1/t_0$ is a scale factor, and α determines the bandwidth of the pulse.

It is instructive, before investigating the nonlinear dynamics of Airy pulses, to take a look at the nonlinear propagation of an optical Gaussian pulse under anomalous ($\beta_2 < 0$) and normal ($\beta_2 > 0$) dispersion. In particular, the self-phase modulation (SPM) of Gaussian pulse is investigated by considering an input chirped pulse whose spectrum is given by:

$$\Phi\left(v\right) = exp(-\alpha v^2)exp[isgn(\beta_2)v^2], \tag{4.47}$$

Likewise, α determines the bandwidth of the Gaussian pulse and $v = \omega/\omega_s$ is the normalized angular frequency, in which ω is the original angular frequency and ω_s is a scaling factor. The term $exp(-\alpha v^2)$ is the amplitude, while $exp[i\,\mathrm{sgn}(\beta_2)v^2]$ is the quadratic phase modulation. The numerical simulations, modelling the linear and nonlinear propagations under the effect of either anomalous or normal dispersion, are shown in the Fig. 4.12. For the linear propagation case ($\gamma = 0$), the temporal evolution of chirped Gaussian pulses appears to be the same under both the anomalous and the normal dispersion, given that an identical absolute value of β_2 is used [Fig. 4.12(a)].

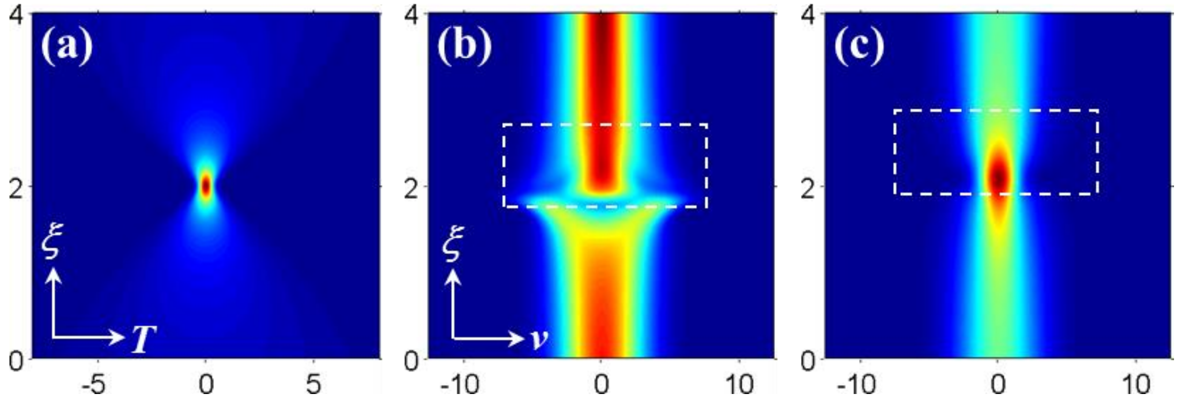

Figure 4.12: Self-phase modulation of a Gaussian pulse. (a) Intensity distribution under linear propagation. (b, c) Spectra in the case of nonlinear propagation under (b) an anomalous and (c) a normal dispersion using the same input conditions as in (a).

The maximum peak power (MPP) for these pulses appears inside the fibers at $\xi = 2$, due to the combined effect of chirp and dispersion. Upon a mild Kerr effect, the spectra reshape dramatically near the MPP location of the linear case. At $\beta_2 < 0$, the spectrum tends to transfer energy from the center part of frequency to the outer one [Fig. 4.12(b)], and a negative defect appears close to $\xi = 2$. At $\beta_2 > 0$, the spectral energy flow is in the opposite direction and most spectrum concentrates instead near the central frequency [Fig. 4.12(c)], so reshaping into a positive defect around $\xi = 2$.

4.10 Nonlinear propagation of optical Airy pulses

Keeping in mind the nonlinear behavior of a Gaussian pulse, we now study the SPM of Airy pulses under both normal and anomalous dispersion. At first, we start from the linear dynamics $(\eta = 0)$, and then we consider the nonlinear propagation of Airy pulses.

4.10.a Linear Airy pulse propagation

In the linear regime ($\eta = 0$), the normalized Schrödinger equation is expressed as:

$$\frac{\partial \varphi}{\partial \xi} = -\frac{i}{2}\operatorname{sgn}\left(\beta_2\right)\frac{\partial^2 \varphi}{\partial T^2}. \tag{4.48}$$

A solution to Eq. (4.48) can be found in the Fourier domain as:

$$\varphi(\xi,T)=\frac{1}{2\pi}\int_{-\infty}^{+\infty}\Phi(v,0)e^{\frac{i}{2}\mathrm{sgn}(\beta_2)v^2\xi}e^{ivT}dv, \tag{4.49}$$

in which $\Phi(v,0)=\int_{-\infty}^{+\infty}\varphi(T,0)e^{-ivT}dT$ is the Fourier transform of the input pulse. More specifically, we study the linear dynamics of an Airy pulse by considering a more general input condition:

$$\Phi(v)=exp(-\alpha v^2)exp\left[i\frac{(v-v_m)^3}{3}\right]. \tag{4.50}$$

The input spectrum is featured by a Gaussian amplitude $exp(-\alpha v^2)$, modulated by a cubic phase structure $exp[-i(v-v_m)^3/3]$. The parameter v_m introduces an offset to the phase modulation. Using this initial condition, the solution to Eq. (4.49) is given by:

$$\varphi(\xi,T)=\frac{1}{2\pi}\int_{-\infty}^{+\infty}e^{-\alpha v^2}e^{-i\frac{(v-v_m)^3}{3}}e^{\frac{i}{2}\mathrm{sgn}(\beta_2)v^2\xi}e^{ivT}dv. \tag{4.51}$$

Solving Eq. (4.51), the linear pulse propagation is obtained as:

$$\begin{aligned}\varphi(\xi,T)=\sqrt{2\pi}\,Ai\left[T-\varsigma^2/4+\alpha^2+v_m^2-i\,\mathrm{sgn}(\beta_2)\alpha\varsigma\right]&\\ \times\exp\left(iv_m^3/3\right)\exp\left(\alpha T-i\,\mathrm{sgn}(\beta_2)\varsigma T/2\right)&\\ \times\exp\left[i2\left(i\alpha+\mathrm{sgn}(\beta_2)\varsigma/2\right)^3/3-iv_m^2\left(i\alpha+\mathrm{sgn}(\beta_2)\varsigma/2\right)\right]&\end{aligned}\quad, \tag{4.52}$$

where $\varsigma=\xi+2v_m/sgn(\beta_2)$, and $Ai(\cdot)$ is the Airy function. The Airy pulse follows a parabolic time trajectory given by:

$$T_p=\varsigma^2/4-v_m^2-\alpha^2 \tag{4.53}$$

The MPP is located at $\xi=-2v_m/sgn(\beta_2)$. By setting $v_m=0$, the peak power appears at $\xi=0$, and the linear dynamics of the Airy pulse is analogous to that in the spatial domain [13,54]. Introducing a shift to the cubic phase structure, the linear dynamics of the Airy pulse can be delayed or advanced [54,62]. We purposely move the MPP inside the fiber at $\xi = 8$, which can be achieved by setting $v_m = -4sgn(\beta_2)$, since in this condition, the acceleration properties of Airy pulses can be preserved.

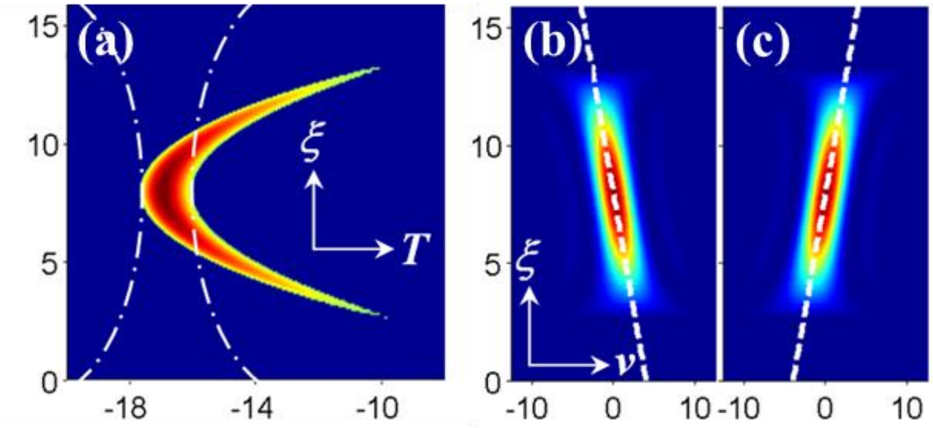

Figure 4.13: Linear propagation of Airy pulses in optical fiber. (a) intensity distribution of the filtered main hump obtained by discarding the sub-lobes of the linear Airy pulse. (b) and (c) spectral distributions corresponding to the main hump under (b) anomalous and (c) normal dispersion.

In Fig. 4.13(a), we plot the main hump evolution of the Airy pulse descripted by Eq. (4.52). The intensity distribution is obtained by discarding the sub-lobes from the Airy pulse, and by leaving only the main hump whose instantaneous power is larger than half of the MPP. Taking into consideration the spectral components corresponding to the main hump in Fig. 4.13(a), we can find that different frequencies dominate different propagation distances [Figs. 4.13(b, c)]. This spectral feature is analogous to what was observed in Chapter 1 for the spatial domain case. More specifically, for each propagation distance ξ in Fig. 4.13(a), we can simply treat the main lobe of the Airy pulse as a chirped Gaussian pulse, as shown schematically by two white dashed dot lines in Fig. 4.13(a). Under the effect of an anomalous dispersion, lower frequencies are responsible for the initial pulse evolution and higher frequency for the subsequent propagations, which can be seen from Fig. 4.13(b). On the other hand, in the presence of a normal dispersion, higher frequencies are responsible for the initial pulse evolution and lower frequency for the subsequent propagations [Fig. 4.13(c)]. Such a frequency change is linear with the distance ξ (dotted white lines in Figs. 4.13(b, c)).

To estimate quantitatively these spectral frequencies, we can apply the phase gradient method in the temporal domain, which is the temporal counterpart to the spatial phase gradient method described in Chapter 1. From Eq. (4.51):

$$\mu(\nu,\xi) = -\frac{(\nu-\nu_m)^3}{3} + \frac{1}{2}\operatorname{sgn}(\beta_2)\nu^2\xi \tag{4.54}$$

The phase gradient is related to the time as follows:

$$T = -\frac{\partial\mu(\nu,\xi)}{\partial\nu} = -(\nu-\nu_m)^2 + \operatorname{sgn}(\beta_2)\nu\xi \tag{4.55}$$

The key temporal frequency ν_d is calculated by Eq. (4.54) via $\partial^2\mu/\partial\nu^2 = 0$, and the instantaneous frequency of the main lobe varies linearly along the propagation distance as:

$$\nu_d = \operatorname{sgn}(\beta_2)\frac{\xi}{2} + \nu_m \tag{4.56}$$

Dashed lines in Figs. 4.13(b, c) are plotted based on this formula. Therefore, in order to understand the linear dynamics, we model the main hump propagation as a Gaussian pulse featured by a liner phase term $exp(-i\nu_d T)$ varying along propagation.

4.10.b Nonlinear Airy pulse propagation

In the presence of a Kerr effect ($\eta \neq 0$), an Airy pulse behaves very differently with respect to the linear case. In Figs. 4.14(a, b) we illustrate the nonlinear evolutions under anomalous and normal dispersion, respectively. White dashed lines mark the parabolic trajectory followed by the Airy pulse in the linear regime ($\eta = 0$). The nonlinear propagation of Airy pulses is simulated by employing the Split Step Fourier method to solve Eq. (4.41) with input condition described by Eq. (4.50). In simulations, a mild nonlinearity and the same offset parameter ν_m are considered. As shown in Figs. 4.14(a, b), the MPPs also appear close to the propagation distance $\xi = 8$.

Under anomalous dispersion the main hump tends to shrink its temporal duration, showing a faster acceleration when compared to a linear Airy pulse [Fig. 4.14(a)]. This nonlinear behavior is analog to the case of a spatial Airy beam under a self-focusing nonlinearity. Taking a look into the spectral domain, we note that at each distance ξ the spectral content concentrates into a negative defect, formed by a notch with two mainly peaks outside [Fig. 4.14(c)].

Under normal dispersion, the Airy pulse exhibits a main hump that broadens in time, analog to the nonlinear dynamics of an Airy beam under a self-focusing nonlinearity [Fig. 4.14(b)]. This temporal expansion indicates a slower acceleration than in the linear regime. In the Fourier space, the spectral content reshapes into a positive defect, constituted by one single peak at each propagation distance ξ [Fig. 4.14(d)]. To understand the nonlinear evolution of an Airy pulse as a function of the distance ξ, we can model the main hump propagation as a Gaussian pulse with a different carrier frequency, as seen for the linear case in the previous section. Similar to the nonlinear Gaussian pulse in Figs 4.12(b) and 4.12(c), the nonlinear spectrum of an Airy pulse under normal and anomalous dispersion exhibits a negative and positive defect, respectively. While the spectra in Figs 4.12(b) and 4.12(c) have no transversal shift, the defects induced by a mild nonlinearity, for a nonlinear Airy pulse, shift linearly with the propagation distance due to the fact that the frequency of the main hump undergoes a linear change with ξ. Although their spectral paths are expected to follow the analytical shift v_d (white dashed lines), some discrepancies occur because of the nonlinear nature of the pulse propagation. This difference is more pronounced for normal than anomalous dispersion, and it can be understood by observing the nonlinear evolutions in the temporal regime.

As seen in Figs. 4.14(a, b), the deviation for the nonlinear Airy pulse with respect to the linear trajectory is tiny under anomalous dispersion, while it is larger for normal dispersion. As a consequence, the path of the spectral defect in the frequency domain (see Fig. 4.14(d)) has a larger discrepancy with respect to the analytical value v_d. Another notable feature in the nonlinear Airy pulse spectra is the appearance of a spectral ripple near the defects region. Such a ripple is more noticeable under anomalous dispersion regime (see Fig. 4.14(c)). These patterns are caused by the interference between the reshaped spectra of the main hump and those of the sub-lobes, which can also induce nonlinearity. The peak power of the sub-lobes (for pulse propagation along ξ) tends to increase during propagation under anomalous dispersion, while it is prone to decrease under normal dispersion. This is the reason why the ripples in Fig. 4.14(c) are more pronounced than those in Fig. 4.14(d).

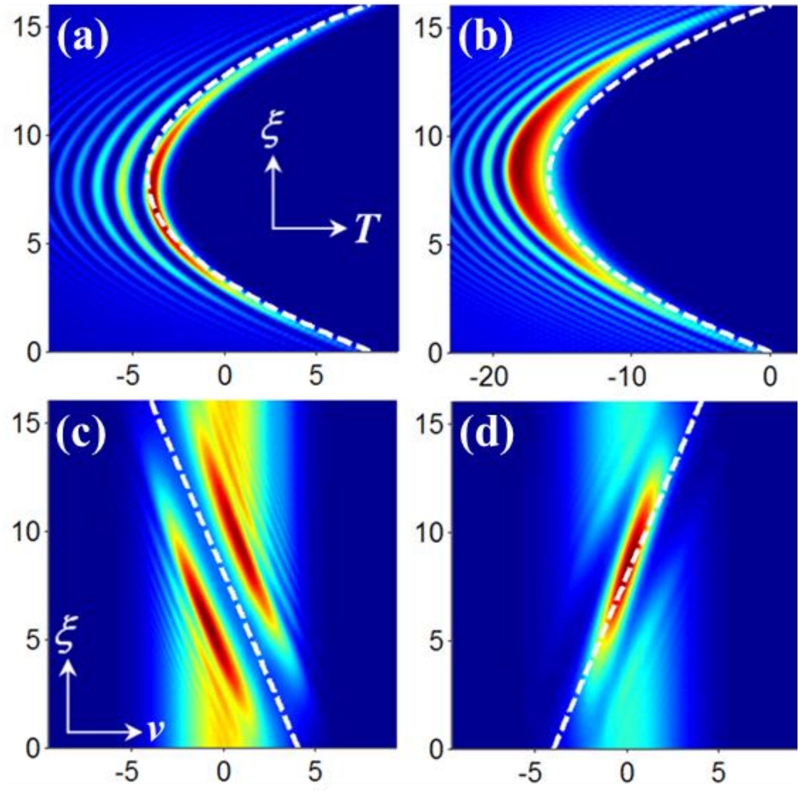

Figure 4.14: Propagation of Airy pulses in a nonlinear optical fiber. (a) and (b) intensity distributions under anomalous and normal dispersion, respectively. (c) and (d) spectral distributions corresponding to (a) and (b).

As a direct outcome of this analysis, the real spectral shift can be estimated by correcting the linear shift v_d through a suitable parameter ε as: $v_{dc} = \varepsilon v_d$. The parameter ε is smaller than 1 for anomalous dispersion, while it is bigger than 1 for normal dispersion. Therefore, in order to describe the nonlinear dynamics of an Airy pulse, we can model the main hump propagation as a Gaussian pulse featured by a linear phase term $exp\left(-iv_{dc}T\right)$ varying along the propagation distance ξ as:

$$v_{dc}\left(v_m\right)=\varepsilon v_m+\varepsilon\,\mathrm{sgn}\left(\beta_2\right)\xi/2 \tag{4.57}$$

For an optical fiber whose length is L, spectral defects can be controlled by shifting the cubic phase mask as:

$$v_{dc}\left(v_m\right)=\varepsilon v_m+\varepsilon\,\mathrm{sgn}\left(\beta_2\right)L/2. \tag{4.58}$$

Eq. (4.58) highlights the fact that the shift on the spectral defect is proportional to the shift of the cubic phase structure. On a practical point of view, this linear relationship may be used to measure the fiber length.

In the next section, we will demonstrate experimentally this spectral control under both normal and anomalous dispersion. We will also estimate experimentally the correction parameter ε and compare it with the values found from our numerical study.

4.11 Space-to-time pulse shaping technique

Airy pulse lasers are still not commercially available and could be realized by reshaping a commonly used Gaussian pulse. A standard device used to shape ultrashort pulse is the "Pulse Shaper". Before describing the experimental setup used to study the propagation of nonlinear Airy pulse, we briefly review the working principle for this apparatus. The scheme of a pulse shaper is shown in Fig. 4.15 [150-152]. It consists of a couple of diffraction gratings and spherical lenses, arranged in a 4*f*- configuration. At the back focal plane of the first lens is placed a programmable Spatial Light Modulator (SLM), whose goal is to encode the amplitude and phase mask patterns to be imposed on the input pulse. The SLM is connected to an external laptop used to upload the amplitude and phase mask. The working principle is based on a space-time conversion technique. At first, the frequency components of the input pulse are angularly dispersed by the first diffraction grating, and are then collimated by the first lens. The spectral components are thus spatially separated along the vertical direction. Basically, the first lens performs a Fourier transform, and therefore maps the angular dispersed components from the first grating to specific spatial positions at its back focal plane. The pattern carried by the SLM individually manipulates both the amplitude and the phase of the spatially dispersed optical Fourier components. Then, the second lens and grating recombine all the frequencies into a single pulse, thus completing the pulse shaping.

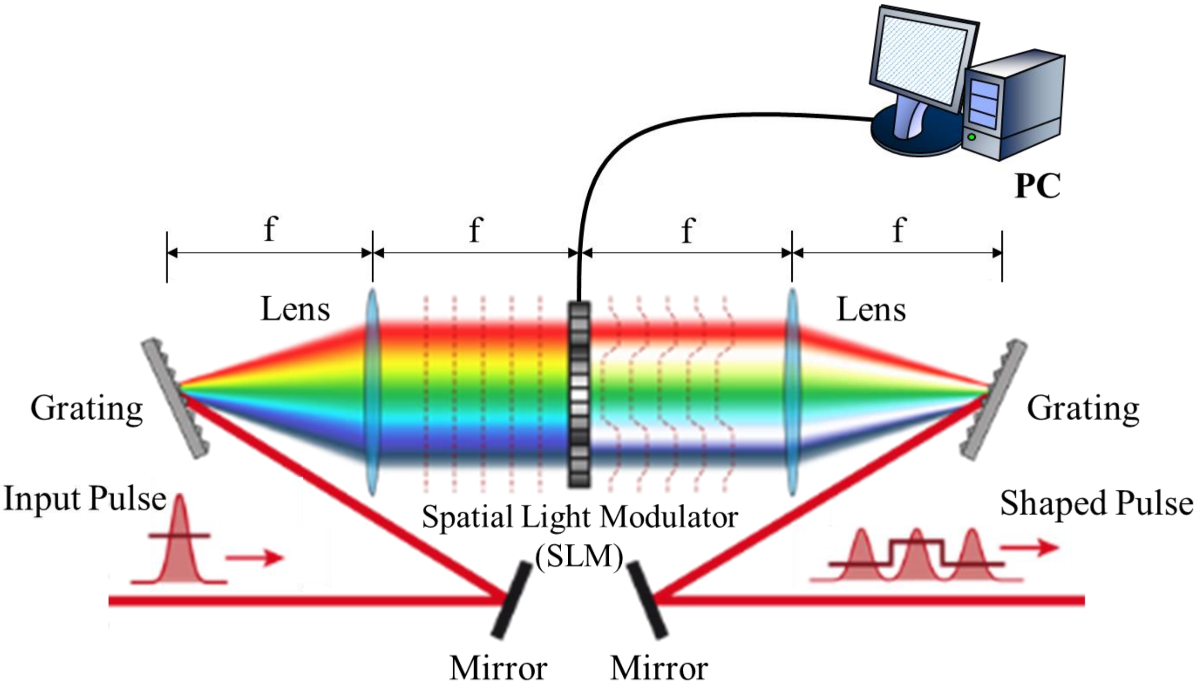

Figure 4.15: Scheme illustrating the working principle of a pulse shaper.

In our setup, the pulse shaper has a double purpose: not only it is employed to reshape the input Gaussian pulse into an Airy pulse by means of a spectral cubic phase mask, but it is also used to electrically modify the characteristics of the phase structure. In particular, we are able to offset electronically the central frequency of the uploaded phase structure, thus greatly simplifying our experimental procedure.

4.12 Experimental observation

The scheme in Fig. 4.16 illustrates the experimental setup used to realize the above mentioned above spectral control. An input Gaussian pulse, generated by a wavelength-tunable sub-picosecond fiber laser from Pritel Inc., is phase-modulated in the spectral domain through a cubic phase structure ($\omega_S = 2\pi\times10^{11}$), uploaded into a pulse shaper. In this way, the input Gaussian pulse is reshaped into an Airy pulse. The output Airy pulse is subsequently coupled into a nonlinear fiber connected to an optical spectrum analyzer (OSA). The OSA is employed to measure the output spectra of the nonlinear fiber. The pulse power is tuned by means of an erbium-doped fiber amplifier, which is used to amplify the Airy pulse just before the propagation into the nonlinear fiber.

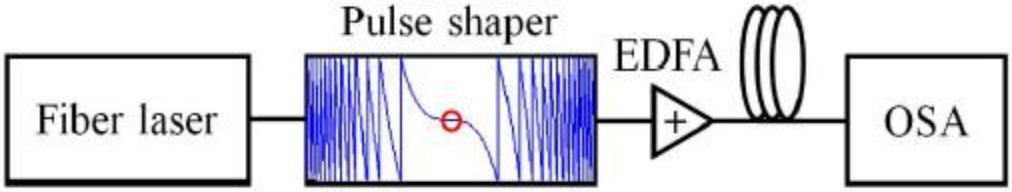

Figure 4.16: Experimental setup for the spectral control of nonlinear Airy pulses. EDFA and OSA stand for erbium-doped fiber amplifier and optical spectrum analyzer, respectively. The plot inside the pulse shaper schematically shows the cubic phase structure wrapped between $-\pi$ and π where the circle indicates its center.

The experimental procedure is based on the spatial dependence of the nonlinear spectral defects: when an Airy pulse propagates under a nonlinear regime, its initial Gaussian spectrum reshapes into a spectral defect at high power values. Such a defect moves along the propagation distance *z* when the impressed cubic phase mask is offset. We note that the output spectrum can be readily controlled via different values of the center frequency of the phase structure, which are changed electronically in the pulse shaper.

4.12.a Propagation of Airy pulses under anomalous dispersion

In the first set of measurements, we study the nonlinear propagation of an Airy pulse under anomalous dispersion. The experiment is performed using a 5 km-long Large Effective Area Fiber (LEAF). We tuned the fiber laser in order to generate sub-picosecond pulses in the range of wavelengths where the LEAF fiber manifests anomalous dispersion. In our framework, the central wavelength of the input Gaussian pulse was set at 1548.5 nm, with a bandwidth of nearly 4nm. After the pulse reshaping and the amplification, the measured average power of the Airy pulse at the input side of LEAF fiber was around 240 μW.

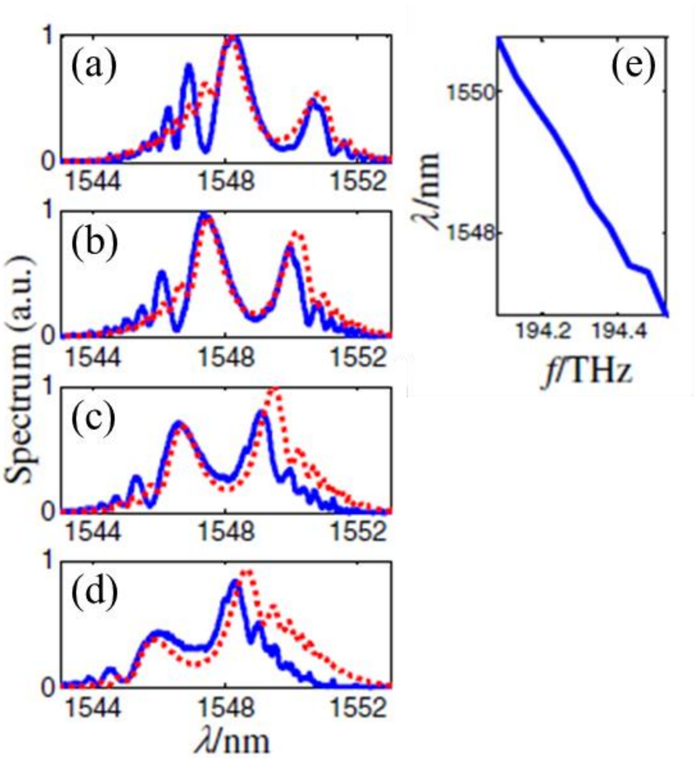

Figure 4.17: Frequency shift control of nonlinear Airy pulse under anomalous dispersion in a LEAF. Comparison between experimental results (solid blue lines) and theoretical predictions (dotted red lines). From top to bottom, the plots in (a-d) correspond to the experimental and analytical results obtained by shifting the central frequency f_{m} of the cubic phase structure at frequencies: (a) f_{m} = 194.2, (b) 194.3, (c) 194.4 and (d) 194.5 THz. (e) plots the positions of the spectral notch defects in (a) as a function of f_{m}.

The spectra measured by the OSA at the output of the LEAF fiber are shown in Figs. 4.17 (a-d). These spectra correspond to different shifting positions of the central frequency $f_m = 2\pi v_m$ in the cubic phase structure, uploaded into the pulse shaper. In our case, the center of the cubic phase mask was shifted at the frequencies: f_m = 194.2, 194.3, 194.4 and 194,5 THz. Our experimental observations (solid blue line) show that the spectrum concentrates into two major peaks separated by a notch (negative defect). We also note that the negative defect moves towards shorter wavelength as the central frequency of the cubic phase structure is shifted to longer frequencies. This behavior is in good agreement with the numerical results obtained by simulating the nonlinear propagation of an Airy pulse with the same parameters used in the experimental setting (red dotted line in Figs. 4.17 (a-d)). To estimate the correction parameter ε corresponding to the spectral evolution of the notch, we plotted in Fig. 4.17(e) the notch position as a function of the central frequency in the cubic phase structure. The notch position has a linear evolution with the central frequency of the mask, and the correction parameter ε is estimated to be 1.07 – via a linear fit of the curve. This value is close to the one expected from theory.

4.12.b Propagation of Airy pulses under normal dispersion

In the second set of measurements, we study the nonlinear propagation of an Airy pulse under normal dispersion. We performed the experiment by injecting the Airy pulse into a 6.6 km dispersion-shifted fiber (DSF) whose zero-dispersion wavelength is located at 1559 nm. The laser fiber is tuned to produce an input Gaussian pulse with a central wavelength of 1538.7 nm, and a bandwidth of 4.7nm. After reshaping and amplification, the reordered average power of the Airy pulse at the input facet of the DSF is around 630 μW. Similar to the anomalous dispersion case, we measured the output spectra from the DSF corresponding to different shifting positions of the central frequency in the cubic phase structure. Figs. 4.18(a-d) shows the output measured spectra (blue solid line) when the central frequency f_m of the cubic phase structure is shifted to: $f_m = 194.35$, 194.45, 194.55 and 194.65 THz. In the presence of normal dispersion, the spectrum concentrate into a single peak (positive defect) surrounded by a tiny ripple appearing on the left-hand side. As the central frequency in the cubic phase mask is shifted towards longer frequencies the positive defect moves from longer to shorter wavelengths. Furthermore, the numerical spectra calculated by simulating the propagation of an Airy pulse under normal dispersion using the same parameters as in the experimental setup, are depicted by the red dashed lines in Figs. 4.18(a-d), and agree qualitatively well with the experimental results from the OSA.

By plotting the position of spectral peak as a function of the central frequency of the phase structure, we found that they are related by a linear profile, as shown in Fig. 4.18(e). The value of the correction parameter ε corresponding to the spectral evolution of the peak is estimated without fitting parameters to be 0.93. Unlike the anomalous dispersion case, the experimental shift rate is bigger than the one expected from theory ($\varepsilon \approx 0.73$), but it can be still considered consistent.

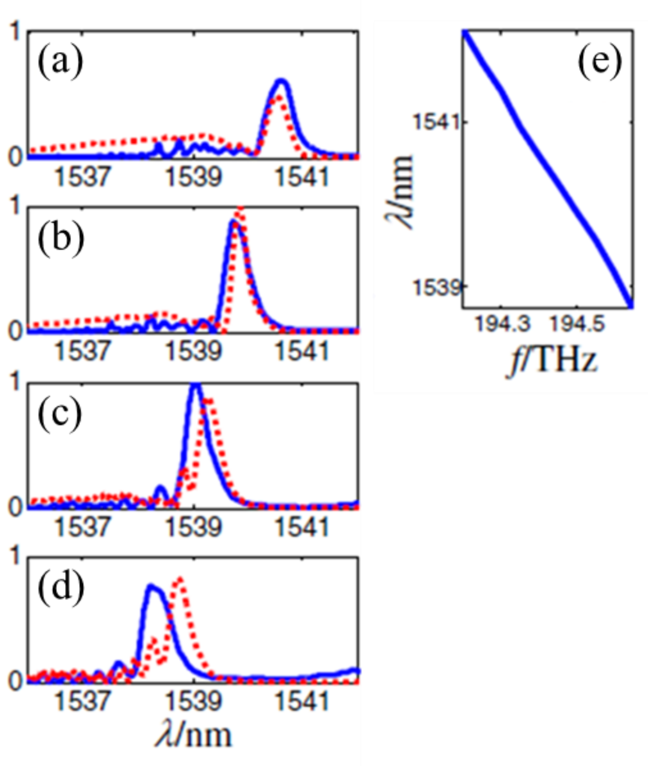

Figure 4.18: Frequency shift control of nonlinear Airy pulse under normal dispersion in a DSF. Comparison between experimental results (solid blue lines) and theoretical predictions (dotted red lines). From top to bottom, the plots in (a-d) correspond to the experimental and analytical results obtained by shifting the central frequency f_m of the cubic phase structure at frequencies: (a) f_m = 194.35, (b) 194.45, (c) 194.55 and (d) 194.65 THz. (e) plots the positions of the spectral peak defects in (a) as a function of f_m .

4.13 Final remarks

In this chapter, we analyzed the nonlinear propagation of both Airy beams and pulses. In space, the propagation of an optical beam is modelled by the NLPWE for diffraction. In particular, the nonlinear propagation of an Airy beam in a saturable PR crystal under the action of self-focusing and -defocusing nonlinearity has been investigated. By simply shifting the applied spectral cubic phase mask, we found a method to preserve the self-accelerating property of an Airy beam inside PR crystals. At the same time, we achieved the control of both trajectories and spatial spectra. Nonlinear Airy beams have propagation characteristics similar to those shown in the linear regime. Conversely, their characteristics are completely different in the Fourier space (spatial frequency). Under a self-focusing nonlinearity, an Airy beam shrinks and shifts towards positive positions in the real domain, with respect to the linear regime. Furthermore, a Gaussian spectrum reshapes into a self-shifting spectral gap defect, formed by a notch and two peaks outside. Instead, in the presence of self-defocusing nonlinearity, an Airy beam broadens and shifts towards negative positions, with a Gaussian spectrum reshaping into a self-shifting spectral peak defect.

In the temporal domain, we expected the nonlinear Airy pulse to behave as in the spatial regime case, due to the analogy existing between the NLPWE and the NLSE describing the nonlinear propagation of optical pulse (in presence of dispersion). For these reasons, we also investigated the self-phase modulation of an Airy pulse under both normal and anomalous dispersion. We have demonstrated that under normal dispersion, the spectrum of an Airy pulse in fiber concentrates into one self-shifting peak, while under anomalous dispersion the spectrum reshapes into two self-shifting peaks. By simply translating the corresponding cubic phase structures, we have envisaged the possibility of performing wavelength selection. Different wavelengths are easily selected, due to the linear dependence between frequency and distances in correspondence of spectral defects. Additionally, we have shown that the propagation length is mapped into the frequency domain. This feature can be exploited for metrological applications, in which the fiber length can be estimated by the spectral position of the defect. In the non-paraxial regime, such nonlinear control can be easily extended even for non-paraxial accelerating beams and pulses.

Chapter 5

Résumé de thèse en langue française

5.1 Introduction

Contrairement à un laser classique se propageant le long d'une ligne droite, un faisceau auto-accélérant a pour caractéristique de suivre une trajectoire courbée dans un milieu homogène linéaire, ce qui implique une accélération transversale. La recherche dans ce domaine a commencé en 2007 avec l'introduction du faisceau d'Airy dans un contexte optique. Un tel faisceau se propage sans diffraction le long d'une trajectoire parabolique, présentant un profil d'amplitude d'Airy. Une autre propriété associée au faisceau d'Airy est sa capacité d'« auto-régénération». Si l'on essayait de bloquer une partie du faisceau à une certaine distance, le faisceau d'Airy se "régénérerait" pendant la propagation. Ces caractéristiques intrigantes ont rendu le faisceau d'Airy idéal pour plusieurs applications dans divers domaines de la science, tels que les balises optiques, les canaux plasma incurvés, les faisceaux accélérant d'électrons et les pièges optiques. Dans le domaine temporel, la contrepartie du faisceau d'Airy est une pulse d'Airy, montrant les mêmes propriétés dans le temps lors de la propagation dans un régime linéaire. Néanmoins, dans les milieux non linéaires, un paquet d'onde Airy se comporte différemment, en raison de la rupture de son accélération par la non-linéarité. Cela constitue un inconvénient évident limitant éventuellement la gamme d'applications possibles de ces paquets d'ondes. Cependant, au cours des dernières années, le concept d'accélération a été étendu au-delà du cas parabolique. En particulier, d'autres avancées de recherche sur ce sujet ont signalé des faisceaux auto-accélérant se propageant tout au long d'une trajectoire arbitraire.

Dans cette dissertation, nous étudions numériquement et expérimentalement les dynamiques linéaires et non linéaires des paquets d'ondes auto-accélérant optiques. Dans le régime linéaire, l'une des techniques utilisées pour générer de tels paquets d'ondes est basée sur la modulation spectrale d'un faisceau laser standard. Dans ce contexte, nous introduisons une approche analytique capable de prédire ou de concevoir les chemins courbes des paquets ondes auto-accélérant. Sur la base de cette étude, nous proposons et démontrons également une technique pratique et simple pour obtenir un confinement énergétique de ces paquets d'ondes. En particulier, nous montrons qu'une amélioration significative de l'intensité maximale de ces faisceaux peut être obtenue tout en préservant leurs propriétés intrinsèques. Enfin, nous étudions la propagation non linéaire des faisceaux et des pulses d'Airy. Plus précisément, nous montrons que ces paquets d'ondes auto-accélérants sont capables de préserver leurs propriétés d'accélération dans les milieux non linéaires Kerr et photoréfractifs lorsque leur modulation spectrale initiale est correctement conçue.

5.2 Contrôle de la trajectoire et conception des faisceaux auto-accélérants

Dans la première section, nous introduisons une méthode pour contrôler et concevoir les trajectoires de propagation des faisceaux auto-accélérants avec une ou plusieurs trajectoires grâce à une caractérisation spectre-distance. Une telle caractérisation permet non seulement une prédiction de l'espace de Fourier de la trajectoire de propagation sur la base de la connaissance a priori de la configuration de phase spectrale imposée, mais permet également de concevoir la phase spectrale initiale du faisceau pour générer un faisceau propageant le long d'une trajectoire convexe arbitraire.

5.2.1 Théorie du mappage spectre-espace

Nous commençons notre analyse en considérant l'équation de diffraction paraxiale, qui décrit la dynamique de propagation de l'enveloppe de champ électrique dans le régime linéaire [1].

$$i\frac{\partial\phi}{\partial z}+\frac{1}{2k}\left(\frac{\partial\phi^2}{\partial x^2}+\frac{\partial\phi^2}{\partial y^2}\right)=0, \tag{5.1}$$

Ici $\phi(x,y,z)$ est l'enveloppe du champ électrique et k est le numéro d'onde. Le schéma de la Fig. (5.1) montre notre système. Les faisceaux auto-accélérants sont générés dans l'espace réel (*x*-*y*-*z*), après la modulation du spectre dans le plan de Fourier. Une onde plane initiale est modulée en phase au plan (*x'*-*y'*) (partie gauche de la Fig. (5.1)), ce qui correspond au plan focal d'une lentille de focale *f*. Ensuite, la transformée de Fourier de l'onde plane modulée est réalisée dans le plan spatiale par l'utilisation d'une lentille cylindrique (ou sphérique), formant ainsi des faisceaux auto-accélérant (1+1) D (ou (2+1)D) dans l'espace réel (*x*-*y*-*z*) (partie droit de la Fig. (5.1)). Dans ce résumé, nous nous limitons uniquement au cas des faisceaux auto-accélérant 1D où aucune variation par rapport à l'axe y n'est supposée. Plus de détails sur les faisceaux auto-accélérés à haute dimension sont rapportés dans le chapitre 3. Dans cette condition, l'enveloppe du champ électrique peut être décrite par cette simple expression:

$$\phi(x,z)=\frac{1}{2\pi}\int_{-\infty}^{\infty}\tilde{E}(k_x,z)e^{ixk_x}dk_x. \tag{5.2}$$

Dans l'équation Eq. (5.2), $\tilde{E}(k_x,z)=\exp[i\mu(k_x,z)]$ est le spectre de Fourier, où le terme $\mu(k_x,z)=-k_x{}^2z/(2k)+\rho(k_x)$ correspond à la phase spectrale et $\rho(k_x)$ est la modulation de phase imprimée sur le plan (*x'*-*y'*). $k_x = x'k/f$ est la fréquence angulaire spatiale, dans laquelle, x'/f est le facteur d'échelle.

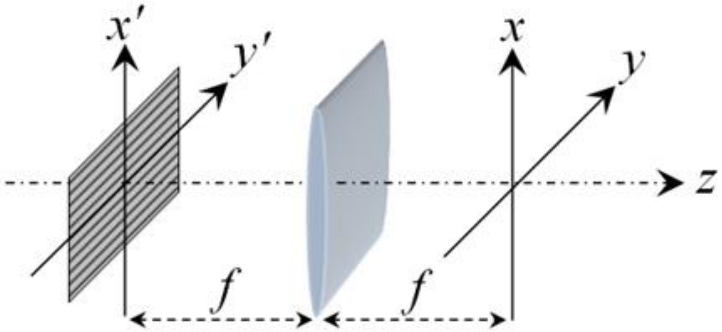

Figure 5.1: Schéma du système expérimental utilisé pour générer des faisceaux auto-accélérants 1D, dans lesquels une modulation de phase et une modulation d'amplitude sont imprimées dans l'espace de Fourier (*x'*-*y'*).

Par analogie avec le domaine temporel, où le gradient de la phase spectrale peut être lié à la vitesse de groupe [122], le gradient de la phase spectrale dans le domaine spatial est lié à la position locale de sorte que:

$$x = -\frac{\partial \mu\left(k_x, z\right)}{\partial k_x} = \frac{k_x}{k} z - \rho'\left(k_x\right). \tag{5.3}$$

Le faisceau peut atteindre l'intensité maximale (IM) lorsque la condition de singularité $\partial^2 \mu\left(k_x, z\right) / \partial k_x{}^2 = 0$ est satisfaite. Cette singularité de densité spectrale détermine le faisceau caustique, strictement lié à la trajectoire suivie par le faisceau auto-accélérant. Il peut également s'exprimer comme suit:

$$\rho''\left(k_x\right) = \frac{z}{k}, \tag{5.4}$$

reliant ainsi les fréquences spatiales à la distance de propagation *z*. En résolvant l'Eq. (5.4), les fréquences spatiales clés (k_{xc}) déterminant la trajectoire de propagation peuvent être exprimées en fonction de *z*. En outre, par l'Eq. (5.4) et la suivante :

$$\frac{dx}{dz} = \frac{k_{xc}\left(z\right)}{k}, \tag{5.5}$$

la trajectoire convexe parcourue par l'intensité maximale du faisceau peut être prédite.

5.2.2 Faisceaux auto-accélérants à trajectoire unique

Pour générer un faisceau auto-accélérant à trajectoire unique, la modulation de phase appliquée $\rho(k_x)$ présente une dérivée seconde qui se comporte doucement comme une fonction monotone de la fréquence spectrale k_x. Un cas bien connu est le faisceau d'Airy, qui est généré par une modulation cubique de phase, comme par exemple $\rho\left(k_x\right) = \left(\alpha k_x / k\right)^3$ ($a = 200$ et $k = 633\text{nm}$).

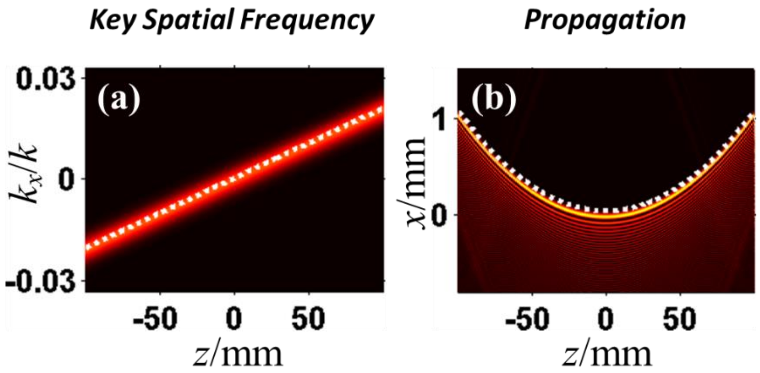

Figure 5.2: Le faisceau auto-accélérant à trajectoire unique généré par une modulation spectrale cubique en phase sous l'approximation paraxiale. (a) Estimation de la fréquence spatiale clé (ligne blanche pointillée) et du spectre résiduel correspondant à la bosse principale de (b); (b) trajectoire de propagation prédite (ligne blanche pointillée) et évolution numérique du faisceau d'intensité.

Comme prévu par l'Eq. (5.4), la fréquence spatiale clé est une fonction linéaire de la distance de propagation z, selon $k_{xc} = k^2 z / (6\alpha^3)$ [ligne en pointillée sur la Fig. 5.2 (a)]. En insérant ce k_{xc} estimé dans l'Eq. (5.5), la trajectoire convexe suivie par l'IM est la courbe parabolique, décrite par $T_r(z) = kz^2 / (12\alpha^3)$ [ligne en pointillée sur la Fig. 5.2 (b)]. La prédiction analytique est encore confirmée par des simulations numériques de la propagation du faisceau obtenues par une transformée de Fourier de l'Eq. (5.2), comme le montre la Fig. 5.2 (b). En outre, si tous les sous-lobes dans la trajectoire d'intensité illustré dans la Fig. 5.2 (b) sont ensuite éliminés, afin de ne considérer que le lobe principal du faisceau, le spectre correspondant à la bosse résiduelle intense suivra l'évolution linéaire de la fréquence spatiale clé décrite ci-dessus [Fig. 5.2 (a)].

5.2.3 Faisceau auto-accélérants à plusieurs trajectoires

Ensuite, nous considérons le cas d'une modulation de phase spectrale arbitraire. Puisque $\rho''(k_x)$ ne s'agit peut-être pas d'une fonction monotone, deux ou plusieurs fréquences spatiales clés pourraient être impliquées dans ce cas, afin de déterminer les localisations multiples des faisceaux. Les résultats pour un exemple typique de fonction non monotone

$\rho''(k_x)$ sont représentés dans les Figs. 5.3(a, b). De tels résultats sont obtenus en analysant la modulation de phase spectroscopique sinusoïdale $\rho(k_x) = 130\sin(80k_x / k)$.

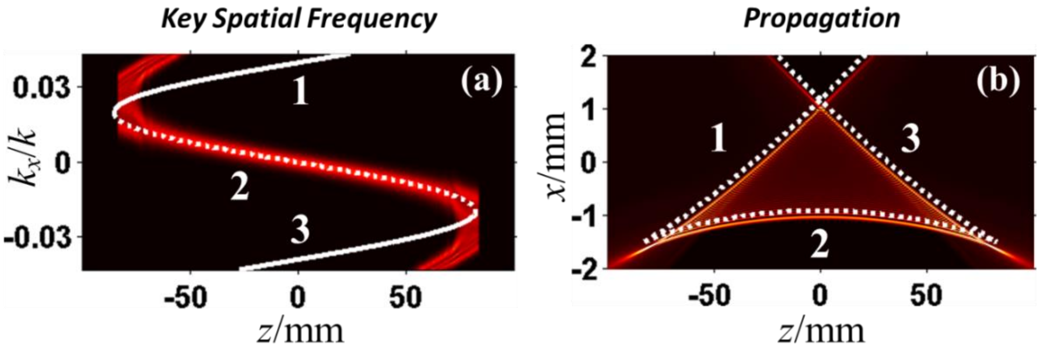

Figure 5.3: Faisceaux auto-accélérant à plusieurs trajectoires générés par une modulation spectroscopique de phase sinusoïdale sous l'approximation paraxiale. (a) Fréquence spatiale clé à valeurs multiples (ligne blanche pointillée) et spectre résiduel correspondant aux trois principales trajectoires de bosses dans (b); (b) le chemin du faisceau prédit (lignes blanches en pointillé) et l'évolution numérique du faisceau. Les chiffres indiquent la correspondance entre la trajectoire et la fréquence clé associée.

En insérant cette structure de phase dans l'Eq.(2.5), la distance de propagation z est liée à la fréquence spatiale clé par la relation:

$$z(k_{xc}) = -8.32\times10^5 \sin\left(80k_{xc} / k\right) / k \tag{5.6}$$

La fréquence spatiale clé ($k_{xc}(z)$) est exprimée comme une fonction multi-valeur de z et est évaluée numériquement à partir de l'Eq. (5.7). Ceci est obtenu en limitant le domaine de k_{xc} aux parties du spectre [souligné par les nombres 1, 2, 3 de la Fig. 5.3 (a)] où l'Eq. (5.8) donne une valeur unique de k_{xc}. Si les portions monotones de la fréquence spatiale clé sont ensuite insérées dans l'Eq. (5.9), nous pouvons prédire que le chemin du faisceau est composé de trois trajectoires (ou branches). Chacune de ces trajectoires est associée à différentes composantes spectrales, du fait que la fréquence spatiale clé est encore monotone dans cette gamme spectrale. Cette correspondance est illustrée dans les Fig. 5.3(a) et (b), où, pour des raisons de clarté, nous avons marqué avec le même nombre chaque fréquence spatiale clé et sa trajectoire connexe. Comme le montre la Fig. 5.3(b), notre approche analytique est encore confirmée par des simulations numériques de l’évolution du faisceau basées sur les transformées de Fourier de l’Eq. (5.2). En outre, si l’un des chemins de faisceau est filtré afin de ne retenir que la bosse principale, comme par exemple la 2$^{\text{ème}}$ trajectoire, le spectre résiduel tend à évoluer comme prévu à partir de la fréquence spatiale clé correspondante [ligne blanche en pointillée de la Fig. 5.3(a)].

5.2.4 Résultats expérimentaux

Pour vérifier l’analyse ci-dessus, nous effectuons une caractérisation expérimentale à l’aide de la configuration illustrée dans la Fig. 5.4. Un faisceau Gaussien 2D (CW à $\lambda = 633$nm) est initialement tronqué par deux lames métalliques, de manière à rapprocher la distribution gaussienne circulaire en un faisceau gaussien 1D. Ensuite, le faisceau est modulé en phase à l’arrière du plan focal d’une lentille cylindrique (f = 100mm) à l’aide d’un masque de phase 1D, qui est chargé numériquement dans un modulateur de lumière spatiale (SLM). La lentille cylindrique calcule la transformée de Fourier du faisceau gaussien modulé en phase au niveau du plan focal frontale de la lentille. Une caméra CCD est utilisée pour enregistrer l’évolution du faisceau et leurs spectres spatiaux correspondants. Ces derniers sont visualisés au moyen d’une lentille cylindrique supplémentaire (f = 100mm), tandis que le filtrage spectral de la bosse principale du faisceau est obtenu à l’aide d’une fente réglable composée par deux lames métalliques.

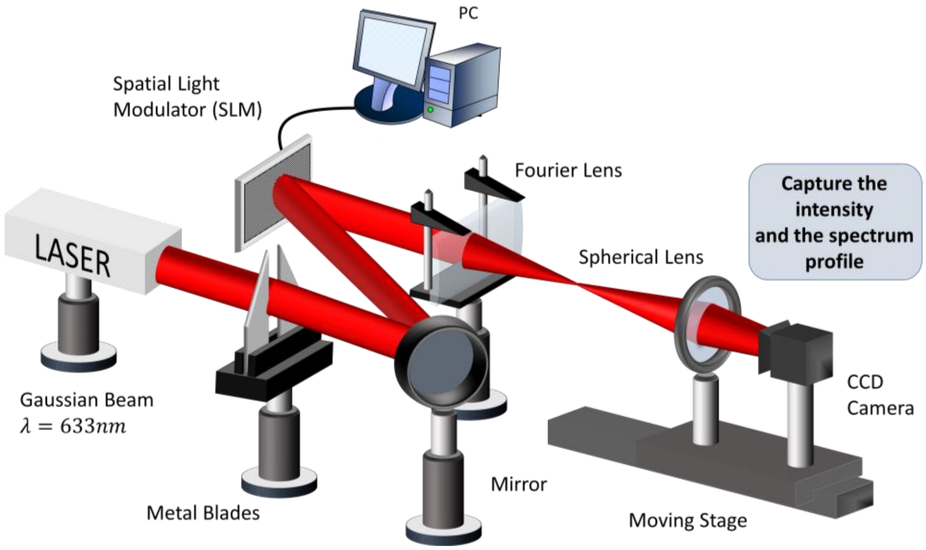

Figure 5.4: Montage expérimental

Les résultats expérimentaux sont présentés dans la Fig. 5.5. Au début, nous avons mesuré à la fois les caractéristiques de propagation et spectrales d’un faisceau d’Airy, qui a été généré par le profil de phase cubique tracé dans le panneau supérieur de la Fig. 5.5(a). Comme l’illustre la Fig. 5.5(b), l’évolution du faisceau suit la trajectoire parabolique prédite par notre modèle et indiquée par la ligne blanche en pointillée de la Fig. 5.5(b). Plus intéressant, si les sous-lobes sont filtrés, le spectre de la bosse principale se déplace linéairement avec la distance de propagation z [Fig. 5.5(c)], avec une tendance similaire à la fréquence spatiale clé estimée. Dans un deuxième ensemble de mesures, nous avons généré deux exemples de faisceaux à trajectoire multiple. Dans ce cas, nous avons utilisé les deux modulations de phase représentées dans la Fig. 5.5(d) et (g). Les modèles de faisceau présentent, respectivement deux et trois bosses principales, comme l’illustrent les Fig. 5.5(e) et (h). Encore une fois, les modèles de faisceau sont en accord avec les prédictions analytiques indiquées par la ligne blanche en pointillée des Fig. 5.5(e, h). En outre, en bloquant alternativement la trajectoire du faisceau dans l’espace réel, chaque branche résiduelle est associée à différentes parties du spectre, comme le montrent les Fig. 5.5(f) et (i). En effet, pour la trajectoire du faisceau constitué de deux (ou trois) trajectoires principales, on peut facilement observer que deux (ou trois) parties spectrales différentes sont liées aux deux branches.

Nos mesures confirment expérimentalement l’existence du mappage spectre-distance pour les faisceaux avec un ou plusieurs trajectoires. Bien que nous nous limitions à étudier des exemples particuliers d’une phase cubique spectrale, notre approche peut également être utilisée pour décrire une classe plus générale de faisceaux à trajectoire unique et multiple.

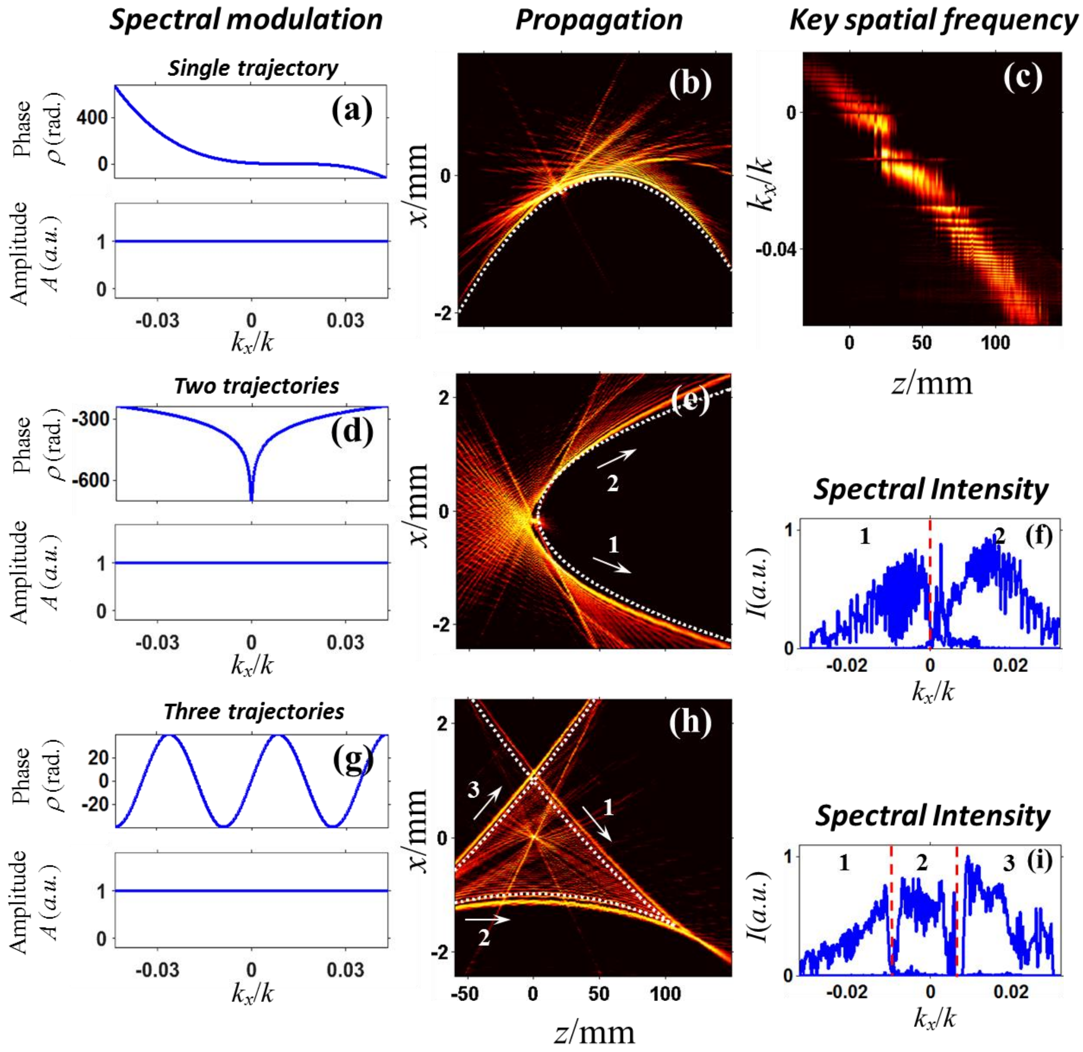

Figure 5.5: Observation expérimentale des faisceaux auto-accélérant avec une et plusieurs trajectoires. (a, d et g) modulations de phase *k*-spatiale et d'amplitude imposées sur le SLM, correspondant respectivement à l'évolution des faisceaux dans (b, e et h). Notez que dans (b, e et h), les trajectoires analytiquement prédites sont représentées par les lignes en pointillés blanches ; les figures (a, b) montrent un cas de faisceau auto-accélérant avec une seule trajectoire liée au faisceau d'Airy; la distribution de fréquence spatiale (c) associée est obtenue en traçant le spectre résiduel de la bosse principale en fonction de la distance de propagation après filtrage spatial. Les figures (d, e) et (g, h) montrent deux cas de faisceaux auto-accélérants à trajectoire multiple, avec respectivement deux et trois trajectoires. Pour chacun de ces cas, (f) et (i) représentent respectivement l'intensité spectrale des faisceaux auto-accélérants à trajectoire multiple extraits à z = 50 mm. En outre, dans les figures (f) et (i), les parties du spectre associées aux différentes trajectoires dans (e) et (h) sont respectivement marquées avec les mêmes nombres dans (e) et (h).

5.2.5 Faisceaux auto-accélérants (2+1)D

Bien que toutes les analyses et observations expérimentales ci-dessus soient liées aux faisceaux auto-accélérant (1+1)D, notre approche peut également être généralisée pour (2+1)D. À titre d'exemple illustratif, dans les Fig. 5.6 et 5.7 sont rapportés les résultats expérimentaux illustrant la propagation et les caractéristiques spectrales associées à trois cas différents de faisceaux (2+1)D mono-trajectoire, se propageant respectivement le long d'un faisceau parabolique (Airy), un polynôme cubique et une trajectoire exponentielle. En partant de ces trajectoires de faisceau souhaitées, les structures de phase appropriées ont été implémentées au moyen du mappage spectre à espace généralisée au régime (2+1)D.

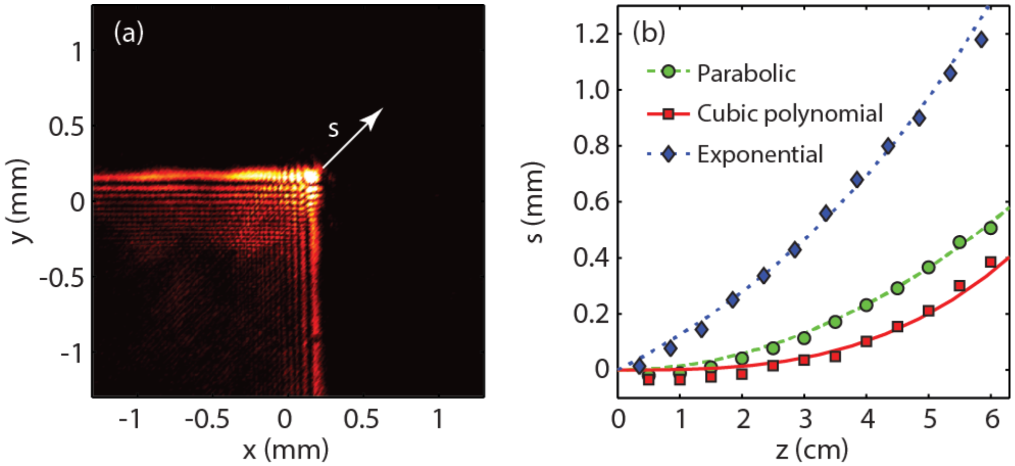

Figure 5.6: Caractéristiques de propagation des faisceaux auto-accélérants générés par un faisceau circulaire gaussien. (a) Modèle de faisceau d'intensité obtenu expérimentalement à $z = 4.2$ cm pour la trajectoire parabolique (faisceau d'Airy). (b) Déplacements de la bosse principale en fonction de la distance de propagation mesurée le long de la direction radiale s pour trois trajectoires de faisceau sélectionnées. Les lignes se réfèrent à la prédiction analytique alors que les points sont les résultats expérimentaux correspondants.

La figure 5.6 (a) montre la distribution d'intensité mesurée à z = 4.2 cm pour le cas typique d'une trajectoire parabolique, qui est présenté par un échantillon d'intensité ayant un lobe à haute intensité entouré de lobes latéraux d'intensité décroissante. Nous avons observé des modèles similaires à Airy pour les deux autres trajectoires considérés. Pour confirmer la fiabilité de notre méthode, nous avons également évalué les trajectoires de ces trois faisceaux en mesurant les déplacements du lobe principal à des distances de propagation sélectionnées. Les résultats sont résumés dans la Fig. 5.6 (b). Les trajectoires convexes expérimentales (points) sont, respectivement, en excellent accord avec les évolutions attendues analytiquement (lignes).

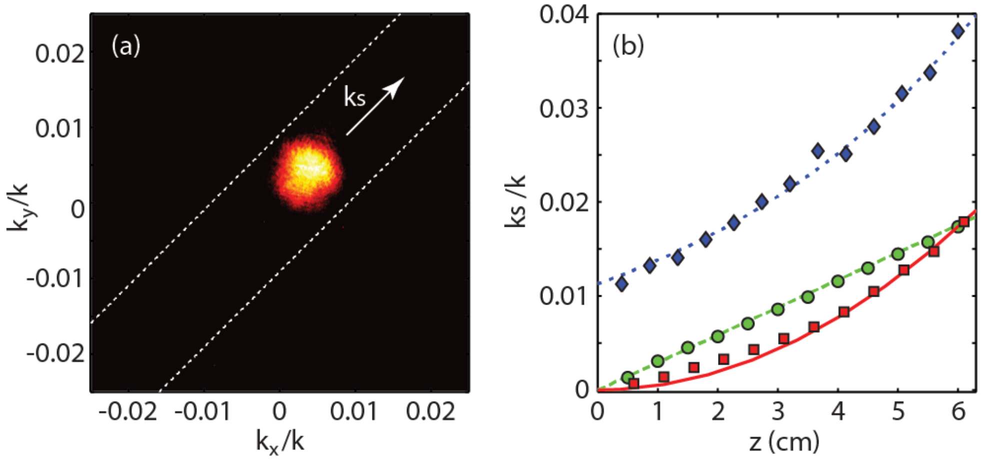

Figure 5.7: Caractéristiques spectrales des faisceaux auto-accélérants générés par un faisceau circulaire gaussien. (a) Le modèle d'intensité spectrale associé à la bosse principale du faisceau d'Airy en Fig. 5.6(a). (b) Les positions radiales spectraux des bosses principales (points) en fonction de la distance de propagation *z* mesurée pour les trois trajectoires de faisceau sélectionnées et des fréquences spatiales clés correspondantes de la théorie (lignes). Le code de couleur est le même que dans la Fig. 5.6.

Dans le domaine de Fourier, le spectre global de ces faisceaux présente une forme gaussienne qui reste inchangée sur toute la gamme des distances de propagation. Néanmoins, en filtrant les lobes latéraux à partir des échantillons d'intensité, le contenu spectral associé à la bosse principale résiduelle se réduit à un point de petite taille, comme illustré par la Fig. 5.7(a) pour le cas du faisceau parabolique. Le spectre du lobe principal présente non seulement une taille réduite, mais il se déplace également le long de la direction radiale de k_s. Dans notre expérience, nous avons également mesuré les déplacements de ces points spectraux en fonction de la distance de propagation z. Les décalages des spectres du lobe principal suivent à la fois des évolutions longitudinales et transversales de leurs correspondantes fréquences spatiales clé prédites [Fig. 5.7(b)].

5.3 Amélioration du confinement énergétique des paquets d'ondes auto-accélérant

Dans la deuxième section, nous introduisons une méthode pratique et directe, adaptée pour améliorer le confinement d'énergie des paquets d'ondes auto-accélérants. Un tel confinement d'énergie est réalisé en récupérant une partie du contenu énergétique associé à ses sous-lobes.

5.3.a Amélioration du confinement énergétique des faisceaux auto-accélérant 2D

Sur toute la gamme des distances, les composants spectraux associés au lobe principal des faisceaux auto-accélérants 2D sont localisés dans la bande marquée par les lignes en pointillés blancs de la Fig. 5.7(a). Cela signifie que les composants spectraux à l'extérieur d'une telle bande spectrale sont donc connectés aux sous-lobes restants. De nombreuses applications impliquant des faisceaux courbes sont principalement intéressées par la propriété accélérante du lobe principal, de sorte que l'énergie stockée dans les sous-lobes est généralement considérée comme indésirable ou gaspillée. L'isolement énergétique de ces faisceaux peut être réalisé en illuminant le masque de phase SLM avec un faisceau elliptique gaussien dont l'axe principal est orienté le long de la bande spectrale délimitée par les deux lignes en pointillés blanches, comme le montre la Fig. 5.8(a). Le faisceau elliptique gaussien a été obtenu en comprimant le faisceau circulaire gaussien au moyen d'un télescope cylindrique placé devant le SLM dans la configuration de la Fig. 5.4, préservant ainsi la teneur énergétique initiale du faisceau. En utilisant les mêmes paramètres et conditions expérimentales de la contrepartie non comprimée, nous avons enregistré expérimentalement les trajectoires accélérantes pour les trois cas étudiés de trajectoire convexe générées précédemment. Comme l'illustre la Fig. 5.8(b), les trajectoires mesurées (points) sont en excellent accord avec les prédictions numériques (lignes). Ces résultats confirment que les trajectoires de propagation restent presque inchangées par la compression spectrale du faisceau, comme le prédisait la théorie. Pour fournir une illustration visuelle des faisceaux auto-accélérants obtenus par le faisceau elliptique gaussien, nous avons mesuré leur distribution d'intensité transversale après la compression spectrale. À titre d'exemple, nous montrons dans les Figs. 5.8(c, d) deux diagrammes d'intensité transversale correspondant au cas de la trajectoire parabolique, enregistrées à deux distances de propagation différentes ($z = 0$ et $z = 5.3$ cm).

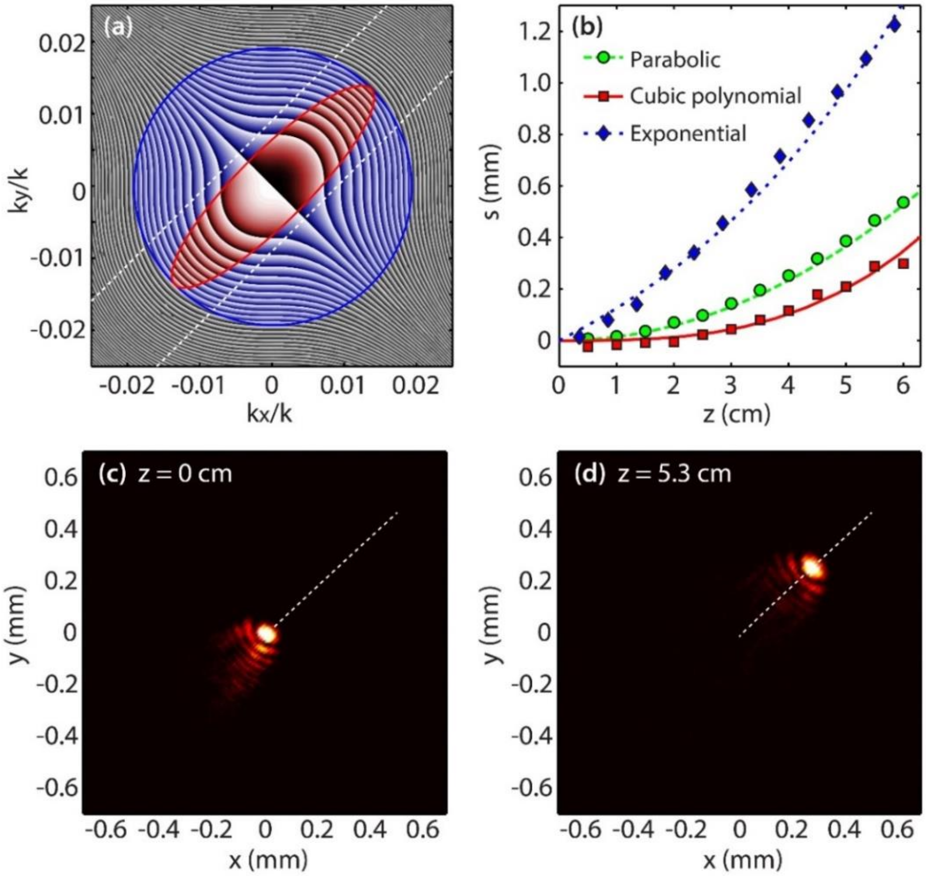

Figure 5.8: Propriétés des faisceaux auto-accélérants après compression spectrale, c'est-à-dire à partir d'un faisceau elliptique gaussien. (a) Masque de phase cubique enveloppé appliqué sur le SLM pour le cas d'une trajectoire parabolique superposée aux profils d'intensité du faisceau (coupure de 95%) de l'effet elliptique (zone rouge - après compression spectrale) et faisceau circulaire gaussien (zone bleue - avant compression spectrale). (b) Position principale de la bosse le long de la direction radiale *s* en fonction de la distance de propagation *z*, mesurée pour les trois trajectoires convexes. Les lignes se réfèrent à des prédictions analytiques, tandis que les points montrent des résultats expérimentaux. (c, d) Modèle d'intensité transversale d'un faisceau "à queue courte" mesuré expérimentalement à $z = 0$ et $z = 5.3$cm pour le cas de la trajectoire parabolique. Notez que pour plus de clarté, l'échelle de couleurs est ici normalisée à la valeur d'intensité maximale de chaque mesure.

Par rapport au cas non comprimé de la Fig. 5.6(a), les profils d'intensité transversale des faisceaux nouvellement obtenus présentent une queue d'expansion spatiale considérablement réduite. De plus, comme l'énergie est conservée avec notre méthode, l'intensité maximale du faisceau devrait augmenter de manière significative par rapport au cas «non comprimé». Pour étudier l'effet d'une telle compression spectrale d'un spectre gaussien circulaire sur l'amélioration de l'intensité maximale du pic, des simulations numériques ont été effectuées pour le cas de la trajectoire parabolique que nous étudions. Le résultat numérique est illustré dans la Fig. 5.9, où nous avons tracé l'amélioration de l'intensité du pic en fonction du diamètre mineur du faisceau elliptique gaussien, c'est-à-dire en variant sa largeur le long de la direction ds' (orthogonal à k_s). Selon ce résultat, le faisceau elliptique expérimental (cercle rouge) fournirait une intensité maximale du faisceau à queue courte environ 60% plus élevée que son faisceau d'Airy correspondant obtenu à partir du faisceau circulaire initial (carré bleu). Pour nos conditions expérimentales, la valeur optimale du confinement énergétique est attendue pour un diamètre mineur de 2 mm. Dans ce cas, le spectre du faisceau gaussien elliptique présente une superposition maximale avec les composantes spectrales du lobe principal du faisceau d'Airy 2D. En augmentant davantage l'excentricité de la forme du faisceau elliptique (c'est-à-dire pour les valeurs de ds en dessous de 2 mm), l'intensité du pic commence à diminuer drastiquement.

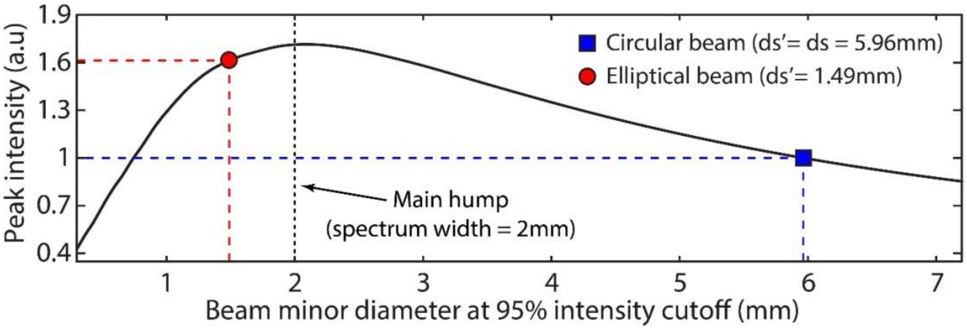

Figure 5.9: Amélioration de l'intensité du pic pour le cas d'une trajectoire parabolique en fonction du diamètre mineur du faisceau Gaussien elliptique (ds'). Le diamètre principal est limité au diamètre circulaire du faisceau gaussien, dont la valeur expérimentale est ds = 5.96 mm. La figure montre que l'amélioration de l'intensité du pic la plus élevé est obtenue lorsque le diamètre mineur approche 2mm.

5.3.b Amélioration du confinement énergétique de la balle spatiotemporelle d'Airy

Jusqu'à présent, nous avons seulement considéré le cas d'un faisceau se propageant sous vide, sans tenir compte de la dynamique de l'évolution temporelle du paquet d'onde. Néanmoins, lors de la propagation dans un milieu diélectrique homogène, un paquet d'onde optique tend naturellement à se propager à la fois dans l'espace et dans le temps en raison des effets combinés de la diffraction et de la dispersion. De manière similaire à l'analogique dans le domaine spatial, dans le domaine temporel, une pulse optique avec un profil temporel d'Airy n'est pas affectée par la dispersion lors de sa propagation (c'est-à-dire que sa forme temporelle reste inchangée). En particulier, le paquet d'ondes d'Airy temporel est exploité comme un bloc de construction clé pour la génération de balles d'Airy optiques linéaires (3+1)D, insensibles aux effets de diffraction et de dispersion. Parmi eux, les balles Airy^3 présentent un intérêt particulier car elles conservent toutes les propriétés de leur contrepartie de faisceau en une ou deux dimensions. Fig. 5.10 montre les intensités directes et d'espace de Fourier (isosurfaces à 95% de coupure) de la balle correspondante à deux distances de propagation différentes (par exemple $Z = 0$ et $Z = 5$). Dans l'espace spatio-temporel (X,Y,T), le paquet d'ondes d'Airy se caractérise par un lobe principal intense (en rouge), ainsi que trois queues principales (longues) formées de nombreux sous-lobes [Figs. 5.10(a, b)]. Bien que l'on puisse identifier une propagation non négligeable en s'approchant de $Z = 5$ (c'est-à-dire l'augmentation de l'expansion de la balle due à son énergie finie), nous avons vérifié que la balle Airy^3 maintient sa forme sur une bande de propagation significative et suit de près la trajectoire parabolique prédite le long de la direction $\vec{S} = \left(X,Y,T\right) = \left(\frac{Z^2}{4},\frac{Z^2}{4},\frac{Z^2}{4}\right)$.

Dans l'espace de Fourier, les isosurfaces d'intensité spectrale montrées dans les Figs. 5.10(c, d) présentent une forme sphérique (isosurface bleue), une propagation invariante et intrinsèquement associée à la symétrie sphérique définie par l'amplitude gaussienne 3D du spectre d'entrée. En revanche, le contenu spectral associé au lobe principal de la balle (petite isosurface rouge) est situé dans la partie centrale du spectre d'entrée, mais son emplacement se déplace dans le spectre principal pour suivre la trajectoire définie par la fréquence spatio-temporelle clé $\vec{K}_S = \left(K_X, K_Y, \omega\right) = \left(\frac{Z}{2}, \frac{Z}{2}, \frac{Z}{2}\right)$, illustré dans la Fig. 5.10 (d). Sur toute la zone de propagation, le contenu spectral du lobe principal se déplace le long de l'axe $\vec{K}_S$ de manière similaire aux cas étudiés dans le régime (2+1)D, mais ici définis comme les diagonales du cube $[K_X, K_Y, \omega]$. Dans ce cas, l'intensité spectrale du lobe principal reste confinée dans un cylindre elliptique (ombrage rouge) avec des demi-axes définis le long des directions (orthogonales) $\vec{K}_Q = (K_X, -K_Y, 0)$ et $\vec{K}_R = (-K_X, -K_Y, 2\omega)$.

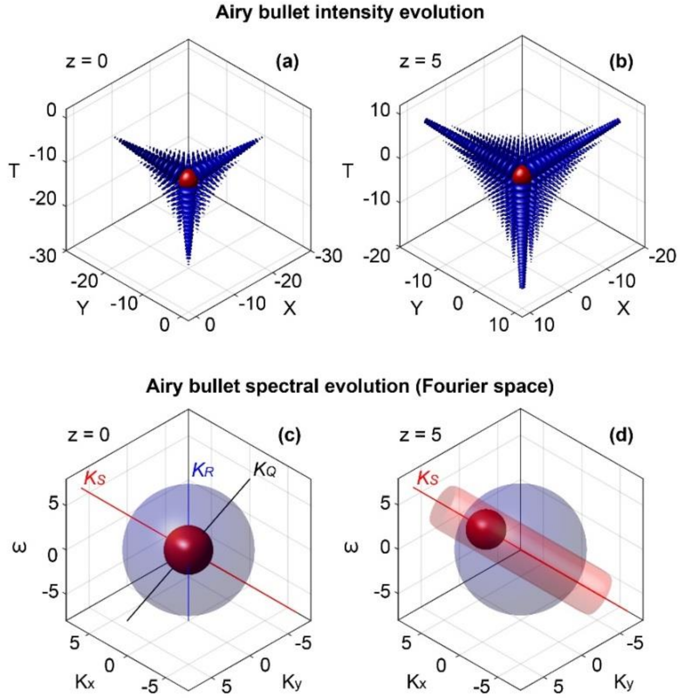

Figure 5.10: Évolution spatio-temporelle d'une balle d'Airy. (a,b) Espaces spatio-temporels et (c,d) intensité spectrale isosurfaces d'une balle Airy^3 (énergie finie) montrée en bleu, et obtenue respectivement à Z = 0 et Z = 5. Les isosurfaces rouges mettent en évidence le lobe principal de la balle dans (a,b) et sa contrepartie spectrale dans l'espace de Fourier représenté en (c,d). Les isosurfaces sont extraites en utilisant un seuil d'intensité de 95%. La ligne rouge dans (c,d) correspond à la trajectoire de fréquence spatiale clé $\vec{K}_S$ suivie des composantes spectrales du lobe principal, dont la position dans l'espace de Fourier dans toute la zone de propagation est représentée par le cylindre rouge ombragé en (d).

5.3.c Balle d'Airy comprimée

Le fait que les composantes spectrales associées au lobe principal de la balle Airy^3 se trouvent dans un emplacement spectral spécifique est d'une importance primordiale pour l'optimisation mirée d'une telle balle Airy^3. En effet, en remodelant l'intensité spectrale spatio-temporelle d'une manière efficace, nous prévoyons qu'une amélioration significative de l'intensité du lobe principal de la balle, associée à une réduite spatio-temporelle globale, peut être facilement obtenue. Cela peut être réalisé de la manière indiquée ci-dessus pour les cas de faisceaux auto-accélérants (2+1)D, c'est-à-dire en confinant le spectre gaussien initial de la balle Airy^3 le long de la fréquence spatiale clé K_S, ce qui comprime l'intensité spectrale spatio-temporelle le long des directions $\vec{K}_Q = (K_X, -K_Y, 0)$ et $\vec{K}_R = (-K_X, -K_Y, 2\omega)$.

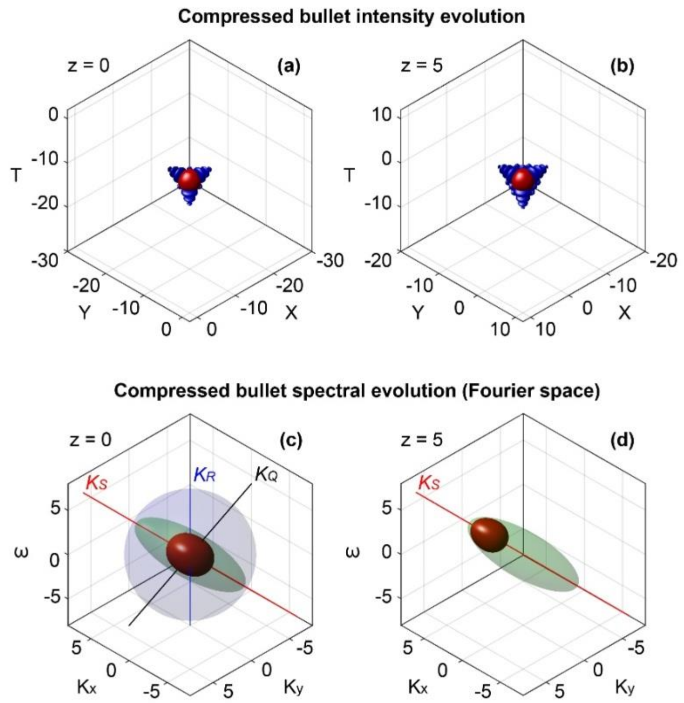

Figure 5.11: Évolution spatio-temporelle d'une "balle à queue courte". (a-d) Figures isosurfaces, comme dans la Fig. 5.10, d'une balle comprimée avec un spectre "pressé" le long de $\vec{K}_Q$ et $\vec{K}_R$. Avec un facteur de compression $C_Q = C_R = 8$, le spectre gaussien initial (sphère bleue) représenté en (c) est remodelé dans une forme ellipsoïde (ombre vert) correspondant de près au déplacement des composantes spectrales du lobe principal tout au long de la propagation [voir Fig. 5.10 (d)].

Dans la Fig. 5.11, nous montrons des résultats numériques en considérant les mêmes paramètres de la balle, mais avec une compression symétrique ($C_Q = C_R = 8$) du spectre spatio-temporel le long $\vec{K}_Q$ et $\vec{K}_R$. Les facteurs de compression indiqués avec C_Q et C_R déterminent le degré de compression spectrale appliquée. Dans les Fig. 5.11(c, d) est montré le spectre comprimé illustré comme isosurfaces verts, par rapport au spectre gaussien initial (ombre bleu). Dans l'espace direct, vu dans 5.11(a) et 5.11(b), la balle comprimée globale (bleu) présente une expansion réduite par rapport au cas précédent, mais la forme du lobe principal (rouge) reste pratiquement inchangée pour les deux distances de propagation. Cette approche offre le double avantage non seulement de réduire l'expansion globale de la balle spatio-temporelle, mais aussi d'augmenter l'intensité / l'énergie du lobe principal de la balle. C'est à quoi l'on s'attend étant donné que l'énergie initial de la balle Airy non comprimée est conservée pendant la compression spectrale.

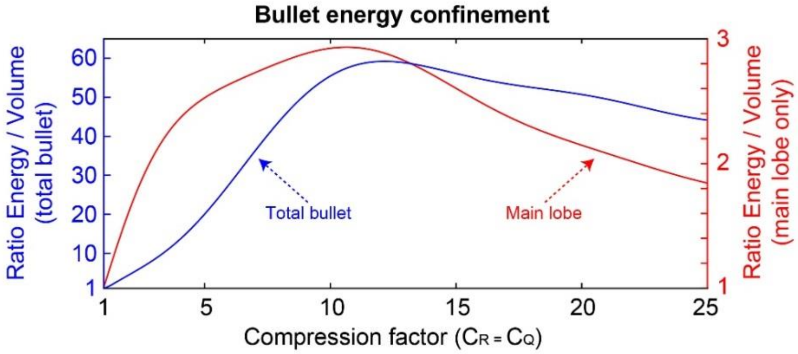

Figure 5.12: Confinement énergétique spatiotemporel de la balle totale (ligne bleue) et son lobe principal (ligne rouge) en fonction de la compression spectrale. Le confinement d'énergie est calculé comme le rapport moyen entre l'énergie et le volume montré dans les Fig. 5.11(c, d), et normalisé à l'unité par rapport à la balle Airy^3 (non compressée).

Évidemment, ces deux aspects sont associés à une amélioration de l'isolement d'énergie de la balle (ici calculé comme le rapport entre l'énergie et le volume), dont l'impact est résumé dans la Fig. 5.12. Nous pouvons ainsi observer que le confinement d'énergie du lobe principal de la balle (ligne rouge) est en effet renforcé d'un facteur d'environ 3 pour un facteur de compression optimal de ~10 avant de diminuer après une compression spectrale supplémentaire. Le principal aspect d'une telle compression est néanmoins associé au confinement général d'énergie de la balle, qui peut être amélioré par un facteur supérieur à 50 pour une telle compression spectrale.

5.4 Propagation non linéaire des paquets optiques d'Airy

Dans la dernière section de la thèse, nous étudions la propagation non linéaire des faisceaux et des pulses d'Airy. Dans la première partie, les faisceaux d'Airy spatiaux sont étudiés à la fois dans les aspects théoriques et expérimentaux en considérant leur propagation dans des matériaux photoréfractifs (PR) polarisés, sous la condition de non linéarité auto-focalisant ou auto-defocalisant. Dans la deuxième partie, la propagation non linéaire des pulses d'Airy en fibre optique est étudiée théoriquement et expérimentalement sous l'effet combiné de la modulation auto-phase (SPM) et de la dispersion (GVD).

5.4.1 Dynamique non linéaire des faisceaux d'Airy dans les cristaux photoréfractifs

Plusieurs intérêts sont portés à l'étude de la propagation d'un faisceau optique dans des cristaux photoréfractifs (PR). Par rapport à d'autres milieux non linéaires, tels que les milieux de Kerr non-linéaires, les milieux PR offrent la possibilité d'observer l'action qu'a un faisceau laser sur le milieu lui-même, tels que des effets de focalisation et de défocalisation à très faible niveau de puissance (~μW). Les milieux de Kerr nécessiteraient un niveau de puissance beaucoup plus élevé (~W) pour observer ce type de processus d'action. En outre, comme l'effet électro-optique modifie l'indice de réfraction sous éclairage lumineux et en présence d'un champ électrique externe, un autre avantage offert par les cristaux PR est la possibilité de basculer le type de non linéarité en inversant simplement le champ électrique appliqué à l'extérieur. Selon l'approximation d'amplitude variant lentement, le modèle théorique pour étudier la propagation non linéaire d'un faisceau d'Airy dans une non linéarité de PR saturable est décrit par l'équation d'onde non linéaire (NLPWE) sans dimension suivante :

$$\frac{\partial \Psi}{\partial \xi} = \frac{i}{2}\frac{\partial^2 \Psi}{\partial s^2} - \frac{i\gamma}{1+|\Psi|^2}\Psi \tag{5.10}$$

Avec $\Psi(s,\xi) = A(s,\xi)/\sqrt{2\eta I_D}$ est l'amplitude complexe normalisée du champ optique, η l'impédance moyenne, et I_D l'irradiation sombre du cristal PR. $s = x/x_0$ et $\xi = z/(k_0 n_0 x_0^2)$ correspondent aux coordonnées transversales et longitudinales normalisées, k_0 le nombre d'onde sous vide, n_0 l'indice de réfraction extraordinaire non perturbé du cristal PR, et x_0 est une échelle de longueur arbitraire. Dans l'Eq. (5.7), $\gamma = 0.5k_0^2 n_0^4 x_0^2 r_{33} E_0$ représente le coefficient non linéaire normalisé, dans lequel E_0 est le champ de polarisation externe et r_{33} le coefficient d'électro-optique pour les faisceaux extraordinairement polarisés. Le signe du champ électrique externe détermine le type de non-linéarité: $E_0 > 0$ (donc $\gamma > 0$) conduit à une non linéarité auto-focalisante, tandis que $E_0 < 0$ (donc $\gamma < 0$) correspond à une non linéarité auto-défocalisante. Lorsqu'aucun champ de polarisation n'est présent ($\gamma = 0$), l'analyse est la même que dans le régime linéaire. À la face d'entrée du cristal PR, nous considérons le profil de faisceau d'Airy suivant:

$$\Psi(s,0) = \sqrt{I_0}\exp(\alpha s)Ai(s + i2\alpha\omega_m)e^{i\omega_m s} , \qquad (5.11)$$

Avec I_0 l'intensité du pic, α est le coefficient de troncature déterminant l'énergie initiale du faisceau d'Airy, ω_m le paramètre de lancement qui définit l'angle de lancement initial du faisceau d'Airy et $Ai(\cdot)$ la fonction Airy. La Fig. 5.13 montre les distributions d'intensité correspondant à trois exemples de faisceaux d'Airy linéaires et non linéaires générés numériquement, qui sont obtenus en lançant la condition d'entrée à $\omega_m = -6$ et en utilisant $\gamma = 0, \pm 2.72$, $I_0 = 4.08$ et $\alpha = 0.08$ comme valeurs des paramètres. Comme le montre la Fig. 5.13(a1), un faisceau d'Airy linéaire évolue selon une trajectoire balistique [62]. Dans le régime non linéaire, la dynamique du faisceau est semblable à celle représentée pour son homologue linéaire, comme le montre les Fig. 5.13(b1) et (c1). Néanmoins, le faisceau d'Airy non linéaire présente un léger déplacement vers les directions positives s ainsi qu'un léger retrait de la largeur lors de la propagation sous une non linéarité auto-focalisant [Fig. 5.13(b1)]. D'autre part, une non linéarité auto-défocalisante déplace le faisceau d'Airy non linéaire vers les directions s négatives, tout en élargissant la largeur du faisceau [Fig. 5.13(c1)]. Un tel déplacement transversal des faisceaux d'Airy non linéaires le long de l'axe s

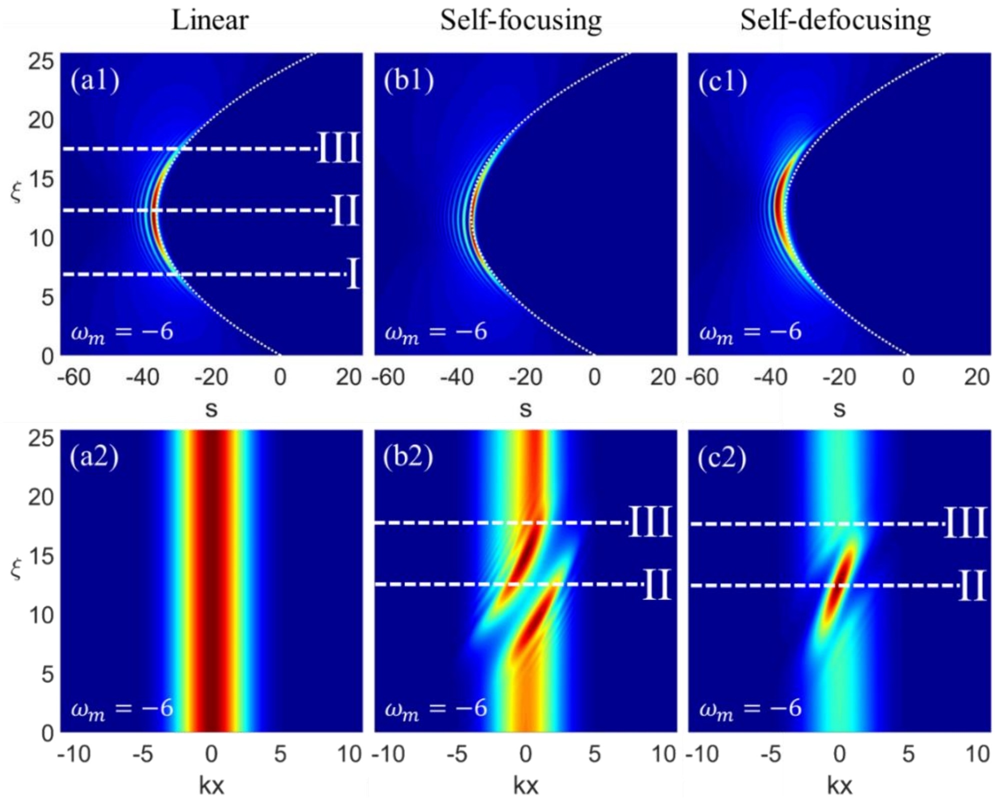

Figure 5.13: Modifications spectrales des faisceaux d'Airy non linéaires. Les graphiques du haut, de gauche à droite, montrent les distributions d'intensité d'un faisceau d'Airy correspondant à un paramètre de décalage ω_m = -6 sous une condition (a1) linéaire, (b1) auto-focalisante non linéaire et (c2) auto-défocalisante non linéaire. Les panneaux inférieurs (a2-c2) de gauche à droite montrent les distributions d'intensité spectrale correspondant respectivement à (a1-c1). Les lignes blanches pointillées marquent l'entrée (I), (II) le milieu et (III) la sortie du cristal PR.

peut être à l'origine des structures de la phase spectrale à ω_m = -6, qui sont représentées sur les Fig. 5.13(b2) et (c3). En regardant le régime de Fourier, le spectre linéaire d'un faisceau d'Airy à énergie finie suppose un profil gaussien, qui se maintient inchangé pour toutes les distances de propagation ξ [Fig. 5.13(a2)]. À l'inverse, le spectre gaussien se transforme en une encoche spectrale (pic) se déplaçant dépendamment de la position sous la non-linéarité auto-focalisante (auto-défocalisante) [Fig. 5.13(b2) et (c2)]. Les défauts spectraux apparaissent dans la région de valeurs d'intensité élevée et la plupart des contenus spectraux se concentrent à proximité de défauts avec des ondulations voisines. En dehors de ces régions, étant donné que l'intensité du faisceau est suffisamment faible, les spectres conservent toujours les distributions gaussiennes. Dans ce qui suit, nous fournirons une démonstration expérimentale de ces faisceaux d'Airy non linéaires dans les domaines spatial et spectral.

5.4.1.a Observation expérimentale du faisceau d'Airy non linéaire dans le cristal photoréfractif SBN

Pour observer expérimentalement les phénomènes obtenus numériquement ci-dessus, nous utilisons une configuration illustrée dans la Fig. 5.14.

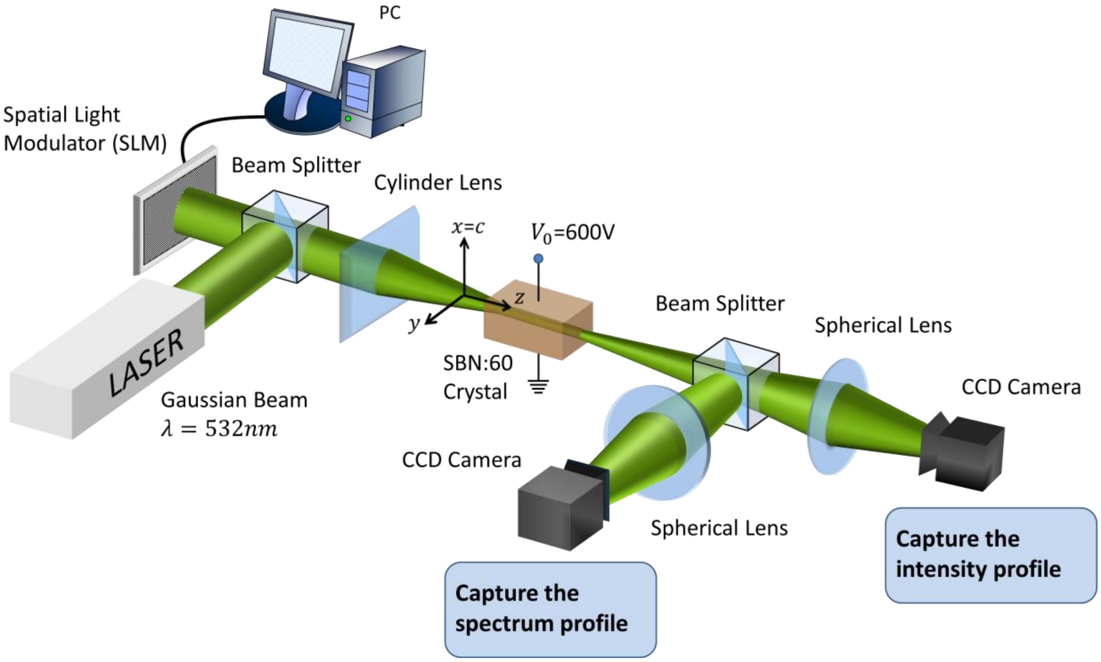

Figure 5.14: Configuration expérimentale pour mesurer la propagation non linéaire d'un faisceau d'Airy à énergie finie dans un milieu PR saturable (SBN: 60) sous non-linéarité auto-focalisante et auto-defocalisante.

Un faisceau d'Airy tronqué est créé en modulant en phase un faisceau gaussien linéairement polarisé (λ = 532nm) à travers un masque de phase cubique, chargé dans un modulateur de lumière spatiale (SLM). Le SLM est placé au plan focal (f = 40mm) d'une lentille de transformée de Fourier cylindre. La polarisation du champ électrique est orientée le long de la direction x, en parallèle avec l'axe optique c d'un cristal PR ($5\times5(c)\times10$mm) de Nitrate Borate de Strontium (SBN: 60) biaisé. Après la génération, le faisceau d'Airy est livré dans le cristal SBN, et l'intensité de sortie et les profils spectraux sont enregistrés par des caméras CCD.

Pour avoir un coefficient non linéaire $|\gamma| = 2.72$, une tension statique de 600 V ($|E| = 1.2\text{x}10^5$ V/m) est appliquée au cristal PR sur les axes optiques c. La valeur absolue de la tension de polarisation est maintenue constante tout au long de la mesure expérimentale. La détection s'effectue en capturant les échantillons de faisceau d'Airy et les spectres d'espace k au moyen de deux systèmes d'imagerie composés de deux lentilles sphériques et de deux caméras CCD. Le masque de phase cubique est déplacé électroniquement dans l'ordinateur par l'intermédiaire de l'interface graphique du logiciel qui gère le SLM. En outre, le masque de phase cubique a été mis à l'échelle intentionnellement pour correspondre à la zone concernée avec l'échelle longitudinale du cristal.

5.4.1.b Intensité de pic du faisceau d'Airy au milieu du cristal SBN

Dans le premier ensemble de mesures, des observations expérimentales ont été effectuées en décalant le masque de phase cubique dans le but d'amener l'intensité du pic au centre du cristal et le long de la direction de propagation ξ, comme l'indique la ligne blanche en pointillé II dans la Fig. 5.13 (a1). Les deux autres lignes blanches en pointillé, I et III, marquent la zone du défaut spectral localisée entre $\xi \approx 7$ et 17. En dehors de cette zone, la propagation peut être considérée comme linéaire. La figure 5.15 illustre les échantillons de faisceau d'Airy captés à la sortie du cristal SBN. La ligne verticale des Fig. 5.15 (a1) et (c1) marque la position transversale de l'intensité du pic le long de la direction s pour le faisceau d'Airy linéaire. En effet, l'intensité de sortie d'un faisceau d'Airy linéaire a une bosse principale localisée à la même position transversale que celle de la face d'entrée [Fig. 5.15 (a1)]. En présence d'une non-linéarité auto-focalisante, la Fig. 5.15 (b1) montre un modèle de sortie dont la bosse principale n'est pas auto-piégée et, par conséquent, conserve la propriété de l'auto-accélération. Cependant, le lobe principal se rétrécit et se déplace vers la droite par rapport au cas linéaire. À l'inverse, la non-linéarité auto-défaillante élargit la bosse principale de l'échantillon de sortie et entraîne un décalage vers la gauche par rapport à la sortie linéaire [Fig. 5.15 (c1)].

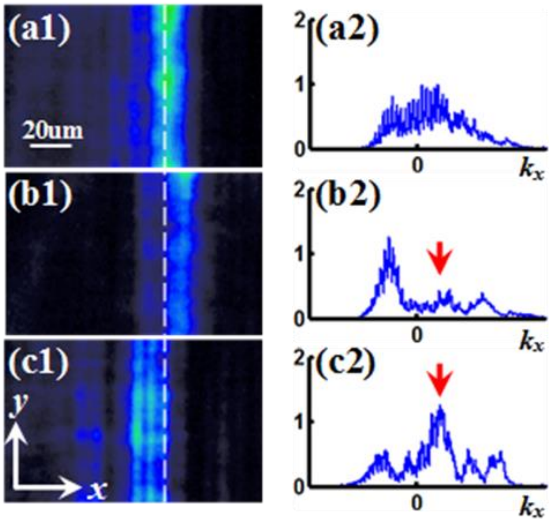

Figure 5.15: Observations expérimentales des faisceaux d'Airy se propageant dans un cristal PR biaisé en fixant son intensité de pic au milieu du cristal. De haut en bas, les figurent correspondent à la propagation du faisceau sous (a) des conditions linéaires, non linéaires (b) auto-focalisantes et (c) auto-défocalisantes. (a1-c1) montrent les échantillons de faisceau d'Airy captés à la sortie du cristal. (a2-c2) montrent les spectres aux sorties de (a1-c1). Les flèches rouges dans (a2-c2) indiquent la position des défauts spectraux dans l'espace *k*.

Dans le régime de Fourier, les spectres *k* imagés correspondants présentent un profil gaussien pour le faisceau d'Airy linéaire [Fig. 5.15 (a2)], et l'apparition d'un écart spectral et d'un défaut de pic sous des non linéarités auto-focalisants et focalisées respectivement [Figs. 5.15(b2, c2)]. Ces défauts spectraux, dont les positons sont indiqués par les flèches rouges pointant vers le bas, résident au côté droit du centre *k*-space.

5.4.1.c Intensité de pic du faisceau d'Airy à la sortie du cristal SBN

Dans un deuxième ensemble de mesures, nous avons déplacé la face de sortie du cristal le long de la direction ξ en direction de la position d'intensité de pic indiquée sur la Fig. 5.16(a1) par la ligne en pointillé blanc II. La sortie des faisceaux d'Airy dans les Fig. 5.16(a1) et (c1) présentent un comportement similaire à ceux représentés sur les Fig. 5.15(a1) et (c1). Dans l'espace *k*, le profil gaussien est toujours conservé pour le régime linéaire [Fig. 5.16(a2)], alors que sous une condition non linéaire, le défaut spectral se déplace vers le centre de l'espace de Fourier [Fig. 5.16(b2) et (c2)]. Ce comportement non linéaire est attendu car le faisceau présente une distance à demi raccourcie par rapport au premier ensemble de mesures.

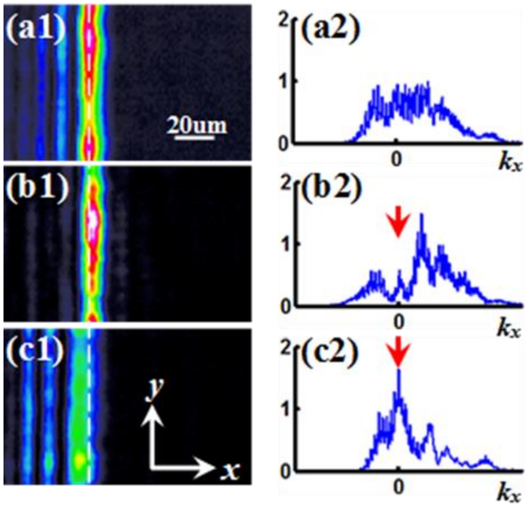

Figure 5.16: Observations expérimentales des faisceaux d'Airy se propageant dans un cristal PR polarisé en fixant son intensité de pic à la sortie du cristal. De haut en bas, les figures correspondent à la propagation du faisceau sous (a) des conditions linéaires, non linéaires (b) auto-focalisants et (c) auto-défocalisantes. (a1-c1) montrent les échantillons de faisceau d'Airy capté à la sortie du cristal. (a2-c2) montrent les spectres aux sorties dans (a1-c1). Les flèches rouges dans (a2-c2) indiquent la position des défauts spectraux dans l'espace *k***.**

5.4.2 Propagation non linéaire des pulse d'Airy

Les intérêts sur les pulses d'Airy non linéaires s'inspirent du fait que l'équation non linéaire de Schrödinger (NLSE) décrivant la propagation des pulses dans le temps a une forme mathématique similaire à la NLPWE décrivant l'évolution des faisceaux dans l'espace. En raison de cette analogie, les pulses d'Airy dans le régime non linéaire devraient se comporter de manière similaire aux faisceaux d'Airy non linéaires dans le matériau PR. Nous limiterons notre étude à l'environnement de la fibre optique, même si les pulses d'Airy pourraient également être étudiées dans les médias non linéaires en vrac. Dans la fibre optique, la propagation de l'impulse peut être décrite en suivant NLSE sans dimension :

$$\frac{\partial \varphi}{\partial \xi} = -\frac{i}{2}\operatorname{sgn}(\beta_2)\frac{\partial^2 \varphi}{\partial T^2} + i\eta|\varphi|^2 \varphi. \tag{5.12}$$

Avec $\varphi(\xi,T)=A(\xi,T)$ l'enveloppe du pulse dans les unités normalisées $\xi = z\,|\,\beta_2\,|\,/t_0^{\,2}$ et $T=(t-z/v_g)/t_0$ la distance et le temps normalisé dans le cadre de la vitesse de groupe v_g, où z et t sont la distance et le temps physique, β_2 est le coefficient de dispersion, et t_0 est une échelle de temps. Le symbole *sgn*(·) représente l'opérateur de signe, $\eta=\gamma/(t_0^{\,2}\,|\,\beta_2\,|)$ le coefficient non linéaire normalisé, où γ est le coefficient non linéaire. Dans l'Eq. (5.12), le premier terme sur le côté droit explique la dispersion de vitesse de groupe (GVD), tandis que le deuxième terme explique la non-linéarité de Kerr. Dans le régime linéaire ($\eta = 0$), l'Eq. (5.12) admet la solution Airy suivante:

$$\begin{aligned}\varphi(\xi,T) = \sqrt{2\pi}\, Ai\left[T-\varsigma^2/4+\alpha^2+v_m^2-i\,\mathrm{sgn}(\beta_2)\alpha\varsigma\right] \\ \times\exp\left(iv_m^3/3\right)\exp\left(\alpha T-i\,\mathrm{sgn}(\beta_2)\varsigma T/2\right) \\ \times\exp\left[i2\left(i\alpha+\mathrm{sgn}(\beta_2)\varsigma/2\right)^3/3-iv_m^2\left(i\alpha+\mathrm{sgn}(\beta_2)\varsigma/2\right)\right]\end{aligned}\quad, \tag{5.13}$$

dans laquelle $\varsigma=\xi+2v_m/\mathrm{sgn}(\beta_2)$ et comme dans le cas spatial α est le coefficient de troncature, v_m est le paramètre de lancement, et *Ai*(·) est la fonction d'Airy. Le pulse d'Airy suit une trajectoire de temps parabolique donnée par:

$$T_p=\varsigma^2/4-v_m^2-\alpha^2 \tag{5.14}$$

La puissance de pic maximale (MPP) est située à $\xi=-2v_m/sgn(\beta_2)$. Nous établissons délibérément le MPP à l'intérieur de la fibre à $\xi = 8$, ce qui peut être atteint en définissant $v_m = -4sgn(\beta_2)$.

L'intensité de la bosse principale et les évolutions spectrales du pulse d'Airy décrite par l'Eq. (5.13) sont tracés dans la Fig. 5.17. Cette distribution d'intensité est obtenue en éliminant les sous-lobes du pulse d'Airy et en ne laissant que la bosse principale dont la puissance instantanée est supérieure à la moitié du MPP. En tenant compte des composants spectraux, correspondant à la bosse principale de la Fig. 5.17 (a), nous pouvons constater que différentes fréquences dominent différentes distances de propagation. Sous l'effet d'une dispersion anormale, les fréquences plus basses sont responsables de l'évolution du pulse initial et les fréquences supérieures pour les propagations ultérieures, ce qui peut être vu à partir de la Fig. 5.17(b).

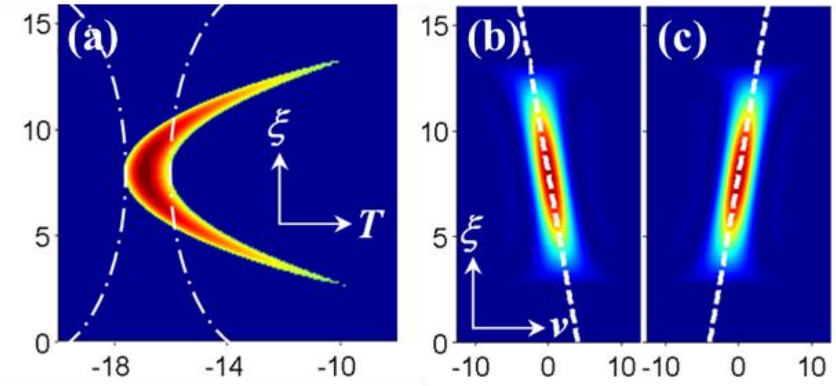

Figure 5.17: Propagation linéaire des pulses d'Airy dans une fibre optique. (a) distribution d'intensité de la bosse principale filtrée obtenue en éliminant les sous-lobes du pulse d'Airy linéaire. (b) et (c) les distributions spectrales correspondant à la bosse principale sous dispersion avec (b) anormales et (c) normale.

D'autre part, en présence d'une dispersion normale, les fréquences plus élevées sont responsables de l'évolution du pulse initial et des fréquences inférieures pour les propagations ultérieures [Fig. 5.17(c)]. Un tel changement de fréquence est linéaire avec la distance ξ (lignes blanches en pointillé sur les Fig. 5.17(b) et (c)). La fréquence instantanée du lobe principal varie linéairement (lignes pointillées sur les Fig. 5.17(b) et (c)) le long de la distance de propagation comme suit:

$$v_d = \operatorname{sgn}(\beta_2)\frac{\xi}{2} + v_m \tag{5.15}$$

5.4.2.a Propagation des pulses d'Airy non linéaires

En présence d'un effet Kerr ($\eta \neq 0$), le pulse d'Airy se comporte de façon très différente par rapport au cas linéaire. Les évolutions non linéaires sous une dispersion anormale et normale, respectivement, sont illustrées dans les Fig. 5.18(a) et 5.19(b). Les lignes en pointillés blancs marquent la trajectoire parabolique suivie par le pulse d'Airy en régime linéaire ($\eta = 0$). Les MPP apparaissent proches de la distance de propagation $\xi = 8$. Sous une dispersion anormale, la bosse principale tend à réduire sa durée temporelle, ce qui montre une accélération plus rapide par rapport au pulse d'Airy linéaire [Fig. 5.18(a)]. Ce comportement non linéaire est analogue au cas d'un faisceau d'Airy spatial sous une non-linéarité auto-focalisante. En regardant le domaine spectral, à chaque distance ξ le contenu spectral est concentré en un défaut négatif, formé par une coche avec deux pics principaux à l'extérieur [Fig. 5.18(c)].

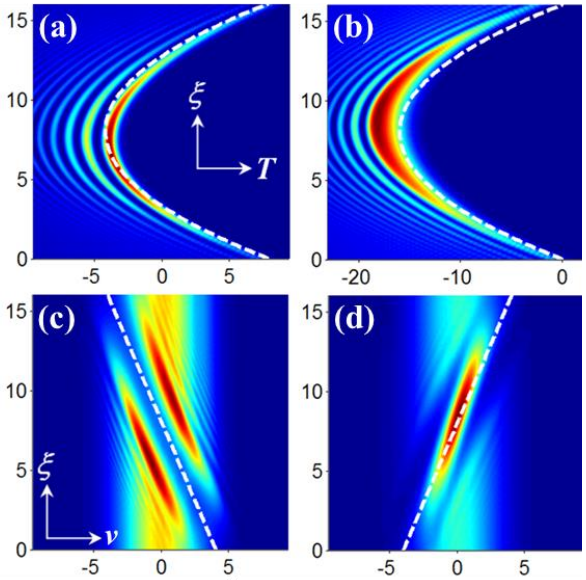

Figure 5.18: Propagation des pulse d'Airy dans une fibre optique non linéaire. (a) et (b) distributions d'intensité sous une dispersion anormale et normale, respectivement. (c) et (d) distributions spectrales correspondant à (a) et (b).

Sous l'état de dispersion normale, le pulse d'Airy présente une bosse principale qui s'élargit dans le temps, analogue à la dynamique non linéaire d'un faisceau d'Airy sous la non-linéarité auto-focalisante [Fig. 5.18 (b)]. Cette expansion temporelle indique une accélération plus lente que celle du régime linéaire. Dans l'espace de Fourier, le contenu spectral se transforme en un défaut positif constitué par un seul pic à chaque distance de propagation ξ [Fig. 5.18(d)]. Une autre caractéristique intéressante pour les spectres non linéaires du pulse d'Airy est une ondulation spectrale qui apparaît près de la région des défauts. Ces échantillons sont causés par l'interférence entre le spectre modifié de la bosse principale et celui des sous-lobes, ce qui peut également induire une non-linéarité. La puissance de pic des sous-lobes tend à augmenter pendant la propagation sous la dispersion anormale, alors qu'elle tend à diminuer sous une dispersion normale le long de ξ. C'est la raison pour laquelle les ondulations de la Fig. 5.18(c) sont plus prononcées que ceux de la Fig. 5.18(d).

Bien que les chemins spectraux soient sensés suivre le décalage analytique v_d (lignes en pointillés blancs), un certain écart se produit en raison de la nature non linéaire de propagation des pulses. Cette différence est plus prononcée pour une dispersion normale que pour la dispersion anormale. En conséquence directe de cette analyse, le changement spectral réel peut être estimé en corrigeant le décalage linéaire v_d à travers le paramètre de correction ε comme: $v_{dc} = \varepsilon v_d$. Le paramètre ε est inférieur à 1 dans le cas d'une dispersion anormale, alors qu'il est supérieur à 1 pour une dispersion normale.

5.4.2.b Observation expérimentale

Le schéma dans la Fig. 5.19 illustre la configuration expérimentale utilisée pour réaliser le contrôle spectral comme mentionné ci-dessus.

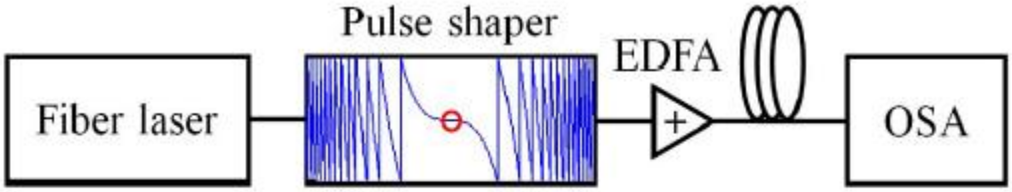

Figure 5.19: Configuration expérimentale pour l'observation du contrôle spectral des pulses d'Airy non linéaires. EDFA et OSA représentent respectivement un amplificateur à fibre dopée à l'erbium et un analyseur de spectre optique. La trame à l'intérieur du formateur des pulses montre schématiquement la structure de la phase cubique enveloppée entre -π et π où le cercle indique son centre.

Un pulse gaussien d'entrée, générée par un laser à fibre accordable en longueur d'onde sous-picoseconde de Pritel Inc., est modulée en phase dans le domaine spectral par une structure de phase cubique ($\omega_S = 2\pi \times 1011$), téléchargée dans un modificateur des pulses. De cette façon, le pulse gaussien d'entrée est remodelée en pulse d'Airy. La sortie du pulse d'Airy est ensuite envoyée dans une fibre non linéaire connectée à un analyseur de spectre optique (OSA), utilisé pour mesurer les spectres de sortie de la fibre non linéaire. La puissance du pulse est accordée au moyen d’un amplificateur à fibre dopée à l’erbium, qui est utilisé pour amplifier le pulse d’Airy juste avant la propagation dans la fibre non linéaire.

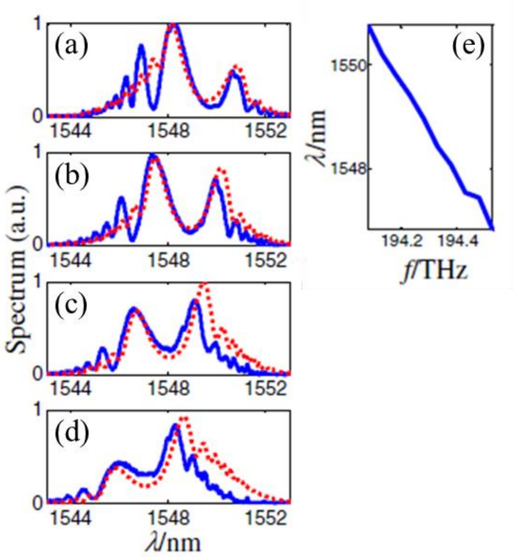

Figure 5.20: Contrôle du changement de fréquence des pulses d’Airy non linéaires sous dispersion anormale dans une fibre LEAF. Comparaison des résultats expérimentaux (lignes bleues solides) avec les prédictions théoriques (lignes en pointillé). De haut en bas, les figures représentées dans (a-d) correspondent aux résultats expérimentaux et analytiques obtenus en déplaçant la fréquence centrale f_m de la structure de phase cubique aux fréquences: (a) f_m = 194.2, (b) 194.3, (c) 194.4 et (d) 194.5 THz. (e) trace les positions des défauts du pic spectral dans (a) en fonction de f_m.

Pour observer les pulses d’Airy sous une dispersion anormale, nous avons effectué l’expérience en injectant le pulse d’Airy dans une fibre décalée en dispersion (DSF) de 6,6 km dont la longueur d’onde de dispersion nulle est située à 1559 nm. Pour les pulses d’Airy sous dispersion normale, l’expérience a été réalisée en utilisant une fibre de grande surface efficace (LEAF) de 5 km de longueur. Les spectres mesurés sont représentés sur les Fig. 5.10 (a), (b), (c) et(d) et 5.21 (a), (b), (c) et (d). Ces spectres correspondent à différentes positions de déplacement de la fréquence centrale $f_m = 2\pi v_m$ dans la structure de phase cubique du formateur des pulses. Nos résultats (ligne bleue solide) montrent que le spectre se concentre en un (défaut positif) ou deux pics majeurs (défaut négatif). Nous notons également que les défauts se déplacent vers une longueur d’onde plus courte car la fréquence centrale de la structure de phase cubique est décalée vers des fréquences plus longues. Ce comportement est en accord avec les résultats numériques obtenus en simulant la propagation non linéaire d’une pulse d’Airy avec les mêmes paramètres utilisés dans le réglage expérimental (ligne en pointillé rouge sur les Fig. 5.20(a), (b), (c) et (d) et 5.21(a), (b), (c) et (d)). Pour estimer le paramètre de correction ε correspondant à l’évolution spectrale des défauts, nous avons tracé dans les Fig. 5.20(e) et 5.21(e) la position centrale des défauts en fonction de la fréquence centrale dans la structure de phase cubique. Les positions des défauts ont une évolution linéaire avec la fréquence centrale du masque et les paramètres de correction ε obtenus par un ajustement linéaire de la courbe sont estimés à 1,07 et 0,93 respectivement dans des conditions de dispersions normales et anormales.

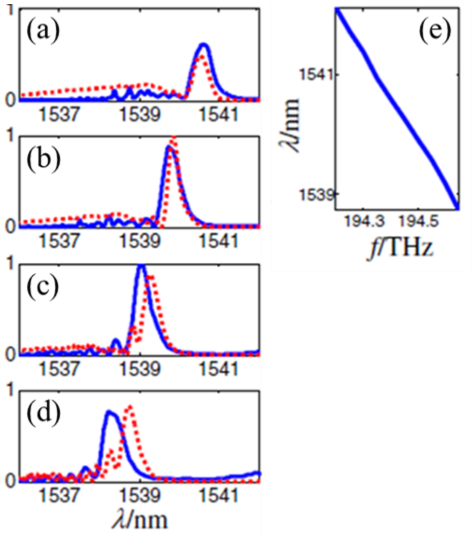

Figure 5.21: Contrôle du changement de fréquence des pulses d’Airy non linéaires sous dispersion normale dans un fibre DSF. Comparaison entre résultats expérimentaux (lignes bleues solides) et prédictions théoriques (lignes en pointillé). De haut en bas, les figures aux résultats expérimentaux et analytiques obtenus en variant la fréquence centrale f_{m} de la structure de phase cubique, avec: (a) f_{m} = 194.35, (b) 194.45, (c) 194.55 et (d) 194,65 THz. (e) représente les positions des défauts du pic spectral dans (a) en fonction de f_{m}.

5.5 Conclusions

Dans cette dissertation, nous avons étudié la dynamique de propagation des paquets d'ondes auto-accélérants dans les régimes de propagation linéaire et non linéaire. Les propriétés de ces paquets d'ondes ont été étudiées en analysant et réglant soigneusement les propriétés intrigantes de leurs composantes spectrales dans le régime de Fourier. Nous avons introduit et démontré expérimentalement une approche polyvalente pour générer et contrôler la dynamique d'espace libre des faisceaux auto-accélérant à une ou à plusieurs dimensions, fondée sur l'existence d'un mappage spectre-distance. Selon un tel mappage, différentes fréquences spatiales sont mappées à différentes positions pendant que le faisceau se propage. Dans notre étude, nous avons également généralisé le concept de gradient spatial de phase spectrale aux deux régimes de propagation (2+1) et (3+1)D. De plus, en profitant du fait que les spectres de lobes principaux associés à ces paquets d'ondes sont suffisamment confinés, nous avons également montré la possibilité d'améliorer significativement le confinement énergétique des faisceaux auto-accélérants 2D ainsi que des balles d'Airy linéaires optiques. Notre approche repose sur la modulation du spectre d'entrée afin de faire correspondre le contenu spectral du faisceau / balle associé au lobe principal tout au long de la propagation. Enfin, nous avons étudié la dynamique des faisceaux d'Airy et des pulses se propageant dans des conditions non linéaires. Dans le domaine spatial, nous avons proposé un contrôle des trajectoires et des spectres spatiaux pour les faisceaux d'Airy non linéaires se propageant dans un cristal photoréfractif sous l'action de non-linéarité auto-focalisante ou auto-défocalisante. De plus, dans le domaine temporel, nous avons étudié la modulation auto-phase des pulses d'Airy entrainée par la non-linéarité de Kerr (c'est-à-dire l'effet de modulation auto-phase). Nous avons démontré numériquement et expérimentalement qu'en déplaçant la structure de phase cubique dans le domaine de Fourier, les paquets spatiaux et temporels des ondes d'Airy sont en mesure de conserver leur propriété d'accélération sous un régime non linéaire. En particulier, les paquets d'ondes d'Airy non linéaires présentent des caractéristiques de propagation similaires à celles du régime linéaire, mais leurs caractéristiques spectrales sont cependant complètement différentes.

Conclusions

In this thesis, we have investigated the propagation dynamics of self-accelerating wave packets in both the linear and nonlinear propagation regimes. The properties of such wave packets have been studied by carefully engineering the intriguing properties of their spectral components in the Fourier regime.

After a succinct overview of the state-of-the-art of the field and associated concepts, we have introduced and experimentally demonstrated, in Chapter 2, a versatile approach to generate and control the free-space dynamics of 1D single- or multi-path self-accelerating beams. Based on the concept of spatial phase gradient, we reported on the existence of a spectrum-to-distance mapping. According to such a correspondence, different spatial frequencies are being mapped to different positions while the beam is propagating. For self-accelerating beams with a single convex path, the key frequency monotonously varies along propagation. When the beam sub-lobes are filtered out, the spectrum associated to the residual main lobe follows the evolution of the key spatial frequency. For multi-path self-accelerating beams, each beam component traveling along a different trajectory is related to a different portion of the spectrum. At different distances, the main lobe spectrum of each beam component is linked to a different key spatial frequency within the corresponding spectral portion. The properties of these beams, such as self-bending and self-healing, are endowed with a new understanding in term of frequency. Thanks to our approach, the beam path can be predicted from the *a priori* knowledge of the applied phase modulation in the Fourier domain. Conversely, the spectral phase to be imprinted on the spectrum can be readily estimated from theory, and this for any desired convex beam path. We have also proved that our scheme can be applied to large angle (i.e. non-paraxial) and vector self-accelerating beams. Incidentally, these results provide a clear explanation of the fact that Airy beam are breaking down while propagating under non-paraxial condition.

In addition, we also studied the combined effects of both phase and amplitude spectral modulation on the propagation dynamics of both paraxial and non-paraxial accelerating beams. By applying a Heaviside-shape amplitude modulation, we observed that the convex path corresponding to the suppressed key spatial frequencies was modified and turned into a straight path. When considering a "spectral well" amplitude structure, we reported the formation of a "V"-shaped beam path, that we used as an elementary cell for constructing periodic self-accelerating beams. Such periodic beams can be properly described through the concept of spectrum-to-distance mapping.

In Chapter 3, we have generalized the concept of spatial spectral phase gradient to the both (2+1) and (3+1) D propagation regimes. We demonstrated that the trajectory of higher dimension wave packets can also be determined by a spectrum-to-distance mapping, where different key frequencies in the spectrum are mapped to different main hump localizations. We numerically verified our analysis by designing the spectral phase modulations corresponding to three typical beam trajectories in the (2+1) D regime. Furthermore, by taking advantage of the fact that the main lobe spectra associated to these wave packets are confined in both the (2+1) and (3+1) D regimes, we also showed the possibility of significant energy-confinement enhancement of both 2D self-accelerating beams and optical linear Airy bullets. Our approach is based on reshaping the input spectrum in order to match the spectral content of the beam/bullet associated to the main lobe throughout propagation.

For 2D self-accelerating beams, the spectrum associated to the filtered main lobe is reduced to a small spot, progressively shifting along the 45° radial direction of the Fourier plane during propagation. As a consequence, the entire main lobe spectrum remains confined within a "spectral stripe" with the same orientation. The residual spatial frequencies located outside this stripe are only 'in charge' of the beam sub-lobes. Therefore, we proposed a rather straightforward way to generate energetically-confined 2D self-accelerating beams by reshaping the input circular Gaussian beam into an elliptical Gaussian shape, and illuminating the SLM phase mask with a spectral energy mostly concentrated within this spectral stripe.

For several convex trajectories, we experimentally observed a significantly increase of the peak intensity (more than 60% compared to traditional 2D self-accelerating beams), and a corresponding reduction of the beams transverse spatial expansion. We also verified that the newly obtained “short-tail beams” are capable of preserving all the intrinsic characteristics of 2D self-accelerating beams, such as bending propagation and self-healing.
In the (3+1) D regime, the spectrum associated to main lobe of an“classical” Airy^3 bullet exhibits a small sphere-shaped profile. In the spatio-temporal Fourier space, the main lobe spectrum evolves along a diagonal in such a way that its entire spectral content is localized into an elliptical cylinder. By appropriately compressing the input spectrum of an Airy^3 bullet in order to match closely this spectral cylinder, we numerically demonstrated a significant enhancement of its spatio-temporal energy confinement. We observed that the spectral compression has the potential to generate an Airy^3 bullet of a greatly reduced spatio-temporal expansion. The overall energy confinement of the compressed bullet can be improved by a factor above 50. In this case, we once again verified that the bullet peculiar properties (i.e. non-diffractive, non-dispersive and self-healing) are conserved for the desired trajectory over the whole propagation range considered.

In Chapter 4, we investigated the dynamics of both Airy beams and pulses propagating under nonlinear conditions. In the spatial domain, we proposed a way to control both trajectories and spatial spectra for nonlinear Airy beams propagating in a saturable photorefractive (PR) crystal, under the action of either a self-focusing or defocusing nonlinearity. In the temporal domain, we studied the self-phase modulation (SPM) of Airy pulses mediated by a Kerr nonlinearity, when those propagate in optical fibers featured with either a normal or anomalous dispersion. In general, an Airy wave packet tends to break up, especially under a self-focusing nonlinearity. Nevertheless, we have demonstrated numerically and experimentally that by shifting the cubic phase structure in the Fourier domain, spatial and temporal Airy wave packets are able to preserve their accelerating property in the presence of either a self-focusing or -defocusing nonlinearity. In particular, nonlinear Airy wave packets show propagation features similar to those shown in the linear regime, but their spectral characteristics are completely different. In the temporal domain, under the action of nonlinearity, the profile of an Airy beam is shifted transversally over propagation, while its main lobe exhibit either a spatial compression/expansion depending on the sign of nonlinearity. However, the most relevant effect of nonlinearity is observed in the Fourier space, for which the Gaussian spectrum associated to a linear Airy beam undergoes a dramatic reshaping. Under a self-focusing nonlinearity, the spectrum of the nonlinear Airy beam exhibits a self-shifting spectral defect, resulting in a notch between two peaks. Conversely, in the presence of a self-defocusing nonlinearity, the nonlinear spectrum presents a self-shifting spectral defect, formed by a single peak. Similar spectral reshaping is also observed when considering an Airy pulse within a temporal framework. Indeed, the linear Gaussian spectrum of an Airy pulse under the combined effects of nonlinearity and dispersion is reshaped into a self-shifting spectral peak, or a self-shifting spectral notch (depending on the sign of the dispersion), analogously to its spatial counterpart. We observed that, in the nonlinear regime, it is possible to establish a linear correspondence between the central frequency of the defect and the propagation distance. We furthermore provide a physical explanation to the observed preservation of the bending acceleration, by studying the nonlinear accelerating modes in photorefractive media. We have found that such a spectral reshaping is associated with the evolution of these modes. In particular, their spectral profiles show similar defect shapes as observed for nonlinear Airy beams, indicating that the Airy beam preserve its acceleration as it evolves into one nonlinear mode. In the temporal domain, we also envisaged the possibility of wavelength section by simply shifting the applied cubic phase structures. Furthermore, we have demonstrated that the propagation length can be retrieved from the characterization of the spectral defect observed at the output of the fiber.

In conclusion, we have shown that self-accelerating wave packets are characterized by intriguing spectral features. Notably, it is possible to define a correspondence between the real and Fourier domain. In the linear regime, the propagation distance is mapped into the spectrum of the main lobe while in the nonlinear regime (typically induced in Kerr and photorefractive media), we found out the existence of another type of mapping induced by the nonlinearity itself, i.e. between the central frequency of the defect and the propagation distance. Using these properties, not only we can generate arbitrary trajectory convex paths, but we have shown the ability to control and optimize their linear and nonlinear propagation, as well as their associated energy confinement enhancement. We therefore expect that the work reported in this thesis will find direct and widespread applications in optics, as well as in other areas of physics, especially due to the ubiquitous nature of such peculiar wave-packets in numerous systems intrinsically described by wave propagation dynamics.

Appendix A

A.1 Software and numerical methods

Numerical simulations reported in this thesis have been carried out by using the tools provided with the commercial software MATLAB®. The wave packets evolutions shown in Chapter 2 and 3 have been computed by solving the (1+1)D, (2+1)D and (3+1)D Helmholtz equations in the paraxial approximation (i.e. by neglecting the second derivative along the propagation direction) via the Fast Fourier Transform (FFT) method. In particular, for the (1+1)D and (2+1)D, a number of points equal to 4096 has been used for each coordinates, both in real and spatial domain. For the (3+1)D, only 1028 points have been computed for each direction, since in the latter case the requirement of memory storage for too much demanding for the available workstation. The time of execution was around 5 minutes for the simulations accounting until two dimensions, whereas each simulation regarding the Airy bullet took more than half an hour. The intensity field distributions have been plotted by using the MATLAB functions: plot, pcolor, and isorsurface. The main lobe spectral evolutions are obtained by truncating the wave packet main lobes from the overall wave packet intensity profiles with opportunely designed rectangular filters. The wave packet trajectories have been extracted from Eq. (2.5) by writing an opportune sub-routine in order to isolate the key spatial frequencies from the applied phase mask and to estimate the trajectory from Eq. (2.6). The phase mask structures numerically calculated in Chapter 2 have been extracted by solving an integral equation that involves the phase modulation derivative $\partial\rho\left(k_x\right)/\partial k_x$ which is analytically retrieved from Eqs. (2.5) and (2.3).

In the nonlinear regime, the Airy wave packet evolutions have been carried out by using the standard Split Step Fourier Transform method (SSFM). This method consists in the separation of the linear from the nonlinear part of the differential equation. In such a way, the pulse propagation have been solved by alternatively solving first the linear term (by FFT) and then the nonlinear term by following particular procedures depending on the computational complexity of the solution. In particular, some different cases have been treated by changing the values of amplitude and nonlinearities. The nonlinear accelerating modes have been found by using the Runge-Kutta (R4K) numerical method. They have been found by choosing as initial conditions an Airy solution and its first-order derivative for different values of their amplitude. Once obtained, the accelerating mode propagations have been simulated by SSFM using as initial condition the estimated nonlinear mode.

Appendix B

B.1 List of scientific journals

1. **Domenico Bongiovanni**, Benjamin Wetzel, Yi Hu, Zhigang Chen and Roberto Morandotti, "*Optimal compression and energy confinement of optical Airy^3 bullets*," Optics Express **24**(23), 26454 (2016).

2. Benjamin Wetzel, **Domenico Bongiovanni**, Michael Kues, Yi Hu, John Michael Dudley, Stefen Wabnitz, Zhigang Chen and Roberto Morandotti, "*Experimental Generation of Riemann Waves in Optics: A Route to Shock Wave Control*," Physical Review Letters **117**(7), 073902 (2016).

3. **Domenico Bongiovanni**, Yi Hu, Benjamin Wetzel, Raul Amaury Robles, Gregorio Mendoza González, Erwin Armando Marti-Panameño, Zhigang Chen and Roberto Morandotti, "*Efficient optical energy harvesting in self-accelerating beams*," Sci. Rep. **5**, 13197 (2015).

4. Yi Hu, **Domenico Bongiovanni**, Zhigang Chen and Roberto Morandotti, "*Multipath multicomponent self-accelerating beams through spectrum-engineered position mapping*," Physical Review A **88**(4), 043809 (2013).

5. Yi Hu, **Domenico Bongiovanni**, Zhigang Chen and Roberto Morandotti, "*Periodic self-accelerating beams by combined phase and amplitude modulation in Fourier space*," Optics Letters **38**(17), 3387-3389 (2013).

6. Yi Hu, Ming Li, **Domenico Bongiovanni**, Matteo Clerici, Jianping Yao, Zhigang Chen, José Azaña and Roberto Morandotti "*Spectrum to distance mapping via nonlinear Airy pulses*," Optics Letters **38**(3), 380-382 (2013).

7. Yi Hu, Zhe Sun, **Domenico Bongiovanni**, Daohong Song, Zhuoyi Ye, Cibo Lou, Jingjun Xu, Zhigang Chen, and Roberto Morandotti, "*Reshaping the trajectory and spectrum of nonlinear Airy beams*," Optics Letters **37**(15), 3201-3203 (2012).

B.2 List of conference proceedings

1. **Domenico Bongiovanni**, Benjamin Wetzel, Yi Hu, Zhigang Chen and Roberto Morandotti, "*Optimal energy confinement of optical Airy^3 bullets,"* in CLEO, OSA Technical Digest (Optical Society of America, 2017), paper FW1D.4.

2. Benjamin Wetzel, **Domenico Bongiovanni**, Michael Kues, Yi Hu, John Michael Dudley, Stefen Wabnitz, Zhigang Chen and Roberto Morandotti, "*Experimental observation of inviscid Burgers' equation dynamics in nonlinear fiber optics,"* in CLEO, OSA Technical Digest (Optical Society of America, 2016), paper FF2A.1.

3. Benjamin Wetzel, **Domenico Bongiovanni**, Michael Kues, Yi Hu, John Michael Dudley, Stefen Wabnitz, Zhigang Chen and Roberto Morandotti, "*Inviscid Burgers' equation and Riemann waves in optics,"* in Photonics and Fiber Technology, OSA Technical Digest (Optical Society of America, 2016), paper NT5A.3.

4. Benjamin Wetzel, **Domenico Bongiovanni**, Michael Kues, Yi Hu, John Michael Dudley, Stefen Wabnitz, Zhigang Chen and Roberto Morandotti, "*Inviscid Burgers' equation and Riemann waves in optics,"* in Frontiers in Optics, OSA Technical Digest (Optical Society of America, 2016), paper FTu3I.1.

5. Benjamin Wetzel, **Domenico Bongiovanni**, Michael Kues, Yi Hu, John Michael Dudley, Stefen Wabnitz, Zhigang Chen and Roberto Morandotti, *"Experimental signature of Riemann wave shoaling in optical fiber,"* in European CLEO, OSA Technical Digest (Optical Society of America, 2015), paper CD_13_5.

6. **Domenico Bongiovanni**, Yi Hu, Raul Amaury Robles, Gregorio Mendoza González, Erwin Armando Marti-Panameño, Zhigang Chen and Roberto Morandotti, "*Dynamical two-dimensional accelerating beams and enhancement of their peak intensities,"* in CLEO, OSA Technical Digest (Optical Society of America, 2014), paper FM4D.5.

7. Yi Hu, **Domenico Bongiovanni**, Zhigang Chen, Roberto Morandotti, *"Free-space trajectory management of self-accelerating beams through Fourier-space phase engineering* in CLEO, OSA Technical Digest (Optical Society of America, 2013), paper QM2E.4.

8. Yi Hu, Ming Li, **Domenico Bongiovanni**, Matteo Clerici, Jianping Yao, Zhigang Chen, José Azaña and Roberto Morandotti, "Spectrum to distance mapping via nonlinear Airy pulses," in Nonlinear Optics, OSA Technical Digest (Optical Society of America, 2013), paper NW2A.7.

9. Yi Hu, Ming Li, **Domenico Bongiovanni**, Matteo Clerici, Jianping Yao, Zhigang Chen, José Azaña and Roberto Morandotti, "*High-intensity self-accelerating Airy pulses and controllable spectral shifting in nonlinear Kerr media,*" in CLEO, OSA Technical Digest (Optical Society of America, 2012), paper QM3E.4.

10. Yi Hu, Zhe Sun, **Domenico Bongiovanni**, Daohong Song, Zhuoyi Ye, Cibo Lou, Jingjun Xu, Zhigang Chen, and Roberto Morandotti, *"Nonlinear control of the trajectory and spectrum of Airy beams,"* in Advanced Photonics Congress, OSA Technical Digest (Optical Society of America, 2012), paper NTu3D.4.

B.3 List of peer reviewed conferences

1. **Domenico Bongiovanni**, Benjamin Wetzel, Yi Hu, Zhigang Chen and Roberto Morandotti, "*Energy Confinementof Enhancement of optical Airy^3 Bullets***,***" Photonics North*, Ottawa, (ON), Canada, June 2017. *(Oral Presentation)*

2. **Domenico Bongiovanni**, Benjamin Wetzel, Yi Hu, Zhigang Chen and Roberto Morandotti, "*Peak Intensity and Energy Confinement Enhancementof Airy^3 Bullets," CAP Congress*, Ottawa, (ON), Canada, June 2016. *(Poster Presentation)*

3. **Domenico Bongiovanni**, Benjamin Wetzel, Yi Hu, Zhigang Chen and Roberto Morandotti, "*Spatio-temporal Confinementof Airy^3 Bullets," Colloque de Plasma Québec*, Montréal, (QC), Canada, June 2016. *(Poster Presentation)*

4. Benjamin Wetzel**, Domenico Bongiovanni**, Michael Kues, Yi Hu, Zhigang Chen, Stefano Trillo, John Michael Dudley, Stefen Wabnitz, and Roberto Morandotti, *"The Inviscid Burgers' Equation Dynamics in Nonlinear Fiber Optics", Nonlinear Waves-Theory and Applications*, Beijing, China (2016). *(Invited Oral Presentation)*

5. Benjamin Wetzel**, Domenico Bongiovanni**, Michael Kues, Yi Hu, Zhigang Chen, Stefano Trillo, John Michael Dudley, Stefen Wabnitz, and Roberto Morandotti, *"The Inviscid Burgers' Equation in Nonlinear Fiber Optics," Frontiers in Optics*, Rochester, United States (2016). *(Invited Oral Presentation)*

6. Benjamin Wetzel**, Domenico Bongiovanni**, Michael Kues, Yi Hu, Zhigang Chen, Stefano Trillo, John Michael Dudley, Stefen Wabnitz, and Roberto Morandotti, "*Observation of Inviscid Burgers' Equation Dynamics in Nonlinear Fiber Optics," Photonics North*, Québec city, (QC), Canada, May 2016. *(Oral Presentation)*

7. **Domenico Bongiovanni**, Benjamin Wetzel, Yi Hu, Zhigang Chen and Roberto Morandotti, "*Intensity Enhancement of Self-Accelerating Beams," IONS-NA*, Québec city, (QC), Canada, May 2016. *(Poster Presentation)*

8. **Domenico Bongiovanni**, Benjamin Wetzel, Yi Hu, Zhigang Chen and Roberto Morandotti, "*Spatio-temporal confinement of Airy*^{3} *bullets," Photonics North*, Ottawa, (ON), Canada, June 2015. *(Oral Presentation)*

9. **Domenico Bongiovanni**, Yi Hu, Benjamin Wetzel, Alessandro Tomasino, Raul Amaury Robles, Gregorio Mendoza González, Erwin Armando Marti-Panameño, Zhigang Chen and Roberto Morandotti, "*Efficient optical energy harvesting in self-accelerating beams," Colloque de Plasma Québec*, Montréal, (QC), Canada, June 2015. *(Poster Presentation)*

10. **Domenico Bongiovanni**, Yi Hu, Benjamin Wetzel, Alessandro Tomasino, Raul Amaury Robles, Gregorio Mendoza González, Erwin Armando Marti-Panameño, Zhigang Chen and Roberto Morandotti, "*Two-dimensional accelerating beams along arbitrary trajectories and enhancement of their peak intensities," CAP Congress*, Edmonton, (AB), Canada, June 2015. *(Poster Presentation)*

11. Benjamin Wetzel**, Domenico Bongiovanni**, Michael Kues, Yi Hu, John Michael Dudley, Stefen Wabnitz, Zhigang Chen and Roberto Morandotti, "*Experimental Observation of Riemann Wave Shoaling in Nonlinear Optical Fiber," Banff International Research Station*, Banff, (AB), Canada, May 2015. *(Invited Oral Presentation)*

12. **Domenico Bongiovanni**, Yi Hu, Benjamin Wetzel, Alessandro Tomasino, Raul Amaury Robles, Gregorio Mendoza González, Erwin Armando Marti-Panameño, Zhigang Chen and Roberto Morandotti, "*Two-dimensional accelerating beams and enhancement of their peak intensities," Fotonica*, Torino, Italy, May 2015. *(Oral Presentation)*

13. Alessandro Tomasino, Manoj Kumar Mridha, Anna Mazhorova, Diego Caraffini, Holger Breitenborn, Matteo Clerici, Marco Peccianti, Luca Razzari, **Domenico Bongiovanni**, A. C. Cino, Salvatore Stivala, Alessandro Busacca and Roberto Morandotti, "*Two-wire waveguide-based THz spectral filter," Fotonica*, Torino, Italy, May 2015. *(Oral Presentation)*

14. **Domenico Bongiovanni**, Yi Hu, Raul Amaury Robles, Gregorio Mendoza González, Erwin Armando Marti-Panameño, Zhigang Chen and Roberto Morandotti, "*Dynamical two-dimensional accelerating beams and enhancement of their peak intensities," Photonics North*, Montréal, (QC), Canada, June 2014. *(Oral Presentation)*

15. Yi Hu, **Domenico Bongiovanni**, Zhigang Chen, and Roberto Morandotti, "*Periodic self-accelerating beams along convex trajectories,*" *CAP Congress*, Sudbury, (ON), Canada, June 2014. *(Poster Presentation)*

16. **Domenico Bongiovanni**, Yi Hu, Zhigang Chen, and Roberto Morandotti, "*Trajectory management of self-accelerating beams through Fourier-space phase engineering,*" *CAP Congress*, Sudbury, (ON), Canada, June 2014. *(Poster Presentation)*

17. Yi Hu, **Domenico Bongiovanni**, Zhigang Chen, and Roberto Morandotti, "*Management of self-accelerating beams in free space,*" *Colloque de Plasma Québec,* Montréal, (QC), Canada, May 2014. *(Poster Presentation)*

18. Yi Hu, **Domenico Bongiovanni**, Zhigang Chen, and Roberto Morandotti, "*Beam localization management in free space,*" *IONS-NA8*, Montréal, (QC), Canada, May 2014. *(Poster Presentation)*

19. Yi Hu, **Domenico Bongiovanni**, Zhigang Chen, and Roberto Morandotti, "*Beam trajectory management in free space,*" *Photonics North*, Ottawa, (ON), Canada, June 2013. *(Oral Presentation)*

20. Yi Hu, **Domenico Bongiovanni**, Zhigang Chen, and Roberto Morandotti, "*Free-space zigzag beams along convex trajectories*," *Photonics North*, Ottawa, (ON), Canada, June 2013. *(Oral Presentation)*

21. Yi Hu, **Domenico Bongiovanni**, Zhigang Chen, and Roberto Morandotti, "*Self-accelerating optical beams along zigzag convex trajectories,*" *IONS-NA5*, Ottawa, (ON), Canada, June 2013. *(Poster Presentation)*

22. Yi Hu, **Domenico Bongiovanni**, Zhigang Chen, and Roberto Morandotti, "*Spectrum and trajectory control of nonlinear Airy beams,*" *CAP Congress*, Montréal, (QC), Canada, May 2013. *(Poster Presentation)*

23. **Domenico Bongiovanni**, Yi Hu, Zhigang Chen, and Roberto Morandotti, "*Peak intensity delivery and spectrum-reshaping control of nonlinear Airy beams,*" *CAP Congress*, Montréal, (QC), Canada, May 2013. *(Poster Presentation)*

24. Yi Hu, **Domenico Bongiovanni**, Zhigang Chen, and Roberto Morandotti, "*Generation of zigzag beams along convex trajectories,*" *Colloque de Plasma Québec*, Montréal, (QC), Canada, May 2013. *(Oral Presentation)*

25. Yi Hu, Zhe Sun, **Domenico Bongiovanni**, Daohong Song, Zhuoyi Ye, Cibo Lou, Jingjun Xu, Zhigang Chen, and Roberto Morandotti, "*Tunable trajectory and spectra reshaping of Airy beams in biased photorefractive crystal*," *Photonics North*, Montréal, (QC),Canada, June 2012. *(Poster Presentation)*

26. **Domenico Bongiovanni**, Yi Hu and Roberto Morandotti, "*Peak intensity delivery and spectrum-reshaping control of nonlinear Airy beams*," *Colloque de Plasma Québec*, Montréal, (QC), Canada, May 2012. *(Oral Presentation)*

Acknowledgements

Firstly, I would like to express my very special thanks to Prof. Roberto Morandotti, for giving me the opportunity to join his research group as a PhD student within INRS international doctoral program, especially given the particular moment of my life. In these five years, he has followed me so carefully and patiently during both the ongoing research project and the dissertation preparation. Whenever I was discouraged, he cheered me up, teaching me that academic research is very different from book studying. How cannot I mention our countless conversations regarding a widespread range of topics? Thank you very much, dear Professor, for such an experience. I will never forget it.

Special acknowledgments also go to Prof. Yi Hu and Dr. Benjamin Wetzel, who were the principal collaborators of my research on self-accelerating beams. They introduced me to this research field and taught me numerous useful and fruitful skills. They also followed me during these five years of PhD studies, and their role and patience have been more than essential in obtaining the results presented here. In addition, they have helped me a lot in the moments of discouragement.

I would like to sincerely thank all the people who have trusted and pushed me to do my best during these five years. I really appreciate their support, and their willingness to stay close to me all this time.

An additional thank goes to all the members of the nonlinear photonics group, and also to all the people and students of the INRS-EMT, with whom I have shared unforgettable experiences. In particular, I would like to thank all the colleagues who are also my friends, and whose names I will not mention, not to forget anyone.

I would like to express my sincere thanks to Rosalia and Santina Bongiovanni, my sisters, whose presence is indispensable for both me and my choices. Thanks to my brother in law Vittorio Lucá, my niece Noemi Lucá and my nephew Andrea Lucá.

Last, but not least, I would like to thank my dear parents. Although my dad, Salvatore Bongiovanni, is not alive anymore, I will always be grateful to him for everything he taught me and everything he did for me and my family. Finally, I express my most special thanks to my mum Vincenza Puccio, the only person who really knows and understand me. In order to support me, she moved to Canada and lived with me during these five years.

This thesis is dedicated to her.

References

1. B. E. Saleh, M. C. Teich, and B. E. Saleh, *Fundamentals of Photonics*. (Wiley New York, 1991).
2. M. Born and E. Wolf, *Principles of optics: electromagnetic theory of propagation, interference and diffraction of light*. (CUP Archive, 2000).
3. J. Durnin, "Exact solutions for nondiffracting beams. I. The scalar theory," JOSA A **4** (4), 651-654 (1987).
4. J. Durnin, J. Miceli Jr, and J. Eberly, "Diffraction-free beams," Physical Review Letters **58** (15), 1499 (1987).
5. D. McGloin and K. Dholakia, "Bessel beams: diffraction in a new light," Contemporary Physics **46** (1), 15-28 (2005).
6. M. A. Bandres, J. C. Gutiérrez-Vega, and S. Chávez-Cerda, "Parabolic nondiffracting optical wave fields," Optics Letters **29** (1), 44-46 (2004).
7. S. Chávez-Cerda, J. Gutiérrez-Vega, and G. New, "Elliptic vortices of electromagnetic wave fields," Optics Letters **26** (22), 1803-1805 (2001).
8. J. C. Gutiérrez-Vega, M. Iturbe-Castillo, and S. Chávez-Cerda, "Alternative formulation for invariant optical fields: Mathieu beams," Optics Letters **25** (20), 1493-1495 (2000).
9. J.-Y. Lu and J. F. Greenleaf, "Nondiffracting X waves-exact solutions to free-space scalar wave equation and their finite aperture realizations," IEEE Transactions on Ultrasonics, Ferroelectrics, and Frequency Control **39** (1), 19-31 (1992).
10. D. N. Christodoulides, N. K. Efremidis, P. Di Trapani, and B. A. Malomed, "Bessel X waves in two-and three-dimensional bidispersive optical systems," Optics Letters **29** (13), 1446-1448 (2004).
11. M. V. Berry and N. L. Balazs, "Nonspreading wave Packets," American Journal of Physics **47**, 264 (1979).
12. O. Vallée and M. Soares (eds), *Airy functions and applications to physics*. (Imperial College Press, 2004).
13. G. A. Siviloglou and D. N. Christodoulides, "Accelerating finite energy Airy beams," Optics Letters **32** (8), 979-981 (2007).
14. G. A. Siviloglou, J. Broky, A. Dogariu, and D. N. Christodoulides, "Observation of Accelerating Airy Beams," Physical Review Letters **99**, 213901 (2007).
15. J. Broky, G. A. Siviloglou, A. Dogariu, and D. N. Christodoulides, "Self-healing properties of optical Airy beams," Optics Express **16** (17), 12880 (2008).
16. E. Greenfield, M. Segev, W. Walasik, and O. Raz, "Accelerating Light Beams along Arbitrary Convex Trajectories," Physical Review Letters **106**, 213902 (2011).

17. L. Froehly, F. Courvoisier, A. Mathis, M. Jacquot, L. Furfaro, R. Giust, P. A. Lacourt, and J. M. Dudley, "Arbitrary accelerating micron-scale caustic beams in two and three dimensions," Optics Express **19** (17), 16455-16465 (2011).
18. Y. Hu, D. Bongiovanni, Z. Chen, and R. Morandotti, "Multipath multicomponent self-accelerating beams through spectrum-engineered position mapping," Physical Review A **88**, 043809 (2013).
19. P. Zhang, Y. Hu, D. Cannan, A. Salandrino, T. Li, R. Morandotti, X. Zhang, and Z. Chen, "Generation of linear and nonlinear nonparaxial accelerating beams," Optics Letters **37** (14), 2820-2822 (2012).
20. I. Kaminer, R. Bekenstein, J. Nemirovsky, and M. Segev, "Nondiffracting Accelerating Wave Packets of Maxwell's Equations," Physical Review Letters **108**, 163901 (2012).
21. P. Zhang, Y. Hu, T. Li, D. Cannan, X. Yin, R. Morandotti, Z. Chen, and X. Zhang, "Nonparaxial Mathieu and Weber Accelerating Beams," Physical Review Letters **109**, 193901 (2012).
22. R.-S. Penciu, V. Paltoglou, and N. K. Efremidis, "Closed-form expressions for nonparaxial accelerating beams with pre-engineered trajectories," Optics Letters **40** (7), 1444-1447 (2015).
23. M. A. Alonso and M. A. Bandres, "Generation of nonparaxial accelerating fields through mirrors. I: Two dimensions," Optics Express **22** (6), 7124-7132 (2014).
24. M. A. Alonso and M. A. Bandres, "Generation of nonparaxial accelerating fields through mirrors. II: Three dimensions," Optics Express **22** (12), 14738-14749 (2014).
25. R.-P. Chen, C.-F. Yin, X.-X. Chu, and H. Wang, "Effect of Kerr nonlinearity on an Airy beam," Physical Review A **82** (4), 043832 (2010).
26. Y. Hu, S. Huang, P. Zhang, C. Lou, J. Xu, and Z. Chen, "Persistence and breakdown of Airy beams driven by an initial nonlinearity," Optics Letters **35** (23), 3952-3954 (2010).
27. Y. Fattal, A. Rudnick, and D. M. Marom, "Soliton shedding from Airy pulses in Kerr media," Optics Express **19** (18), 17298-17307 (2011).
28. T. Ellenbogen, N.Voloch-Bloch, A. Ganany-Padowicz, and A. Arie, "Nonlinear generation and manipulation of Airy beams," Nature Photonics **3**, 395 - 398 (2009).
29. Z. Ye, S. Liu, C. Lou, P. Zhang, Y. Hu, D. Song, J. Zhao, and Z. Chen, "Acceleration control of Airy beams with optically induced refractive-index gradient," Optics Letters **36** (16), 3230-3232 (2011).
30. R. Chen, C. Yin, X. Chu, and H. Wang, "Effect of Kerr nonlinearity on an Airy beam," Physical Review A **82**, 043832 (2010).
31. I. Kaminer, M. Segev, and D. N. Christodoulides, "Self-Accelerating Self-Trapped Optical Beams," Physical Review Letters **106**, 213903 (2011).
32. A. Lotti, D. Faccio, A. Couairon, D. Papazoglou, P. Panagiotopoulos, D. Abdollahpour, and S. Tzortzakis, "Stationary nonlinear Airy beams," Physical Review A **84** (2), 021807 (2011).
33. Y. Hu, M. Li, D. Bongiovanni, M. Clerici, J. Yao, Z. Chen, J. Azaña, and R. Morandotti, "Spectrum to distance mapping via nonlinear Airy pulses," Optics Letters **38**, 380-383 (2013).
34. R. Driben, Y. Hu, Z. Chen, B. A. Malomed, and R. Morandotti, "Inversion and tight focusing of Airy pulses under the action of third-order dispersion," Optics Letters **38** (14), 2499-2501 (2013).

35. L. Zhang, J. Zhang, Y. Chen, A. Liu, and G. Liu, "Dynamic propagation of finite-energy Airy pulses in the presence of higher-order effects," JOSA B **31** (4), 889-897 (2014).
36. Y. Hu, A. Tehranchi, S. Wabnitz, R. Kashap, Z. Chen, and R. Morandotti, "Improved intrapulse Raman scattering control via asymmetric Airy pulses," Physical Review Letters **114** (7), 073901 (2015).
37. A. Chong, W. H. Renninger, D. N. Christodoulides, and F. W. Wise, "Airy-Bessel wave packets as versatile linear light bullets," Nature Photonics. **4**, 103-106 (2010).
38. D. Abdollahpour, S. Suntsov, D. G. Papazoglou, and S. Tzortzakis, "Spatio-temporal Airy Light Bullets in the Linear and Nonlinear Regimes," Physical Review Letters **105**, 253901 (2010).
39. P. Polynkin, M. Kolesik, J. V. Moloney, G. A. Siviloglou, and D. N. Christodoulides, "Curved Plasma Channel Generation Using Ultraintense Airy Beams," Science **324** (5924), 229-232 (2009).
40. J. Baumgartl, M. Mazilu, and K. Dholakia, "Optically mediated particle clearing using Airy wavepackets," Nature Photonics. **2**, 675-678 (2008).
41. N. Voloch-Bloch, Y. Lereah, Y. Lilach, A. Gover, and A. Arie, "Generation of electron Airy beams," Nature **494**, 331 (2013).
42. M. Clerici, Y. Hu, P. Lassonde, C. Milián, A. Couairon, D. N. Christodoulides, Z. Chen, L. Razzari, F. Vidal, and F. Légaré, "Laser-assisted guiding of electric discharges around objects," Science Advances **1** (5), e1400111 (2015).
43. E. Greenfield, I. Kaminer, and M. Segev, presented at the Frontiers in Optics, 2012 (unpublished).
44. A. Mathis, F. Courvoisier, R. Giust, L. Furfaro, M. Jacquot, L. Froehly, and J. M. Dudley, "Arbitrary nonparaxial accelerating periodic beams and spherical shaping of light," Optics Letters **38** (13), 2218-2220 (2013).
45. M. A. Bandres, "Accelerating parabolic beams," Optics Letters **33** (15), 1678-1680 (2008).
46. J. A. Davis, M. J. Mitry, M. A. Bandres, and D. M. Cottrell, "Observation of accelerating parabolic beams," Optics Express **16** (17), 12866-12871 (2008).
47. P. Aleahmad, M.-A. Miri, M. S. Mills, I. Kaminer, M. Segev, and D. N. Christodoulides, "Fully Vectorial Accelerating Diffraction-Free Helmholtz Beams," Physical Review Letters **109**, 203902 (2012).
48. L. I. Schiff, "Quantum Mechanics 3rd," New York: M cGraw-Hill, 61-62 (1968).
49. D. M. Greenberger, American Journal of Physics **48**, 256 (1980).
50. Y. Kaganovsky and E. Heyman, "Wave analysis of Airy beams," Optics Express **18** (8), 8440-8452 (2010).
51. I. D. Chremmos, Z. Chen, D. N. Christodoulides, and N. K. Efremidis, "Abruptly autofocusing and autodefocusing optical beams with arbitrary caustics," Physical Review A **85**, 023828 (2012).
52. E. Greenfield, M. Segev, W. Walasik, and O. Raz, "Accelerating Light Beams along Arbitrary Convex Trajectories," Physical Review Letters **106**, 213902 (2011).
53. M. Zamboni-Rached, K. Z. Nóbrega, and C. A. Dartora, "Analytic description of Airy-type beams when truncated by finite apertures," Optics Express **20** (18), 19972-19977 (2012).

54. G. A. Siviloglou, J. Broky, A. Dogariu, and D. N. Christodoulides, "Ballistic dynamics of Airy beams," Optics Letters **33** (3), 207-209 (2008).
55. I. M. Besieris and A. M. Shaarawi, "A note on an accelerating finite energy Airy beam," Optics Letters **32** (16), 2447-2449 (2007).
56. J. W. Goodman, *Introduction to Fourier Optics*. (Mc-Graw-Hill, New York, 1996).
57. Z. Bouchal, J. Wagner, and M. Chlup, "Self-reconstruction of a distorted nondiffracting beam," Optics Communications **151** (4), 207-211 (1998).
58. H. I. Sztul and R. R. Alfano, "The Poynting vector and angular momentum of Airy beams," Optics Express **16** (13), 9411-9416 (2008).
59. M. Bandres, "Accelerating beams," Optics Letters **34** (24), 3791 (2009).
60. Y. Hu, D. Bongiovanni, Z. Chen, and R. Morandotti, "Periodic self-accelerating beams by combined phase and amplitude modulation in the Fourier space," Optics Letters **38** (17), 3387-3389 (2013).
61. Y. Wen, Y. Chen, Y. Zhang, H. Chen, and S. Yu, "Winding light beams along elliptical helical trajectories," Physical Review A **94** (1), 013829 (2016).
62. Y. Hu, P. Zhang, C. Lou, S. Huang, J. Xu, and Z. Chen, "Optimal control of the ballistic motion of Airy beams," Optics Letters **35**, 2260 (2010).
63. Y. Hu, P. Zhang, S. Huang, C. Lou, J. Xu, and Z. Chen, presented at the SPIE Optical Engineering + Applications, 2010 (unpublished).
64. Y. Qian and S. Zhang, "Quasi-Airy beams along tunable propagation trajectories and directions," Optics Express **24** (9), 9489-9500 (2016).
65. N. K. Efremidis, "Airy trajectory engineering in dynamic linear index potentials," Optics Letters **36** (15), 3006-3008 (2011).
66. C.-Y. Hwang, K.-Y. Kim, and B. Lee, "Dynamic control of circular Airy beams with linear optical potentials," IEEE Photonics Journal **4** (1), 174-180 (2012).
67. Y. Zhang, M. R. Belić, L. Zhang, W. Zhong, D. Zhu, R. Wang, and Y. Zhang, "Periodic inversion and phase transition of finite energy Airy beams in a medium with parabolic potential," Optics Express **23** (8), 10467-10480 (2015).
68. Y. Zhang, X. Liu, M. R. Belić, W. Zhong, M. S. Petrović, and Y. Zhang, "Automatic Fourier transform and self-Fourier beams due to parabolic potential," Annals of Physics **363**, 305-315 (2015).
69. A. V. Novitsky and D. V. Novitsky, "Nonparaxial Airy beams: role of evanescent waves," Optics Letters **34** (21), 3430-3432 (2009).
70. M. Abramowitz and I. A. Stegun, "Handbook of Mathematical Functions. Ninth printing", (New York: Dover, 1972).
71. M. V. Berry and C. Upstill, "IV catastrophe optics: morphologies of caustics and their diffraction patterns," Progress in Optics **18**, 257-346 (1980).
72. J. A. Davis, D. M. Cottrell, J. Campos, M. J. Yzuel, and I. Moreno, "Encoding amplitude information onto phase-only filters," Applied Optics **38** (23), 5004-5013 (1999).
73. Y. S. Kivshar and G. Agrawal, *Optical solitons: from fibers to photonic crystals*. (Academic press, 2003).

74. A. Couairon, "Dynamics of femtosecond filamentation from saturation of self-focusing laser pulses," Physical Review A **68** (1), 015801 (2003).
75. D. N. Christodoulides and M. Carvalho, "Bright, dark, and gray spatial soliton states in photorefractive media," JOSA B **12** (9), 1628-1633 (1995).
76. C. Denz, M. Schwab, and C. Weilnau, *Transverse-pattern formation in photorefractive optics*. (Springer Science & Business Media, 2003).
77. Y. Fattal, A. Rudnick, and D. M. Marom, "Soliton shedding from Airy pulses in Kerr media," Optics Express **19**, 17298 (2011).
78. P. Panagiotopoulos, D. Abdollahpour, A. Lotti, A. Couairon, D. Faccio, D. Papazoglou, and S. Tzortzakis, "Nonlinear propagation dynamics of finite-energy Airy beams," Physical Review A **86** (1), 013842 (2012).
79. S. Jia, J. Lee, J. W. Fleischer, G. A. Siviloglou, and D. N. Christodoulides, "Diffusion-trapped Airy beams in photorefractive media," Physical Review Letters **104** (25), 253904 (2010).
80. Y. Hu, Z.Sun, D. Bongiovanni, D. Song, C. Lou, J. Xu, Z. Chen, and R. Morandotti, "Reshaping the trajectory and spectrum of nonlinear Airy beams," Optics Letters **37**, 3201 (2012).
81. B. H. Kolner, "Space-time duality and the theory of temporal imaging," IEEE Journal of Quantum Electronics **30** (8), 1951-1963 (1994).
82. I. M. Besieris and A. M. Shaarawi, "Accelerating Airy wave packets in the presence of quadratic and cubic dispersion," Physical Review E **78** (4), 046605 (2008).
83. W. Cai, L. Wang, and S. Wen, "Evolution of airy pulses in the present of third order dispersion," Optik-International Journal for Light and Electron Optics **124** (22), 5833-5836 (2013).
84. L. Zhang, K. Liu, H. Zhong, J. Zhang, Y. Li, and D. Fan, "Effect of initial frequency chirp on Airy pulse propagation in an optical fiber," Optics Express **23** (3), 2566-2576 (2015).
85. G. P. Agrawal, *Nonlinear fiber optics*. (Accademic, New York, 2001), 3rd ed.
86. L. Zhang and H. Zhong, "Modulation instability of finite energy Airy pulse in optical fiber," Optics Express **22** (14), 17107-17115 (2014).
87. V. E. Zakharov and L. Ostrovsky, "Modulation instability: the beginning," Physica D: Nonlinear Phenomena **238** (5), 540-548 (2009).
88. J. M. Dudley, G. Genty, and S. Coen, "Supercontinuum generation in photonic crystal fiber," Reviews of Modern Physics **78** (4), 1135 (2006).
89. R. W. Boyd, *Nonlinear Optics*. (Academic press, 2003).
90. L. Zhang, H. Zhong, Y. Li, and D. Fan, "Manipulation of Raman-induced frequency shift by use of asymmetric self-accelerating Airy pulse," Optics Express **22** (19), 22598-22607 (2014).
91. C. Ament, P. Polynkin, and J. V. Moloney, "Supercontinuum generation with femtosecond self-healing Airy pulses," Physical Review Letters **107** (24), 243901 (2011).
92. W.-P. Zhong, M. R. Belić, and T. Huang, "Three-dimensional finite-energy Airy self-accelerating parabolic-cylinder light bullets," Physical Review A **88** (3), 033824 (2013).
93. W.-P. Zhong, M. R. Belić, and Y. Zhang, "Airy-Tricomi-Gaussian compressed light bullets," The European Physical Journal Plus **131** (2), 1-8 (2016).
94. P. Panagiotopoulos, D. G. Papazoglou, A. Couairon, and S. Tzortzakis, "Sharply autofocused ring-Airy beams transforming into non-linear intense light bullets," Nature Communications **4**, 2622 (2013).

95. D. W. Koopman and T. Wilkerson, "Channeling of an ionizing electrical streamer by a laser beam," Journal of Applied Physics **42** (5), 1883-1886 (1971).
96. M. Miki, Y. Aihara, and T. Shindo, "Development of long gap discharges guided by a pulsed CO2 laser," Journal of physics D: Applied Physics **26** (8), 1244 (1993).
97. X. M. Zhao and J.-C. Diels, "Femtosecond pulses to divert lightning," Laser Focus World **29**, 113 (1993).
98. J. Baumgartl, M. Mazilu, and K. Dholakia, "Optically mediated particle clearing using Airy wavepackets," Nature Photonics **2**, 675 - 678 (2008).
99. J. Baumgartl, T. Čižmár, M. Mazilu, V. Chan, A. Carruthers, B. Capron, W. McNeely, E. M. Wright, and K. Dholakia, "Optical path clearing and enhanced transmission through colloidal suspensions," Optics Express **18** (16), 17130-17140 (2010).
100. A. Braun, G. Korn, X. Liu, D. Du, J. Squier, and G. Mourou, "Self-channeling of high-peak-power femtosecond laser pulses in air," Optics Letters **20** (1), 73-75 (1995).
101. P. Polynkin, M. Kolesik, and J. Moloney, "Filamentation of femtosecond laser Airy beams in water," Physical Review Letters **103** (12), 123902 (2009).
102. N. Voloch-Bloch, Yossi Lereah, Y. Lilach, A. Gover, and A. Arie, "Generation of electron Airy beams," Nature **494**, 331–335 (2013).
103. A. Mathis, F. Courvoisier, L. Froehly, L. Furfaro, M. Jacquot, P.-A. Lacourt, and J. M. Dudley, "Micromachining along a curve: Femtosecond laser micromachining of curved profiles in diamond and silicon using accelerating beams," Applied Physics Letters **101** (7), 071110 (2012).
104. A. Mathis, L. Froehly, L. Furfaro, M. Jacquot, J. M. Dudley, and F. Courvoisier, "Direct machining of curved trenches in silicon with femtosecond accelerating beams," Journal of the European Optical Society - Rapid Publications **8**, 13019 (2013).
105. G. Porat, I. Dolev, O. Barlev, and A. Arie, "Airy beam laser," Optics Letters **36** (20), 4119-4121 (2011).
106. P. Rose, F. Diebel, M. Boguslawski, and C. Denz, "Airy beam induced optical routing," Applied Physics Letters **102** (10), 101101 (2013).
107. T. Vettenburg, H. I. Dalgarno, J. Nylk, C. Coll-Lladó, D. E. Ferrier, T. Čižmár, F. J. Gunn-Moore, and K. Dholakia, "Light-sheet microscopy using an Airy beam," Nature Methods **11** (5), 541-544 (2014).
108. I. Dolev, T. Ellenbogen, and A. Arie, "Switching the acceleration direction of Airy beams by a nonlinear optical process," Optics Letters **35** (10), 1581-1583 (2010).
109. I. Dolev, T. Ellenbogen, N. Voloch-Bloch, and A. Arie, "Control of free space propagation of Airy beams generated by quadratic nonlinear photonic crystals," Applied Physics Letters **95** (20), 201112 (2009).
110. I. Dolev and A. Arie, "Three wave mixing of airy beams in a quadratic nonlinear photonic crystals," Applied Physics Letters **97** (17), 171102 (2010).
111. A. Salandrino and D. N. Christodoulides, "Airy plasmon: a nondiffracting surface wave," Optics Letters **35** (12), 2082-2084 (2010).
112. P. Zhang, S. Wang, Y. Liu, X. Yin, C. Lu, Z. Chen, and X. Zhang, "Plasmonic Airy beams with dynamically controlled trajectories," Optics Letters **36** (16), 3191-3193 (2011).

113. W. Liu, D. N. Neshev, I. V. Shadrivov, A. E. Miroshnichenko, and Y. S. Kivshar, "Plasmonic Airy beam manipulation in linear optical potentials," Optics Letters **36** (7), 1164-1166 (2011).
114. A. Minovich, A. E. Klein, N. Janunts, T. Pertsch, D. N. Neshev, and Y. S. Kivshar, "Generation and near-field imaging of Airy surface plasmons," Physical Review Letters **107** (11), 116802 (2011).
115. L. Li, T. Li, S. Wang, C. Zhang, and S. Zhu, "Plasmonic Airy beam generated by in-plane diffraction," Physical Review Letters **107** (12), 126804 (2011).
116. D. G. Papazoglou, N. K. Efremidis, D. N. Christodoulides, and S. Tzortzakis, "Observation of abruptly autofocusing waves," Optics Letters **36** (10), 1842-1844 (2011).
117. P. Zhang, J. Prakash, Z. Zhang, M. S. Mills, N. K. Efremidis, D. N. Christodoulides, and Z. Chen, "Trapping and guiding microparticles with morphing autofocusing Airy beams," Optics Letters **36** (15), 2883-2885 (2011).
118. Y. Hu, G. A. Siviloglou, P. Zhang, N. K. Efremidis, D. N. Christodoulides, and Z. Chen, "Self-accelerating Airy Beams: Generation, Control, and Applications", in *Nonlinear Photonics and Novel Optical Phenomena*, edited by Zhigang Chen and Roberto Morandotti (Springer, 2012), Vol. 170, pp. 1-46.
119. M. A. Bandres, I. Kaminer, M. S. Mills, B. M. Rodríguez-Lara, E. Greenfield, M. Segev, and D. N. Christodoulides, "Accelerating Optical Beams," Optics & Photonics News **24** (6), 30-37 (2013).
120. F. Courvoisier, A. Mathis, L. Froehly, R. Giust, L. Furfaro, P.-A. Lacourt, M. Jacquot, and J. M. Dudley, "Sending femtosecond pulses in circles: highly nonparaxial accelerating beams," Optics Letters **37** (10), 1736-1738 (2012).
121. J. Zhao, P. Zhang, D. Deng, J. Liu, Y. Gao, I. D. Chremmos, N. K. Efremidis, D. N. Christodoulides, and Z. Chen, "Observation of self-accelerating Bessel-like optical beams along arbitrary trajectories," Optics Letters **38**, 498-500 (2013).
122. B. Boashash, "Estimating and interpreting the instantaneous frequency of a signal. I. Fundamentals," Proceedings of the IEEE **80** (4), 520-538 (1992).
123. S. Barwick, " Reduced side-lobe Airy beams" Optics Letters **36**, 2827 (2011).
124. M. V. Berry and S. Klein, "Colored diffraction catastrophes," Proceedings of the National Academy of Sciences **93**, 2614 (1996).
125. N. Wiersma, N. Marsal, M. Sciamanna, and D. Wolfersberger, "All-optical interconnects using Airy beams," Optics Letters **39** (20), 5997-6000 (2014).
126. M. Clerici, Y. Hu, P. Lassonde, C. Milián, A. Couairon, D. N. Christodoulides, Z. Chen, L. Razzari, F. Vidal, F. Légaré, D. Faccio, and R. Morandotti, "Laser-assisted guiding of electric discharges around objects," Science Advances **1** (5), e1400111 (2015).
127. B. K. Singh, R. Remez, Y. Tsur, and A. Arie, "Super-Airy beam: self-accelerating beam with intensified main lobe," Optics Letters **40** (20), 4703-4706 (2015).
128. H. Jeffreys and B. Jeffreys, *Methods of Mathematical Physics*. (Cambridge university press, 1999).
129. Y. Silberberg, "Collapse of optical pulses," Optics Letters **15** (22), 1282-1284 (1990).
130. A. M. Boris, M. Dumitru, W. Frank, and T. Lluis, "Spatio-temporal optical solitons," Journal of Optics B **7** (5), R53 (2005).

131. P. Di Trapani, G. Valiulis, A. Piskarskas, O. Jedrkiewicz, J. Trull, C. Conti, and S. Trillo, "Spontaneously Generated X-Shaped Light Bullets," Physical Review Letters **91** (9), 093904 (2003).
132. M. A. Porras and P. Di Trapani, "Localized and stationary light wave modes in dispersive media," Physical Review E **69** (6), 066606 (2004).
133. P. Saari, "Laterally accelerating Airy pulses," Optics Express **16** (14), 10303-10308 (2008).
134. J. Sharpe, U. Ahlgren, P. Perry, B. Hill, A. Ross, J. Hecksher-Sørensen, R. Baldock, and D. Davidson, "Optical projection tomography as a tool for 3D microscopy and gene expression studies," Science **296** (5567), 541-545 (2002).
135. J. G. Fujimoto, "Optical coherence tomography for ultrahigh resolution in vivo imaging," Nature Biotechnology **21** (11), 1361-1367 (2003).
136. D. Bongiovanni, Y. Hu, B. Wetzel, R. A. Robles, G. Mendoza González, E. A. Marti-Panameño, Z. Chen, and R. Morandotti, "Efficient Optical Energy Harvesting in Self-Accelerating Beams," Scientific Reports **5**, 13197 (2015).
137. F. Deng and D. Deng, "Three-dimensional localized Airy-Hermite-Gaussian and Airy-Helical-Hermite-Gaussian wave packets in free space," Optics Express **24** (5), 5478-5486 (2016).
138. I. Dolev, I. Kaminer, A. Shapira, M. Segev, and A. Arie, "Experimental observation of self-accelerating beams in quadratic nonlinear media," Physical Review Letters **108** (11), 113903 (2012).
139. Y. Zhang, M. R. Belić, H. Zheng, H. Chen, C. Li, Y. Li, and Y. Zhang, "Interactions of Airy beams, nonlinear accelerating beams, and induced solitons in Kerr and saturable nonlinear media," Optics Express **22** (6), 7160-7171 (2014).
140. L. Solymar, D. J. Webb, and A. Grunnet-Jepsen, *The Physics and Applications of Photorefractive Materials*. (Clarendon Press, 1996).
141. N. Kukhtarev, V. Markov, S. Odulov, M. Soskin, and V. Vinetskii, "Holographic storage in electrooptic crystals. II. Beam coupling—light amplification," Ferroelectrics **22** (1), 961-964 (1978).
142. S. Gatz and J. Herrmann, "Anisotropy, nonlocality, and space-charge field displacement in (2+1)-dimensional self-trapping in biased photorefractive crystals," Optics Letters **23** (15), 1176-1178 (1998).
143. B. Crosignani, P. Di Porto, A. Degasperis, M. Segev, and S. Trillo, "Three-dimensional optical beam propagation and solitons in photorefractive crystals," JOSA B **14** (11), 3078-3090 (1997).
144. E. DelRe, G. De Masi, A. Ciattoni, and E. Palange, "Pairing space-charge field conditions with self-guiding for the attainment of circular symmetry in photorefractive solitons," Applied Physics Letters **85** (23), 5499-5501 (2004).
145. A. Zozulya, D. Anderson, A. Mamaev, and M. Saffman, "Self-focusing and soliton formation in media with anisotropic nonlocal material response," EPL (Europhysics Letters) **36** (6), 419 (1996).
146. M. Wesner, C. Herden, D. Kip, E. Krätzig, and P. Moretti, "Photorefractive steady state solitons up to telecommunication wavelengths in planar SBN waveguides," Optics Communications **188** (1), 69-76 (2001).

147. M. Segev, G. C. Valley, B. Crosignani, P. Diporto, and A. Yariv, "Steady-state spatial screening solitons in photorefractive materials with external applied field," Physical Review Letters **73** (24), 3211 (1994).
148. L. Jinsong and L. Keqing, "Screening-photovoltaic spatial solitons in biased photovoltaic–photorefractive crystals and their self-deflection," JOSA B **16** (4), 550-555 (1999).
149. A. Lotti, D. Faccio, A. Couairon, D. G. Papazoglou, P. Panagiotopoulos, D. Abdollahpour, and S. Tzortzakis, "Stationary nonlinear Airy beams," Physical Review A **84**, 021807 (2011).
150. C. Froehly, B. Colombeau, and M. Vampouille, *Progress in Optics*. (Amsterdam, North-Holland, 1983), E. Wolf ed.
151. J. Heritage, R. Thurston, W. Tomlinson, A. Weiner, and R. Stolen, "Spectral windowing of frequency-modulated optical pulses in a grating compressor," Applied Physics Letters **47** (2), 87-89 (1985).
152. A. Weiner, J. Heritage, and R. Thurston, "Synthesis of phase-coherent, picosecond optical square pulses," Optics Letters **11** (3), 153-155 (1986).

List of figures